CHAPTER 5

Steel-Hull Corrosion Analysis of USS *Arizona*

Donald L. Johnson, Brent M. Wilson, John D. Makinson, Robert De Angelis, William N. Weins, and James D. Carr

INTRODUCTION

Corrosion research on USS *Arizona* focused on understanding and characterizing the specific nature of corrosion occurring on the vessel and determining the corrosion rate for different structural elements of the ship. The goal was to establish a curve of deterioration and "plot" where *Arizona* currently falls on that curve. Predictive modeling of USS *Arizona* hull deterioration was accomplished by developing a Finite Element Model (FEM), constructed by the National Institute of Standards and Technology (NIST) in Gaithersburg, MD (see Chapter 6). The FEM was designed to model *Arizona*'s structural deterioration and eventual collapse—information critical for developing a sound, scientifically-based management plan and for determining when, or if, intervening in the vessel's natural deterioration should be considered. The FEM, however, was designed to model increasing hull stress as a function of decreasing percentage of remaining hull steel, and therefore lacks a specific time element. Corrosion analysis reported in this chapter supplies the necessary corrosion rate to make the FEM predictive. A key first-step in determining the steel-hull corrosion rate was to determine the remaining thicknesses of surviving steel-hull components. This could then be compared to as-

built steel thicknesses from surviving ship's plans. Because direct measurement of remaining steel thickness could only be completed in limited areas, a corrosion rate model had to be created for application to areas of *Arizona*'s hull in different environmental conditions, including exterior, interior, above the harbor bottom, and below the harbor bottom. Because the battleship is a large, complex three-dimensional structure, and it is impossible to directly measure corrosion rates for all critical elements, there was necessarily some generalizing and use of inferential data to derive rates of deterioration, particularly for inaccessible internal structures. In order for a general corrosion rate model to be accurate, the overall corrosion process must be recognized and described, including identifying relevant environmental variables that affect the corrosion process.

This chapter presents a comprehensive synthesis of 1998–2007 research on corrosion of USS *Arizona*'s steel-hull. It begins by describing the background necessary to evaluate the corrosion process taking place on *Arizona*'s hull, including a review of parameters relevant to electrochemical corrosion of steel in seawater, a discussion of hull steel chemistry and microstructure, and seawater chemistry. The chapter then describes the corrosion process in detail through a combination of theoretical and direct experimental applications, such as *in situ* corrosion measurements and constituent analysis of concretion covering the ship. Finally, the chapter details current understanding of hull corrosion rate variability (including factors which control the rate) and presents an analysis of *Arizona*'s long-term structural integrity, with a particular focus on primary oil containment spaces within the hull.

ELECTROCHEMICAL CORROSION OF STEEL IN SEAWATER

CORROSION PROCESS

Corrosion is an electrochemical process, which means that direct current, though very small (on order of microamperes), flows in a cell made up of three necessary components: (1) areas of opposing polarity; (2) an electrolyte; and (3) a return electrical circuit path. If any one of the three electrochemical components is missing, corrosion will not occur.

As in a battery, positive and negative poles define areas that exhibit a potential difference that constitute the driving force for the flow of current. Potential, or voltage, is the difference in

electrical charge between two points in a circuit expressed in volts or millivolts (mV). Two modes of current are used to explain the corrosion process. Current flowing from the negative pole or anode, through the electrolyte to the positive pole or cathode, and returning to the anode via a metallic return circuit path is referred to as positive current, and is associated with the flow of ions in the electrolyte. Current flowing in the opposite direction from the anode through the metallic circuit to the cathode is referred to as negative current, and is associated with the flow of electrons. To put this into perspective, adjacent regions on the metal hull act separately as anode and cathode, and the hull metal between the anode and cathode completes the metallic circuit needed to conduct electrons between them. The electrolyte in contact with hull metal conducts ions in solution in the opposite direction. Corrosion always occurs at areas where positive current leaves the structure and enters the electrolyte or corroding medium, and is identified as the anode (Figure 5.1).

Opposing polarity or potential difference between two areas is created in a variety of ways: the most obvious is the relative activity of elements in the electromotive force (EMF) series when any two (or more) are immersed in an aqueous solution saturated with that metal's ions (Table 5.1). It should be noted that the reactions are written as reduction reactions, for example, $Fe^{+2} + 2e = Fe$, where the reduction potentials are given in Table 5.1 as the Standard Hydrogen Electrode (SHE). Reduction potentials match the polarity of experimentally measured potentials, in accordance with the Stockholm convention. When comparing potentials in a given system, the higher potential is cathodic to the lower potential. For example, comparison of copper (Cu) and iron (Fe) shows a potential difference of 789 millivolts (mV). Assuming that both metals are placed in an electrolyte, such as sea water, and connected to each other by a conductor, Fe will corrode because it is more negative than Cu, and Cu will act as the opposing pole, or cathode, and will not corrode. This is the basis for the principle of cathodic protection, since the Fe in effect protects the Cu (see below for a more detailed analysis of cathodic protection). Zinc (Zn) is often connected to Fe structures to purposely cause the Zn to corrode and render the Fe a cathode; in this case the Zn is known as a sacrificial anode. In sea water, an alloy of aluminum is normally chosen to protect Fe (and steel) structures because it performs better than Zn in the presence of chloride ions present in sea water. The EMF series is based on concentrations of one mole per liter of that metal ion in the solution. In real situations,

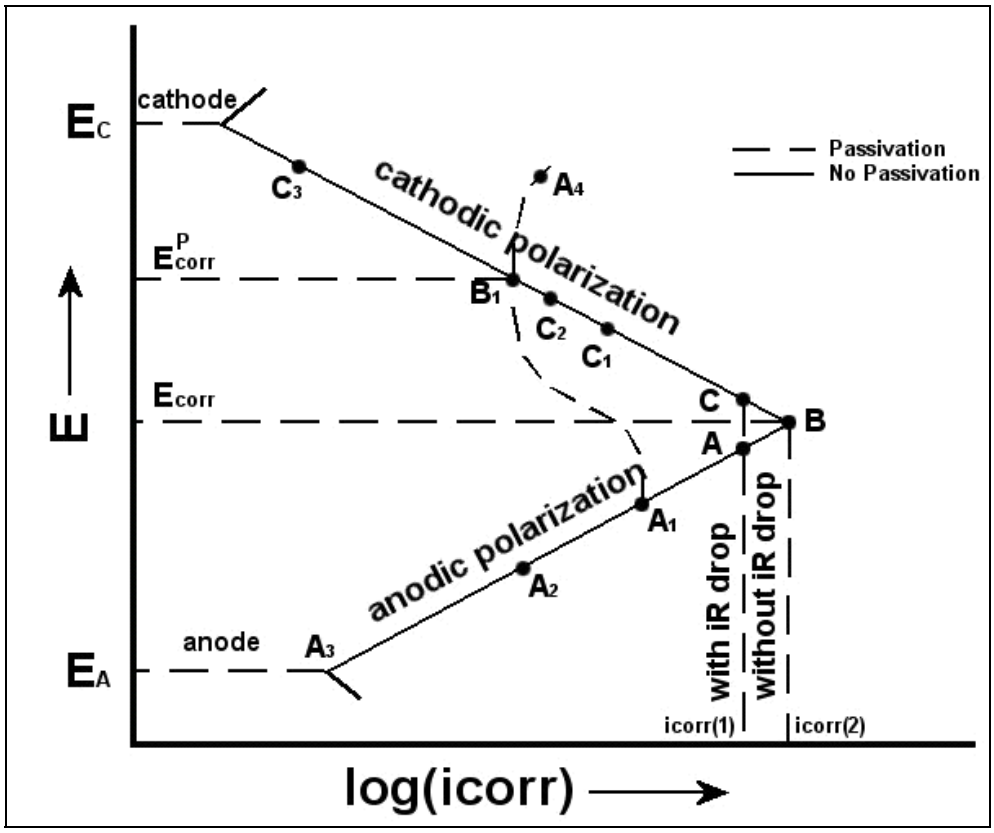

Figure 5.1. Typical polarization diagram with passivation superimposed (dashed).

Element E^0	Potential (millivolts) Relative to hydrogen electrode
Au/Au+	1498
Ag/Ag+	799
Cu/Cu+	342
Hydrogen	0
Fe/Fe++	-447
Zn/Zn++	-762
Al/Al+++	-1,662

Table 5.1. EMF Series for Selected Elements.

concentrations are much lower and correction for concentration and temperature is made by applying the Nerst equation:

$$E = E^0 + 2.3\ (RT / nF)\ [\log (C)] \qquad [1]$$

where

E^0 (SHE) is standard potential at 1 mole/liter concentration of metal ion
R is the gas constant 8.314 J/mole °K
T is temperature (° K)
n is valence
F is Faraday constant, 96,500 Coulombs/equivalent (One coulomb = one ampere second and one equivalent = atomic wt./ valence)
C is concentration of oxidized species, Fe^{+2} (mole/liter)

While a bi-metallic (or two metal) cell is operative in many complex structures, there are a variety of cells which can cause corrosion without the existence of a second metal. First, oxygen cell corrosion is common in situations where the oxygen is not uniformly distributed over the surface. The areas low in oxygen corrodes faster than the area higher in oxygen—in such a case the area lower in oxygen is anodic to the area higher in oxygen. A specific class of metals forms an inherently thin yet very stable, uniform and protective layer in oxidizing environments. The metals in this class "passivate" readily and are corrosion resistant in the presence of oxygen. Examples of such metals include stainless steels and aluminum alloys. Steel will passivate in strong oxidizing solutions such as dilute nitric acid, but normally not in seawater. Second, temperature differential cells develop when a temperature difference occurs across a metal structure. An area at higher temperature is theoretically predicted to be anodic or negative to an area at lower temperature as Equation [1] indicates. Due to the very small shift in potential occurring at ordinary temperatures, this effect is often masked by other variables. Third, microconstituent corrosion cells, another form of corrosion cell, are common since most structural materials are alloys made up of a combination of other metals or non-metals. For example, mild steel used in ship construction may contain less than 0.2 % carbon yet undergo corrosion because the compound iron carbide, formed during cooling after fabrication, is

cathodic to the adjacent nearly pure iron making up the matrix. This is particularly significant when the pH is low or acidic. It should be noted that iron carbide is not an impurity since it imparts added strength to the steel. Fourth, a stress cell is often evident on steel where the metal has been stressed at sharp bend areas. The stressed area becomes anodic to the remaining structure. Finally, the differential electrolyte cell is typical of corrosion in which the composition of the electrolyte varies over the metal surface. In theory, the area lowest in concentration of oxidized species (Fe^{+2}) is anodic to the area higher in concentration. In practical terms, the most common differential cell is oxygen cell corrosion, in which the oxygen concentration varies on the surface on a micro-scale.

An aqueous solution of water combined with other ions is normally the corroding medium or electrolyte. An electrolyte is ion conductive and will provide transport for cations (positively charged ions) and anions (negatively charged ions). In the case of steel, iron cations enter the solution at a rate proportional to the current flow, usually in the range of microamps per square centimeter ($\mu A/cm^2$). If the electrolyte is distilled water with no impurities or dissolved oxygen, corrosion will not occur because the electrolyte will not conduct positive current.

The return circuit path must be an electron conductor. For a bi-metallic (galvanic) cell, such as a steel hull in structural contact with copper alloy propellers, the hull will corrode, in part, because steel is anodic to copper. Since the hull (anode) is much larger than the propellers (cathode), the corrosion caused by the galvanic cell would be minimal because the corrosion current supported by the small propellers is spread over a much larger hull surface. If the propeller were made of aluminum, however, the propeller would be anodic to the hull and would corrode in a very short time because it is small relative to the hull, and a high current supported by a large cathodic hull would be focused on a small anodic propeller (high current density). A non-conducting insulator is sometimes used to isolate areas of opposing polarity by interrupting the electron conducting metallic circuit. In most cases it impossible to isolate such areas physically. For example, microconstituent corrosion between iron (alpha iron) and iron carbide in the steel microstructure cannot be prevented by electrical isolation because the two microconstituents in steel cannot be insulated from each other.

When iron or steel is placed in seawater, corrosion begins as a reaction in which the oxidation of metal is the anodic or corroding portion of a corrosion cell. Chemical reactions at the anode are usually fairly simple and involve the release of electrons and conversion of metal

from a solid to an ion that is soluble in aqueous solutions. Since the corrosion process in this discussion involves steel, the anode reaction is illustrated by the oxidation of iron:

$$Fe = Fe^{+2} + 2e^{-} \quad [2]$$

where

Fe is iron in steel

Fe^{+2} is iron ions in solution (oxidized specie)

2 electrons ($2e^{-}$) are released per gram-atom of iron

The cathode reaction can take many different forms depending upon the corroding electrolyte, flow conditions and temperature. Whatever form it takes, cathode reactions serve the purpose of consuming electrons produced at the anode. Since charge balance must be maintained, the rate of production and consumption of electrons must be equal. The two most common reduction reactions occurring at the cathode are hydrogen formation and oxygen consumption. Therefore, the rate of electron consumption, proportional to the corrosion rate, is typically governed in seawater by one or both of the following reactions:

$$\tfrac{1}{2} O_2 + H_2O + 2e^{-} = 2OH^{-} \quad \text{(Oxygen consumption)} \quad [3]$$

where

OH^{-} is the hydroxyl ion

or

$$2H^{+} + 2e^{-} = H_2 \quad \text{(Hydrogen evolution)} \quad [4]$$

where

H^{+} is the hydrogen ion

The corrosion product is loosely attached and does not become a diffusion barrier to oxygen. Combining equations [3] and [4], the overall corrosion reaction is given by:

$$Fe + \tfrac{1}{2} O_2 + H_2O = Fe(OH)_2 \quad [5]$$

$$4Fe(OH)2 + O2 = 2H2O + 2Fe2O3 \cdot H2O \quad [6]$$

The iron oxide formed in equation [6] is red brown and is the familiar rust on cars and buildings.

In areas where oxygen has limited access, chlorine ions, if present in the electrolyte, diffuse into those areas to maintain charge balance. On *Arizona*, limited oxygen is caused by the presence of concretion loosely bonded to the metal surface and acting as a diffusion barrier to the influx of oxygen to the metal. The thicker the barrier, the slower the diffusion and a condition is reached in which the iron consumes oxygen faster than it is replenished. The resulting process is termed hydrolysis and creates acidic conditions that promote hydrogen discharge. Such reactions may also occur at crevices and pits on metal surfaces. A typical hydrolysis reaction is given by Jones (1996):

$$Fe^{+2} + 2\ H_2O + 2Cl^- = Fe(OH)_2 + 2HCl \qquad [7]$$

Charge balance is maintained in reactions [5], [6] and [7], thus electrons no longer appear in the reactions. The product $Fe(OH)_2$ converts to green hydrated magnetite or black magnetite in areas where oxygen is limited, such as the interface between metal steel hull and concretion.

Iron is not a biologically toxic metal, so when immersed in seawater it will be colonized by marine organisms. As a result, the formation of calcareous concretions on the surfaces of iron-based alloys such as steel produces a barrier to oxygen (Jones 1996:59, 212, 447-448). With oxygen depletion in the microenvironment between the concretion and the metal surface, chloride ions diffuse inward, and the pH drops to 4 or less as a result of hydrolysis reactions given by equation [7]. The concretion acts like a semipermeable membrane with an electrical resistivity of approximately 2,000 Ω-cm when wet in seawater (MacLeod 1989). MacCleod (1982) suggests that as concretion thickness increases, cathodic reactions migrate into the concretion rather than remaining sited at the metal surface. However, since concretion electron conductivity is low, it is more plausible to assume that cathodic reactions as well as anodic reactions occur at the concretion/metal interface. The iron ions Fe^{+2} and Fe^{+3} diffuse into the marine organisms' skeletal material, which is predominately aragonite (CaCO3), to produce siderite (FeCO3), as well as oxides of iron. Concretion containing iron sulfide (FeS) and elemental sulfur indicate the presence of sulfate-reducing bacteria (SRB). Normally, hydrogen reduction in support of corrosion is a slow process, but is stimulated in the presence of SRB

(North and MacLeod 1987). The influence of microbiologically influenced corrosion (MIC) is discussed elsewhere (see Chapter 7).

CORROSION VARIABLES

Steel corrosion in seawater is extensively documented in the professional literature (Schumacher 1979). From an archaeological perspective, archeologists and conservation specialists in Australia conducted pioneering research on iron and steel shipwreck deterioration and have determined that the major factors affecting shipwreck corrosion are metal composition and metallurgical structure, water composition, temperature, extent of water movement, marine growth, seabed composition and depth of burial beneath the seabed (North and MacLeod 1987:68). Collecting data necessary to characterize critical corrosion processes on USS *Arizona* involved evaluating each of these factors, all of which are complex and interrelated, and affect corrosion in different ways. When attempting to evaluate the corrosion history of an object it must be considered individually—there are very few oceanographic and environmental parameters that are uniform between sites. An excellent review of corrosion fundamentals with applications to marine environments is presented by North and MacLeod (1987); the following discussion draws heavily on their work.

A variety of factors have been identified that directly influence metal corrosion on shipwrecks, including water composition (dissolved oxygen, pH, salinity and conductivity), temperature and extent of water movement (North and MacLeod 1987:68). Oxygen reduction is typically the most important cathodic reaction occurring in steel exposed to seawater, so dissolved oxygen availability at the cathodic site may control the corrosion rate depending on the thickness of the concretion, mass transport rate of oxygen and metal ions through the concretion and microbial activity at the interface. Water at the ocean's surface is generally oxygen-saturated, so overall dissolved oxygen content depends on the amount of mixing that occurs with surface water—increased water movement and mixing results in elevated dissolved oxygen levels. In addition, temperature and dissolved oxygen are inversely proportional, so lower temperature results in increased dissolved oxygen. The pH level is another indicator of corrosion activity. In normal seawater, pH ranges from 7.5 to 8.2, but levels below 6.5 are found under concretion covering actively corroding metal. Lower pH levels (more acidic) characterize

accelerated corrosion when sulfate reducing bacteria (SRB) are present. Salinity is closely related to the corrosion rate of steel in water since increased salinity usually results in higher corrosion rates. This is evident when comparing metal preservation in freshwater compared to seawater environments—freshwater lakes typically exhibit better preservation of iron and steel. There are several ways that higher salinity affects corrosion, including increasing conductivity (which facilitates movement of ions between anodic and cathodic areas), increasing dissolved oxygen and supplying ions that can catalyze corrosion reactions, among others (North and MacLeod 1987:74). Higher conductivity can increase corrosion by increasing the movement of ions during the corrosion process.

In general, corrosion rate increases as temperature increases. This is complicated, however, by the effect of temperature on both dissolved oxygen and biological growth. Warmer water supports increased marine growth, which contributes to concretion formation on steel in seawater and that, in turn, generally reduces corrosion rates. In addition, as discussed above, lower temperature results in higher dissolved oxygen content, which consequently means increased corrosion (North and MacLeod 1987:74).

Water movement from waves and currents on a site affects corrosion in several ways, but generally high-energy environmental conditions results in higher corrosion rates. Active water movement can contribute to mechanical erosion of metal surfaces and can also impede development of protective concretion layers by removing accumulating ions before they can precipitate and begin the concretion formation process. Waves and currents also contribute to water mixing and aeration that result in increased dissolved oxygen levels (North and MacLeod 1987:74).

Factors that affect corrosion on metal shipwrecks are complicated and interrelated. Reducing one key factor can increase another, and the results are often unpredictable. It is clear, however, that in order to understand the corrosion history of an object, even a complex object like a World War II battleship, and to begin to define the nature and rate of deterioration affecting the object, an understanding of the various environmental factors at play is necessary. An important aspect of the current research program is long-term monitoring of oceanographic and environmental parameters on USS *Arizona* (see Chapter 4).

CORROSION POTENTIAL (E_{corr}) AND POURBAIX DIAGRAMS

During the corrosion process, when the oxidation and reduction rates are equal, there will be a voltage that characterizes the specific reaction rate or corrosion rate for a particular system—that characteristic voltage is known as the corrosion potential (E_{corr}). E_{corr} is indicated by voltage (expressed in millivolts in the range of 0 to -1000 mV) and is measured using a reference electrode, which measures localized electron flow from different parts of a metal into and out of surrounding electrolyte, and displayed on a standard digital multimeter. Although there are exceptions, a more negative E_{corr} value generally indicates a lower corrosion rate, while a more positive E_{corr} indicates a higher corrosion rate (MacLeod 1987:49-50). In all cases, the negative electrode is the anode and the positive electrode is the cathode. Although practitioners in the pipeline and oil industry identify a more negative potential as indicative of a higher corrosion rate, the opposite is true for concreted steel in seawater because steel is in a film free state and does not passivate (Uhlig 1971:49, 93). E_{corr} does not translate directly to an absolute corrosion rate; however, it does yield a relative measurement that is proportional to corrosion rate for different parts of the same structure in the same electrolyte. In sea water, then, the area of the steel structure where E_{corr} is lowest (most negative) reflects the area where the corrosion rate is lowest.

The reference electrode is essentially a small battery which produces a characteristic potential. Since the steel hull of the ship likewise produces a characteristic potential, the difference between the potential at the hull and the potential produced by the reference electrode is measured and documented as the corrosion potential (E_{corr}). Since the choice of reference electrode depends upon the electrolyte and the test circumstances, it is often necessary to convert potentials to a common potential, the standard hydrogen electrode (SHE). Although the hydrogen reference electrode is not used in the field because of its complexity, it is arbitrarily chosen to have a potential of 0.0 volts. There are numerous kinds of reference electrodes used in the field. The most common is the copper/copper sulphate ($Cu/CuSO_4$) reference electrode, in which a copper rod is placed in a glass or plastic tube and filled with distilled water, then brought to saturation with excess copper sulphate crystals. This electrode is used primarily in fresh water. Two other electrodes, commonly used in sea water, are both silver/silver chloride (Ag/AgCl) electrodes. In these electrodes, a silver coated rod is placed in a solution of either

silver salt or sea water. We used normal Ag/AgCl reference electrodes on the USS *Arizona* Preservation project.

An important tool to use in corrosion analysis is the Pourbaix diagram (Figure 5.2) (Pourbaix 1974). The Pourbaix diagram is a two dimensional map of the oxidizing power (E) and acidity (pH) of a selected metal or other ions immersed in an aqueous solution. Pourbaix diagrams present stability fields of corrosion products in terms of the independent variables potential (hydrogen electrode) and pH. Since potential and pH are readily measurable in the field, Pourbaix diagrams become a very important tool in understanding corrosion for specific systems (see below). Lines on the diagram, calculated from the Nerst equation (equation [1]) identify regions where specific ions (charged elements or compounds) are stable. The way that a Pourbaix diagram is most often used is to transfer E_{corr} and corresponding pH to the diagram directly (in this case iron-water). The region in which the intersection point of the two variables is located identifies possible supporting cathodic reactions and the corrosion products that result at the location where the parameters are being measured (Figure 5.2). It should be emphasized that the Pourbaix diagram only predicts whether or not corrosion will occur and identifies the corrosion products. The rate of corrosion cannot be determined from the diagram.

As an example of how the Pourbaix diagram for the iron-water system can be used, consider the solid lines on the diagram first (Figure 5.3). Superimposing typical pH and E_{corr} field measurements as small solid dots, all points that appear in the area labeled Fe^{+2} indicate active corrosion. The points are well below the region of Fe^{+3} stability, so ferrous ions (Fe^{+2}) dominate. Below the line identified by $(Fe^{+2}) = 10^{-6}$, steel is said to be immune because the concentration of iron is extremely low corresponding to a region of insignificant corrosion. The concentration of (Fe^{+2}) continues to decrease as the potential decreases. In addition to the large cross-hatched region to the left, there is a small triangular cross-hatched region to the right in which corrosion occurs. The region defined as passivation means that corrosion product oxides form on the surface and become protective. Passivation only occurs under specific conditions for selected iron-based alloys but does not normally occur for steel in seawater. Consider next the two dotted lines labeled (a) on the bottom and (b) above it. On line (a), reaction [8] occurs:

$$2H_2O + 2e = H_2 + 2OH(-) \qquad [8]$$

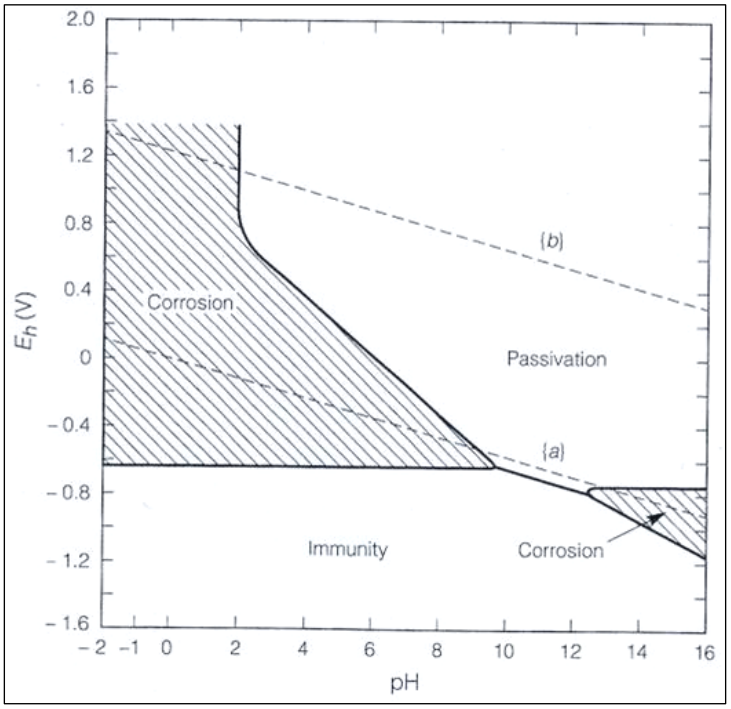

Figure 5.2. Simplified Pourbaix diagram for iron dissolved in water (Jones 1996:53).

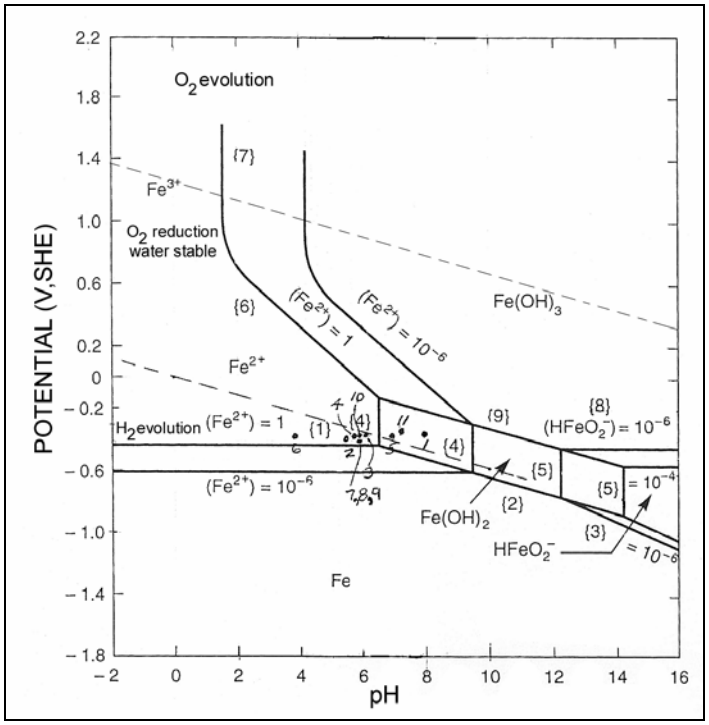

Figure 5.3. Pourbaix diagram for iron in water with E_{corr} / pH data taken on the USS *Arizona*, September 2000 (modified from Jones 1996:59).

Below line (a), water is unstable and hydrogen is evolved. Between lines (a) and (b), water is stable and oxygen is reduced to water or oxygen is consumed as a cathodic reaction in support of corrosion. On line (b), reaction [9] occurs:

$$O_2 + 4H^+ + 4e = 2H_2O \quad [9]$$

Above line (b), oxygen is stable and oxygen evolution takes place, although it seldom does because E_{corr} normally does not reach such a high potential. As will be noted later, the points appear to follow closely along the lower dotted line, hence, hydrogen evolution or oxygen consumption dominates the cathode reaction. At the lower pH values observed at the metal/concretion interface, the cathode reaction at or near the interface in the concretion involves hydrogen evolution as noted above (which explains the observation that initial penetration of the concretion sometimes releases gases and divers occasionally observe bubbles emerging from concretions in isolated locations on *Arizona*'s hull). The Pourbaix diagram for the carbon-water system (Figure 5.4) is also useful in identifying gases observed during diving operations. For example, at an E_{corr} of -400 mV, methane gas is stable in solution at a pH below about 6, carbon is stable between pH 6 to 8, and carbon dioxide is stable above pH 8. At E_{corr} of -300 mV, methane is stable below pH 4, carbon is stable between pH 6 to 7 and carbon dioxide is stable above pH 7. As will be discussed later, this diagram may be useful to explain why potentials suddenly rise in some interior compartments. While Figure 5.4 applies only at atmospheric pressure and temperature, extreme high pressure and low temperature at great depths result in very high solubility of methane gas. The result is solid hydrate, a stable form of methane under such conditions.

CORROSION RATE THEORY

The preceding discussion relates only to the potential for corrosion and does not address the issue of corrosion rate. Since corrosion produces or consumes electrons, the corrosion rate is directly proportional to current and inversely proportional to cross sectional area. A common expression for corrosion rate when expressed in terms of current is microamperes per centimeter squared ($\mu A/cm^2$). A more practical expression for corrosion rate incorporates metal loss into the expression and this can be accomplished by imposing Faraday's Law. The law states that

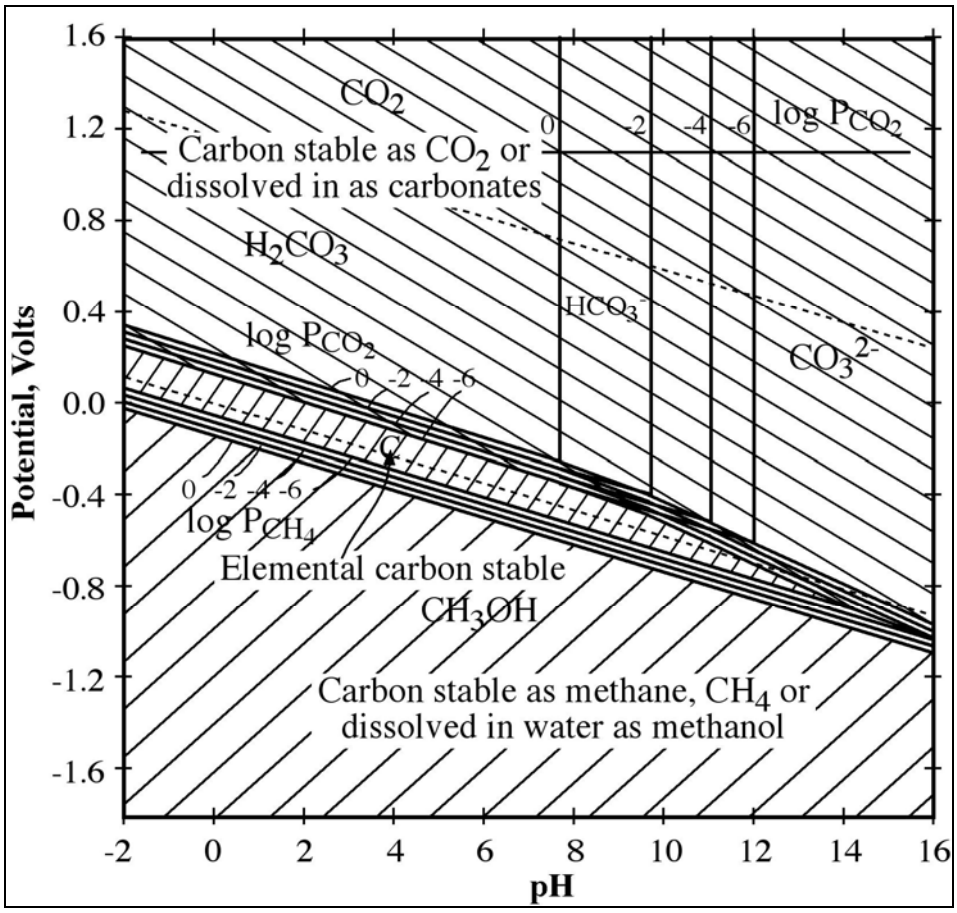

Figure 5.4. Pourbaix diagram for carbon in water system.

one equivalent weight of metal consumes 96,500 ampere seconds of current. Combining physical and chemical properties of iron with Faraday's Law and using the appropriate constants, expressions for corrosion rate are derived in following sections.

Polarization

Two types of polarization are identified in an electrochemical cell. The first type, activation polarization, is related to corrosion product formation on the metal surface. As oxides and gases begin to accumulate on that surface, the rate of electrochemical reactions reach a steady state rate that depends on many factors, including the chemistry of the electrolyte, the composition of the metal or alloy, the condition of the metal surface and temperature. The second type, concentration polarization, is related to the rate at which reaction species reach the metal surface. For example, if diffusion of oxygen is slower than corrosion reactions consuming

it, the corrosion rate is controlled by availability of oxidants rather than the rate at which the reactions themselves take place. As an analogy, the kinetic energy of a moving object is expended theoretically in proportion to the square of the velocity. At 30 mph, the kinetic energy is proportional to 30 x 30 = 900 and the moving object, such as an automobile, will reach speed with a specific fuel consumption rate. At 60 mph, the kinetic energy is proportional to 60 x 60 = 3600 and the consumption rate of fuel increases. According to kinetic theory, energy expended increases in this example by a factor of four although the speed only doubles. However, at a given speed, a dynamic equilibrium develops between wind resistance, engine and drive train friction and road resistance, and these factors can be thought of as polarizing in the sense that they effect the actual speed of the car and the kinetic energy actually expended. Although the above analogy is crude, it illustrates the fact that the process itself creates its own bias, and conditions change to meet these biases. In electrochemical processes, analogous effects are almost instantaneous and the transient condition is not measurable. What is measured are two empirical parameters, corrosion rate (i_{corr}) and corrosion potential (E_{corr}). Numerous environmental variables can also be measured such as pH, oxygen concentration, temperature, salinity and oxidation reduction potential. These parameters are used to better understand the corrosion processes reflected in i_{corr} and E_{corr}, and identify the type of polarization occurring. Since potential and pH are thermodynamic parameters, they combine to determine a point on a Poubaix diagram, as discussed earlier. The region where the point lies identifies the corrosion products and hence factors that control the process.

Activation Polarization

While the kinetic theory of corrosion is beyond the scope of this chapter, there are practical aspects of this theory that are necessary to interpret field corrosion data. Activation polarization reflects conditions, in which the corrosion rate is determined by the rate of electrochemical reactions such as hydrogen evolution (equation [4]) or oxygen consumption (equation [3]) occurring at the cathode surface. In practical terms, this means that oxidants (oxygen or hydrogen ions) are available in excess and impose no limit on the rate of corrosion. Dissolution of ions from the anode and their dispersal from the anode site, as in equation [2], is normally so fast that activation polarization is the rule at the anode. This concept is illustrated in

Figure 5.1, where potential is plotted on the vertical axis and corrosion rate (i_{corr}), expressed as the logarithm of the current density (log (i_{corr})), is plotted on the horizontal axis. The top descending solid line represents the path of cathodic polarization and the bottom ascending solid line represents the path of anode polarization for a hypothetical cell. It should be noted that the two lines converge to a point of intersection virtually instantaneously. At the point of intersection, i_{corr} is determined by projecting vertically downward to the horizontal (x) axis. E_{corr} is determined by projecting horizontally to the vertical (y) axis. According to activation or Tafel theory, a plot of E (potential) versus log (i_{corr}) is linear according to equation [10]:

$$y = mx + b \qquad [10]$$

In terms of potential and current, this equation is given by:

$$E = \beta(\log i_{corr}) + K \qquad [11]$$

where

E is plotted on the vertical axis

log (i_{corr}) is plotted on the horizontal axis.

The constant β is the Tafel constant and is expressed in millivolts (mV) per decade of current (mV per decade is defined as the potential change required to cause a 10-fold increase in the corrosion rate). β is an important parameter defining the corrosion process, as will be discussed later. Normally, the anode is under activation control, as mentioned above, but the cathode can be under either activation or concentration control. The constant K includes potential (E°) and exchange current density (i°). The vertical line between C and A corresponds to a potential difference between anode and cathode at the corrosion potential and referred to as an ohmic resistance drop. From Ohms Law:

$$I\ (\Delta E)/R \qquad [12]$$

where

I is the total current (A)

Δ E is the potential difference between anode and cathode (volts)
R is the resistance (ohms)

The most significant feature of Figure 5.1 is the continuously decreasing i_{corr} along the anode line as the potential decreases. This is the theoretical basis for the experimental observation that i_{corr} decreases as anode E_{corr} becomes more negative (anode line B to A(3)). This observation was experimentally verified after acquisition and analysis of steel hull samples on *Arizona* in August 2002 (see below). If passivation were to occur, the sign would reverse such that an increasing potential would momentarily cause the corrosion rate to increase (corrosion product formation) but then suddenly decrease at a specific potential referred to as the passivation potential. A thin, stable and protective corrosion product layer forms and the corrosion rate decreases (dashed anode line A(3) to A(1) and on to B(1) and A(4)).
The corrosion current, expressed in terms of microamperes per square centimeter ($\mu A/cm^2$), is converted to mils per year (mpy—a mil is 1/1000 of an inch) by applying Faraday's Law. The conversion constant is 0.46 for mild steel but varies depending on the metal or alloy:

$$1\ \mu A/cm^2 = 0.46\ mpy = 11.68\ \mu mpy \qquad [13]$$

Concentration Polarization

Diffusion of oxidants to the cathode normally governs the consumption rate of electrons and, hence, the corrosion rate. The corrosion rate limiting equation [14] is expressed by:

$$i_L = i_{corr} = KDnFC/d \qquad [14]$$

where

i_L is limiting current density (mpy or μmpy)
i_{corr} is corrosion current (mpy or μmpy)
D is the diffusion coefficient for H^+ ion or O_2 through concretion barrier (cm^2/sec)
n is charge (valence)
F is Faraday's constant

C is concentration of H^+ ion or O_2 (mg/L)

d is diffusion thickness (cm)

K = 0.46 for mpy (11.68 for μmpy)

According to equation [14], the corrosion rate is directly proportional to the diffusion coefficient and concentration, and indirectly proportional to the thickness of the diffusion barrier (concretion) on the surface that impedes the diffusion of reactants, most commonly oxygen. Line l–l' in Figure 5.1 characterizes cathodic polarization and shows intersection with the anodic line at point B(1). It should be noted that if oxygen consumption were the only supporting cathode reaction, the corrosion rate could be determined knowing the consumption rate of oxygen—it would not be necessary to measure the corrosion rate directly. However, to measure the volume of oxygen consumed would be impossible to do in the field. Projecting vertically from point B(1) to the x axis, i_{corr} is determined. As will be noted later in this chapter, i(L), equation [14], reveals whether or not oxygen availability is sufficient to support corrosion.

CORROSION ANALYSIS OF USS *ARIZONA*

METHODOLOGY

Analysis of corrosion on USS *Arizona* includes determining corrosion rate, the most pertinent variable needed to address overall research questions regarding hull structural integrity and longevity. An evaluation of the corrosion process began by investigating *Arizona*'s steel metallurgy from initial construction to later reconstruction. Methods included chemical analysis, metallographic examination and Charpy impact testing—all standard metallurgical evaluations. Next, seawater chemistry and other environmental variables were collected over a two-year period to establish an environmental baseline for the site. Environmental parameters recorded during long-term deployment of water quality and oceanographic monitoring instruments includes dissolved oxygen, temperature, salinity, pH, oxygen reduction potential, conductivity, current speed and direction, and wave height and direction. In addition, water quality parameters were recorded inside *Arizona*'s hull periodically with a monitoring instrument deployed on a remotely operated vehicle (ROV). Specific dissolved oxygen measurements both inside and

outside the ship were also recorded on different occasions. A comprehensive analysis of oceanographic and water chemistry variables appears in Chapter 4; however, because of their importance to the corrosion process, they will be reviewed here. Because both properties of steel and environmental parameters directly affect the corrosion process, and therefore the corrosion rate, both need to be factored into an evaluation of *Arizona*'s overall corrosion.

After establishing background conditions, an evaluation of the corrosion process itself was accomplished by applying corrosion theory discussed above with specific experimental results from *in situ* corrosion measurements taken on *Arizona*'s hull, in combination with laboratory analysis of concretion samples. *In situ* values for E_{corr} and pH were measured at varying depths through the concretion from the exterior surface to metal/concretion interface. These measurements were taken over the course of multiple field seasons and in a variety of locations, and represent a comprehensive corrosion assessment of *Arizona*'s exterior hull. In addition, concretion samples from *Arizona*'s exterior hull were collected and analyzed using both x-ray diffraction and environmental scanning electron microscopy (ESEM). The former identified mineral species dominant in the concretion while the ESEM quantified the corresponding element concentrations in weight and atomic percent. These data provided evidence that it would be feasible to quantify the iron content in a given cross section of concretion and relate it back to corrosion rate.

The rate of *Arizona*'s steel hull corrosion fluctuates directly with numerous variables, and is somewhat different at various hull locations. Corrosion rate was investigated through a number of lines of inquiry, including direct metallographic and thickness measurements of steel hull samples, *in situ* ultrasonic thickness measurements, and correlating environmental parameters with limiting current density (i(L)). The minimum-impact method of choice for determining corrosion rate developed during the USS *Arizona* Preservation Project is the Concretion Equivalent Corrosion Rate (CECR). Corrosion rate of the interior and areas of the hull deep below the harbor bottom was estimated from environmental variables alone. Through multiple lines of evidence, an important understanding has been gained about conditions that exist on *Arizona*'s hull, interior and exterior, above the harbor bottom to just below it, and how they affect the steel-hull corrosion rate.

RESULTS

Metallurgical Evaluation

Because steel chemistry and microstructure have a direct effect on corrosion, steel samples from USS *Arizona* were examined by conventional metallurgical techniques, including optical metallography, Charpy impact and chemical analyses. Test work included both *Arizona*'s original 1913–1915 structural steels as well as steels used in 1929–1931 reconstruction. All test work was conducted in the Metallurgical Engineering Laboratories at the University of Nebraska–Lincoln (Johnson, et al. 2000). Analysis focused on steel collected from superstructure elements stored on land at Waipio Point in Pearl Harbor, which were removed from the battleship before Memorial construction began in 1960.

Chemical Analysis

Chemical analysis of steel samples taken from the ship used in the original construction beginning in 1913, and reconstruction from 1929–1931, were compared to hull steel from RMS *Titanic* (Felkins, et al. 1998) and a modern grade of ASTM A-36 steel (Anonymous 1975:49) (Table 5.2). Saveur (1935) reports impurities in early twentieth century steel varied for phosphorous (P) from a trace to 0.1%, silicon (Si) from a trace to 0.5% with most grades between 0.05–0.30 percent. Examination of Table 5.2 indicates that all of the steels contain less than 0.05% P and satisfy the maximum for Si. With one exception (*Titanic* steel), S contents are below 0.05%. Cook (1937) reports that in 1910, basic open hearth production was close to 17 million tons whereas Bessemer production was about 9.5 million tons. Based on the chemistries and statistics, it seems certain that USS *Arizona* structural steels were basic open hearth products. Somewhat higher S and P are reported for *Titanic* steel, most likely due to the fact that the steel used in the *Titanic* was an acid open hearth product, hence the reason for the higher sulfur. The higher copper content in W1-B2 is probably due to the addition of scrap to the open hearth during the production process. This is further evidence of open hearth production since the Bessemer process could not use scrap.

SAMPLE (wt %)							
Element	**W3**	**W1-B2**	**WB2**	**WB3**	**WB5**	**Titanic**	**A36**
	Rivet - 1913	Plate -1913	Main mast - 1929 -1931	Locker - 1913	Channel - 1913	1911	ASTM
C	0.207	0.102	0.226	0.450	0.228	0.210	0.200
P	0.031	0.046	0.013	0.028	0.006	0.045	0.012
S	0.043	0.023	0.039	0.024	0.046	0.069	0.037
Mn	0.510	0.450	0.502	0.521	0.435	0.470	0.550
Si	0.013	0.004	0.024	0.067	0.007	0.017	0.007
Cu	0.061	0.244	0.011	0.013	0.025	0.024	0.010
Al			0.029	0.006			

Table 5.2. Steel Chemistry: USS *Arizona* Original Materials through 1913 and Reconstruction Materials 1929–1931.

Metallography

Conventional metallographic methods were used to prepare specimens obtained from Waipio Point in March 1999 and again during a second field operation in September 2000 (Figures 5.5 and 5.6). Etching was done with 2% Nital after grinding and polishing. The microstructure of sample W1 consists of ferrite and pearlite, and the carbon content is estimated to be around 0.2%. The microstructure shows evidence of heavy banding—banded microstructure such as this is typical of plate steels from this time period (Figure 5.7).

Banding is a result of the solidification practices used for the ingot from which the steel was rolled and appears as a segregated structure of nearly parallel bands aligned in the direction of working (Yiming, et al. 1992). Photomicrographs of Sample W3 in the area around the rivet show the microstructure of both the rivet and the plate (Figure 5.8) and the plate (Figure 5.9) separately. The plate shows the same basic microstructure as W1, but the banding is less severe. The rivet has a microstructure which indicates that it was cooled rather quickly from the austenite range (Figure 5.10). The microstructure of the rivet consists of primary grain boundary ferrite and very fine pearlite interspersed with Widmanstatten ferrite. This microstructure would

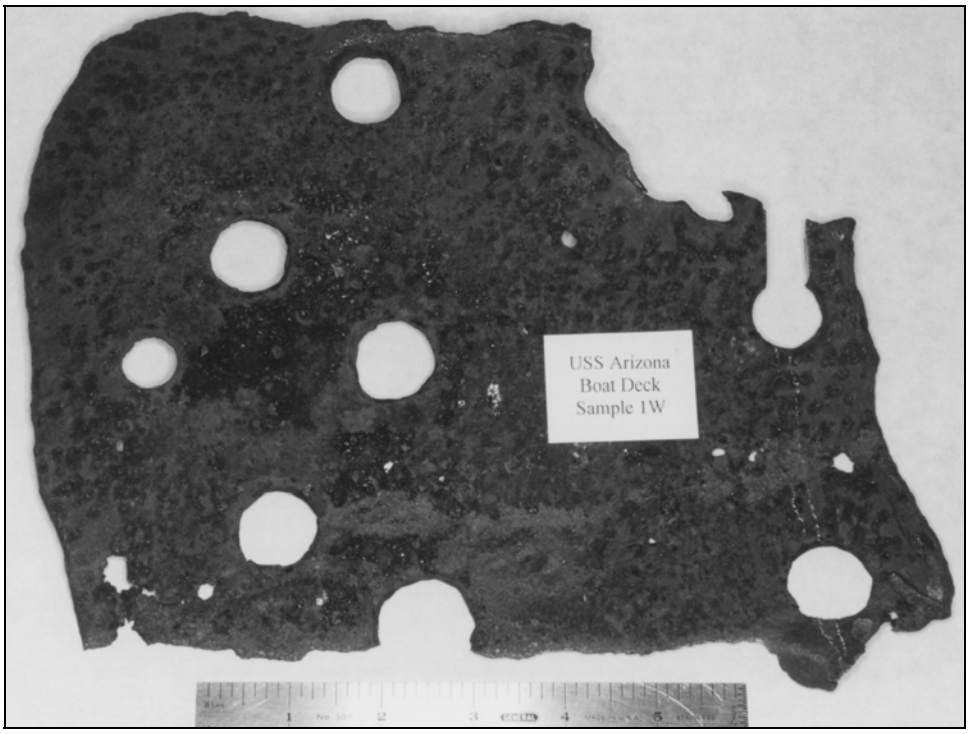

Figure 5.5. Sample W1, plate from boat deck with rivet holes.

Figure 5.6. Sample W3, section with rivet in place from boat deck.

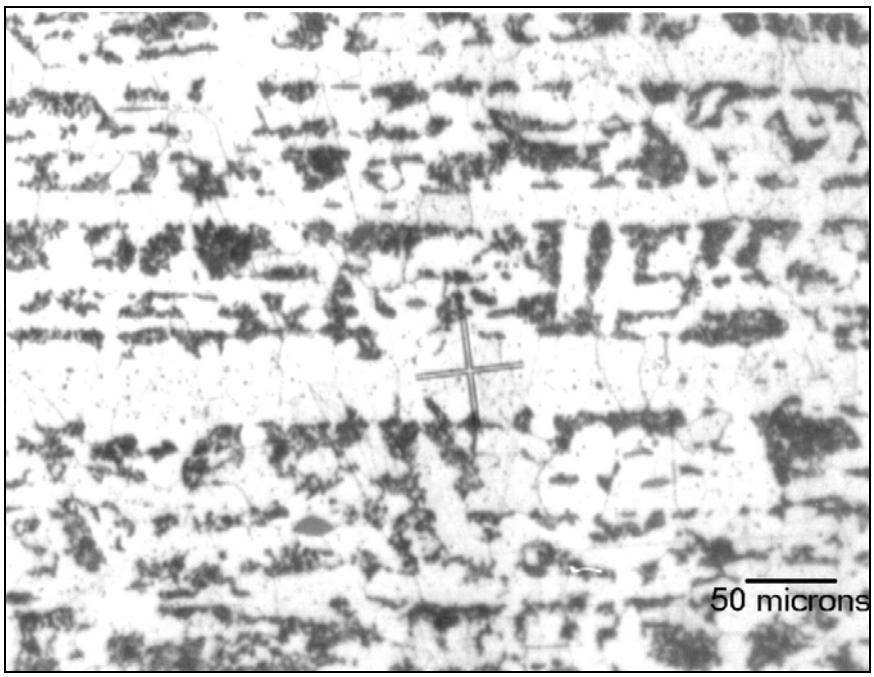

Figure 5.7. Microstructure of W1, 175X, 0.2% Nital etch.

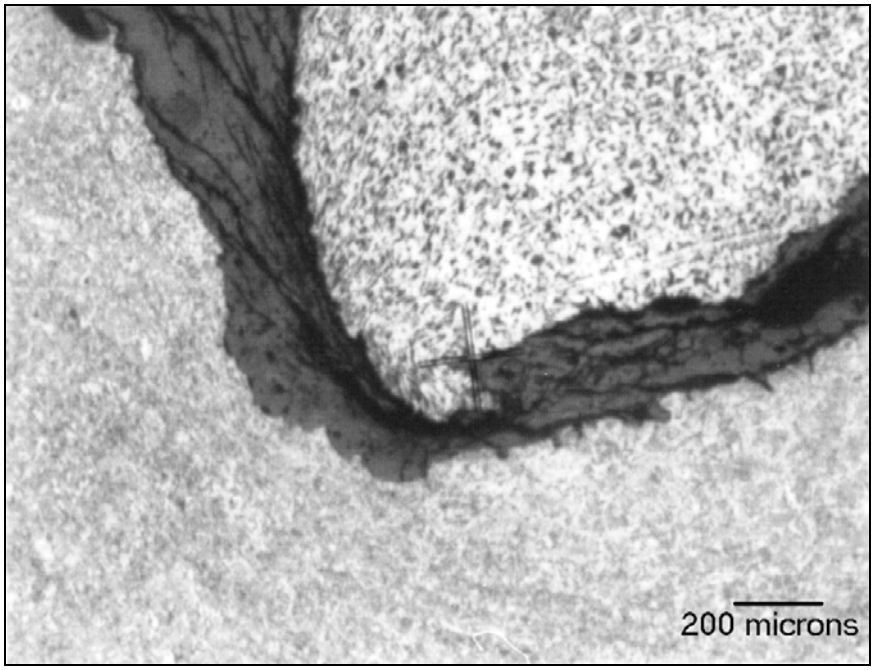

Figure 5.8. Microstructure of W3. Plate is at top right, rivet is at lower left. 45X, 2% Nital etch.

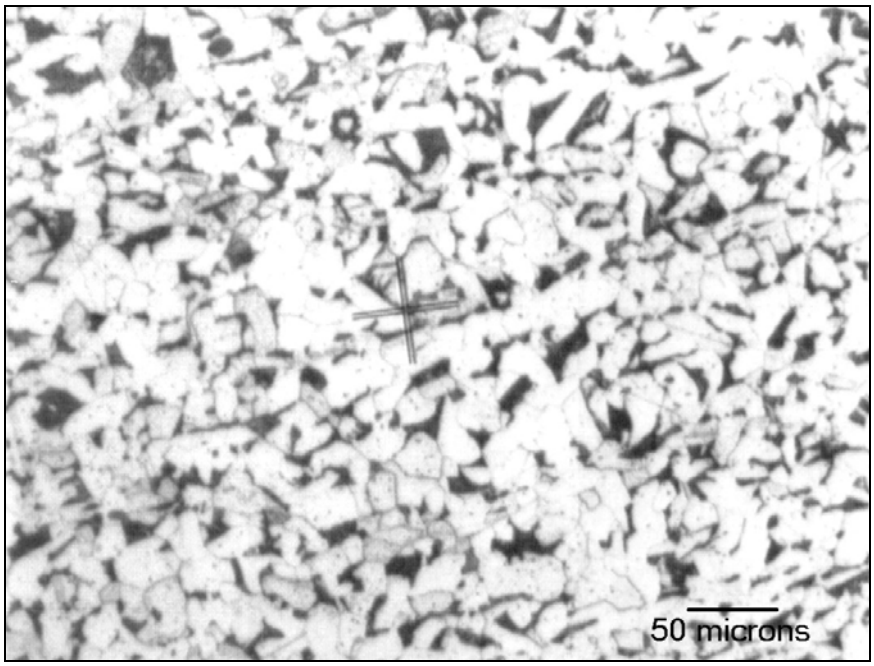

Figure 5.9. Microstructure of plate W3, 175X, 2% Nital etch.

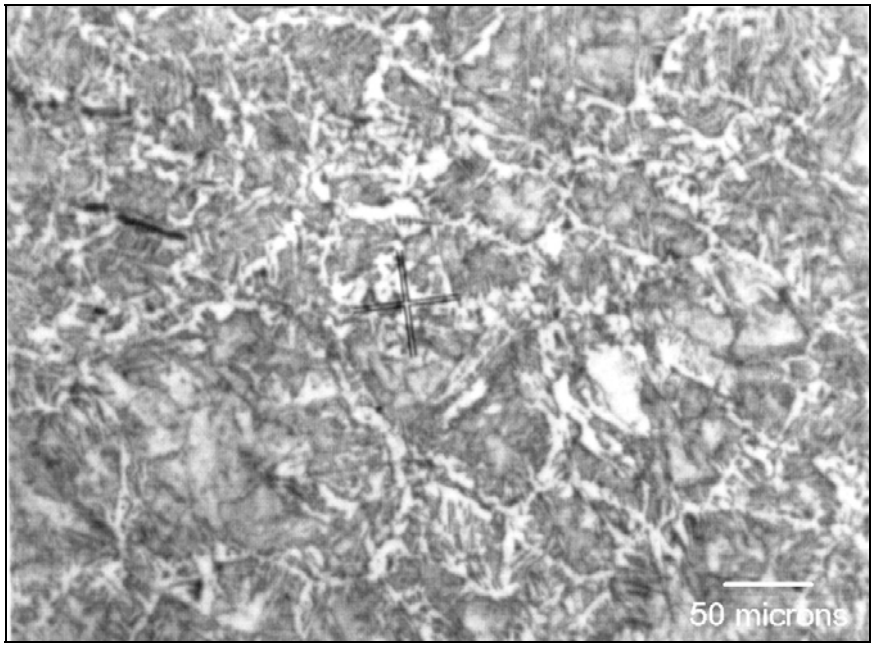

Figure 5.10. Microstructure of rivet in sample W3, 175X, 2% Nital etch.

be typical for hot riveting processes in which the rivets are heated red hot and swaged into place. The carbon content of the rivet is believed to be slightly higher than that of the plate.

The microstructure of samples W1 and W3 are typical for the time period and operations when this vessel was built. The banded microstructure seen in sample W1 can affect the rate and mechanism of corrosion of the steel over a period of time, but is not expected to be a significant factor. The fact that the microstructure of the rivet and plate (Figures 5.5 and 5.6) are different indicates that at least this part of the ship did not see extremely high temperatures. If it had seen temperatures above 1,340 °F (727 °C), the steel would have gone through a phase transformation and the microstructures of the rivet and plate would have been similar on cooling. Since banding appeared in sample W1, samples WB2, WB3 and WB5 from September 1999 were sectioned for examination in both the longitudinal and transverse directions.

Longitudinal and transverse sections of main mast tripod sample WB2 show Widmanstatten ferrite with slight evidence of banding (Figures 5.11 and 5.12). Microstructures are consistent with carbon content between 0.2–0.25%. Grain size of this material was measured to be ASTM 7.3

A longitudinal section of galvanized locker plate, WB3, has microstructure typical of medium carbon steel (Figure 5.13)(Table 5.2). Pearlite is resolved and grain size is finer than that of the much thicker walled mainmast. Galvanizing is still evident on the exterior of the plate. The reason for the use of medium carbon steel in this application is not clear, although this is believed to be an exterior panel in which medium carbon steel would offer some level of protection over low carbon grades. New York Navy Yard correspondence, however, does not identify galvanized sheet steel as being a medium carbon grade (New-York-Navy-Yard 1913).

A longitudinal section of boat deck channel member WB5 shows elongated MnS inclusions and oxide particle alignment clearly evident and also pronounced banding (Figure 5.14).

Charpy Impact

Charpy impact tests were performed on seven standard specimens obtained from the mainmast tripod sample WB2. Samples were machined with the specimen axis parallel to the longitudinal or rolling direction. Tests were performed on a Tinius Olsen instrumented impact

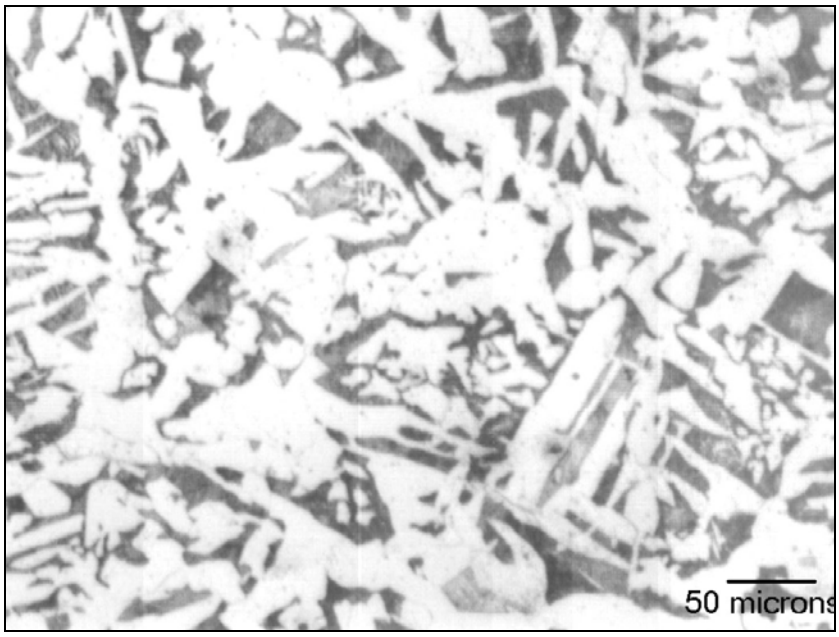

Figure 5.11. Microstructure of mainmast tripod leg, sample WB2, longitudinal, 175X, 2% Nital etch.

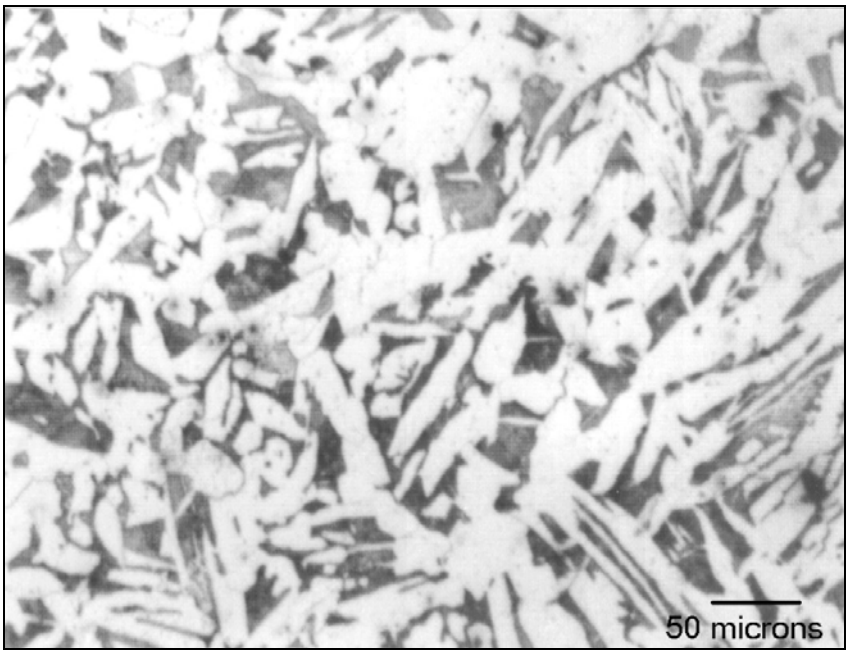

Figure 5.12. Microstructure of mainmast tripod leg, sample WB2, transverse, 175X, 2% Nital etch.

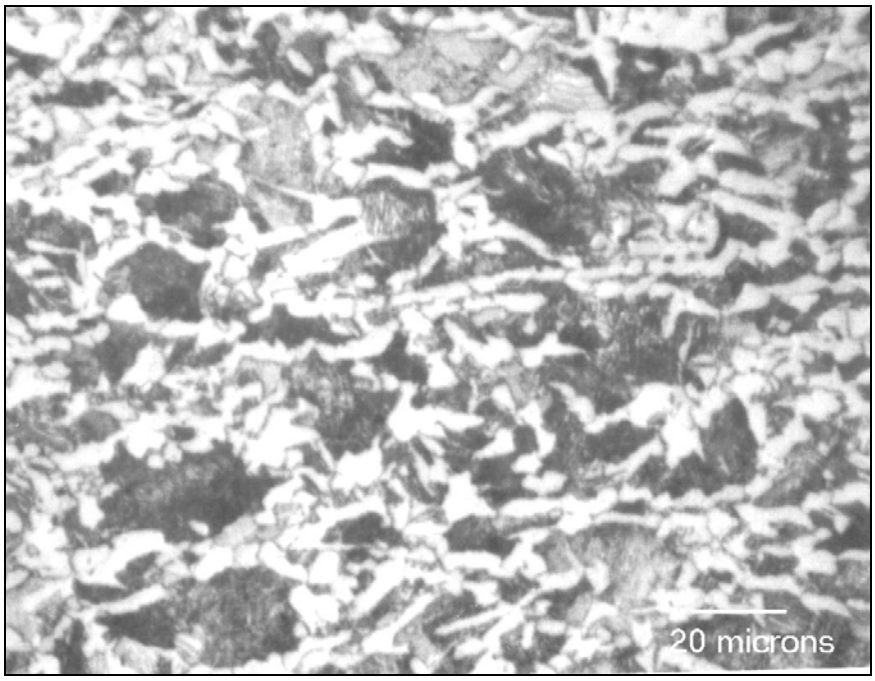

Figure 5.13. Boat deck locker sample WB3, longitudinal galvanized section, 450X, 0.2% Nital etch.

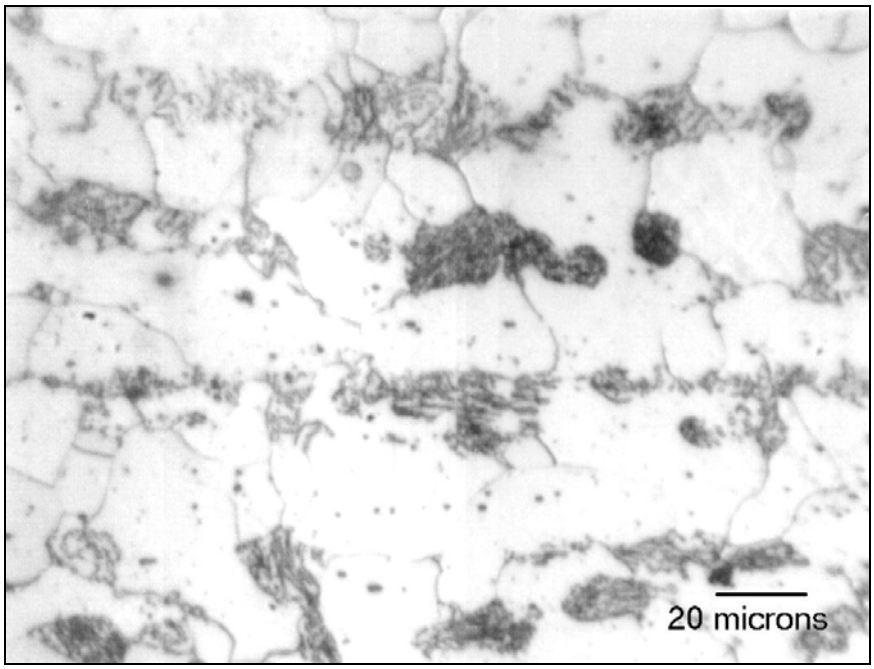

Figure 5.14. Microstructure of boat deck channel, sample WB5, longitudinal, 450X, 2% Nital etch.

tester using a Dynaup data acquisition system. Tests were run at temperatures of -196, -100, 25, 100 and 200 °C. Results from the Charpy impact testing are plotted using three commonly used reporting methods: temperature vs. energy absorbed, percent shear (ductile failure), and percent contraction at the fracture surface (Figure 5.15). Charpy impact curves for longitudinal plate from *Titanic*, *Arizona*, and A-36 grade were also compared using three common methods for comparing ductile vs. brittle fracture: the temperature at which the average of the upper and lower shelf occur at, the upper shelf energy and the temperature at which the material will absorb 20 J (15 ft.-lbs.) of energy (Figure 5.16)(Table 5.3) (Felkins, et al. 1998). Several factors are known to have significant effects on the toughness of steels, and in particular on the ductile to brittle transition behavior (Anonymous 1975:49).

The carbon content has the largest effect and raises the ductile to brittle transition temperature as measured by (DBTT) by 25 °F (14 °C) for every additional 0.1%. Manganese lowers the transition temperature by 10 °F (5.5 °C) for every 0.1% added whereas P raises it by 13 °F (7 °C) for every 0.1% added. Transition temperature is lowered as the grain size decreases by $D^{-1/2}$. These factors will also raise the upper shelf energy in conjunction with a lowering of the transition temperature. Using these guidelines for the effects of C, Mn, P and grain size, it can be calculated that the DBBT for *Arizona* and *Titanic* steels compared to the A-36 steel, measured by the average between the upper and lower shelf energies, should vary predictably (Table 5.4)—note that the A-36 and USS *Arizona* materials have essentially identical S contents (0.037% and 0.039% respectively) and P contents (0.012% and 0.013% respectively) whereas *Titanic* material has higher contents of 0.069% S and 0.045% P. The differences in transition temperature as computed between *Arizona* steels and A-36 grade can be explained through the C, Mn, P and grain size, whereas the differences between *Titanic* and A-36 grades takes into account of the higher S content in order to explain the differences. This is a direct result of the use of acid open hearth steelmaking practices which understandably were state-of-the art at that time in Europe. The mainmast steel from *Arizona* was of the same general quality from the metallurgical aspect as was the modern A-36 grade, with the differences being noted that the DBBT data were obtained from the mainmast steel manufactured in the late 1920s when cage masts were replaced with tripods.

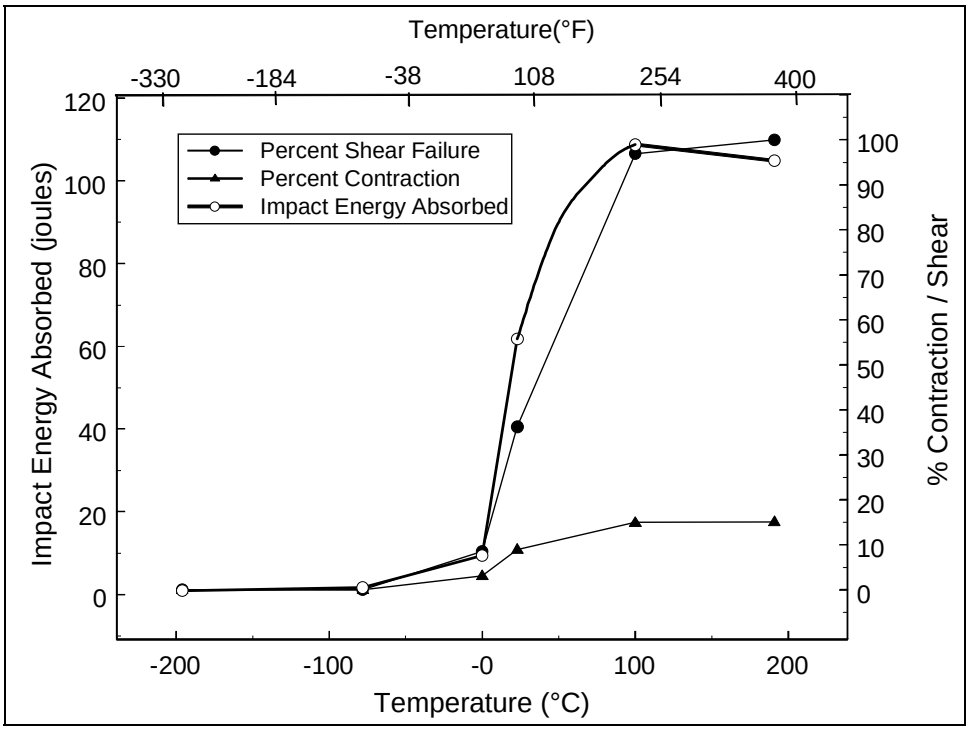

Figure 5.15. Charpy impact results plotted as temperature vs. energy absorbed, % shear failure, and % contraction for longitudinal steel samples taken from the mainmast of the USS *Arizona*.

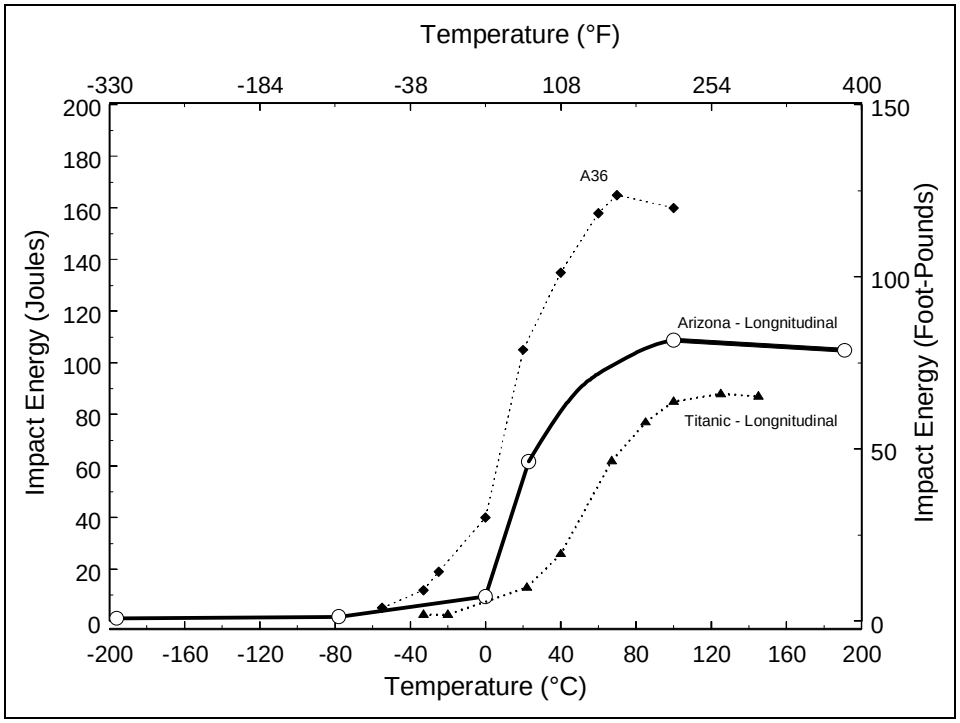

Figure 5.16. Charpy impact energy vs. temperature for longitudinal specimens from USS *Arizona*, HMS *Titanic*, and A36 steels.

Steel	DBTT	ΔT compared to A-36						Remarks
		Total	%C	%Mn	%P	G.S.	sum	
A-36	10°C / 50°F	0°C / 0°F	·····	·····	·····	·····	····	
USS AZ	20°C / 68°F	10°C/ 18°F	6.5	4.8	0	7	18.3	ok
Titanic	55°C / 131°F	45°C/ 81°F	2.5	8.0	4.2	31	55.7	(1)

Table 5.3. Comparison of the data for the impact results for USS Arizona tripod steel, titanic steel and a modern grade of A-36 steel.

	***Arizona* Mast**	**A36**	**Rebar**	***Titanic***	**Effects**
Grain size (ASTM/ μm)	7.3 / 30	7.5 / 26	10.5 / 11	5-6 / 42 – 60	$d^{-1/2}$
Carbon (wt%)	0.226	0.20	0.26	.021	+25°F / 0.1%
Mn (wt%)	0.502	0.55	0.97	0.47	-10°F / 0.1%
P (wt%)	0.013	0.012	0.01	0.045	+13°F / 0.1%
S (wt%)	0.039	0.037	0.042	0.069	
Mn/S	12.8	15.0	23.0	6.8	(1)
T (°F) @ 20 joules	5°C / 41°F	-23°C / -10°F	-79°C / -110°F	29°C / 85°F	(2)
Upper Shelf (J)	110	165	90	85	(3)
DBTT as Average at ½ upper shelf	20°C / 68° F	10°C / 50°F	-20°C / -4°F	55°C / 131°F	(4)

(1) Measure of degree of free sulfur.
(2) Often used criterion for ship steel.
(3) Measure of toughness with 100% ductile failure.
(4) Often used measure for Ductile-Brittle Transition.

Table 5.4. Calculation of the DBTT for USS *Arizona* and *Titanic* steels as compared to A-36 as a function of C, Mn, P and grain size (GS).

Metallurgical Summary

Steel used to fabricate USS *Arizona* battleship during original construction, 1913–1915 and reconstruction, 1929–1931 were consistent with the best steel available during each time period. Due to the force of the forward magazine detonation, the best steel available today would not have had any impact on the outcome. Heavy banding in steels from both periods could adversely affect the corrosion resistance under anaerobic conditions that prevail during a corrosion cycle that developed under hard concretion layers that began to develop when the ship sank. Banding would have no effect on corrosion rate under aerobic conditions that may occur on local areas on the hull. In the part of the ship from which samples for this report were obtained, high temperatures above 1,340 °F (727 °C) did not occur.

The structural steel used in original construction was of surprisingly good quality for a basic open hearth steel technology that was only about 25 years old at the time the first materials were ordered for delivery to the New York Navy Shipyard. The somewhat lower quality of the early steel in terms of chemistry and microstructure had no measurable consequences on the damage that occurred on December 7, 1941 or on the results of the present investigation into the deterioration of the *Arizona*'s hull. Typical analysis and comparison with present day ASTM A-36 (Table 5.5) show minor differences in chemistry between the USS *Arizona*-era steel and present-day ASTM A-36 steel, however they are not considered significant with regard to corrosion response.

Environmental Evaluation

In all, more than 503,730 observations of currents, waves and water-column properties were collected on 362 days over the course of 14 months between November 2002 and January 2004, and an additional 580,000 observations of currents and near-bed water temperatures were collected during April 2005. As discussed in more detail in Chapter 4, oceanographic data indicate that tides are of a mixed, semi-diurnal type with a minimum, mean

	Carbon	Phosphorus	Sulpher	Silicon
USS Arizona	0.25	0.028	0.034	0.023
ASTM A36	0.20	0.012	0.037	0.007

Table 5.5. Chemistry of typical USS *Arizona* steel compared to modern day ASTM A36. All values wt %.

and maximum tidal range of 1.3 ft., 2.0 ft. and 3.0 ft. (0.4 m, 0.6 m and 0.9 m), respectively. Waves are not an important factor in the vicinity of *Arizona*'s hull. Those observed were, long period (~ 20 sec), but very small (order of cm's) and likely due to open ocean long-period swell. Vessels passing close to the study site are likely responsible for the high-amplitude, low-period motions that were also observed. Flow along the 33-ft. (10-m) isobath is dominated by semi-diurnal and diurnal tidal motions, which are modulated to some degree by what appears to be wind forcing during the mid- to late afternoon. Flow throughout most of the water column is primarily parallel to the *Arizona*'s hull at ~ 0.065 ft./sec (~ 0.02 m/sec) and net flow is to the northeast. Flow within a meter of the seafloor, however, is weaker and more variable in direction. Flow velocities are greater off the port side than the starboard side, and thus the water replenishment times on the port side of the hull are shorter than off the starboard side. Shear, both vertically in the water column and across the hull, was observed. This results in vertical variations in replenishment times and current-induced forces on the hull. This shear also likely increases vertical mixing of the water column. Acoustic backscatter was generally higher in the winter months and during the falling tide, suggesting advection of material introduced into the northern sections of Pearl Harbor due to winter precipitation and its movement south past the hull by ebbing tidal currents. Higher measurements of acoustic backscatter often occurred in the afternoon, suggesting increased Trade wind-induced mixing or, perhaps, increased vessel activity, which facilitates water column mixing and fine-grained particulate resuspension.

The water quality monitoring instruments indicate water temperatures along the 33-ft. (10-m) isobath had a slightly higher mean of 78.85 °F (26.03 °C) and a less variable one standard deviation of 1.17 °C than along the 10-ft. (3-m) isobath, which had a mean of 78.19 °F (24.55 °C) with one standard deviation of 2.08 °C. A thermocline was often present in the harbor's waters, with the shallower (10 ft./3 m) and deeper (33 ft./10 m) water temperatures often differing by more than 3.6 °F (2 °C). Water temperatures were generally cooler and less variable off the port side of the hull than off the starboard side, possibly due to faster replenishment times and greater mixing of the water column.

Salinity varied from 16.78 PSU and 42.56 PSU, with a mean ± one standard deviation of 34.33 ± 4.25 PSU. Salinity appears to positively correlate with water temperature and suggests that Pearl Harbor's waters are influenced by freshwater runoff or groundwater effluence in the winter months.

Open seawater pH varied between 7.60 and 9.10, with a mean ± one standard deviation of 8.04 ± 0.15 and dissolved oxygen 0% and 288.5%, with a mean ± one standard deviation of 69.5 ± 58.8%. Both pH and dissolved oxygen tended to correlate with the daily insolation cycle, increasing during the morning into the early afternoon followed by decreasing through the night to minimum levels just before sunrise.

Oxygen-reduction potential (ORP) varied between 150.0 mV and 397.2 mV, with a mean ± one standard deviation of 289.2 ± 50.6 mV. ORP often had an inverse relationship with pH and the percentage of dissolved oxygen, with oxygen-reduction potential decreasing during the daytime and increasing into the night, attaining it greatest values just before sunrise. During the vertical profiling, near-surface temperatures were on average 1.85 °F (1.03 °C) warmer than the near-bed temperatures, near-surface temperatures were 0.85 PSU less saline on average than the near-bed salinities and near-surface dissolved oxygen levels were on average roughly 43.9% higher than the near-bed dissolved oxygen levels.

A YSI dissolved oxygen instrument was used to obtain oxygen concentration at varying depths in the water column adjacent to *Arizona*'s hull, as well as internal measurements taken inside selected core drill holes during hull sample removal in 2002. During one measurement in August 2002, dissolved oxygen concentration varied as a function water depth in the water column from 6.47 mg/L at the surface to 5.08 mg/L at the harbor bottom at a depth of 30 ft. (Table 5.6; for additional data and analysis, see Chapter 4). For internal measurements, the instrument was attached to the end of a 6-ft. section of PVC pipe and inserted into the hole after removal of a plug seal inserted into each drill hole after the hull sample was removed. Exterior measurements in ambient seawater before inserting the dissolved oxygen meter into the hull varied from 4.74 to 5.68 mg/L (Note: mg/L is an alternative unit of measure for dissolved oxygen, but one not easily converted to percent saturation after the fact). Once inserted into the hull through the core sample holes approximately 1–2 ft., the readings dropped, varying between 0.0 and 3.99 mg/L once they stabilized. These interior spaces reveal a wide range of oxygen concentrations depending upon access to ambient seawater. For the sample locations on the second deck (USAR-02-002 and USAR-02-008), which have some seawater exchange through open port holes, dissolved oxygen concentration dropped an average of 27% below ambient, exterior seawater measurements. For the sample locations in the torpedo blisters (USAR-02-003, USAR-02-004, and USAR-02-009), the dissolved oxygen concentration varied from 2.47 to 0.0

Water Depth (ft.)	Dissolved Oxygen (mg/L)
0	6.47
2	6.36
4	6.33
6	6.41
8	6.3
10	6.16
12	6.28
14	6.14
16	6.04
18	5.92
20	5.57
22	5.55
24	5.16
26	5.1
28	5.07
30	5.08

Table 5.6. August 2002 dissolved oxygen data. Measurements taken 20-30 ft. off starboard side of *Arizona*'s hull, at approximately frame 75.

mg/L depending on proximity to breaches in the otherwise sealed torpedo blister, 56–100% less than ambient exterior measurements. Dissolved oxygen levels dropped to zero or near-zero in the two locations where the torpedo blister was completely sealed and had no seawater exchange. (see Table 4.5).

Finally, an ROV-deployed YSI water quality instrument recorded seawater parameters at selected locations within *Arizona*'s hull. In general, parameters recorded with the YSI sonde were nearly the same inside the ship, at least on the second deck level, as outside: pH = 8.0–8.1, temperature = 80–81º F, and salinity approximately 33.5 parts per thousand (ppt). Dissolved oxygen (DO%), however, dropped dramatically upon entering the ship. Outside, DO% = 86–88; typical inside DO% = 65–68 and in some instances dropped considerably lower. One of the more interesting observations is that interior cabin water is stratified by a subtle thermocline of about 0.5ºF however DO% changed significantly across this thermocline, from nearly 70 above to about 50 below the thermocline. This indicates very little water movement within interior cabins, even with open portholes. Researchers are also studying the extent of microbially-induced corrosion (MIC) in interior spaces of Arizona's hull (see Chapter 7).

Corrosion Analysis

An assessment of corrosion processes active on USS *Arizona*'s submerged hull consisted of theoretical evaluation, as well as both *in situ* and laboratory experimental measurements and analyses. Data collected relevant to a comprehensive investigation of corrosion process include *in situ* E_{corr} and pH measurements taken from 2000–2004.

In Situ Corrosion Potential (E_{corr}) and pH Measurements

E_{corr} /pH Measurements from Sequential Drilling through Concretion

In situ corrosion measurements taken systematically on *Arizona*'s hull include pH and E_{corr}. During this study. , *in situ* E_{corr} was obtained with Ag/AgCl reference electrodes giving a voltage measurement in mV. ThermoOrion (Beverly, MA) reference electrodes (Ag/AgCl, +200 mV to SHE) and Model 265A portable pH/mV meters with external ground adaptor were employed for primary data collection. In normal seawater, pH ranges from 7.5 to 8.2, but levels below 6.5 and as low as 4 are found under concretion covering actively corroding metal (North and MacLeod 1987:74). ThermoOrion pH electrodes were used in conjunction with the Model 265A portable meter. The general methodology for this procedure was developed by MacLeod (1995), who describes taking *in situ* E_{corr} measurements at the metal surface by drilling through the concretion, inserting pH and reference electrodes into the hole and taking sequential readings. During the present study, initial readings were made with ground contact made through a platinum disc on the bottom of the electrode. However, ground contact was modified, as discussed later, to avoid the possibility of poor contact at the bottom of the drilled hole. As an additional data set, a GMC-Staperm (Gardena, CA) Model AG-4-PT2 reference electrode (Ag/AgCl, seawater equivalent, +245 mV to SHE) with 200 ft. of #14 cable and 200 ft. of ground wire was used with a Wavetech HD-160 multimeter. The GMC electrode was deployed for exterior concretion surface measurements and was also used for ROV-mounted interior survey data collection.

At selected stations on the vessel, pH and E_{corr} were measured at various concretion-depths using reference electrodes inserted into holes drilled into the concretion. A drill rig

assembly and depth gage were constructed to drill ½-in. (1.3-cm)-diameter holes for inserting E_{corr} and pH probes (Figures 5.17 and 5.18). Hole depths were controlled by several depth jigs to provide uniform depths relative to the metal surface. Both E_{corr} and pH instruments were read out to the surface by 100 ft. cables; the topside recorder had voice communication with the diver. Multiple samples were drilled in a vertical transect at each station at varying water depths to characterize how the corrosion process changes with water depth and concretion thickness. These data have been collected in 14 transects arrayed from bow to stern, port and starboard, over several field seasons; however the largest cumulative data set of *in situ* corrosion measurements was collected between frame 70 and frame 90 (Figure 5.19). This 80-ft. hull section was chosen because the most complete original ship's plans, including original hull plate thickness was available between these frames. In addition, this hull section is the focus of the FEM completed by NIST (see Chapter 6).

In the first field season (2000), the focus was frame 85, completing vertical transects of *in situ* corrosion data on both the port and starboard sides of the ship (Figure 5.20). Only one E_{corr} measurement was taken for each drill sequence because the reference electrode was initially grounded through a platinum disc imbedded in the bottom of the electrode itself; no readings could be taken other than at the steel surface. Typical measurement procedures at a given water depth included surface pH; drilling to a depth of 0.4 in. (10 mm), taking pH reading at the bottom of the hole; drilling to 0.7 in. (18 mm), taking pH reading; and drilling to steel surface, where both pH and E_{corr} were obtained.

Data from the 2000 field season are tabulated (Table 5.7) and plotted in various graphs. A plot of pH vs. concretion depth shows that pH consistently decreases from a maximum at the exterior surface of the concretion to a minimum at the steel surface (Figures 5.21 and 5.22). The observation that pH decreases through the concretion from exterior to steel surface is consistent with reports on wrought and cast iron marine artifacts that note the cause for the decrease as similar to the crevice effect common in corrosion processes. Depletion of oxygen occurs as the concretion thickness increases and the low porosity of the concretion does not allow the oxygen to be replenished as fast as it consumed in the corrosion process (North 1976; North and MacLeod 1987). Chloride ions (Cl^-), with relatively high transport rates, migrate more rapidly than molecular oxygen through the concretion to the metal surface. The pH drops to as low as 4 at the metal surface as a result of hydrolysis reactions (equation [7]). The anodic reaction

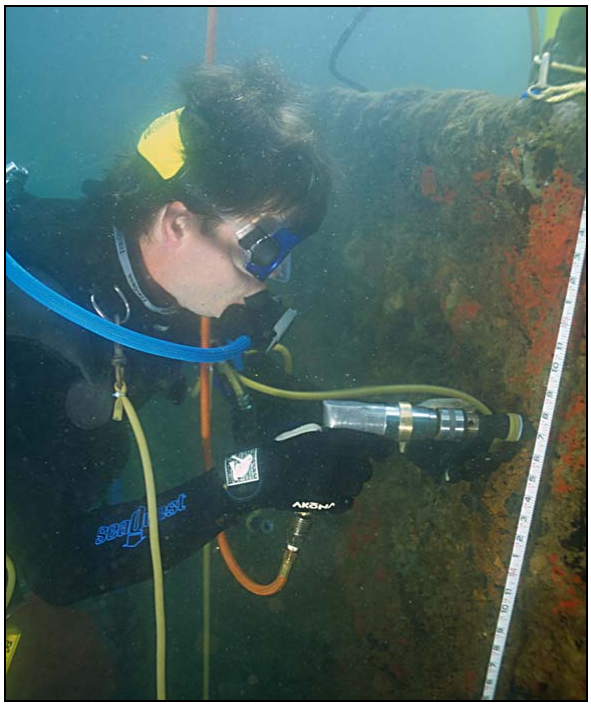

Figure 5.17. Drilling through USS *Arizona*'s exterior concretion in preparation to measuring E_{corr} and pH (NPS Photo by Brett Seymour).

Figure 5.18. Measuring E_{corr} and pH through *Arizona*'s concretion (NPS Photo by Brett Seymour).

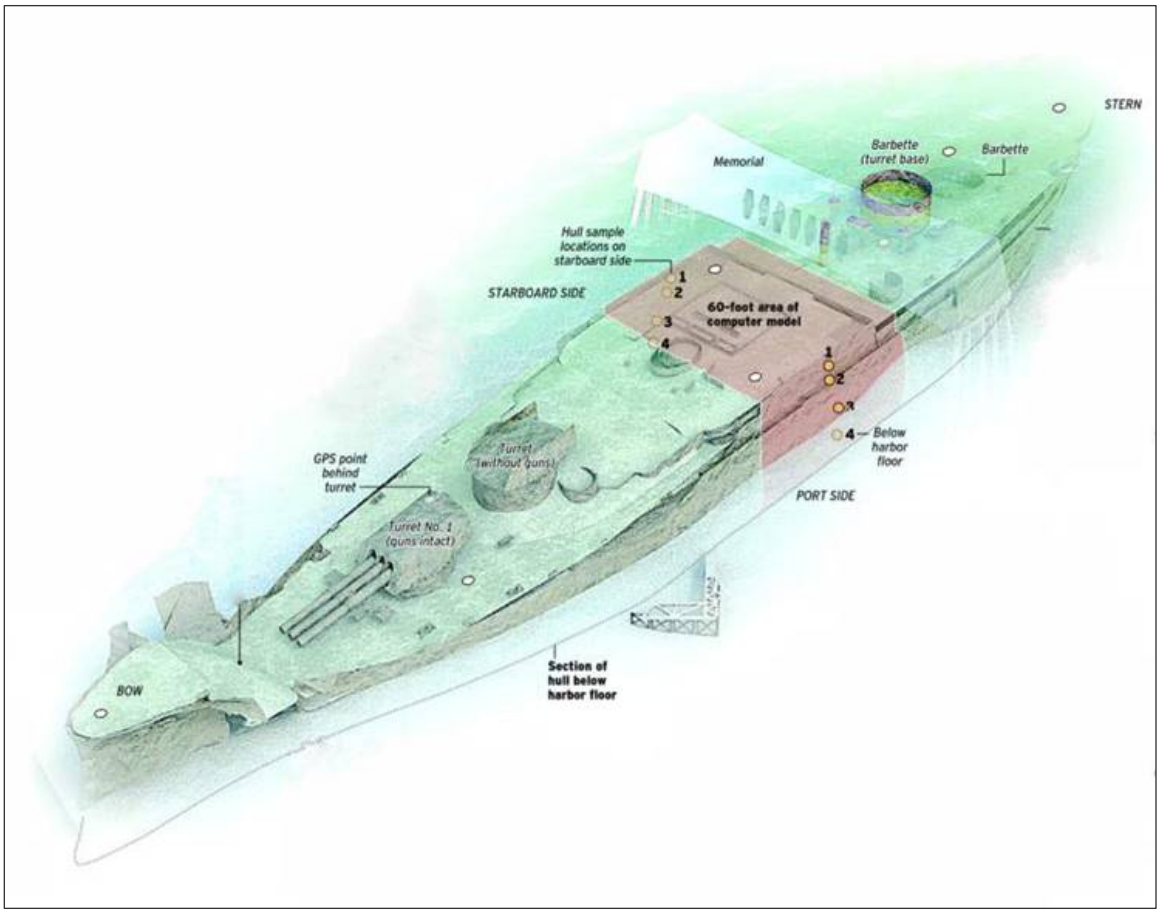

Figure 5.19. Graphic highlighting the 80-ft. long frame 70 to frame 90 section of USS *Arizona*'s hull (Graphic Courtesy of San Diego Union-Tribune).

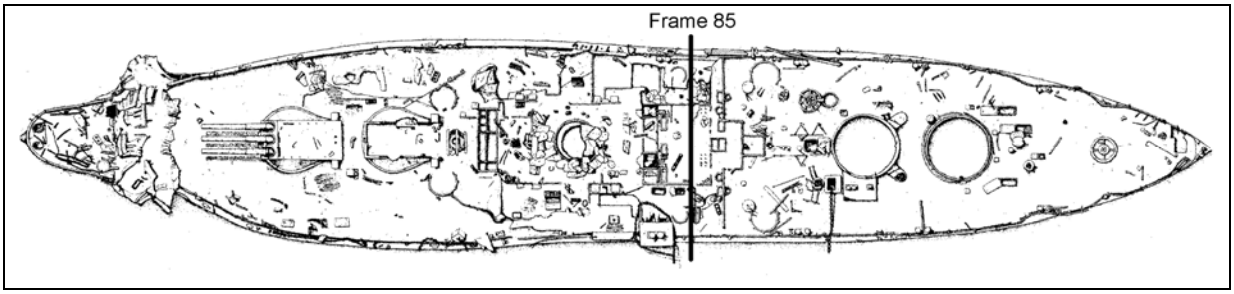

Figure 5.20. Frame 85 on USS *Arizona*'s hull, the focus for much of the corrosion analysis.

Sample	Vessel Side	Water Depth (ft.)	Drill Depth (mm)	Distance from Hull (mm)	pH	Ecorr (mV) vs. Ag/AgCl	Ecorr (mV) vs. SHE
+15C	Port	6	0	15	7.8		
+15C	Port	6	15	0	5.92	-591	-391
+14A	Port	7	0	8	8.05		
+14A	Port	7	8	0	7.99	-558	-358
+14B	Port	7	0	18	7.89		
+14B	Port	7	10	8	6.02		
+14B	Port	7	17	1	4.91		
+14B	Port	7	18	0	5.39	-590	-390
+14C	Port	7	0	18	7.89		
+14C	Port	7	13	5	7.39		
+14C	Port	7	18	0	6.09	-598	-398
+5A	Port	16	0	20.5	7.7		
+5A	Port	16	14	6.5	6.37		
+5A	Port	16	17	3.5	5.82		
+5A	Port	16	20.5	0	6.34	-564	-364
+5B	Port	16	0	17	n/a		
+5B	Port	16	13	4	6.46		
+5B	Port	16	15.5	1.5	6.07		
+5B	Port	16	17	0	5.77	-578	-378
-5A	Port	26	0	14	7.77		
-5A	Port	26	8	6	7.64		
-5A	Port	26	14	0	7.44	-572	-372
-5B	Port	26	0	17	7.69		
-5B	Port	26	11	6	6.09		
-5B	Port	26	12	5	3.83		
-5B	Port	26	17	0	3.86	-581	-381
+14D2	Starboard	3	0	15	7.64		
+14D2	Starboard	3	9	6	6.65		
+14D2	Starboard	3	15	0	5.85	-602	-402
+5D2	Starboard	12	0	20	7.62		
+5D2	Starboard	12	8	12	7.56		
+5D2	Starboard	12	20	0	5.48	-566	-366
-5D2	Starboard	22	0	10	7.03		
-5D2	Starboard	22	8	2	5.96		
-5D2	Starboard	22	10	0	7.26	-554	-354

Table 5.7. September 2000 *in situ* corrosion data. All data collected at frame 85 with Orion Ag/AgCl reference electrode using external ground. Elevation above (+) or below (-) top of torpedo blister. On port side, top of torpedo blister is at 21 ft. water depth; on starboard side, top of torpedo blister is at 17 ft. water depth

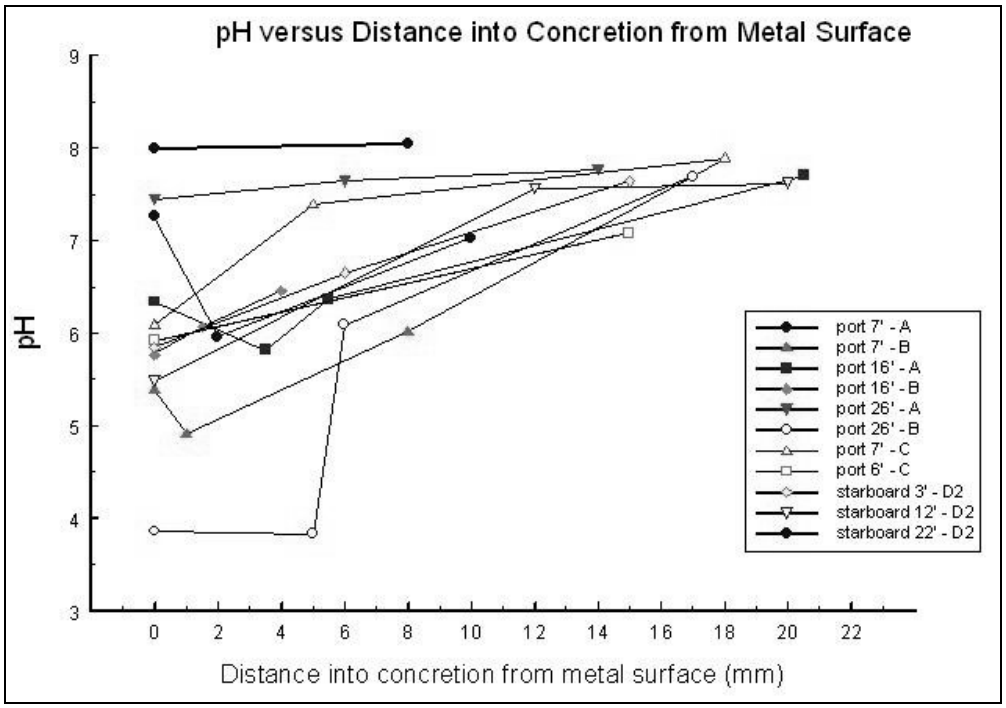

Figure 5.21. Relationship between pH and concretion thickness, based on September 2000 data in Table 5.7.

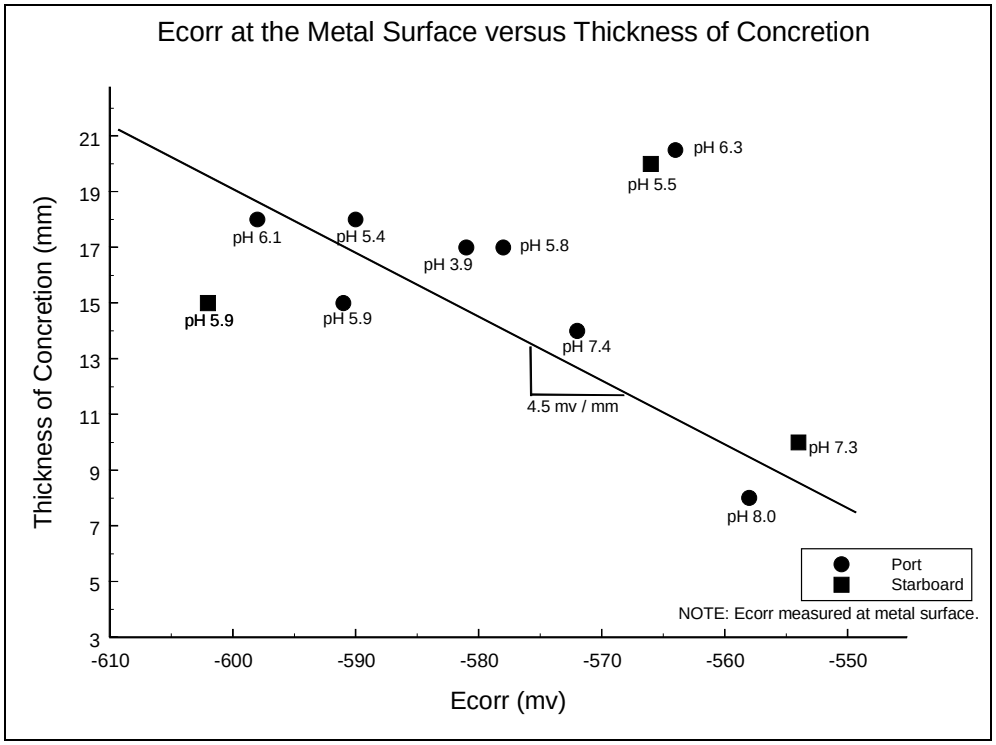

Figure 5.22. Relationship between E_{corr}, pH and concretion thickness, from data in Table 5.7.

continues at the steel surface and produces a solution rich in Fe^{+2}. Charge neutrality is maintained by outward diffusion of cations, mainly Fe^{+2} and H^{+} ions as Cl^{-} ions continue their inward migration through the concretion to the underlying steel. Changes in the concretion's chemistry and stoichiometry (quantitative relationship between reactants and products in a chemical reaction) as a result of iron ion diffusion from the steel hull toward the concretion's exterior surface will be discussed below.

The lack of consistently good contact between the base of the probe and hull metal at the bottom of the drill hole resulted in inconsistent readings during the 2000 field season. As a result, it was decided to incorporate a separate ground connection to the hull, removed from the drill hole. A separate ground also had the advantage that E_{corr} readings could be taken at the concretion's exterior surface as well as at interior positions in the concretion, rather than just at the bottom of the drill hole on the steel surface.

E_{corr}/pH data from the 2000 field season is superimposed on the iron-water Pourbaix diagram in Figure 5.3. All of the points fall within the region of active corrosion because they appear in the area labeled Fe^{+2}, yielding iron ions in water solution. Note that the points are well below the region of Fe^{+3} stability, so ferrous ion (Fe^{+2}) dominates. Since the points appear to follow closely along the lower dotted line, the cathode appears to be dominated by equations [3] or [4]. Lower pH values observed at the steel/concretion interface suggests the cathode reaction involves hydrogen evolution, in addition to oxygen consumption, as observed by divers after the first penetration of the concretion.

Assuming that oxygen diffusion through the concretion is the single factor determining the corrosion rate, the corrosion rate is therefore proportional to the reciprocal of the concretion thickness (d), according to equation [14]. As concretion thickens, oxygen must diffuse through a longer path and the availability of oxygen at the metal/concretion interface decreases.

During the second field season collecting *in situ* corrosion data (2001), the external ground was incorporated using a large C-clamp attached to the end of the ground cable. As mentioned above, the external ground to the hull allowed both E_{corr} and pH to be measured at various depths into the concretion. As before, final readings were taken at the bottom of the drill hole in contact with hull steel. In addition to taking measurements at frame 85, *in situ* data collection was expanded to other areas of the hull including vertical transects of pH and E_{corr} data at frames 9, 28, 82, 128 and 148, on both the port and starboard sides of the ship (Figure 5.23).

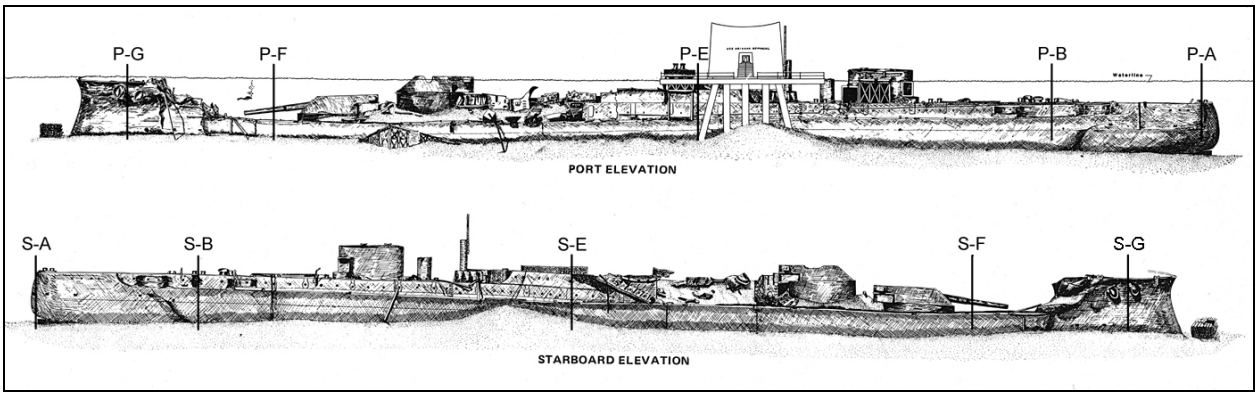

Figure 5.23. Location of *in situ* corrosion transects measured in June 2001.

Researchers in a small NPS launch recorded data relayed to them via hard wire communications from divers. Mobility allowed for attachment of the ground clamp in close proximity to the desired test site and easier deployment of test leads from meter readouts on the boat to diver positions. A comprehensive assessment of corrosion on *Arizona*'s hull was documented in terms of corrosion potential.

Data from the June 2001 field season were again tabulated (Tables 5.8–5.17) and plotted graphically. The most important observation from this data set is that E_{corr} is inversely proportional to water depth; that is, E_{corr} decreases (becomes more negative) as water depth increases (Figure 5.24). Figure 5.24 displays two values for each drill hole, appearing at the two ends of a vertical line—the top of the line corresponds to values taken at the steel hull surface, while the bottom of the line corresponds to values taken on the concretion's exterior surface. Visual observation indicates that E_{corr} decreases as the water depth increases. E_{corr} also decreases from the exterior surface of the concretion inward toward the steel hull, with the lowest E_{corr} value occurring at the steel surface (Figure 5.25). E_{corr} is most negative at the steel surface and the most positive at the concretion's exterior surface, as observed by North and MacLeod (1987).

Results of the June 2001 field season also clearly confirm that a decrease in pH, caused by reduced oxygen and increased choride ion, occurs as the steel surface is approached through the concretion (Figures 5.26 and 5.27). While this result is consistent at each location measured on *Arizona*'s hull, the effect is random with respect to water depth and frame location on the hull.

Sample	Location	Vessel Side	Water Depth (ft.)	Drill Depth (mm)	Distance from Hull (mm)	pH	E_{corr} (mV) vs. Ag/AgCL	E_{corr} (mV) vs. SHE
-5P-A	Frame 148	Port	13	0	27.5	8.03	-691	-491
-5P-A	Frame 148	Port	13	10	17.5	7.7	-675	-475
-5P-A	Frame 148	Port	13	21	6.5	6.25	-676	-476
-5P-A	Frame 148	Port	13	27.5	0	6.84	-674	-474
-18P-A	Frame 148	Port	29	0	15	5.09	-608	-408
-18P-A	Frame 148	Port	29	9	6	4.93	-608	-408
-18P-A	Frame 148	Port	29	15	0	3.08	-624	-424
-25P-A	Frame 148	Port	32	0	23	5.2	-597	-397
-25P-A	Frame 148	Port	32	16	7	5.22	-594	-394
-25P-A	Frame 148	Port	32	19	4	5.13	-594	-394
-25P-A	Frame 148	Port	32	23	0	3.54	-622	-422

Table 5.8. June 2001 *in situ* corrosion data, transect P-A. All data collected with Orion Ag/AgCl reference electrode using external ground. Elevation noted is distance below (-) gunwale, with gunwale depth at 8 ft.

Sample	Location	Vessel Side	Water Depth (ft.)	Drill Depth (mm)	Distance from Hull (mm)	pH	E_{corr} (mV) vs. Ag/AgCL	E_{corr} (mV) vs. SHE
-4.75S-A	Frame 148	Starboard	12	0	51	5.64	-548	-348
-4.75S-A	Frame 148	Starboard	12	11	40	5.8	-549	-349
-4.75S-A	Frame 148	Starboard	12	30	21	5.78	-562	-362
-4.75S-A	Frame 148	Starboard	12	51	0	5.58	-603	-403
-14.75S-A	Frame 148	Starboard	23	0	15	7	-545	-345
-14.75S-A	Frame 148	Starboard	23	8	7	5.93	-545	-345
-14.75S-A	Frame 148	Starboard	23	11	4	1.61	-548	-348
-14.75S-A	Frame 148	Starboard	23	15	0	5.26	-559	-359
-24.75S-A	Frame 148	Starboard	32	0	26	5.97	-544	-344
-24.75S-A	Frame 148	Starboard	32	17	9	6.12	-544	-344
-24.75S-A	Frame 148	Starboard	32	20	6	6.09	-544	-344
-24.75S-A	Frame 148	Starboard	32	26	0	5	-567	-367

Table 5.9. June 2001 *in situ* corrosion data, transect S-A. All data collected with Orion Ag/AgCl reference electrode using external ground. Elevation noted is distance below (-) gunwale, with gunwale depth at 7.25 ft.

Sample	Location	Vessel Side	Water Depth (ft.)	Drill Depth (mm)	Distance from Hull (mm)	pH	Ecorr (mV) vs. Ag/AgCL	Ecorr (mv) vs. SHE
+5P-B	Frame 128	Port	15	0	28	6.07	-542	-342
+5P-B	Frame 128	Port	15	n/a	16	5.62	-549	-349
+5P-B	Frame 128	Port	15	12	n/a	5.13	-565	-365
+5P-B	Frame 128	Port	15	28	0	4.85	-587	-387
-5P-B	Frame 128	Port	26	0	10	-	-546	-346
-5P-B	Frame 128	Port	26	10	0	5.55	-583	-383
-11P-B	Frame 128	Port	32	0	14	6.1	-547	-347
-11P-B	Frame 128	Port	32	12	2	6.01	-547	-347
-11P-B	Frame 128	Port	32	14	0	5.89	-558	-358

Table 5.10. June 2001 *in situ* corrosion data, transect P-B. All data collected with Orion Ag/AgCl reference electrode using external ground. Elevation noted is distance above (+) and below (-) torpedo blister.

Sample	Location	Vessel Side	Water Depth (ft.)	Drill Depth (mm)	Distance from Hull (mm)	pH	Ecorr (mV) vs. Ag/AgCL	Ecorr (mv) vs. SHE
+5S-B	Frame 128	Starboard	15	0	33	6.31	-542	-342
+5S-B	Frame 128	Starboard	15	10	23	6.73	-547	-347
+5S-B	Frame 128	Starboard	15	33	0	n/a	-570	-370
-5S-B	Frame 128	Starboard	25	0	14	n/a	-547	-347
-5S-B	Frame 128	Starboard	25	13	1	n/a	-572	-372
-5S-B	Frame 128	Starboard	25	14	0	n/a	-583	-383
-11S-B	Frame 128	Starboard	30	0	21	n/a	-548	-348
-11S-B	Frame 128	Starboard	30	10	11	n/a	-549	-349
-11S-B	Frame 128	Starboard	30	17	4	n/a	-551	-351
-11S-B	Frame 128	Starboard	30	21	0	n/a	-569	-369

Table 5.11. June 2001 *in situ* corrosion data, transect S-B. All data collected with Orion Ag/AgCl reference electrode using external ground. Elevation above (+) and below (-) torpedo blister, which is 20 ft.

Sample	Location	Vessel Side	Water Depth (ft.)	Drill Depth (mm)	Distance from Hull (mm)	pH	Ecorr (mV) vs. Ag/AgCL	Ecorr (mv) vs. SHE
+14P-E	Frame 82	Port	6	0	14.5	8.96	n/a	n/a
+14P-E	Frame 82	Port	6	11	3.5	8.6	n/a	n/a
+14P-E	Frame 82	Port	6	14.5	0	8.5	n/a	n/a
+5P-E	Frame 82	Port	18	0	26	8.09	-561	-361
+5P-E	Frame 82	Port	18	10	16	8.04	-552	-352
+5P-E	Frame 82	Port	18	18	8	5.67	-566	-366
+5P-E	Frame 82	Port	18	26	0	5.94	-614	-414
-5P-E	Frame 82	Port	26	0	21	4.54	-580	-380
-5P-E	Frame 82	Port	26	4	17	4.65	-560	-360
-5P-E	Frame 82	Port	26	11	10	2.97	-567	-367
-5P-E	Frame 82	Port	26	21	0	2.64	-584	-384

Table 5.12. June 2001 *in situ* corrosion data, transect P-E. All data collected with Orion Ag/AgCl reference electrode using external ground. Elevation above (+) and below (-) torpedo blister, which is 22 ft.

Sample	Location	Vessel Side	Water Depth (ft.)	Drill Depth (mm)	Distance from Hull (mm)	pH	Ecorr (mV) vs. Ag/AgCL	Ecorr (mv) vs. SHE
+14S-E	Frame 82	Starboard	3	0	>150	6.71	-542	-342
+14S-E	Frame 82	Starboard	3	10	140	6.72	-541	-341
+14S-E	Frame 82	Starboard	3	19	131	6.91	-538	-338
+14S-E	Frame 82	Starboard	3	>150	0	6.63	-533	-333
+5S-E	Frame 82	Starboard	12	0	63	6.48	-544	-344
+5S-E	Frame 82	Starboard	12	11	52	5.71	-547	-347
+5S-E	Frame 82	Starboard	12	52	11	3.89	-563	-363
+5S-E	Frame 82	Starboard	12	63	0	3.67	-562	-362
-5S-E	Frame 82	Starboard	23	0	14	6.24	-547	-347
-5S-E	Frame 82	Starboard	23	11	3	4.79	-551	-351
-5S-E	Frame 82	Starboard	23	14	0	5.04	-571	-371

Table 5.13. June 2001 *in situ* corrosion data, transect S-E. All data collected with Orion Ag/AgCl reference electrode using external ground. Elevation above (+) and below (-) torpedo blister, which is 18 ft. Sample +14S-E never reached metal, depth of concretion too great. At sample +5S-E, water flowed out of the hole, precipitating from black to red (see below).

Sample	Location	Vessel Side	Water Depth (ft.)	Drill Depth (mm)	Distance from Hull (mm)	pH	Ecorr (mV) vs. Ag/AgCL	Ecorr (mv) vs. SHE
0P-F	Frame 28	Port	27	0	23	6.14	No Data	No Data
0P-F	Frame 28	Port	27	10	13	6.21	No Data	No Data
0P-F	Frame 28	Port	27	23	0	4.1	No Data	No Data
-5P-F	Frame 28	Port	32	0	32	6.14	No Data	No Data
-5P-F	Frame 28	Port	32	12	20	6.14	No Data	No Data
-5P-F	Frame 28	Port	32	30	2	6.14	No Data	No Data
-5P-F	Frame 28	Port	32	32	0	4.75	No Data	No Data

Table 5.14. June 2001 *in situ* corrosion data, transect P-F. All data collected with Orion Ag/AgCl reference electrode using external ground. Elevation above (+) and below (-) torpedo blister, which is 27 ft.

Sample	Location	Vessel Side	Water Depth (ft.)	Drill Depth (mm)	Distance from Hull (mm)	pH	Ecorr (mV) vs. Ag/AgCL	Ecorr (mv) vs. SHE
0S-F	Frame 28	Starboard	23.5	0	21	6.14	-543	-343
0S-F	Frame 28	Starboard	23.5	8	13	6.28	-544	-344
0S-F	Frame 28	Starboard	23.5	18	3	5.51	-569	-369
0S-F	Frame 28	Starboard	23.5	21	0	5.85	-570	-370
-5S-F	Frame 28	Starboard	28.5	0	26	6.27	-537	-337
-5S-F	Frame 28	Starboard	28.5	17	9	5.93	-537	-337
-5S-F	Frame 28	Starboard	28.5	26	0	5.3	-547	-347

Table 5.15. June 2001 *in situ* corrosion data, transect S-F. All data collected with Orion Ag/AgCl reference electrode using external ground. Elevation above (+) and below (-) torpedo blister, which is 23.5 ft.

Sample	Location	Vessel Side	Water Depth (ft.)	Drill Depth (mm)	Distance from Hull (mm)	pH	Ecorr (mV) vs. Ag/AgCL	Ecorr (mv) vs. SHE
-5P-G	Frame 9	Port	10	0	18	6.71	-538	-338
-5P-G	Frame 9	Port	10	11	7	6.52	-538	-338
-5P-G	Frame 9	Port	10	18	0	5.12	-552	-352
-10P-G	Frame 9	Port	15	0	15	6.67	-540	-340
-10P-G	Frame 9	Port	15	10	5	6.45	-542	-342
-10P-G	Frame 9	Port	15	15	0	4.57	-568	-368
-15P-G	Frame 9	Port	20	0	19	6.62	-545	-345
-15P-G	Frame 9	Port	20	8	11	5.32	-551	-351
-15P-G	Frame 9	Port	20	17	2	3.64	-574	-374
-15P-G	Frame 9	Port	20	19	0	3.85	-566	-366
-19P-G	Frame 9	Port	24	0	21	6.53	-539	-339
-19P-G	Frame 9	Port	24	11	10	5.61	-539	-339
-19P-G	Frame 9	Port	24	21	0	4.97	-554	-354

Table 5.16. June 2001 *in situ* corrosion data, transect P-G. All data collected with Orion Ag/AgCl reference electrode using external ground. Elevation noted is distance below (-) gunwale, with gunwale depth at 5 ft.

Sample	Location	Vessel Side	Water Depth (ft.)	Drill Depth (mm)	Distance from Hull (mm)	pH	Ecorr (mV) vs. Ag/AgCL	Ecorr (mv) vs. SHE
-5S-G	Frame 9	Starboard	10	0	28	6.76	-541	-341
-5S-G	Frame 9	Starboard	10	11	17	6.63	-551	-351
-5S-G	Frame 9	Starboard	10	18	10	3.93	-568	-368
-5S-G	Frame 9	Starboard	10	28	0	3.52	-585	-385
-10S-G	Frame 9	Starboard	15	0	19	6.16	-550	-350
-10S-G	Frame 9	Starboard	15	16	3	5.57	-561	-361
-10S-G	Frame 9	Starboard	15	19	0	4.68	-561	-361
-15S-G	Frame 9	Starboard	20	0	11	6.15	-555	-355
-15S-G	Frame 9	Starboard	20	10	1	5.8	-562	-362
-15S-G	Frame 9	Starboard	20	11	0	4.7	-563	-363
-19S-G	Frame 9	Starboard	24	0	13	6.09	-551	-351
-19S-G	Frame 9	Starboard	24	12	1	5.98	-551	-351
-19S-G	Frame 9	Starboard	24	13	0	5.43	-551	-351

Table 5.17. June 2001 *in situ* corrosion data, transect S-G. All data collected with Orion Ag/AgCl reference electrode using external ground. Elevation noted is distance below (-) gunwale, with gunwale depth at 5 ft. At sample -5S-G, water flowed out of the hole, precipitating from black to red (see below).

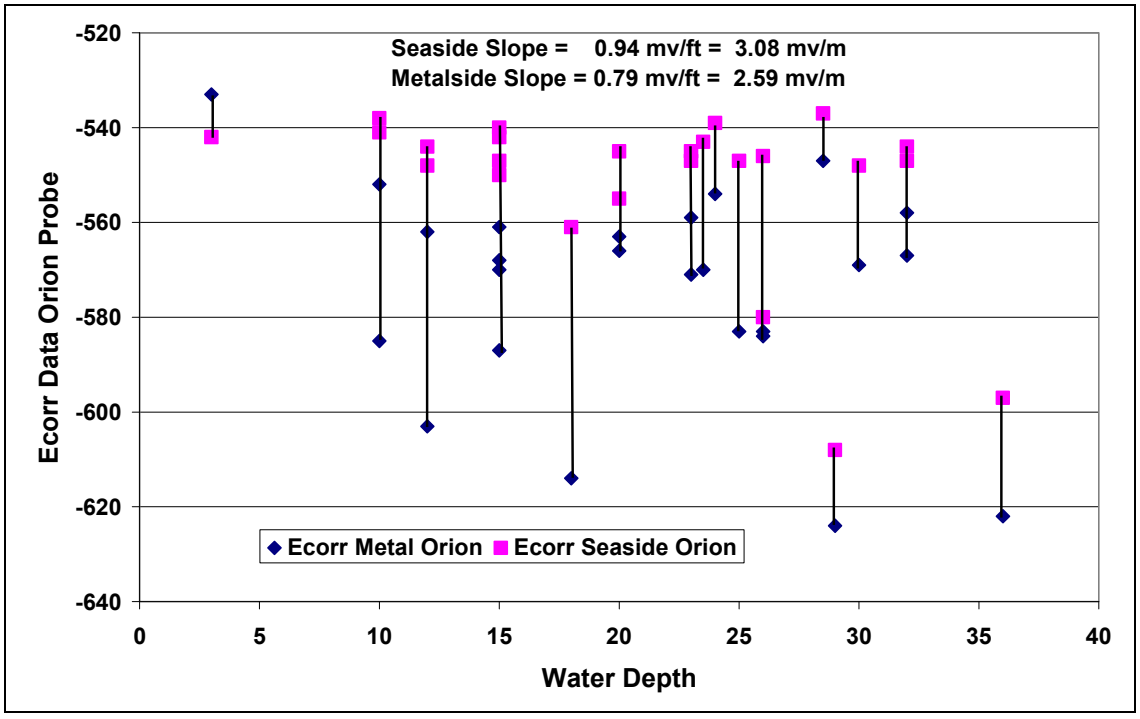

Figure 5.24. Corrosion potential as function of water depth, typical frames from June 2001 data set.

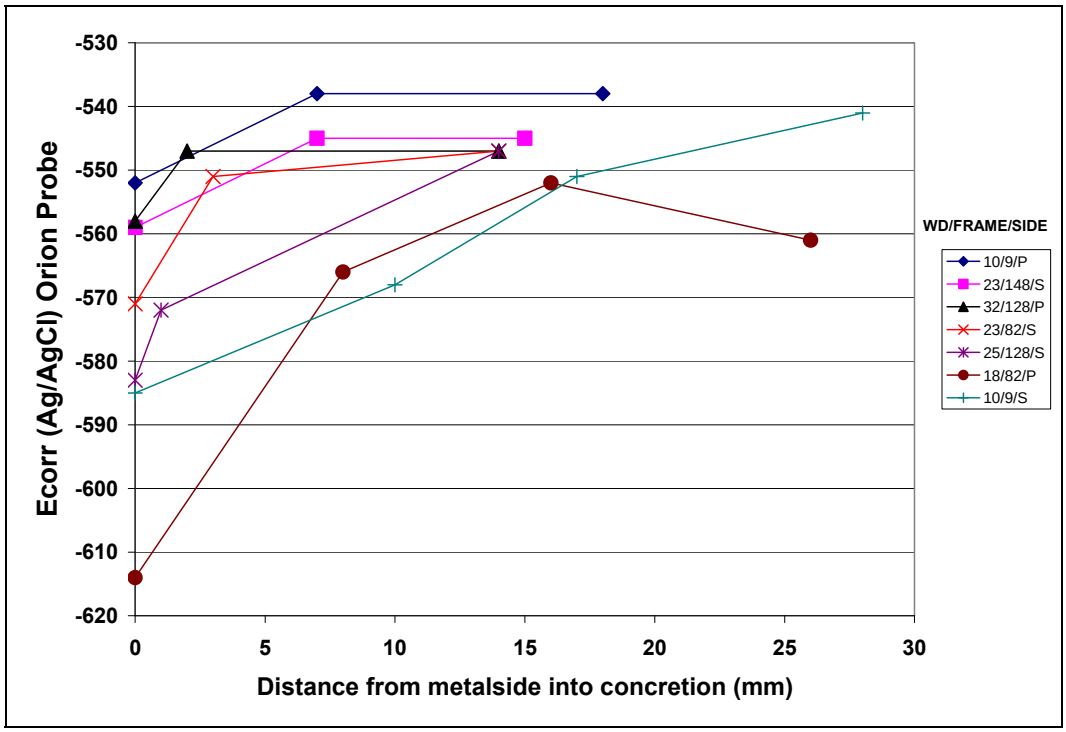

Figure 5.25. Corrosion potential as a function of distance from hull, into concretion to open seawater, typical frames from June 2001 data set.

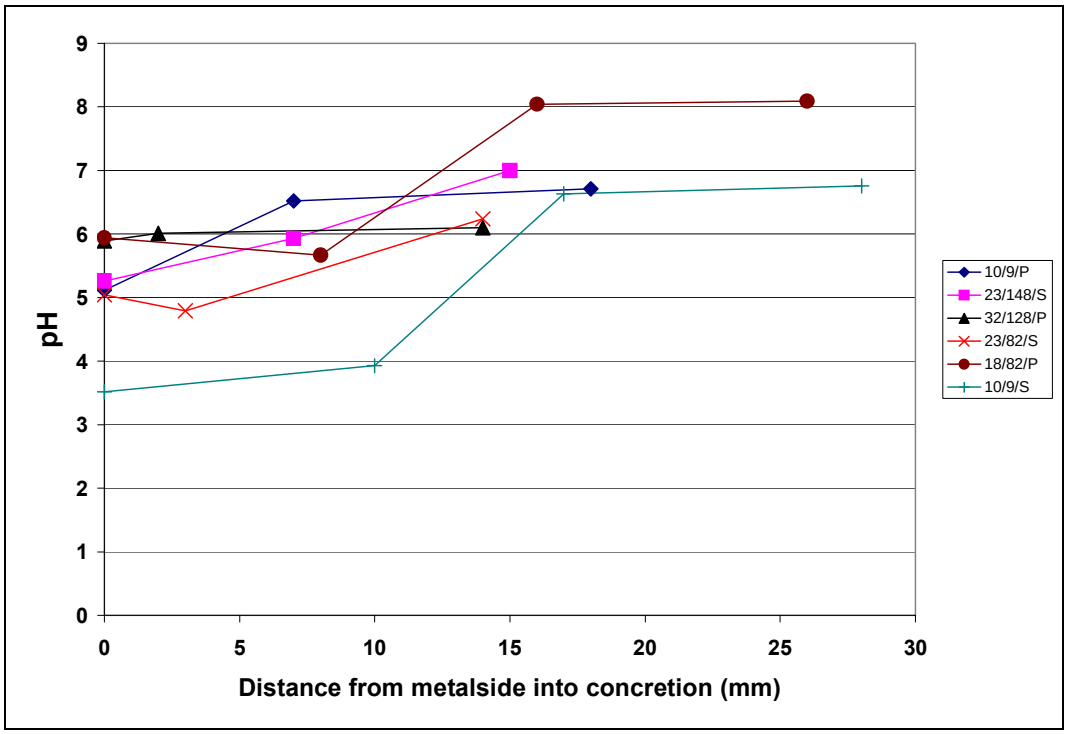

Figure 5.26. pH as a function of distance from hull surface, typical frames from June 2001 data set.

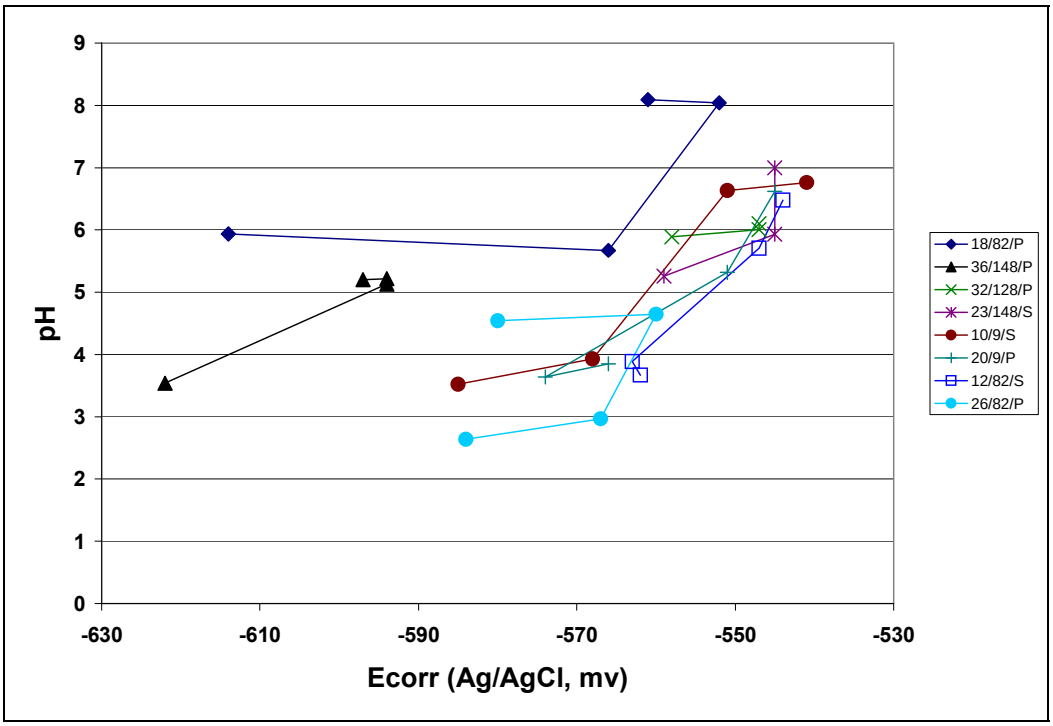

Figure 5.27. pH as a function of E_{corr}, typical frames from June 2001 data set.

The polarization diagram illustrates how the potential difference between points A and C prevents intersection of the cathode and anode polarization lines because of resistance between the E_{corr} probe and the metal surface (see Figure 5.1). From Ohms law:

$$i_{(corr\ IR\ drop)} = (E_{corr}\ (exterior) - E_{corr}\ (interior)) / (r)(d) \qquad [15]$$

where

r (Ω-cm) is the electrical resistivity

d (cm) is concretion thickness

E_{corr} is corrosion potential (volts)

$i_{(corr\ IR\ drop)}$ is concretion current density (amp/cm^2)

Using a value of r = 2000 Ω-cm for the electrical resistivity of the concretion (MacLeod 1982), and E_{corr} and d values for Frame 148, starboard, a typical calculation gives the following value for $i_{(corr,\ IR\ drop)}$ in mpy:

$$i_{(corr,\ IR\ drop)} = V/(\Omega\text{-cm x cm}) = 0.023 / (2000 \times 2.6) \times 0.46 = 2.03\ mpy$$

Computation of $i_{(corr, IR\ drop)}$ for all of data in Tables 5.8–5.17, including E_{corr} values taken inside the concretion, resulted in a wide scatter of data. Figure 5.28 shows a plot of $i_{(corr, IR\ drop)}$ as a function of water depth after eliminating internal E_{corr} readings obtained from 22 sites over the entire hull. The trendline shows increasing $i_{(corr, IR\ drop)}$, just the opposite of i_{corr} obtained from metal samples taken from the hull. It is concluded that current distribution inside the concretion is complex and creates a voltage gradient across the concretion that cannot be related to i_{corr} in simple terms. Furthermore, the electrical resistivity of the concretion is not a constant as assumed in equation [15]. This observation is confirmed from x-ray diffraction results showing that the concretion is not homogeneous.

As discussed above, anodic polarization is shown as a solid line from A(3) to B or as a solid line from A(3) to A(1) and dotted from A(1) through B(1) to A(4) (Figure 5.1). From A(3) to B, the corrosion rate increases as E_{corr} increases and is typical of steel in seawater. For simplicity, anodic polarization is assumed to be linear to point B but in reality may deviate upward as the potential increases. From A(3) to A(4) along A(1) to B(1), passivation occurs as is typical for steel and aluminum in natural water. The metal passivates by initially corroding and

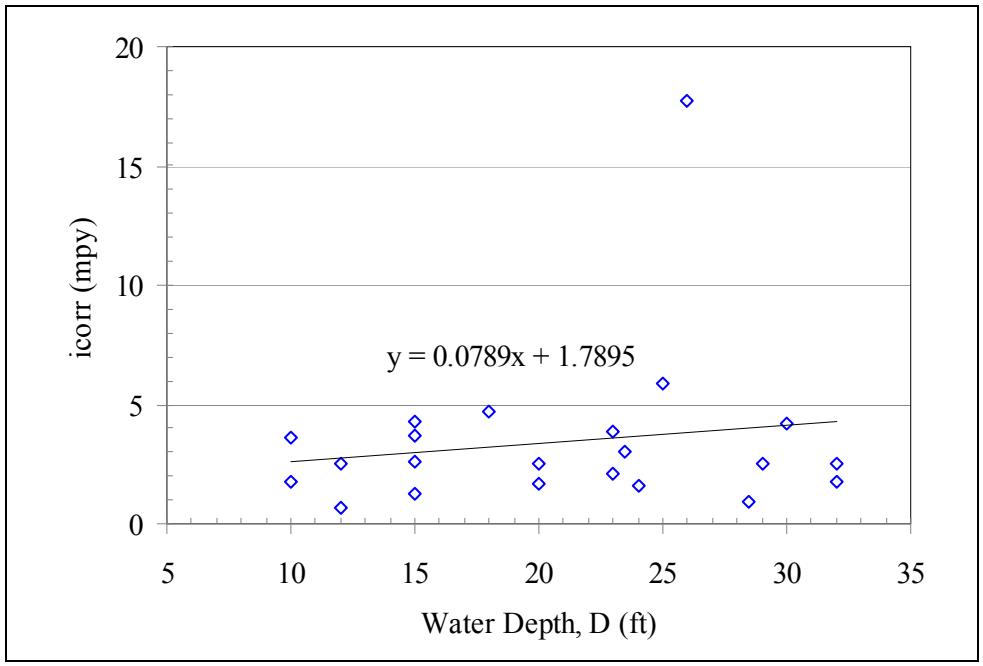

Figure 5.28. i_{corr} (IR Drop across concretion) as a function of water depth.

forming its own protective film. Approaching passivation, anodic polarization increases but peaks at around A(1) dropping to a lower current as the potential increases. Intersection with cathodic polarization at B(1) now occurs at a lower i_{corr} than that identified as i_{corr} (1). This illustrates how an increase in E_{corr} yields a lower rather than a higher i_{corr}. It is important to emphasize that steel does not normally passivate in seawater and anodic polarization continues to increase from A(3) to points A or B depending on the IR drop. The region between C and A, nearly point B, defines E_{corr} and the vertical line through C and A defines i_{corr}(1). The difference between E_{corr} (1) and E_{corr} (2) is small and usually neglected.

As an interesting aside, during concretion drilling at sites -5S-G (frame 9, starboard side, at a water depth of 10 ft.) and +5S-E (frame 82, starboard side, at a water depth of 13 ft.), clear water poured out of the drill hole upon removal of the drill. As it mixed with seawater, the outflow grew dark, then became cloudy and reddish in color and reduced visibility to a few feet. Outflow was strong and streamed out the drill hole approximately 8 in. Adjacent concretion had blistered away from the hull in this area, creating a gap between the steel hull and the concretion. One explanation for this phenomenon is hydrogen accumulation behind the concretion during hydrogen ion reduction as a result of equation [4] and equation [16]. Equation [16], derived from the Nerst equation [1], is useful to estimate the extent of pressure build up that can theoretically develop at the steel surface behind the concretion (Pourbaix 1974):

$$E^0 = E_{corr} = 0.000 - 0.0592pH - 0.0295 \log(P[H_2]) \qquad [16]$$

The theoretical maximum gas pressure, equation [16], is over 950 atmospheres or 14,000 psi at pH = 4 and E_{corr} = 0.325 V (SHE). Obviously, the gas pressure could never reach such high values because hydrogen would slowly diffuse into the steel hull or escape through voids in the concretion before the pressure exceeded more than a few atmospheres. After the event, the hole was plugged. The next day the hole was reopened and clear water continued to pour out of the drill hole as the event was documented on underwater video.

Immediately before removing hull coupons in August 2002 (see below), E_{corr} and pH were obtained at each coupon sample location. Using the same procedure as in past field operations, pH and E_{corr} were measured in holes drilled close to the sample area. Initial E_{corr}/pH data was to be obtained through the concretion 6–8 in. above, forward, below and aft of the site

selected for each core sample before the pad was cleared of concretion. Due to time constraints, the number of readings was reduced as drill operations continued (Table 5.18).

The 2002 sample locations were revisited in November 2003 to once again collect E_{corr} and pH data (Table 5.19). This replication allows researchers to gauge the impact to the ship of removing the hull coupons and surrounding encrustation. Data collected were comparable to 2002 data from the same locations, indicating no negative impact to the ship resulted from coupon removal. The epoxy sealing had succeeded in preventing formation of local areas of increased corrosion during the year since coupon collection. The areas drilled for this data set were also the locations where preliminary ultrasonic thickness testing was conducted (see below).

Finally, in 2004 a final E_{corr}/pH data set was collected during expansion of the ultrasonic thickness survey (Table 5.20). These data continued to confirm earlier findings regarding E_{corr} and pH variability. E_{corr} as a function of water depth from Tables 5.19 and 5.20 are combined and plotted in Figure 5.29.

E_{corr} Transects at Concretion Exterior

In addition to sequential drilling and E_{corr}/pH measurements through the concretion, a potential survey was conducted in June 2001 at selected transects across *Arizona*'s hull using a GMC reference electrode and Wavetech HD-160 meter. Seven transects were selected for measurement from the harbor bottom on the starboard side of the ship, up the starboard side to the starboard gunwale, over exposed deck areas to the port gunwale, and down the port side of the ship to the harbor bottom (Figure 5.30). E_{corr} measurements were taken every 6 ft. along the transect on the exterior surface of the concretion. These transects were a quick, non-intrusive way to collect an additional data set that would complement and could be directly compared to the more detailed data obtained through sequential drilling. The transects indicate a consistent trend toward lower E_{corr} as the water depth increases (Figure 5.31). For example, the horizontal areas on Transects 1, 2, 3, and 4 are closer to the water surface nearer the stern than Transects 6 and 7, and as a result E_{corr} values in the latter two are from 15–25 mV more negative.

Transect 1, taken near the stern at approximately frame 148, reflects a drop in E_{corr} as the transect approaches the harbor bottom on both sides, particularly at and below the harbor bottom

Sample	Location	Vessel Side	Water Depth (ft.)	Drill Depth (mm)	Distance from Hull (mm)	pH	Ecorr (mV) vs. Ag/AgCl	Ecorr (mV) vs. SHE
USAR-02-001	Frame 76.5, 6 in. above sample	Port	5	0	15.4	7.64	-527	-327
USAR-02-001	Frame 76.5, 6 in. above sample	Port	5	9.4	6	6.12	-529	-329
USAR-02-001	Frame 76.5, 6 in. above sample	Port	5	15.4	0	6.51	-554	-354
USAR-02-001	Frame 76.5, 8 in. forward of sample	Port	5	0	23.5	7.7	-528	-328
USAR-02-001	Frame 76.5, 8 in. forward of sample	Port	5	11.3	12.2	7.7	-530	-330
USAR-02-001	Frame 76.5, 8 in. forward of sample	Port	5	23.5	0	6.53	-557	-357
USAR-02-001	Frame 76.5, 10 in. aft of sample	Port	5	0	26	7.43	-531	-331
USAR-02-001	Frame 76.5, 10 in. aft of sample	Port	5	10.2	15.8	6.68	-537	-337
USAR-02-001	Frame 76.5, 10 in. aft of sample	Port	5	26	0	6.5	-551	-351
USAR-02-002	Frame 76.5, 6 in. forward of sample	Port	19.5	0	17	7	-539	-339
USAR-02-002	Frame 76.5, 6 in. forward of sample	Port	19.5	10.5	6.5	6.58	-549	-349
USAR-02-002	Frame 76.5, 6 in. forward of sample	Port	19.5	17	0	5.95	-551	-351
USAR-02-002	Frame 76.5, 6 in. aft of sample	Port	19.5	0	42.5	7.49	-538	-338
USAR-02-002	Frame 76.5, 6 in. aft of sample	Port	19.5	8	34.5	7.24	-539	-339
USAR-02-002	Frame 76.5, 6 in. aft of sample	Port	19.5	42.5	0	5.5	-560	-360
USAR-02-003	Frame 76.5, 6 in. forward of sample	Port	26	0	17.4	6.99	-542	-342
USAR-02-003	Frame 76.5, 6 in. forward of sample	Port	26	7	10.4	7.43	-542	-342
USAR-02-003	Frame 76.5, 6 in. forward of sample	Port	26	17.4	0	6.34	-560	-360
USAR-02-004	Frame 76.5, 1 ft. aft of sample	Port	34	0	9	7.13	-509	-309
USAR-02-004	Frame 76.5, 1 ft. aft of sample	Port	34	6.5	2.5	5.51	-522	-322
USAR-02-004	Frame 76.5, 1 ft. aft of sample	Port	34	9	0	6.19	-523	-323
USAR-02-007	Frame 80.5, 6 in. aft of sample	Starboard	5	0	9.3	7.28	-550	-350
USAR-02-007	Frame 80.5, 6 in. aft of sample	Starboard	5	9.3	0	7.31	-562	-362
USAR-02-008	Frame 80.5, 6 in. forward of sample	Starboard	15	0	15.6	6.95	-549	-349
USAR-02-008	Frame 80.5, 6 in. forward of sample	Starboard	15	14.7	0.9	4.43	-563	-363
USAR-02-008	Frame 80.5, 6 in. forward of sample	Starboard	15	15.6	0	4.46	-561	-361
USAR-02-009	Frame 80.5, 6 in. forward of sample	Starboard	22	0	6.5	6.8	-552	-352
USAR-02-009	Frame 80.5, 6 in. forward of sample	Starboard	22	3.5	3	6.71	-553	-353
USAR-02-009	Frame 80.5, 6 in. forward of sample	Starboard	22	6.5	0	6.15	-557	-357
USAR-02-010	Frame 80.5, 6 in. forward of sample	Starboard	32.5	0	9	6.67	-689	-489
USAR-02-010	Frame 80.5, 6 in. forward of sample	Starboard	32.5	7	2	6.29	-695	-495
USAR-02-010	Frame 80.5, 6 in. forward of sample	Starboard	32.5	9	0	5.53	-699	-499

Table 5.18. *In situ* corrosion data collected August 2002 in location of each hull sample (coupon) collected. All data collected with Orion Ag/AgCl reference electrode.

Sample	Location	Vessel Side	Water Depth (ft.)	Drill Depth (mm)	Distance from Hull (mm)	pH	Ecorr (mV) vs. Ag/AgCl	Ecorr (mV) vs. SHE
USAR-03-001	Frame 76.5	Port	5	0	25	n/a	-547	-347
USAR-03-001	Frame 76.5	Port	5	7	18	n/a	-547	-347
USAR-03-001	Frame 76.5	Port	5	25	0	n/a	-587	-387
USAR-03-002	Frame 76.5	Port	19.5	0	12	n/a	-554	-354
USAR-03-002	Frame 76.5	Port	19.5	9	3	n/a	-555	-355
USAR-03-002	Frame 76.5	Port	19.5	12	0	n/a	-593	-393
USAR-03-003	Frame 76.5	Port	26	0	10	n/a	-555	-355
USAR-03-003	Frame 76.5	Port	26	6	4	n/a	-562	-362
USAR-03-003	Frame 76.5	Port	26	10	0	n/a	-580	-380
USAR-03-007	Frame 80.5	Starboard	5	0	15	n/a	-550	-350
USAR-03-007	Frame 80.5	Starboard	5	7	8	n/a	-559	-359
USAR-03-007	Frame 80.5	Starboard	5	15	0	n/a	-597	-397
USAR-03-008	Frame 80.5	Starboard	15	0	18	n/a	-552	-352
USAR-03-008	Frame 80.5	Starboard	15	8	10	n/a	-552	-352
USAR-03-008	Frame 80.5	Starboard	15	18	0	n/a	-562	-362
USAR-03-009	Frame 80.5	Starboard	22	0	12	n/a	-558	-358
USAR-03-009	Frame 80.5	Starboard	22	3	9	n/a	-558	-358
USAR-03-009	Frame 80.5	Starboard	22	8	4	n/a	-579	-379
USAR-03-009	Frame 80.5	Starboard	22	12	0	n/a	-585	-385

Table 5.19. ***In situ*** **corrosion data collected November 2003 in same locations as the previous year, at the site of each hull sample (coupon) collected. All data collected with Orion Ag/AgCl reference electrode.**

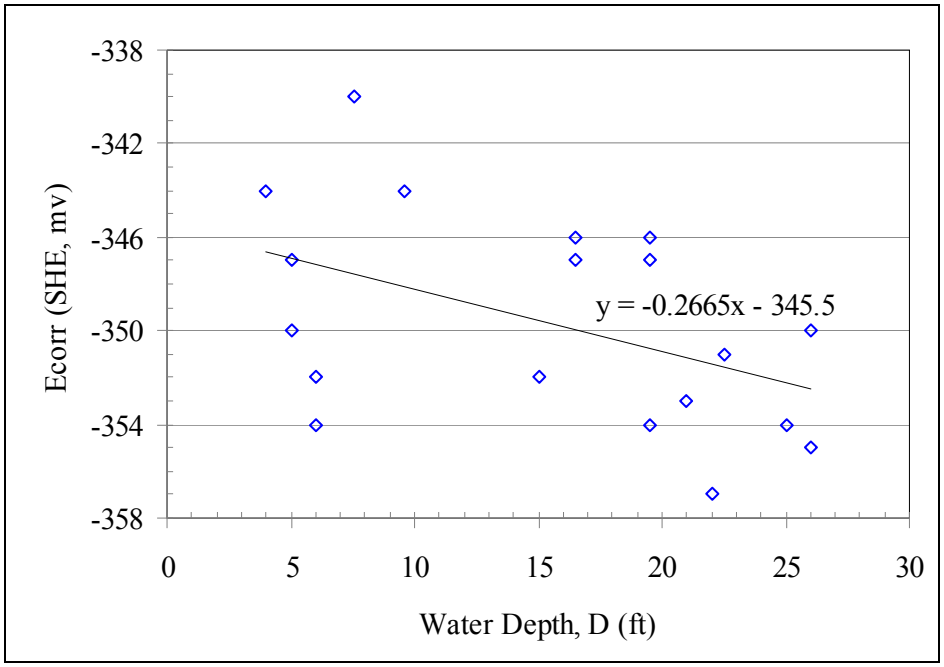

Figure 5.29. E_{corr} **as a function of water depth for in situ data collected in 2003 and 2004.**

Sample	Location	Vessel Side	Water Depth (ft.)	Drill Depth (mm)	Distance from Hull (mm)	pH	Ecorr (mV) vs. Ag/AgCl	Ecorr (mV) vs. SHE
USAR-04-001a	Frame 88	Port	6	0	n/a	n/a	-597	-352
USAR-04-001a	Frame 88	Port	6	n/a	0	n/a	-600	-355
USAR-04-001b	Frame 88	Port	6	0	n/a	n/a	-599	-354
USAR-04-001b	Frame 88	Port	6	n/a	0	n/a	-600	-355
USAR-04-002	Frame 88	Port	19.5	0	21	n/a	-592	-347
USAR-04-002	Frame 88	Port	19.5	21	0	n/a	-596	-351
USAR-04-003	Frame 88	Port	25	0	19	n/a	-599	-354
USAR-04-003	Frame 88	Port	25	19	0	n/a	-601	-356
USAR-04-004	Frame 88	Starboard	4	0	n/a	n/a	-589	-344
USAR-04-004	Frame 88	Starboard	4	n/a	0	n/a	-593	-348
USAR-04-005	Frame 70	Port	7.6	0	18	n/a	-585	-340
USAR-04-005	Frame 70	Port	7.6	18	0	n/a	-588	-343
USAR-04-006	Frame 70	Port	19.5	8	18	n/a	-591	-346
USAR-04-006	Frame 70	Port	19.5	18	0	n/a	-591	-346
USAR-04-007	Frame 70	Port	26	0	14	n/a	-595	-350
USAR-04-007	Frame 70	Port	26	14	0	n/a	-598	-353
USAR-04-008	Frame 68	Starboard	9.6	0	24	n/a	-589	-344
USAR-04-008	Frame 68	Starboard	9.6	24	0	n/a	-591	-346
USAR-04-009	Frame 68	Starboard	16.5	0	20	n/a	-591	-346
USAR-04-009	Frame 68	Starboard	16.5	20	0	n/a	-592	-347
USAR-04-010	Frame 68	Starboard	22.5	0	13	n/a	-596	-351
USAR-04-010	Frame 68	Starboard	22.5	13	0	n/a	-598	-353
USAR-04-011	Frame 88	Starboard	16.5	0	22	n/a	-592	-347
USAR-04-011	Frame 88	Starboard	16.5	22	0	n/a	-594	-349
USAR-04-012	Frame 87	Starboard	21	0	17	n/a	-598	-353
USAR-04-012	Frame 87	Starboard	21	17	0	n/a	-601	-356

Table 5.20. ***In situ*** **corrosion data collected November 2004 in location of each concretion sample collected during ultrasonic thickness testing. All data collected with Orion Ag/AgCl reference electrode.**

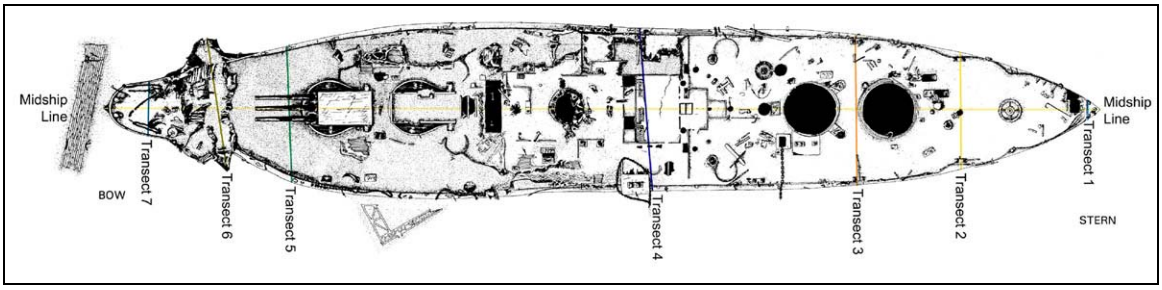

Figure 5.30. Transects for potential survey conducted in June 2001 at selected locations across ***Arizona*****'s hull using a GMC reference electrode.**

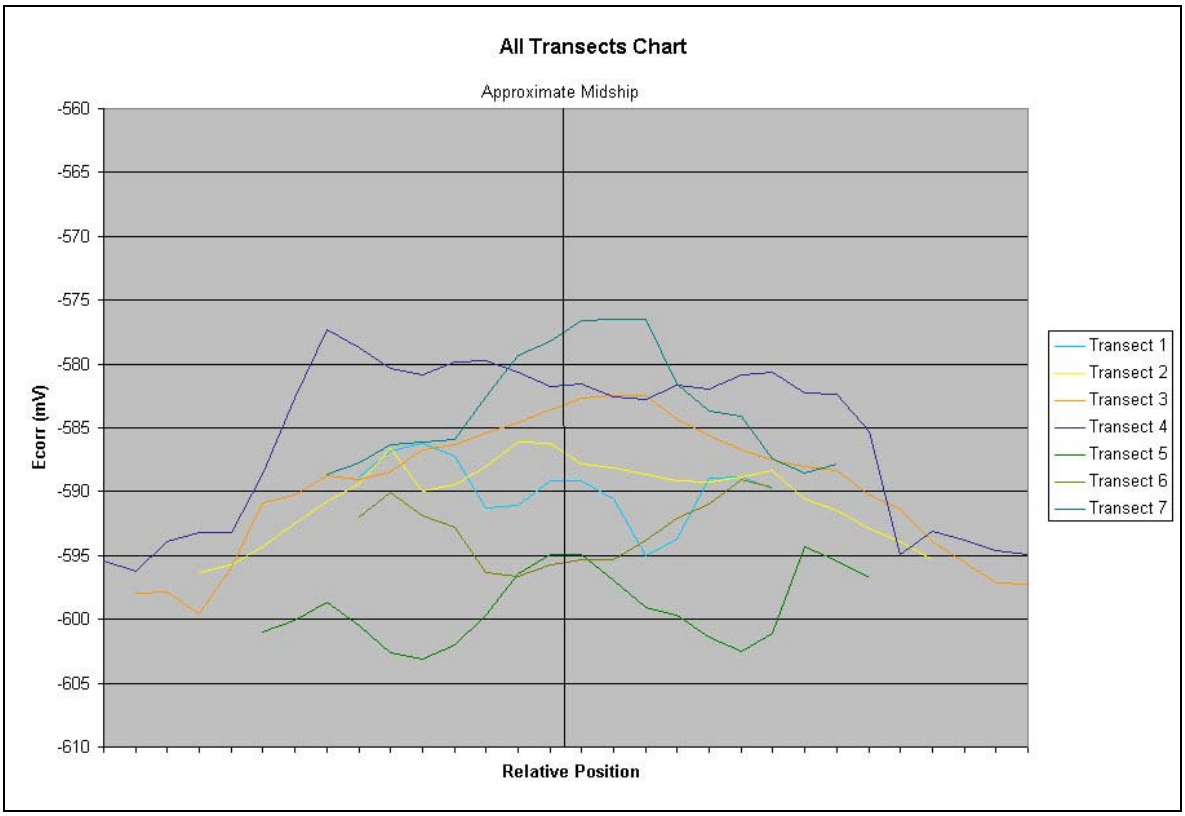

Figure 5.31. Compilation of E_{corr} data from all seven transects from June 2001, plotted from harbor bottom on left, up and over Arizona's hull every 6 ft., to harbor bottom on right.

itself (Table 5.21)(Figure 5.32). Proximity to cuprous propellers may promote less negative readings at 12 ft. above the harbor bottom, port and starboard. The decrease near 24 ft. on both sides of the ship may reflect the initial drop off to the harbor bottom prior to the rise resulting from influence of the propellers. The drop in E_{corr} as the transect approaches the harbor bottom is consistent with E_{corr} data obtained from the ThermoOrion instrument inserted in holes drilled in concretion.

The next transect forward, transect 2, taken at approximately frame 128, shows a similar pattern in which from the gunwales to the harbor bottom E_{corr} decreases on both sides but holds fairly steady across the main deck (Table 5.22)(Figure 5.33). The decrease to the harbor bottom is again attributed to the reduction in oxygen availability.

Transect 3, approximately frame 114, cuts across the main deck just forward of barbette no. 3, which extends about 6 ft. above the water surface and has accelerated water line corrosion vertically on its side. Because of this, E_{corr} amidships on this transect is higher as compared to transects 2, 5, 7, and 6 (Table 5.23)(Figure 5.34).

Location	E_{corr} (mV) vs. Ag/AgCl (GMC Probe)	E_{corr} (mV) vs. Ag/AgCl (Orion Equiv.)	E_{corr} (mV) vs. SHE
Port mudline	-588.8	-543.8	-343.8
6 ft. above bottom	-586.8	-541.8	-341.8
12 ft. above bottom	-586.2	-541.2	-341.2
18 ft. above bottom	-587.2	-542.2	-342.2
24 ft. above bottom	-591.3	-546.3	-346.3
30 ft. above bottom	-591.1	-546.1	-346.1
Port gunwale	-589.2	-544.2	-344.2
6 ft. from port gunwale	-589.1	-544.1	-344.1
Starboard gunwale	-590.6	-545.6	-345.6
24 ft. above bottom	-595	-550	-350
18 ft. above bottom	-593.7	-548.7	-348.7
12 ft. above bottom	-588.9	-543.9	-343.9
6 ft. above bottom	-588.8	-543.8	-343.8
Starboard mudline	-589.8	-543.8	-343.8

Table 5.21. June 2001 *in situ* corrosion data, transect 1 (frame 148).

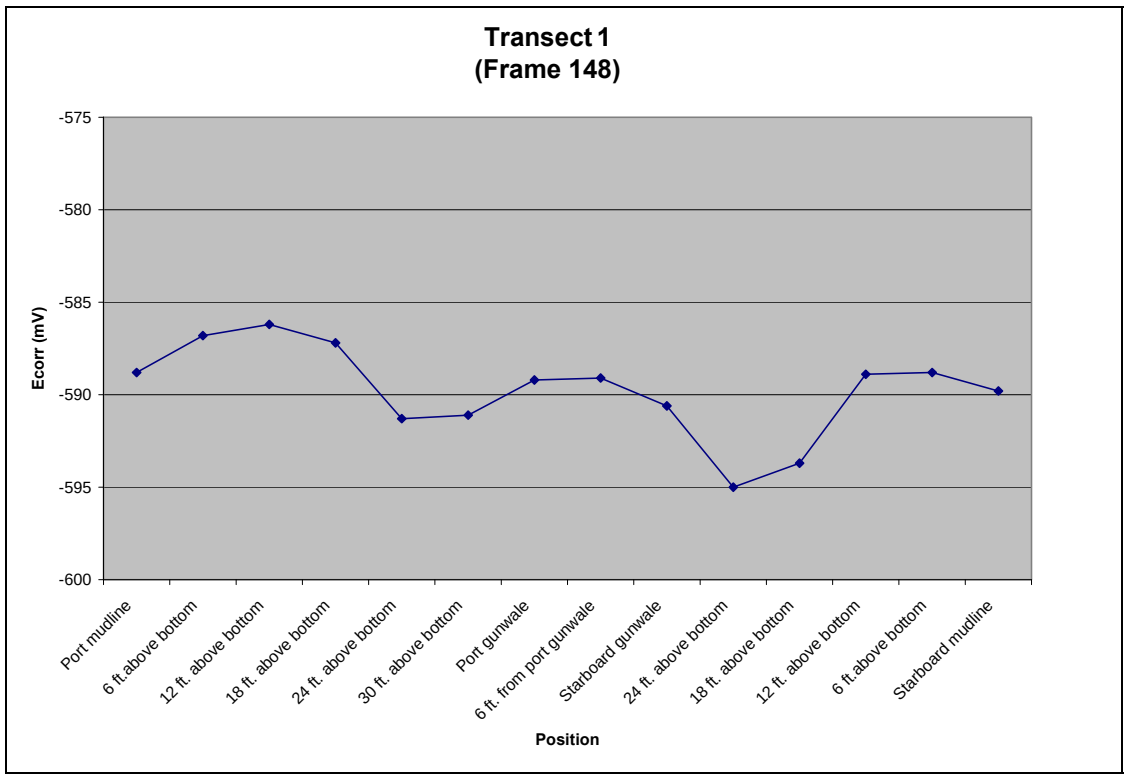

Figure 5.32. Graph of GMC data E_{corr} taken from Table 5.21, relative to hull position.

Location	E_{corr} (mV) vs. Ag/AgCl (GMC Probe)	E_{corr} (mV) vs. Ag/AgCl (Orion Equiv.)	E_{corr} (mV) vs. SHE
Port Mudline	-596.3	-551.3	-351.3
6 ft. above bottom	-595.7	-550.7	-350.7
12 ft. above bottom	-594.3	-549.3	-349.3
Torpedo blister	-592.5	-547.5	-347.5
6 ft. above torpedo blister	-590.8	-545.8	-345.8
Port gunwale	-589.4	-544.4	-344.4
6 ft. from port gunwale	-586.6	-541.6	-341.6
12 ft. from port gunwale	-590	-545	-345
18 ft. from port gunwale	-589.5	-544.5	-344.5
24 ft. from port gunwale	-588	-543	-343
30 ft. from port gunwale, by hatch	-586.1	-541.1	-341.1
36 ft. from port gunwale	-586.2	-541.2	-341.2
42 ft. from port gunwale	-587.8	-542.8	-342.8
48 ft. from port gunwale	-588.1	-543.1	-343.1
54 ft. from port gunwale	-588.6	-543.6	-343.6
60 ft. from port gunwale	-589.2	-544.2	-344.2
66 ft. from port gunwale, at starboard bitt	-589.3	-544.3	-344.3
72 ft. from port gunwale	-588.8	-543.8	-343.8
Starboard gunwale	-588.3	-543.3	-343.3
6 ft. above torpedo blister	-590.6	-545.6	-345.6
Torpedo blister	-591.5	-546.5	-346.5
12 ft. above bottom	-592.9	-547.9	-347.9
6 ft. above bottom	-593.9	-548.9	-348.9
Starboard mudline	-595.3	-550.3	-350.3

Table 5.22. June 2001 *in situ* corrosion data, transect 2 (frame 128).

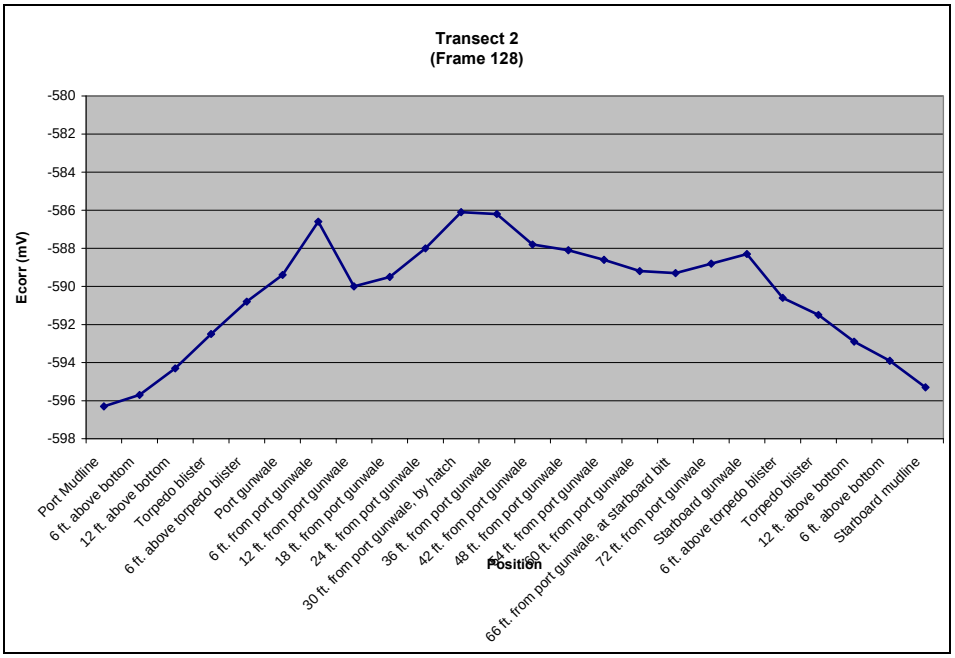

Figure 5.33. Graph of GMC data E_{corr} taken from Table 5.22, relative to hull position.

Location	E_{corr} (mV) vs. Ag/AgCl (GMC Probe)	E_{corr} (mV) vs. Ag/AgCl (Orion Equiv.)	E_{corr} (mV) vs. SHE
Port mudline	-598	-553	-353
6 ft. above bottom	-597.9	-552.9	-352.9
12 ft. above bottom	-599.6	-554.6	-354.6
Torpedo blister	-595.9	-550.9	-350.9
6 ft. above torpedo blister	-590.9	-545.9	-345.9
Port gunwale	-590.3	-545.3	-345.3
6 ft. from port gunwale	-588.7	-543.7	-343.7
12 ft. from port gunwale	-589	-544	-344
18 ft. from port gunwale	-588.4	-543.4	-343.4
24 ft. from port gunwale	-586.7	-541.7	-341.7
30 ft. from port gunwale	-586.3	-541.3	-341.3
36 ft. from port gunwale	-585.4	-540.4	-340.4
42 ft. from port gunwale	-584.6	-539.6	-339.6
48 ft. from port gunwale	-583.6	-538.6	-338.6
54 ft. from port gunwale	-582.7	-537.7	-337.7
60 ft. from port gunwale	-582.5	-537.5	-337.5
66 ft. from port gunwale	-582.5	-537.5	-337.5
72 ft. from port gunwale	-584.3	-539.3	-339.3
78 ft. from port gunwale	-585.6	-540.6	-340.6
84 ft. from port gunwale	-586.7	-541.7	-341.7
90 ft. from port gunwale	-587.5	-542.5	-342.5
96 ft. from port gunwale	-588	-543	-343
Starboard bitts	-588.3	-543.3	-343.3
Staboard gunwale	-590.3	-545.3	-345.3
6 ft. above torpedo blister	-591.4	-546.4	-346.4
Torpedo blister	-593.9	-548.9	-348.9
12 ft. above bottom	-595.5	-550.5	-350.5
6 ft. above bottom	-597.1	-552.1	-352.1
Starboard mudline	-597.2	-552.2	-352.2

Table 5.23. June 2001 *in situ* corrosion data, transect 3 (frame 114).

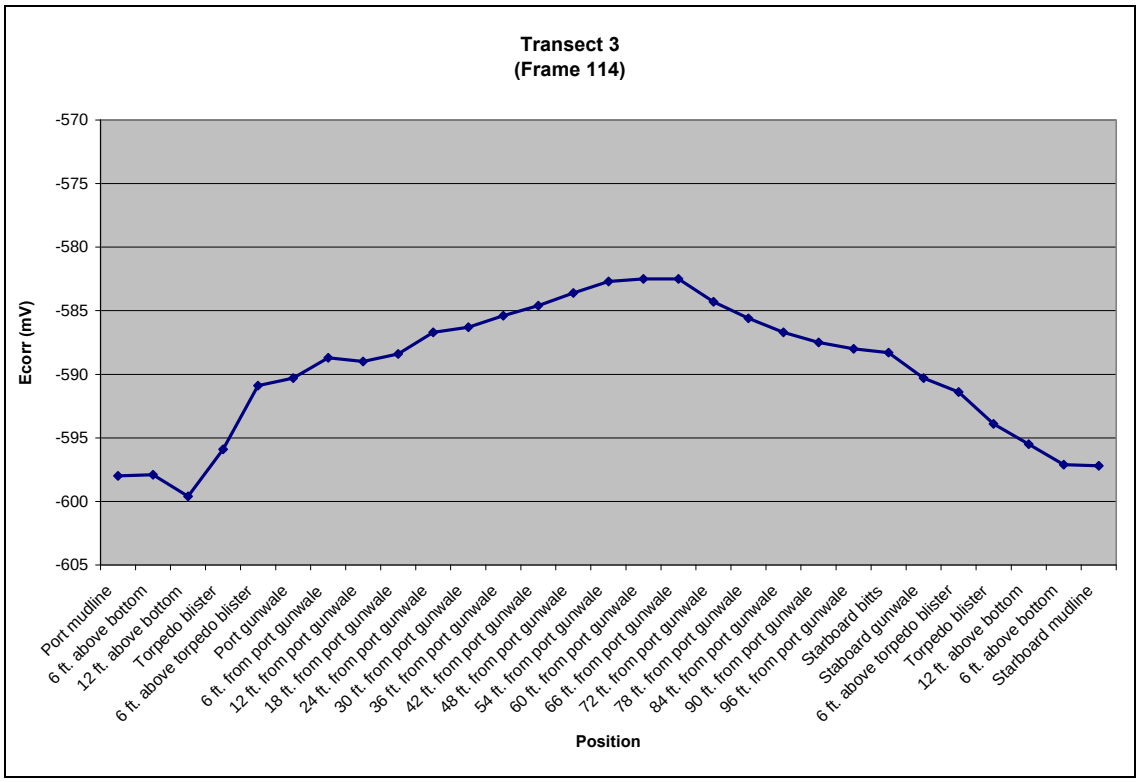

Figure 5.34. Graph of GMC data E_{corr} taken from Table 5.23, relative to hull position.

Transect 4 crosses the upper deck in the crew galley area in shallow water forward of the Memorial, at approximately frame 82. E_{corr} is -583 mV or higher over nearly the entire deck area—recent structural corrosion is consistent with higher E_{corr} in this area (Table 5.24)(Figure 5.35).

Moving forward along the hull, transect 5, at approximately frame 28, has the lowest overall E_{corr} values, which may be due to the fact that the deck is buried by several feet of sediment along the entire transect (Table 5.25)(Figure 5.36). The close proximity and exposure of the gun barrels of turret no. 1 above the harbor bottom may reflect a rise in E_{corr} near the centerline of the hull. A drop in E_{corr} from the torpedo blisters on either side to the harbor bottom is typical. Because the deck is collapsed in this area, the top of the torpedo blister and the gunwale are at about the same elevation.

As is the case for transect 5, transect 6 is in an area of maximum damage from the 1941 explosion that sank *Arizona*, at approximate frames 16–19. Blown out deck plates at what used to be the gunwales are exposed to increased sea water exchange and maximum oxygen

Location	E_{corr} (mV) vs. Ag/AgCl (GMC Probe)	E_{corr} (mV) vs. Ag/AgCl (Orion Equiv.)	E_{corr} (mV) vs. SHE
Port mudline	-595.4	-550.4	-350.4
6 ft. above bottom	-596.2	-551.2	-351.2
Torpedo blister	-593.9	-548.9	-348.9
6 ft. above torpedo blister	-593.2	-548.2	-348.2
12 ft. above torpedo blister	-593.2	-548.2	-348.2
Port gunwale	-588.6	-543.6	-343.6
6 ft. from port gunwale	-582.7	-537.7	-337.7
12 ft. from port gunwale	-577.3	-532.3	-332.3
18 ft. from port gunwale	-578.7	-533.7	-333.7
24 ft. from port gunwale	-580.3	-535.3	-335.3
30 ft. from port gunwale	-580.8	-535.8	-335.8
36 ft. from port gunwale	-579.8	-534.8	-334.8
42 ft. from port gunwale	-579.7	-534.7	-334.7
48 ft. from port gunwale	-580.6	-535.6	-335.6
54 ft. from port gunwale	-581.8	-536.8	-336.8
60 ft. from port gunwale	-581.6	-536.6	-336.6
66 ft. from port gunwale	-582.6	-537.6	-337.6
72 ft. from port gunwale	-582.8	-537.8	-337.8
78 ft. from port gunwale	-581.7	-536.7	-336.7
84 ft. from port gunwale	-582	-537	-337
90 ft. from port gunwale	-580.9	-535.9	-335.9
96 ft. from port gunwale	-580.6	-535.6	-535.6
102 ft. from port gunwale	-582.3	-537.3	-337.3
Starboard bitts	-582.4	-537.4	-337.4
Starboard gunwale	-585.3	-540.3	-340.3
12 ft. above torpedo blister	-594.9	-549.9	-349.9
6 ft. above torpedo blister	-593.1	-548.1	-348.1
Torpedo blister	-593.8	-548.8	-348.8
6 ft. above bottom	-594.6	-549.6	-349.6
Starboard mudline	-594.9	-549.9	-349.9

Table 5.24. June 2001 *in situ* corrosion data, transect 4 (frame 82).

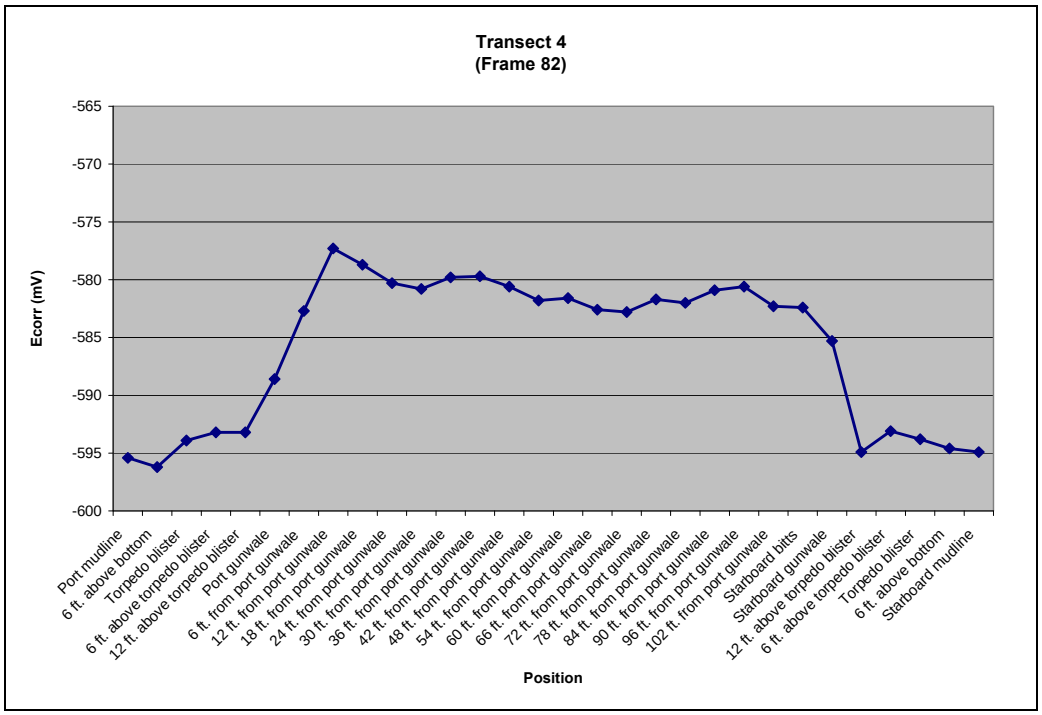

Figure 5.35. Graph of GMC data E_{corr} taken from Table 5.24, relative to hull position.

Location	E_{corr} (mV) vs. Ag/AgCl (GMC Probe)	E_{corr} (mV) vs. Ag/AgCl (Orion Equiv.)	E_{corr} (mV) vs. SHE
Port mudline	-601	-556	-356
6 ft. above bottom	-600.1	-555.1	-355.1
Torpedo blister	-598.7	-553.7	-353.7
6 ft. from port gunwale	-600.5	-555.5	-355.5
12 ft. from port gunwale	-602.6	-557.6	-357.6
18 ft. from port gunwale	-603.1	-558.1	-358.1
24 ft. from port gunwale	-602	-557	-357
30 ft. from port gunwale	-599.7	-554.7	-354.7
36 ft. from port gunwale	-596.4	-551.4	-351.4
42 ft. from port gunwale	-594.9	-549.9	-349.9
48 ft. from port gunwale	-594.9	-549.9	-349.9
54 ft. from port gunwale	-596.9	-551.9	-351.9
60 ft. from port gunwale	-599.1	-554.1	-354.1
66 ft. from port gunwale	-599.7	-554.7	-354.7
72 ft. from port gunwale	-601.4	-556.4	-356.4
78 ft. from port gunwale	-602.5	-557.5	-357.5
84 ft. from port gunwale	-601.1	-556.1	-356.1
Torpedo blister	-594.3	-549.3	-349.3
6 ft. above bottom	-595.4	-550.4	-350.4
Starboard mudline	-596.7	-551.7	-351.7

Table 5.25. June 2001 *in situ* corrosion data, transect 5 (frame 28).

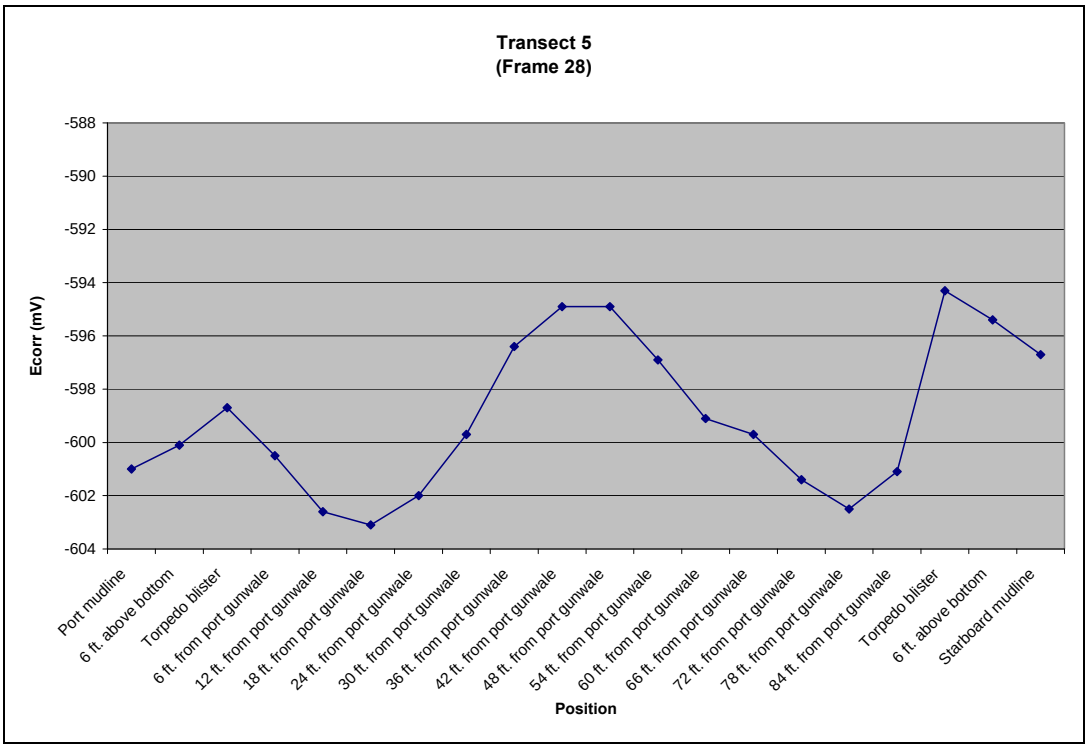

Figure 5.36. Graph of GMC data E_{corr} taken from Table 5.25, relative to hull position.

availability. Because the plates flare out so much in this area, transects could not be taken to the harbor bottom. The lowest E_{corr} appear near the centerline where silt has accumulated (Table 5.26)(Figure 5.37).

The final transect, transect 7, is near the bow, approximately frame 9, forward of the area of maximum damage, where the intact upper deck is in shallow water. As expected, E_{corr} values are relatively high along the exposed upper deck, near -575 mV, and drop to near -590 mV at the harbor bottom (Table 5.27)(Figure 5.38). E_{corr} transects with the GMC probe confirm the overall pattern produced by the sequential drilling and data collection through the concretion, that is that E_{corr} decreases with increased water depth. E_{corr} profiles generally tend to drop to lower potentials from stern (Frame 148) to bow (Frame 9) with maximum E_{corr} near -330 mV (SHE) or -575 mV (Ag/AgCl, GMC) to a minimum approaching -360 mV (SHE) or -605 mV (Ag/AgCl, GMC)(Figure 5.31).

Location	E_{corr} (mV) vs. Ag/AgCl (GMC Probe)	E_{corr} (mV) vs. Ag/AgCl (Orion Equiv.)	E_{corr} (mV) vs. SHE
Port edge	-592	-547	-347
6 ft. from port edge	-590.1	-545.1	-345.1
12 ft. from port edge	-591.9	-546.9	-346.9
18 ft. from port edge	-592.8	-547.8	-347.8
24 ft. from port edge	-596.3	-551.3	-351.3
30 ft. from port edge	-596.6	-551.6	-351.6
36 ft. from port edge	-595.7	-550.7	-350.7
42 ft. from port edge	-595.3	-550.3	-350.3
48 ft. from port edge	-595.3	-550.3	-350.3
54 ft. from port edge	-593.8	-548.8	-348.8
60 ft. from port edge	-592.1	-547.1	-347.1
66 ft. from port edge	-591	-546	-346
72 ft. from port edge	-589	-544	-344
Starboard edge	-589.7	-544.7	-344.7

Table 5.26. June 2001 *in situ* corrosion data, transect 6 (frames 16-19).

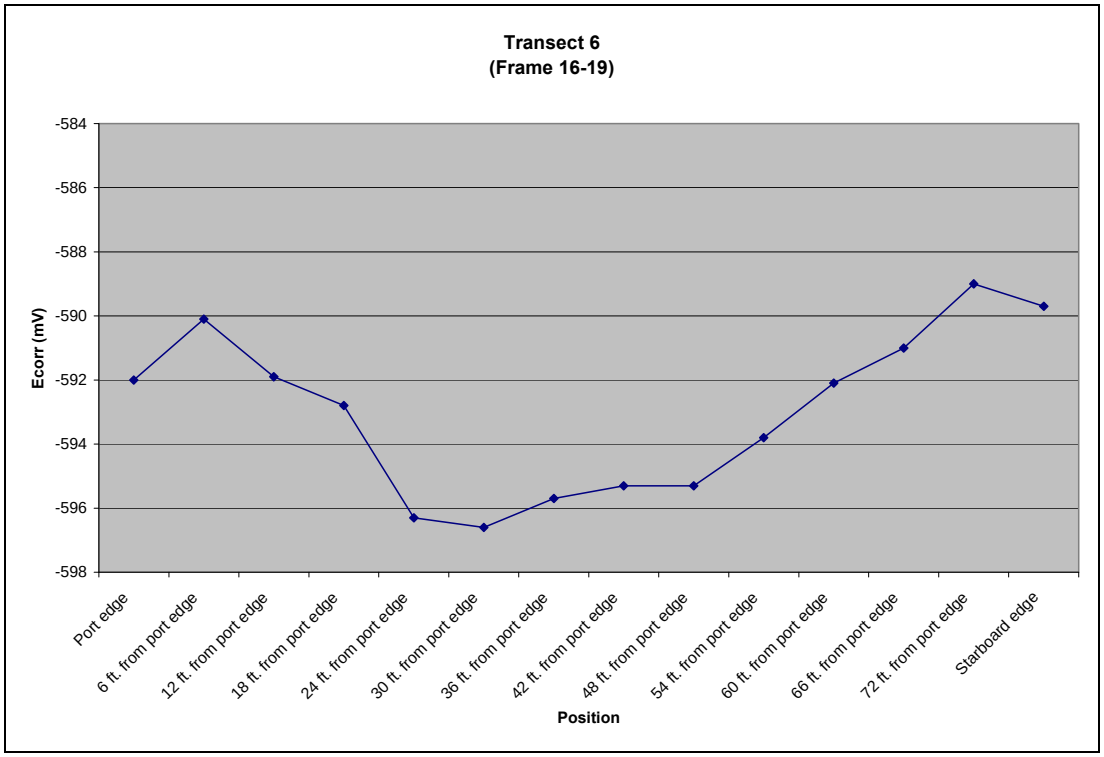

Figure 5.37. Graph of GMC data E_{corr} taken from Table 5.26, relative to hull position.

Location	E_{corr} (mV) vs. Ag/AgCl (GMC Probe)	E_{corr} (mV) vs. Ag/AgCl (Orion Equiv.)	E_{corr} (mV) vs. SHE
Port mudline	-588.6	-543.6	-343.6
6 ft. above mudline	-587.7	-542.7	-342.7
12 ft. above mudline	-586.3	-541.3	-341.3
18 ft. above mudline	-586.1	-541.1	-341.1
24 ft. above mudline	-585.9	-540.9	-340.9
Port gunwale	-582.6	-537.6	-337.6
6 ft. from port gunwale	-579.3	-534.3	-334.3
12 ft. from port gunwale	-578.2	-533.2	-333.2
18 ft. from port gunwale	-576.6	-531.6	-331.6
24 ft. from port gunwale	-576.5	-531.5	-331.5
30 ft. from port gunwale	-576.5	-531.5	-331.5
Starboard gunwale	-581.6	-536.6	-336.6
24 ft. above mudline	-583.7	-538.7	-338.7
18 ft. above mudline	-584.1	-539.1	-339.1
12 ft. above mudline	-587.4	-542.4	-342.4
6 ft. above mudline	-588.5	-543.5	-343.5
Starboard mudline	-587.8	-542.8	-342.8

Table 5.27. June 2001 *in situ* corrosion data, transect 7 (frame 9).

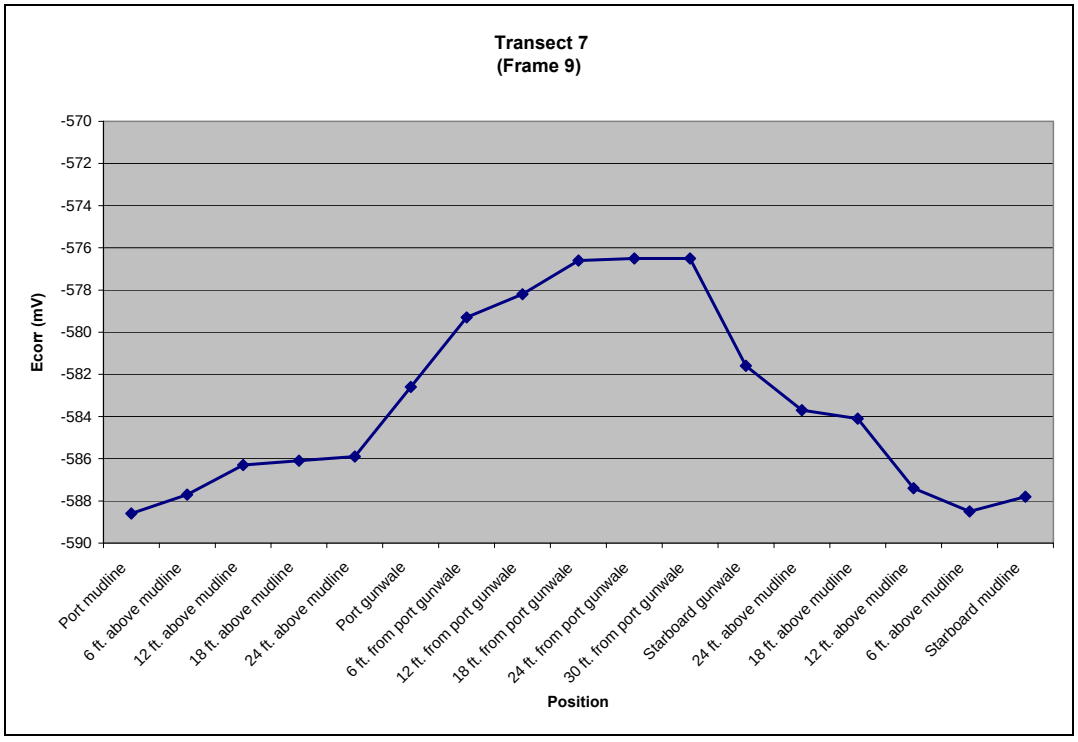

Figure 5.38. Graph of GMC data E_{corr} taken from Table 5.27, relative to hull position.

Interior E_{corr} Measurements

Interior potential measurements were obtained by mounting a GMC reference electrode on a VideoRay ROV. The ROV was operated from the surface with a Wavetech HD-160 meter displaying E_{corr} values alongside the operator. Because there was no direct access to the vessel's interior, E_{corr} measurements were only taken on the exterior of concretion covering interior bulkheads. Interior spaces were entered through open portholes on *Arizona*'s second deck, as well as through open hatches on the main deck aft of the Memorial. E_{corr} measurements were also taken on the inside of barbette no. 3. Methodology included taking baseline measurements outside the hull before entering the interior spaces. A running log of E_{corr} values was recorded along with time displayed on the miniDV video deck, which recorded the video feed from the ROV, and a description of location and features within the interior cabin. In general, measurements were taken a various levels within the cabin interior, from floor to ceiling (silt-line to overhead).

On entry through open port holes, E_{corr} increased from 8 to 18 mV, an average 13 mV; that is interior values are 8–18 mV more positive than baseline readings outside each cabin (Figures 5.39–5.47). This could indicate a slightly higher corrosion rate; however there are many variables at work. Translated to the Fe/H_2O Pourbaix diagram (Figure 5.2) this difference suggests that the corrosion potential is higher depending upon the pH in the compartments and the thickness of the concretion on interior surfaces. Knowledge of temperature, salinity, pH and oxygen concentration in interior compartments is important for contextualizing these results. Descent into hatches starboard of barbette no. 3 and barbette no. 4 to the third deck showed a similar increase in E_{corr}, though not as great (Figures 5.48 and 5.49).

The reason for the rise in E_{corr} inside interior compartments is not fully understood. Perhaps the concretion, or what there is of it, is thin enough to change the balance between available oxygen and oxygen diffusion resistance in favor of higher effective oxygen availability at the interior surface. On the other hand, increased carbon or sulfur availability from overhead fuel oil may be the cause for the higher E_{corr} readings. These and other possible explanations for the rise in E_{corr} in interior compartments come from further examination of the carbon-water Pourbaix diagram (Figure 5.4). At a pH of 7 or lower, elemental carbon from oil trapped in the overheads is at equilibrium with water at slightly higher potentials. For example, carbon

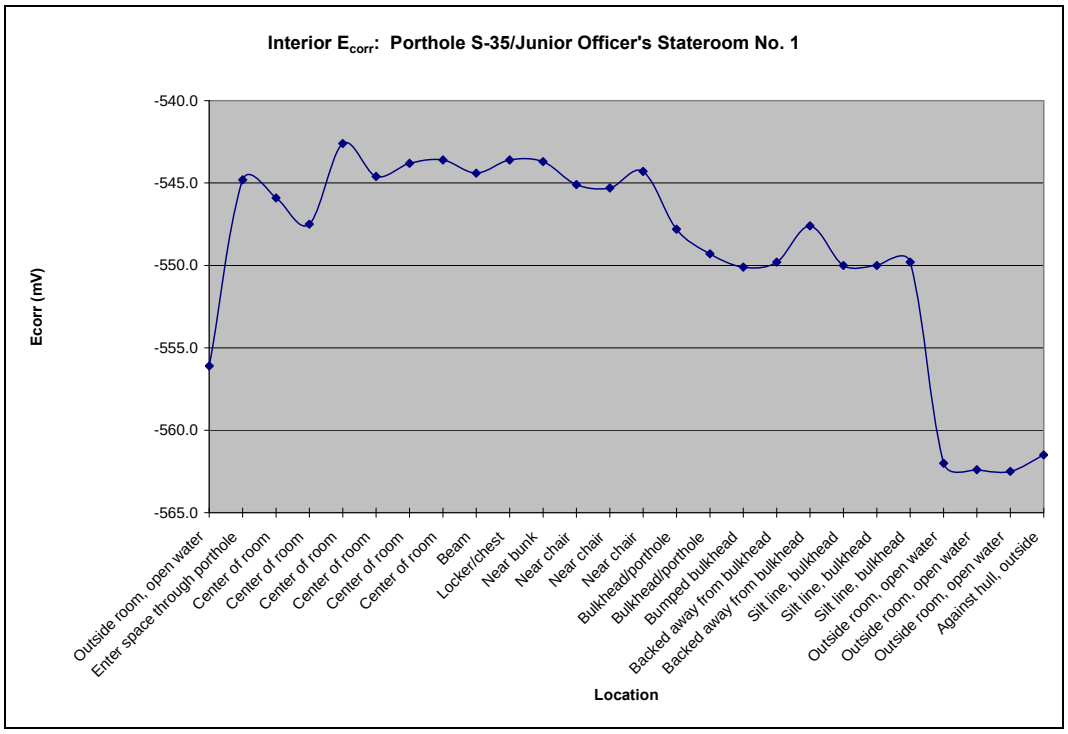

Figure 5.39. Graph of interior E_{corr} relative to location within Porthole S-35/Junior Officer's Stateroom No.1

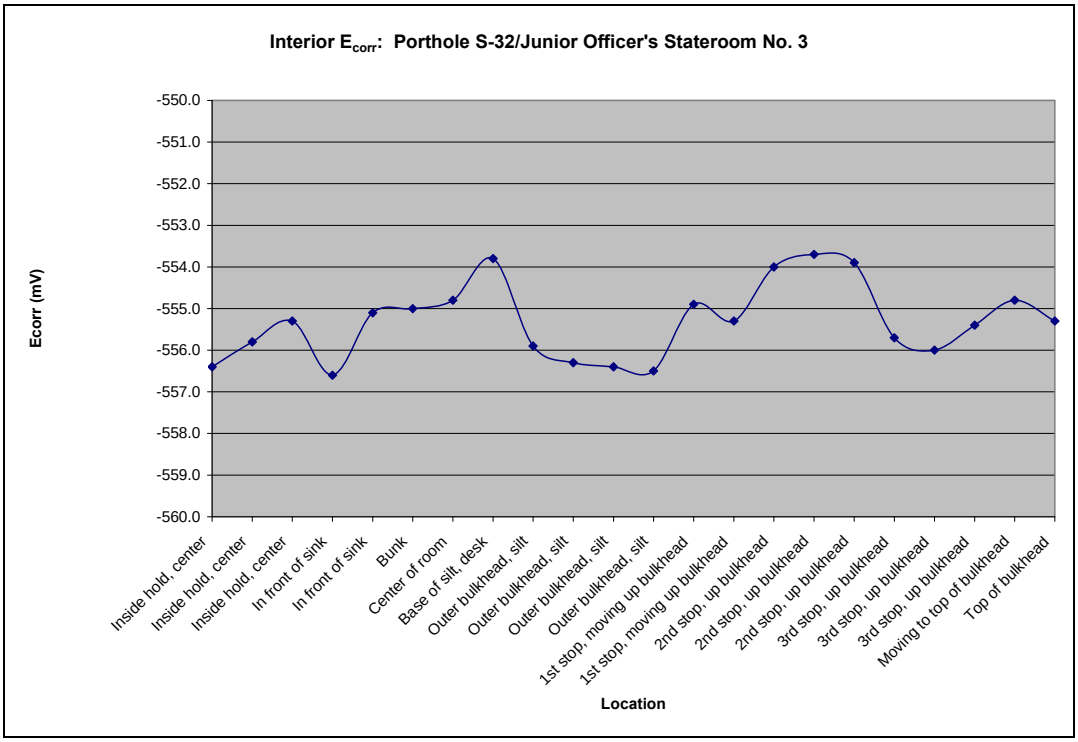

Figure 5.40. Graph of interior E_{corr} relative to location within Porthole S-32/Junior Officer's Stateroom No.3

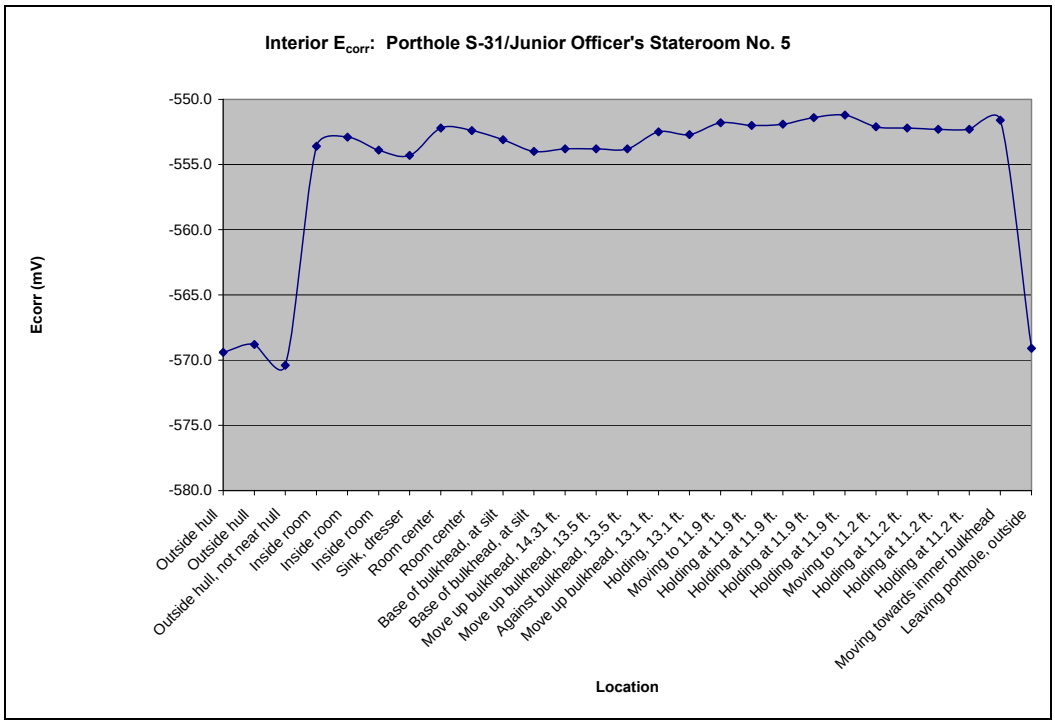

Figure 5.41. Graph of interior E_{corr} relative to location within Porthole S-31/Junior Officer's Stateroom No.5

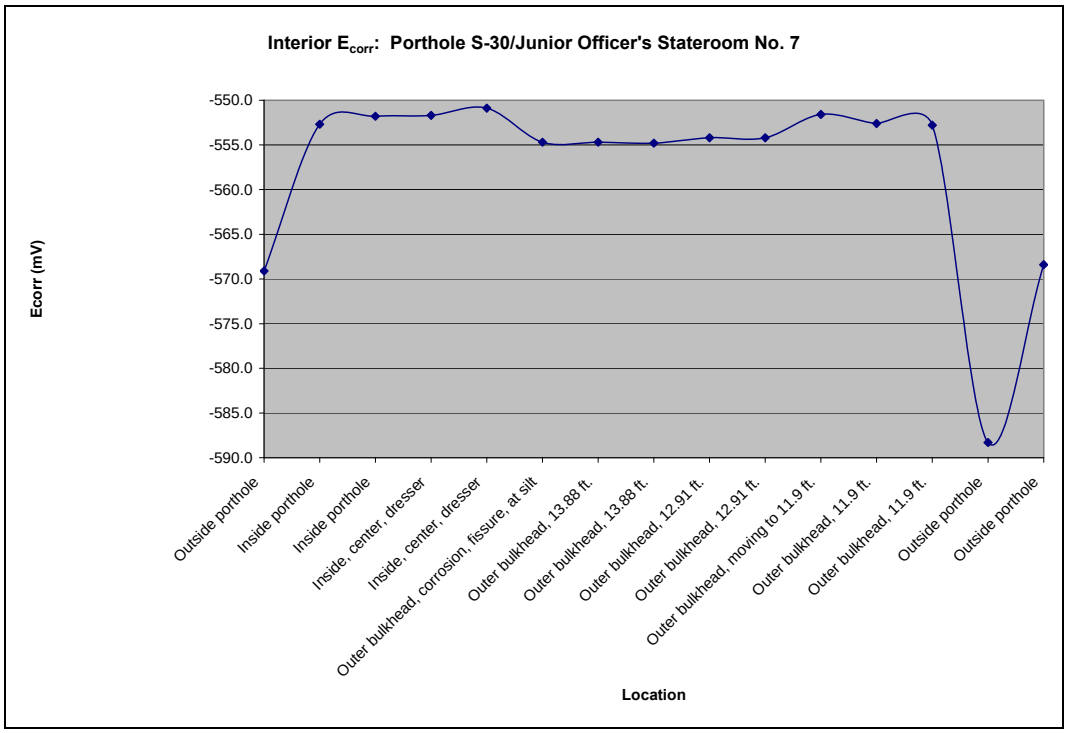

Figure 5.42. Graph of interior E_{corr} relative to location within Porthole S-30/Junior Officer's Stateroom No.7

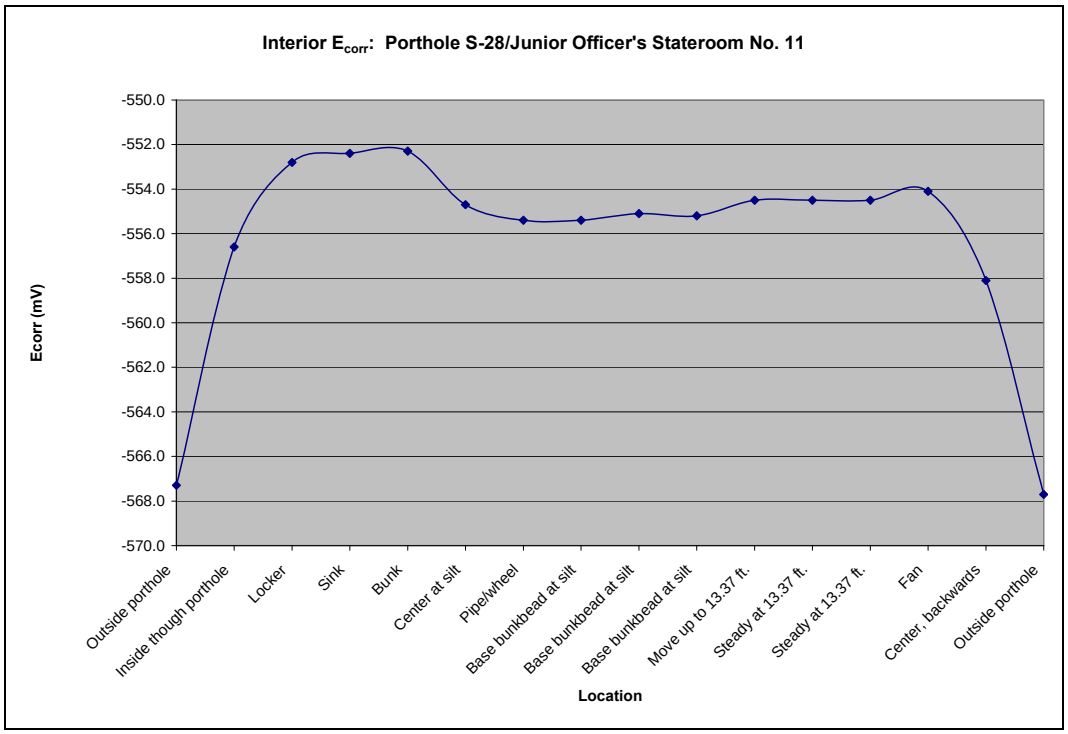

Figure 5.43.Graph of interior E_{corr} relative to location within Porthole S-28/Junior Officer's Stateroom No.11

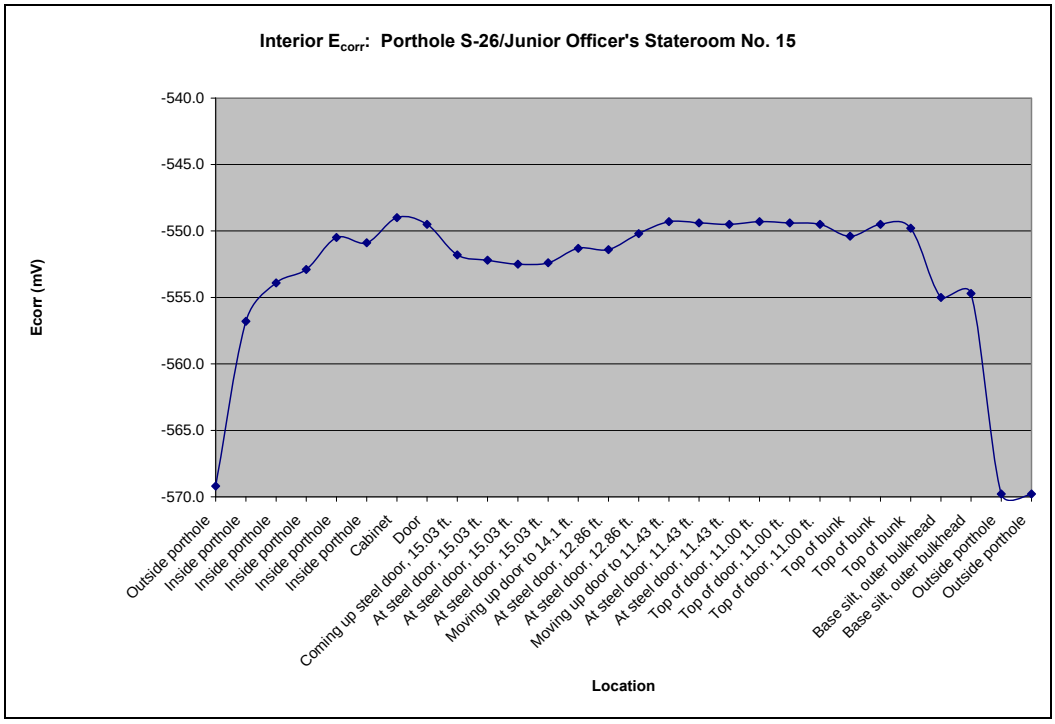

Figure 5.44.Graph of interior E_{corr} relative to location within Porthole S-26/Junior Officer's Stateroom No.15

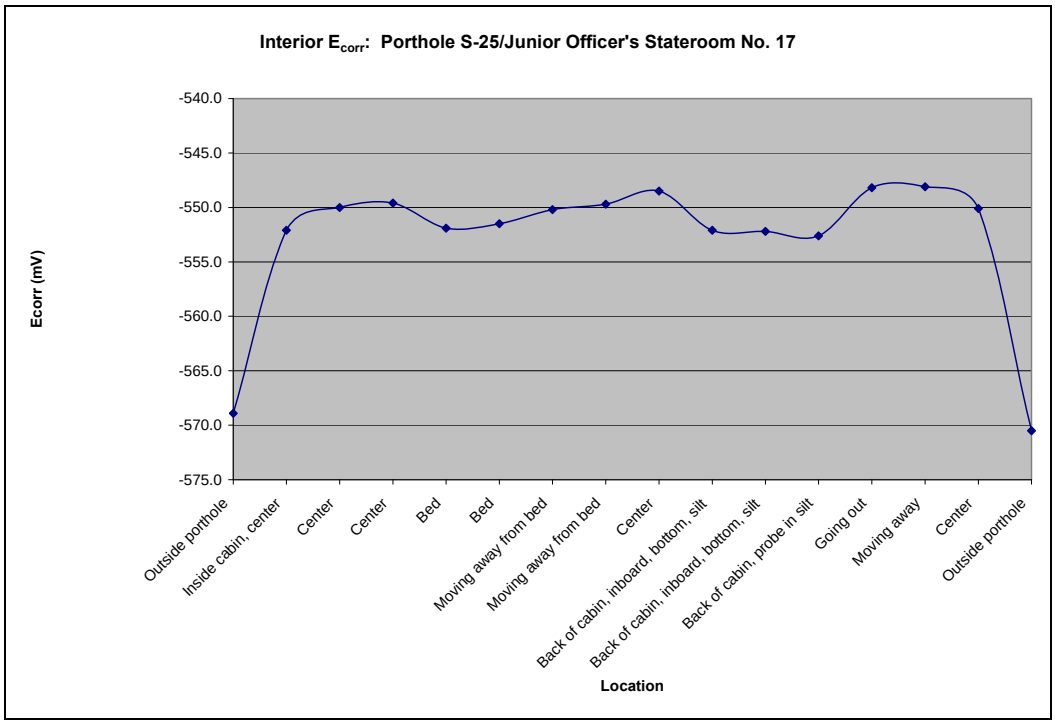

Figure 5.45.Graph of interior E_{corr} relative to location within Porthole S-25/Junior Officer's Stateroom No.17

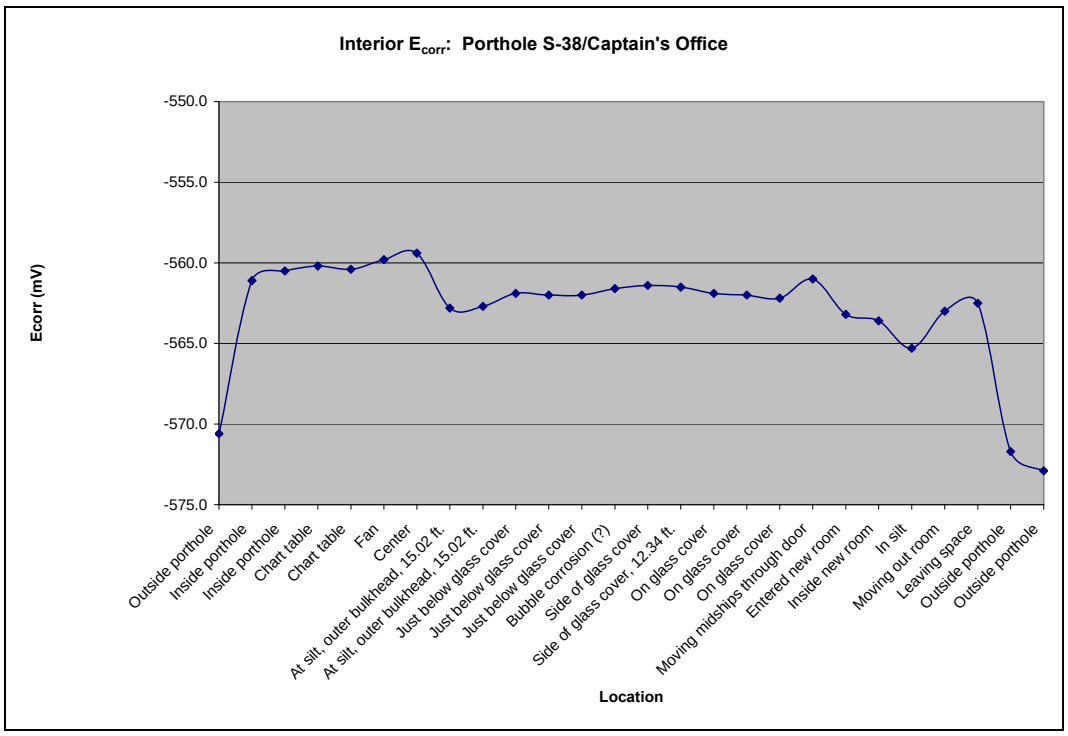

Figure 5.46. Graph of interior E_{corr} relative to location within Porthole S-38/Captain's Office

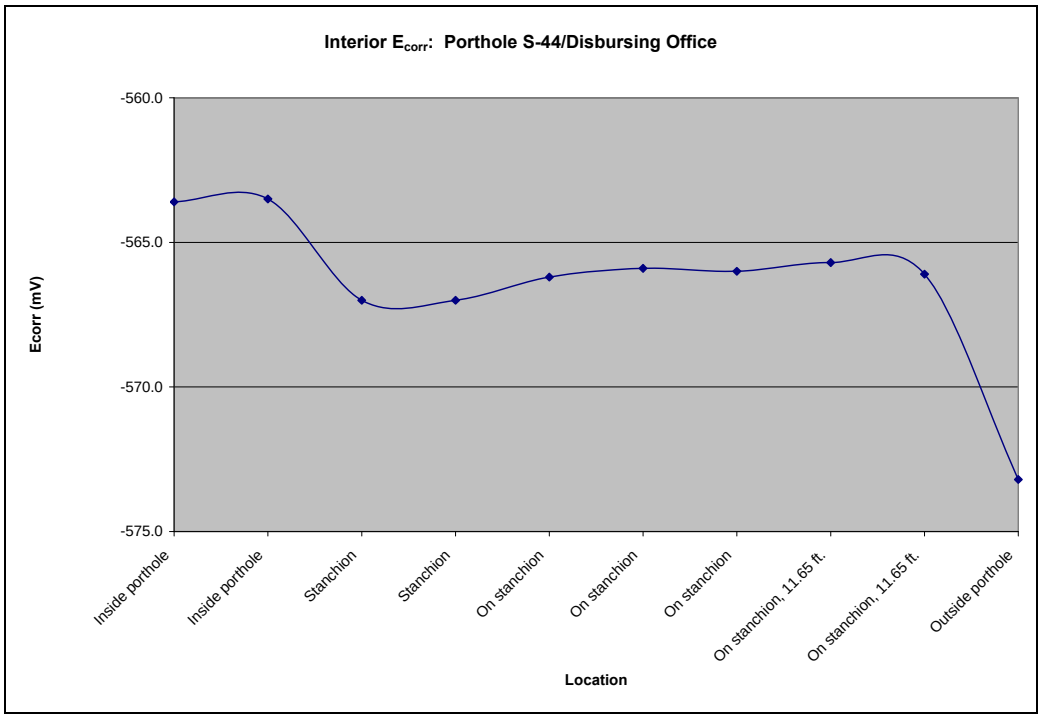

Figure 5.47. Graph of interior E_{corr} relative to location within Porthole S-44/Disbursing Office

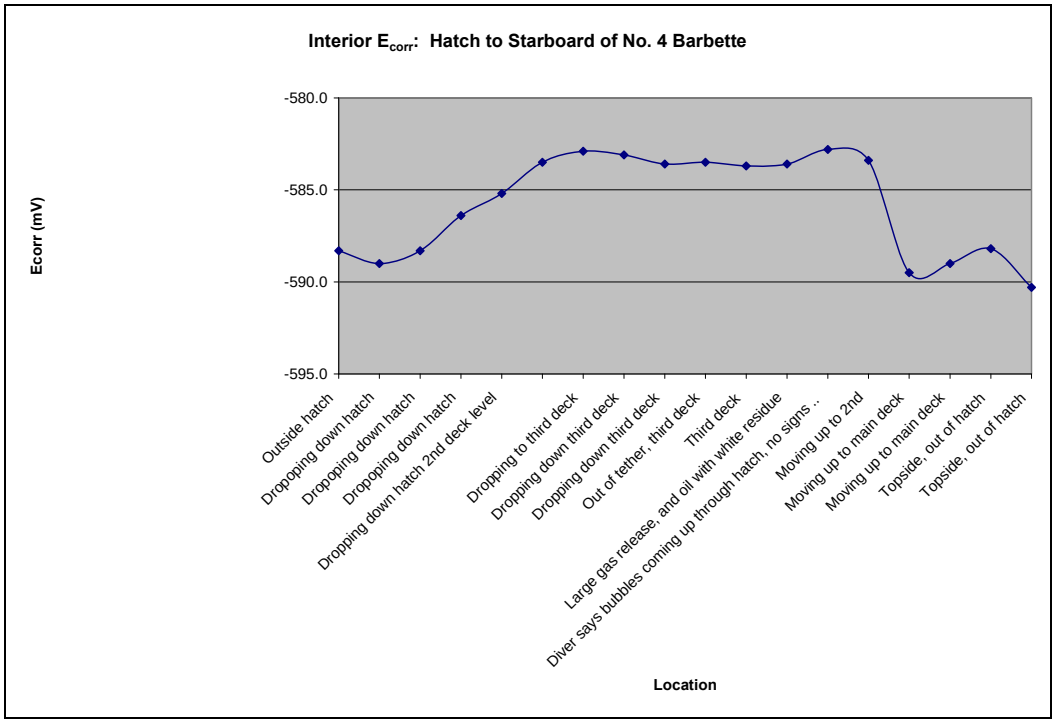

Figure 5.48. Graph of interior E_{corr} relative to location from Hatch to Starboard of No. 4 Barbette

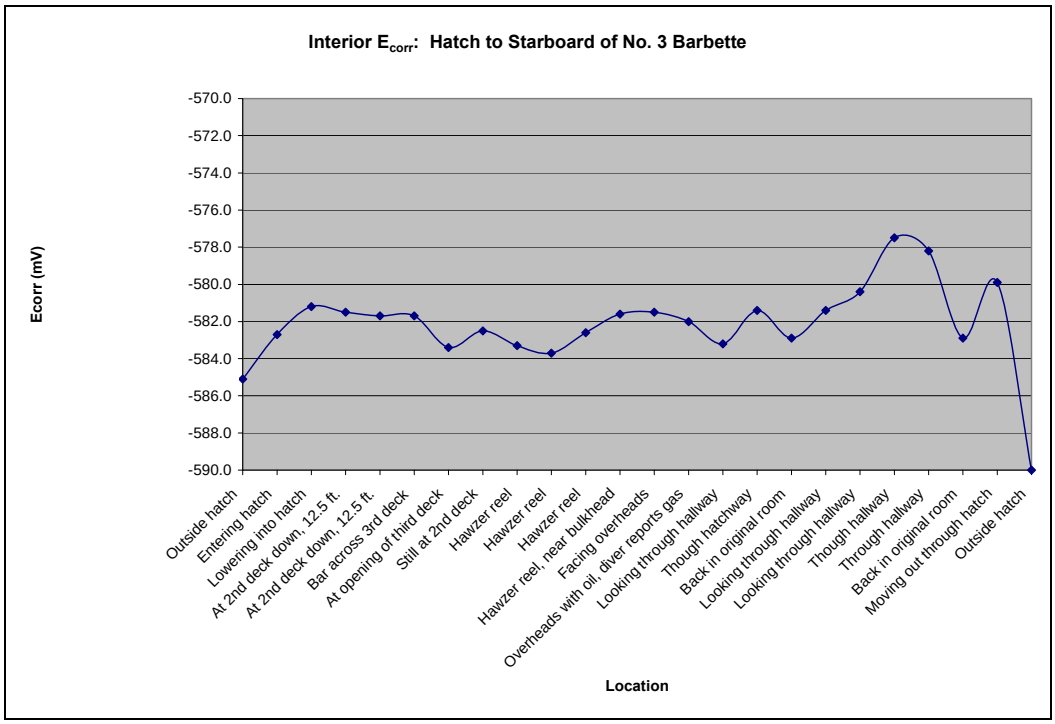

Figure 5.49. Graph of interior E_{corr} relative to location from Hatch to Starboard of No. 3 Barbette

promotes change in water chemistry with E_{corr} at a mixed potential involving more than just freely corroding iron. The carbon-water Pourbaix diagram (Figure 5.4) shows three regions that are of interest as related to interior E_{corr}. Elemental carbon is in equilibrium with water in a narrow diagonal band marked "C". Below the band are four diagonal lines that correspond to increasing partial pressures of methane ($p(CH_4)$ from 10^{-6} to 1 atm as the potential decreases), and above the diagonal band are four lines that correspond to increasing partial pressures of carbon dioxide ($p(CO_2)$ from 10^{-6} to 1 atm as the potential increases). Below the lower diagonal band, the entire region is stable methane or methane dissolved in water as methanol. Above the diagonal band, the entire region is stable carbon dioxide or carbon dioxide dissolved in water as carbonates. Extending a vertical line upward at pH 7, the line intersects the $p(CO_2) = 10^{-6}$ line at a potential of approximately -310 mV. Interior E_{corr} data averages about the same, hence it is feasible that an increase in potential of 8–18 mV is caused by a change in water chemistry in interior spaces as the partial pressure of carbon dioxide increases. In this connection, search for and application of the sulfur-water Pourbaix diagram may cast further light on the cause for the increase in potential. Chemical analysis of interior water samples is recommended to determine

whether or not this environment is more corrosive than exterior seawater and confirm the presence of carbonates and/or methanol predicted in the Pourbaix diagram (Figure 5.4). At greater depths and pressures in interior spaces, it may be possible that E_{corr} is lower, suggesting the presence of methane dissolved as methanol. The report of solid methane as hydrate at great ocean depths draws some interesting parallels. Chemical analysis of interior water would help clarify this issue. Another factor causing a potential increase in interior compartments is the existence of thermoclines (see Chapter 4 and above) and associated variation in oxygen content across them. Temperature or oxygen cells may also be operative.

The trend showing increasing (more positive) E_{corr} in interior compartments was not observed inside barbette no. 3 (Figure 5.50). A descent from the surface to 31 ft. below the surface to the bottom of the barbette (roughly equivalent to the harbor bottom outside the ship) showed a decrease in $E_{corr,}$ similar to the trend for E_{corr} on the external hull. The E_{corr} values inside the barbette are consistent with readings on the external hull in that E_{corr} values decrease with depth. Both observations are consistent with a reduced tendency to corrode. In both cases, the water column is directly open to the atmosphere and gases such as carbon dioxide and methane would dissociate from water and outgas to the atmosphere. In interior compartments, with egress only at open port holes, outgassing is limited.

E_{corr} and pH Measurements Summary

Data clearly confirm the crevice effect at the hull's steel surface created by concretion coverage where the pH is the lowest, and gradually increases through the concretion to the concretion's exterior surface. In addition, results indicate that E_{corr} at both the steel surface and the concretion's exterior surface decrease with water depth.

Superposition of experimental steel surface E_{corr}/pH data on the iron-water Pourbaix diagram indicates active corrosion with hydrogen evolution or oxygen reduction depending on the pH. Hydrolysis causes a continuously lowering of pH in the concretion from exterior concretion surface to the steel surface. The carbon-water Poubaix diagram suggests that carbon presence from oil trapped in overheads may promote higher E_{corr} inside interior compartments. Depending on interior position, water depth, and proximity to fuel oil, either CH_4 as methanol or

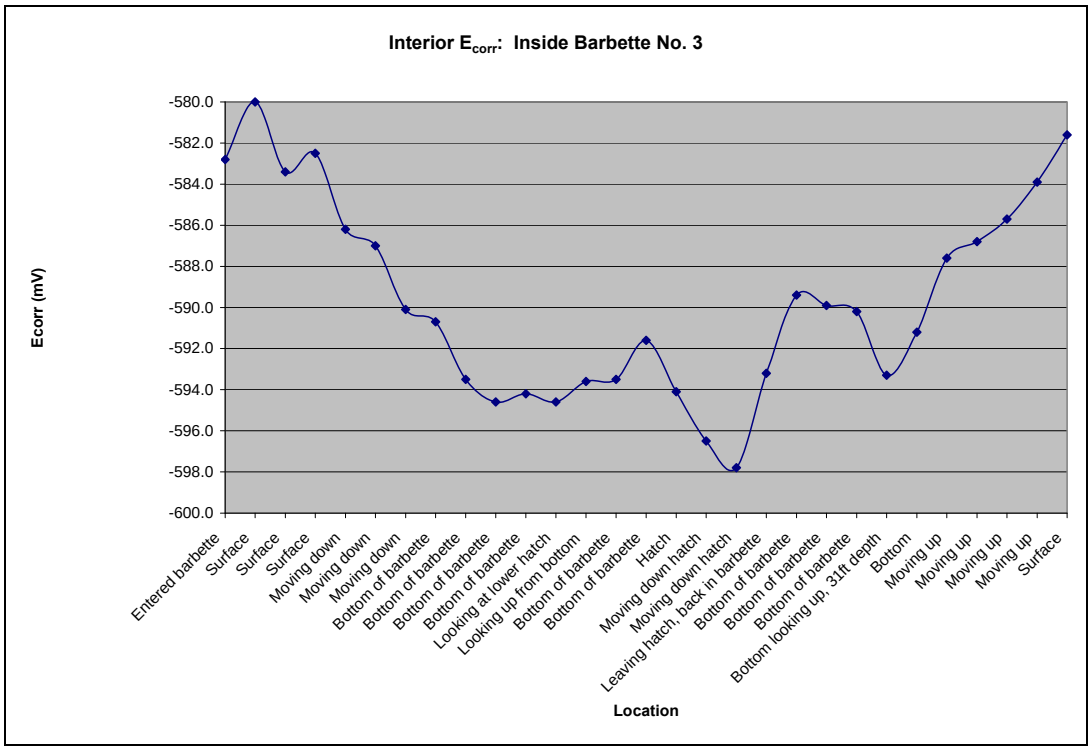

Figure 5.50. Graph of interior E_{corr} relative to location inside Barbette No. 3

CO_2 as carbonate dissolved in interior water cause a change in seawater chemistry and a resulting increase in E_{corr}.

Concretion Analysis

Fundamental research into the composition and characteristics of the concretion covering *Arizona*'s outer hull is being conducted to aid in understanding the kinetics and mechanisms of the corrosion process on the ship and to determine how concretion chemistry correlates with hull metal loss. The hard layer of concretion that forms on iron and steel objects in seawater is a combination of iron corrosion products and marine organisms, beginning with pioneering coralline algae that leave layers of calcium carbonate when they die. The calcium carbonate residue is overlaid by subsequent layers of coralline algae, and the increasing calcium carbonate layers forms a suitable substrate for secondary growth, such as soft corals and mollusks (North 1976:254). Outwardly diffusing iron ions replace some of the calcium resulting in a mix of iron

corrosion products, calcium carbonate and living marine organisms covering the iron or steel object. The concretion forms a semi-permeable barrier between the bare metal and seawater and has a significant influence on corrosion by reducing the amount of dissolved oxygen available for the corrosion reaction, increasing acidity at the metal-concretion interface and increasing the chloride ion concentration at the concretion/metal interface (North 1976:253).

Preliminary Concretion Examination

Fines residue from samples collected from *Arizona* in 1998 were collected for preliminary x-ray diffraction (XRD) analysis performed by the UNL laboratory. The results showed a high background, possibly caused by amorphous crystalline compounds which do not yield identifying peaks. Riding on the background were peaks corresponding to magnetite (Fe_3O_4) and other compounds that could not be identified because of the complexity of the x-ray pattern. In order to analyze a solid sample, a sample holder was installed in the x-ray machine that rigidly mounted a section of the sample. The sample was then milled in sequential 0.5 mil (0.0005 in.), or 12.7 μm (0.0127 mm), sections from the metal side into the concretion and scans run on each. Peaks revealed the same information as did the fines. This preliminary work confirmed the presence of iron in the concretion as reported in Lenihan (1989) and indicated that iron transport between the steel hull and concretion is significant in understanding marine corrosion.

X-Ray Diffraction and Environmental Scanning Electron Microscopy

Initial concretion investigation on USS *Arizona* focused on XRD to isolate and identify compounds that make up the concretion and on environmental scanning electron microscopy (ESEM) and x-ray fluorescence (XRF) to determine relative percentages of each element. The Air Force Research Laboratory, Eglin Air Force Base, conducted XRD and the Composite Materials and Structures Center at Michigan State University conducted the ESEM analysis. The University of New Mexico Analytical Chemical Laboratory in the Department of Earth and Planetary Sciences completed the XRF. In addition to these examinations, the Analytical Chemical Laboratory, Department of Chemistry, University of Nebraska-Lincoln conducted

direct chemical analyses.

A 2.2 in. (5.5 cm) diameter concretion sample (USAR-01-045) was used for XRD and ESEM. The concretion was collected by using an air-powered hole-saw and sectioned on a diamond saw using water containing a 3% TRIMSOL solution to produce the XRD and ESEM sample, which was from the upper half of the disc (Figures 5.51 and 5.52).

Preliminary results are consistent with North's (1976) findings that concretion formed on wrought and cast iron structures contains the mineral siderite, which is formed by the exchange of iron ions for calcium ions. UNL scientists followed up on these findings with studies to determine the feasibility of translating iron content in the concretion to corrosion rate of the hull in the contact region between the metal and the concretion sample, which is presented in more detail below.

X-Ray Diffraction (XRD)

For XRD, the thin slice section was mounted in a Seimens x- ray diffractometer outfitted with a tube containing a copper anode and a graphite beam diffracted monochromator. The beam size at 60 degrees two theta was 0.079 in. x 0.39 in. (2 mm x 10 mm). X-ray patterns were collected over the angular range from 10 to 80 degrees two theta. A measurement was made every millimeter through the thickness of the specimen (Figure 5.53). Seimens search-match software determined the various phases present in the XRD patterns (Figure 5.54). Excellent fits to the observed XRD patterns were obtained with the combination of three phases: aragonite, siderite and magnetite (DeAngelis 2002). The integrated intensities of two Bragg peaks of siderite and aragonite, displayed as a function of position in the concretion indicate that the siderite ($FeCO_3$) was the major component in the concretion in the 0.5 in. (13 mm) of thickness nearest the steel surface (Figure 5.55). Aragonite ($CaCO_3$), almost absent in the first 0.5 in. (13 mm) from the metal surface, appears in the last 0.08 in. (2 mm) of concretion closest to the water/concretion interface. The distribution of magnetite was uniformly low in concentration through the 0.5 in. (13 mm) of concretion nearest the steel surface. The magnetite concentration increased in the last 0.08 in. (2 mm) of thickness (Figure 5.56). In addition to the concretion, a thin layer of oxide containing minerals is evident between the concretion and the hull metal. This layer is normally 0.08 to 0.20 in. (2 to 5 mm) thick and is identified as a mixture of

Figure 5.51. Top view of concretion sample.

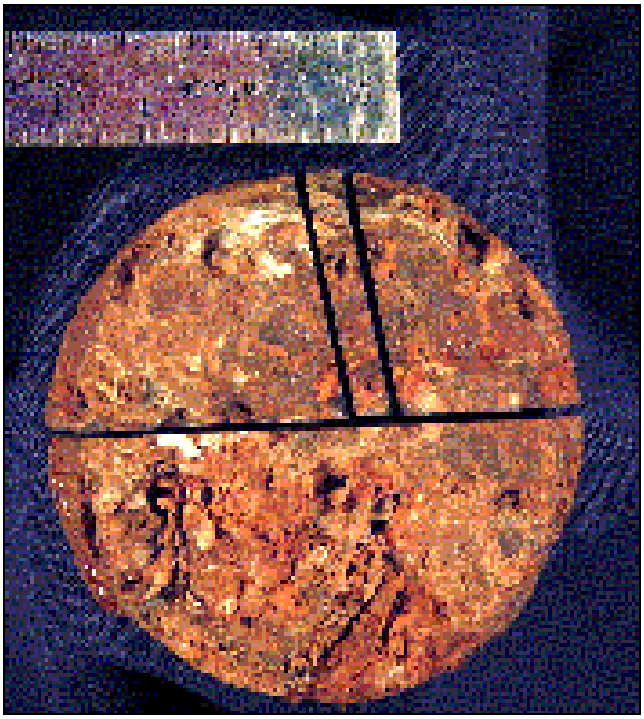

Figure 5.52. Concretion sample after sectioning.

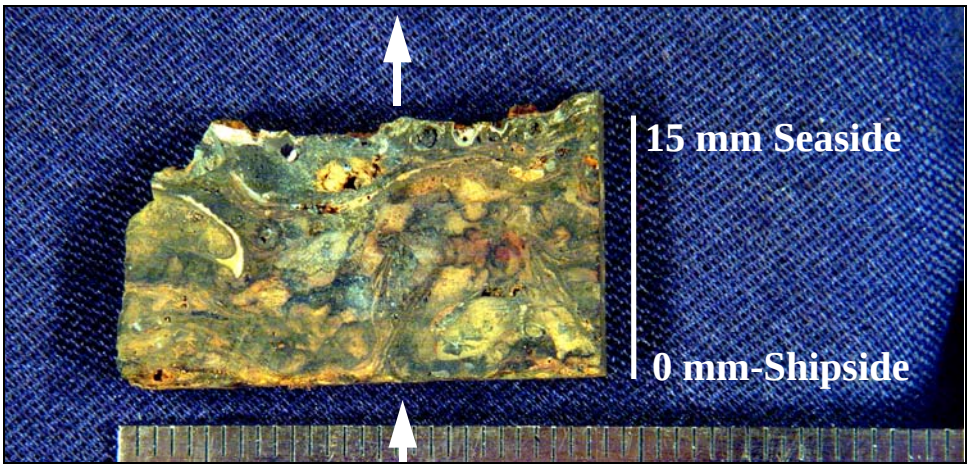

Figure 5.53. X-ray beam sampling path through the thickness of concretion.

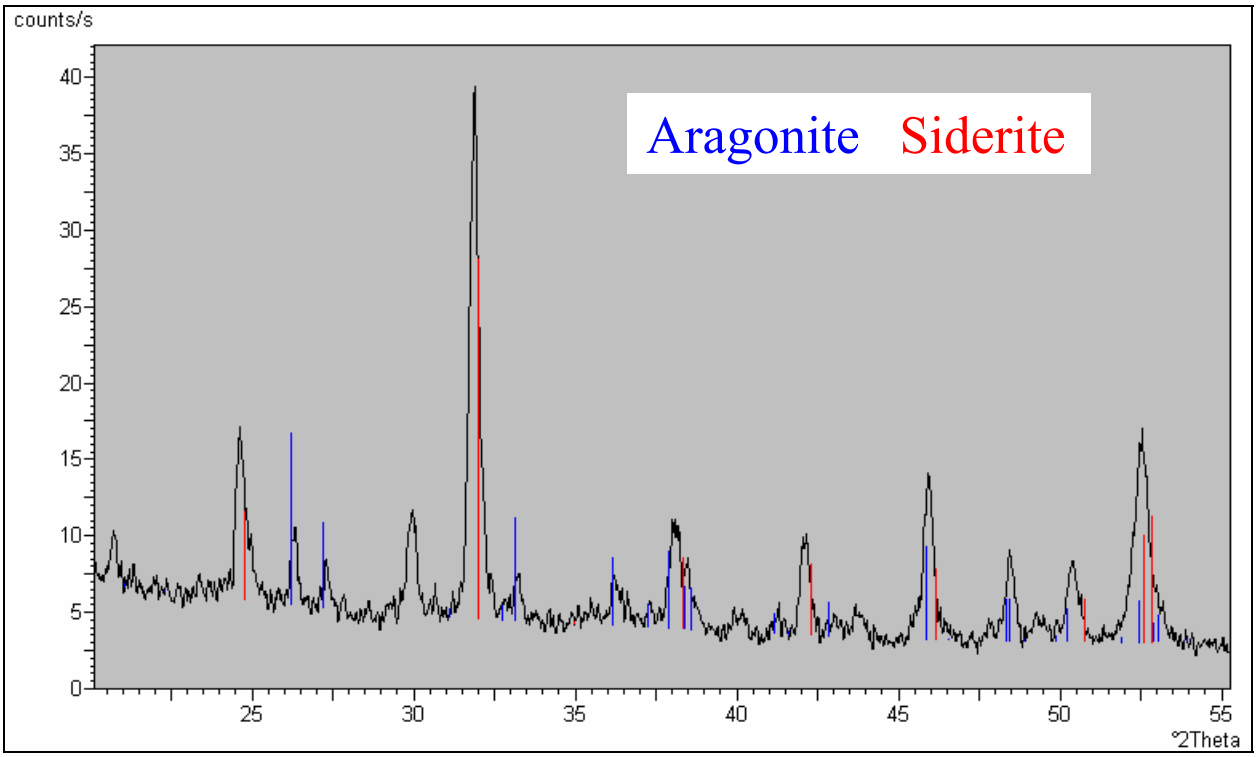

Figure 5.54. Typical experimental x-ray diffraction scan, 2mm from hull surface, 2-theta lines (red) from published standards for siderite, 2-theta lines (blue) from published standards for aragonite.

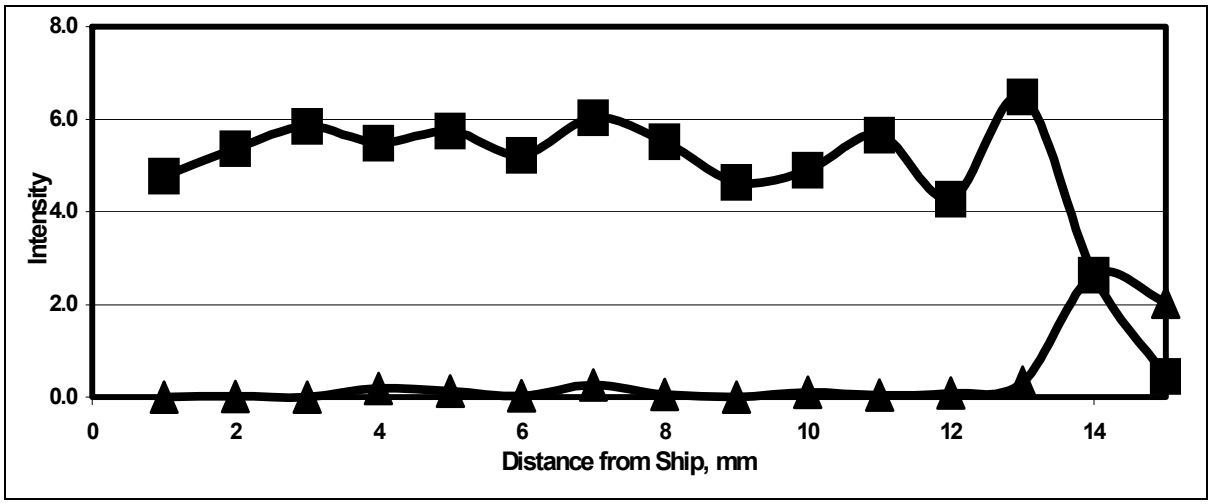

Figure 5.55. Average intensities of siderite and aragonite (lower numbers) peaks as function of distance from hull surface.

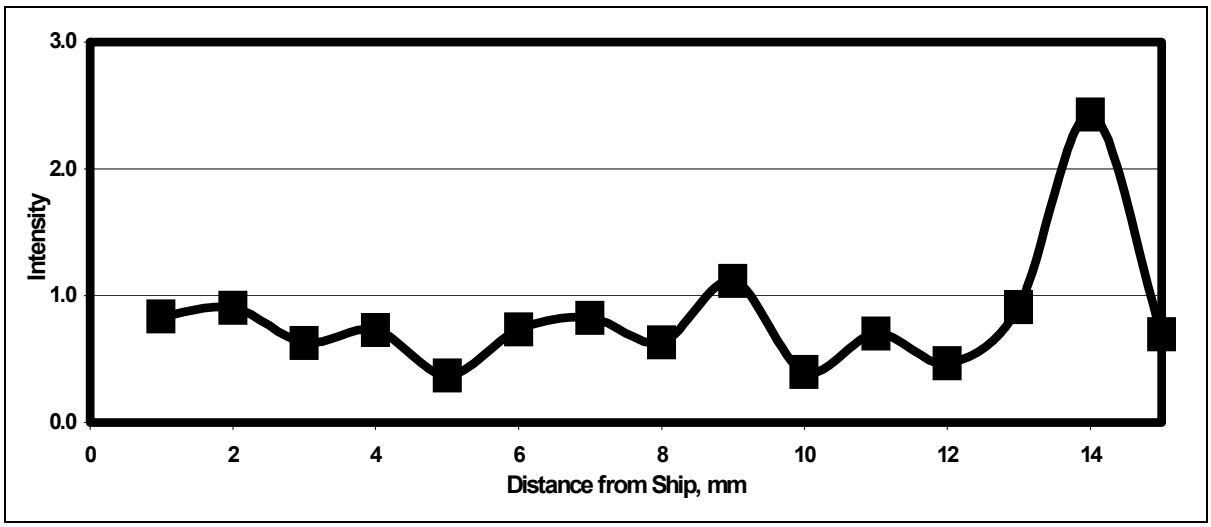

Figure 5.56. Average intensities of the magnetite x-ray diffraction peaks as a function of distance from hull surface.

compounds including chloride containing Akaganeite ($Fe_8(O,OH)_{16}C_{l1.3}$, Iron Chloride Hydrate ($2FeCl_{3.7}H_2O$), as well as Goethite (FeO(OH), Lepidocrocite (FeO(OH), and Magnetite (Fe_3O_4).

The iron/water/carbon dioxide Pourbaix diagram (Figure 5.57) is useful to confirm XRD data since it incorporates stability fields for magnetite (Fe_3O_4), siderite ($FeCO_3$) and hematite (Fe_2O_3). Magnetite and siderite were identified by XRD although hematite is not stable in the range of E_{corr} and pH observed and was not identified. E_{corr}/pH data from data previously discussed is superimposed onto Figure 5.57. Starting from the left side of the diagram at a potential of about -0.4 V (SHE) and pH = 5.0, the green circled dots correspond to iron ions in solution predominantly as Fe^{+2} and exist in the region labeled "corrosion" on the iron/water Pourbaix diagram (Figure 5.2). In this region, the pH decreases slightly as E_{corr} increases. Next, magenta triangulated dots appear in the region labeled siderite at a potential of -0.32 V (SHE) and pH = 5.8. Siderite (with intensity proportional to concentration) exists throughout the concretion cross section, although the concentration is slightly higher at the metal surface, decreasing from a maximum 0.5 in (13mm) to near zero at the water/concretion interface (Figure 5.55). The green triangulated dots start at a potential of about -0.35 V (SHE) and pH = 6.5 and continue through the region labeled magnetite. Magnetite intensity is slightly lower near the steel surface and increases toward the concretion/water interface (Figure 5.56). Although there is some overlap between fields, pH increases as E_{corr} increases in the siderite region and levels off in the magnetite region. These observations are consistent with Figures 5.55 and 5.56 showing maximum siderite near the metal surface and maximum magnetite near concretion/water interface. The absence of hematite in XRD data was confirmed from E_{corr}/pH data since none of the points extend into that region.

Environmental Scanning Electron Microscopy (ESEM)

For ESEM, researchers selected 11 positions on the cross-section of the slice to probe with the electron beam (Figure 5.58). The initial seven of the 11 probe positions tracked the x-ray path and were at the following distances from the steel surface: (1) 0.03 in. (0.8 mm), (2) 0.2 in. (5.4 mm), (3) 0.1 in. (2.5 mm), (4) 0.27 in. (6.9 mm), (5) 0.33 in. (8.4 mm), (6) 0.37 in. (9.4 mm), and (7) 0.42 in. (10.7 mm). The last four probe positions were selected at interesting features in the structure of the concretion, and were located at the following distances from the

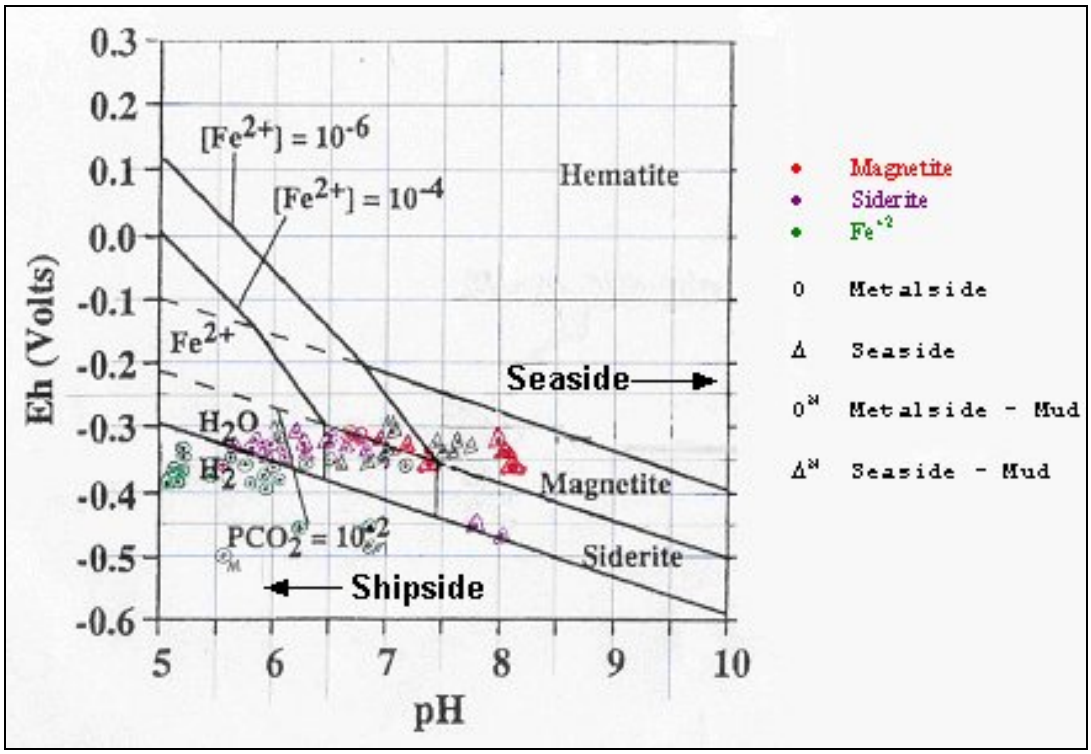

Figure 5.57. E_H - pH stability fields for hematite, magnetite and siderite in water-iron-CO_2 system at 25 °C and 1 atm pressure.

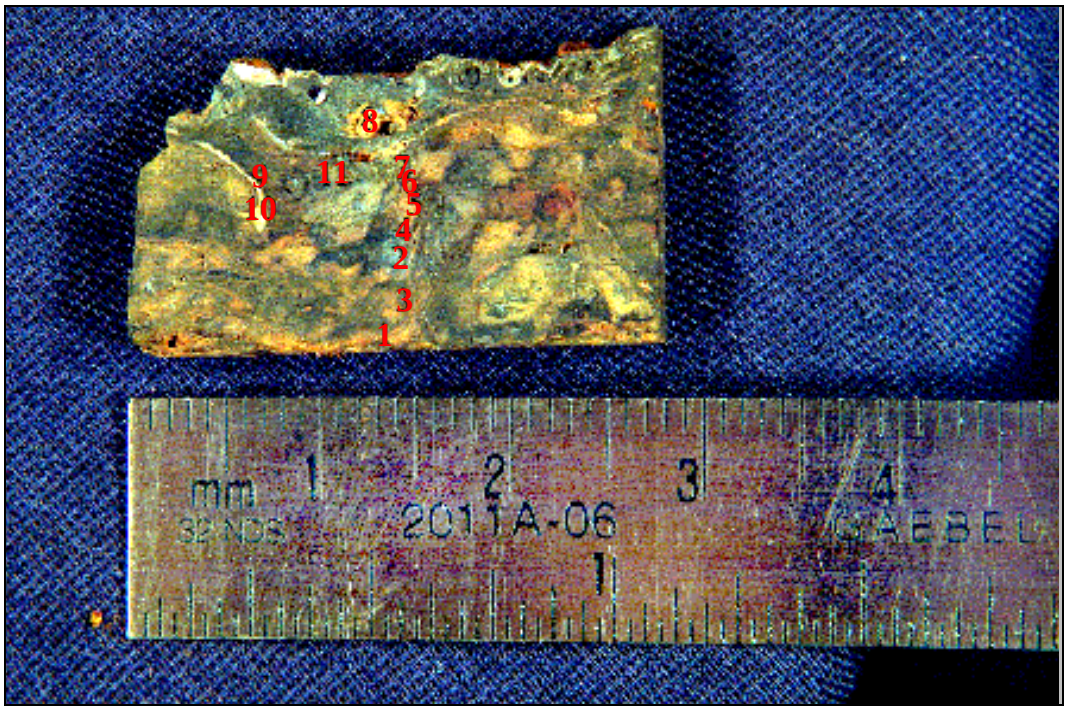

Figure 5.58. Positions of electron microscope probe.

steel surface: (8) 0.53 in. (13.5 mm), (9) 0.41 in. (10.4 mm), (10) 0.34 in. (8.6 mm), and (11) 0.42 in. (10.7 mm). Compositional scans were also made along lines about 10 mils (250 μm) in length to document the inhomogeneous structural characteristics of the concretion (DeAngelis 2002). The data collected consisted of structural images collected from back-scattered electrons and chemical images of the same areas collected from the florescence radiation of the particular element. The elements imaged were Fe, Ca, Ta, Al, Si, Br, O, Cl, C and S. Compositions at the 11 positions were then calculated from the total florescence x-ray spectrum obtained from each of the 11 probe positions (Table 5.28).

Discussion

Based on the positions of the electron microprobe readings and the wt % Fe at those positions, the mean Fe content in the concretion sample USAR-01-045 is calculated by graphical integration as follows:

$$\text{Fe}\,(\text{wt}\,\%) = \frac{1}{\text{L}}\int_0^x \text{C}_{\text{Fe}}\text{dx} \qquad [17]$$

where

L is total thickness of concretion

C_{Fe} is concentration of iron in weight % at position x

x is distance into concretion in mm corresponding to C(Fe)

Fe(wt%) = 1/15mm [798 wt %-mm] = 53 wt % Fe (mean) in concretion

An iron balance on a unit area through the metal/concretion for this sample shows that about 40% of the corroded iron is trapped in the concretion; the remaining iron remains as a thin oxide layer at the concretion/metal interface or is lost to seawater. DeAngelis also conducted XRD analysis of the thin oxide layer on metal coupon sample USAR-01-002. Dominant oxides were magnetite (Fe_3O_4) and Lepidocrocite (limonite) (FeO(OH)).

Based on ESEM results, UNL conducted direct chemical analysis on four concretion samples: USAR-03-001, USAR-03-002, USAR-03-003, USAR-03-007 and USAR-03-008. The average total iron content of these samples was 35 wt%. The University of New Mexico conducted XRF analysis on concretion samples USAR-01-042 and USAR-01-043. The average

Sample	Probe Pos.	C wt%	O wt%	Al wt%	Si wt%	S wt%	Cl wt%	Ca wt%	Fe wt%	Br wt%	Ta wt%
15	1		43.89		0.69	4.7	3.12	0.99	46.51	0	
16	2		25.14		0.35	3.28	4.04	1.87	65.31	0	
18	3		30.11		0.62	2.35	10.38	1.16	39.06	16.32	
16	2 thin part		19.31		0.25	1.73	9.35	2.39	55.78	11.18	
19	4		25.67		1.89	4.02	1.66	3.47	63.87	0	
20	5	5.3	10.41		0.95	1	0.95	1.73	78.2	0	1.45
21	6	4.07	9.67		1.25	1.22	0.54	1.9	60.84		0.52
22	7	6.68	15.21		0.6	9.05	0.32	10.36	57.7		0.07
23	8	9.07	28.31	2.5	3.16	1.59	0.42	3.95	51	0	0
24	8	7.08	24.76	1.68	2.19	1.23	0.49	1.51	61.07		
25	8	9.44	25.78	1.5	2.06	1.12	0.35	1.9	57.86		
26	9	6.64	38.74	0.18	0.53	1.59	0.78	33.49	18.04		
27	10	7.02	36.53	0.22	0.59	18.28	0.38	16.47	20.5		
28	11	8	26.99	1.98	4.45	9.2	0.77	1.59	47.03		
Sample	Probe Pos.	C at%	O at%	Al at%	Si at%	S at%	Cl at%	Ca at%	Fe at%	Br at%	Ta at%
15	1		71.11		0.64	3.8	2.28	0.64	21.54	0	
16	2		52.09		0.41	3.4	3.78	1.55	38.77	0	
18	3		58.76		0.69	2.29	9.14	0.9	21.84	6.38	
16	2 thin part		44.17		0.33	1.98	9.66	2.18	36.56	5.12	
19	4		52.32	0	2.19	4.08	1.53	2.82	37.29	0	
20	5	16.74	24.69		1.29	1.19	1.02	1.64	53.13	0	0.3
21	6	13.34	23.81		1.76	1.5	0.6	1.86	57.02		0.11
22	7	17.87	30.55		0.69	9.07	0.29	8.31	33.2		0.01
23	8	19.86	46.53	2.42	2.96	1.31	0.31	2.59	24.01	0	0
24	8	17.03	44.73	1.8	2.26	1.1	0.4	1.09	31.6		
25	8	21.5	44.09	1.52	2.01	0.96	0.27	1.3	28.35		
26	9	13.08	57.24	0.16	0.45	1.17	0.52	19.75	7.64		
27	10	13.74	53.64	0.19	0.49	13.4	0.25	9.66	8.63		
28	11	17.64	44.69	1.94	4.2	7.6	0.57	1.05	22.31		

Table 5.28. Chemical Compositions in Weight and Atomic Percent at the positions of the ESEM.

total iron content of these samples was 42.6 wt% (Table 5.29). Considering the heterogeneity through the cross section of the concretion, direct chemical analysis appeared to be an acceptable and much less expensive alternative to ESEM. Only minor amounts of other metallic oxides such as TiO2, Al2O3, MnO and MgO are reported (Husler and Dodson 2003).

In addition to Fe, ESEM probe data shows the distribution of other elements (Table 5.28). It is interesting to note that carbon is below detectable levels until position (5) 0.33 in. (8.3 mm) into the concretion from the steel surface is reached. If a portion of this carbon is organic, there may be bacterial activity in the concretion as reported by North and MacLeod (1987). However, FeS was not detected as would be expected if SRB were active there. The level of detectability

Sample	%Fe	%Mg	%Ca
Direct Chemistry - UNL			
USAR-03-001	42.78	0.24	4.19
USAR-03-002	33.86	0.29	10.83
USAR-03-003	21.83	0.83	17.64
USAR-03-007*	48.10	1.49	0.57
USAR-03-008	29.15	1.67	19.0
XRF - UNM			
USAR-01-042	43.1		
USAR-01-043	42.1		
*results inconclusive			

Table 5.29. Wet chemistry and XRF concretion analysis, 2003.

is low; therefore, very low concentrations of sulphides could still exist and not be detected. In all but one case, there is sufficient iron to react with all of the sulphur to form FeS. This means that less than 4 at % of the Fe could be in the concretion in the form of FeS and possibly not be detected by XRD. Sufficient oxygen is available to form $FeCO_3$, $CaCO_3$, and Fe_3O_4, as identified by XRD with minor amounts of other oxides such as SiO_2, Al_2O_3 and Ta_2O_3. Other oxides of elements not reported in Table 5.28 are undoubtedly present. Probe positions (8), (9), (10), and (11) represent inhomogeneous features that were not part of the scan path. For example, analysis of position (8) reveals consistently higher than normal Si (SiO_2) and Al (Al_2O_3) and possible entrapment of silt in shell fragments. Position (9) shows abnormally high Ca in the same region as position (8). Position (10) shows an abnormally high sulfur content as well as high Ca. This indicates the possible presence of $CaSO_4$ or CaS.

From observation and analysis of data to date, oxygen availability determines the controlling corrosion process although equation [3] is not the directly dominant cathodic reaction. Interface anaerobic conditions under and into the concretion, lead to the of SRB activity and microbial induced corrosion (Little, et al. 2000). Over time, as the concretion reaches $FeCO_3$ saturation, Fe^{+2} accumulates between the metal hull and concretion to further limit the corrosion rate.

Corrosion Rate (i_{corr})

During marine corrosion, unlike cast iron, the microstructure of steel (USS *Arizona* is low carbon steel, see Johnson et al., 2000 and Makinson *et al.*, 2002) does not result in a remnant

layer of graphite that preserves the original surface and allow for direct measurement of metal lost over time. Hence, it was impossible to use this technique to determine the iron corrosion rate, a technique pioneered in Australia and later applied elsewhere (e.g. Gregory 1999; MacLeod 1987; MacLeod 1995; McCarthy 1988). For steel vessels, the most accurate measure of metal loss is to determine actual steel thickness and subtract this value from original thickness specified on ship's plans. Once total metal loss is known, average corrosion rate can be calculated. With absolute corrosion rate determined, it is possible to calibrate electrochemical techniques such as linear polarization to determine instantaneous corrosion rate at any assessable location on the ship. Although this technique has not been pursued during this project, it is proposed for possible subsequent investigations (see concluding chapter). Measuring actual steel thickness can be accomplished by direct measurement or by using ultrasonic thickness instruments; however, the latter has serious limitations, as discussed below. Because *Arizona* is both a war grave and has international significance, as an alternative, a minimum-impact method to determine corrosion rate of the steel hull has been developed using density, thickness and total iron content of the concretion. The technique has been termed the Concretion Equivalent Corrosion Rate (CECR) and has provided the best combination of minimum impact and reliability. For interior spaces or other areas where it is impossible to collect concretion samples, an estimate of corrosion rate based on environmental parameters is the only alternative at the present time. However, linear polarization may be readily adaptable to interior as well as exterior corrosion rate measurement.

Previous Work

Initial work on corrosion rate began with an evaluation of previous data collected during the 1980s USS *Arizona* corrosion study. Specifically, Henderson (1989) was reviewed with particular attention to the data in Table 4.3 (Henderson 1989:128), which presents concretion thickness and weight vs. water depth for 12 vertical stations established on *Arizona*'s exterior hull. Concretion appeared in fairly distinct forms, dead and live. Dead, or hard, concretion is composed of skeletal marine organisms with an original high calcium carbonate composition and a maximum thickness of about 1 in. Accumulated live organisms on the exterior surface of the concretion measured up to about 3 in. in thickness. Table 4.3 (Henderson 1989:128) was

modified by Johnson et al. (2003:11) and reproduced here as Table 5.30 to show the original data analysis and conversion to the conventional expression of corrosion rate (i_{corr}) in terms of mpy. Column 1 in Table 5.30 locates (port or starboard) dual samples A and B. Column 2 is water depth. Column 3 is dry weight of corrosion product obtained after the concretion had been scraped from a 36-square inch area of the hull, dried at 100 °C for about 8 hours and the corrosion product separated from the bulk using a bar magnet. Column 4 is the weight of iron calculated assuming that the corrosion product was magnetite (Fe_3O_4) according to:

Weight of Fe = (Dry Weight of Corrosion Product) x 0.724 gr

where

(3 x molecular weight Fe)/molecular weight Fe_3O_4) = 3 x 55.85/232 = 0.724

Column 5 is the i_{corr} in mpy calculated from the following equation:

i_{corr} = (wt Fe) x (1/36) x $(1/2.54)^2$ x (1/7.87) x (1/45) x (1/2.54) x 1000 = (wt Fe) x 0.0048 mpy

According to Henderson (1989:129), the data indicate that the "formation of corrosion products has been maximal at shallower depths and has occurred at lower rates at depths of 20-30 ft." In sea water, Uhlig and Revie (1985:93) note that passivity (thin, adherent protective

Station (Port/Starboard)	Water Depth (ft)	Dry Weight of Corrosion Products	Weight of Iron (gr./36sq.in)*	i_{corr} (mpy)*
17a/b	8	440/718	319/520	1.5/2.5
45a/b	9	161/568	117/411	0.6/2.0
11a/b	13	565/530	409/384	2.0/1.8
53a/b (avg)	17	99	72	0.4
61a/b	17	354/374	256/271	1.2/1.3
21a/b	22	5/25	4/81	0.0/0.1
2a/b	22	14/35	10/25	0.0/0.1
43a/b	24	376/118	272/85	1.3/0.4
12a/b (avg)	27	76	55	0.3
30a/b	27	198/164	143/119	0.7/0.6
33a/b	28	206/270	149/195	0.7/0.9
52a/b (avg)	28	138	100	0.5

Table 5.30. Calculated corrosion rate from original data from June 1986. Colums 4 and 5 adjust for approximately 2 years in dry dock prior to December 7, 1941.

film) of iron is not established and in such media, decreased oxygen concentration, as the water depth increases, results in a decrease in corrosion rate in the absence of concretion. As expected, i_{corr} in mpy (Table 5.30, column 5) is consistent with this observation although the presence of concretion, as discussed earlier, promotes lower pH and changes the chemistry at the concretion /metal interface. As Henderson (1989:129) observes:

> Hard biofouling [concretion] at all stations was found to consist of entwined masses of oyster and vermetid shells. Hard biofouling extended beneath the bottom silt on the hull surfaces, and was exposed by digging holes about 3 feet into the silt at representative locations. The hard fouling layer had apparently grown on the lower hull areas before they were covered with silt by sedimentation or hull settling.
>
> No correlation was found to exist between water depth and thickness of hard biofouling, indicating that, over the long term, growth of oysters and vermetids had been relatively unaffected by depth and water motion. Hard biofouling averaged about ¾-inch thickness on vertical stations, where that layer serves as a primary barrier in protecting steel/oxides from corrosive effects of overlying water and, at present, appears to be stable and well bonded to the hull.

Korb (1987:1255-1256) further addresses this issue by noting that calcareous scale forms at cathode areas on the metal surface. A layer of hard shell and other biofouling restricts available oxygen at the metal surface, creates anoxic conditions and decreases the corrosion rate. However, increased stress on the structure occurs. Scale formation at cathode areas is confirmed by MacLeod (1982) and North and MacLeod (1987), who conclude that the main cathodic reactions take place in the concretion rather than at the metal surface because the metal surface becomes devoid of oxygen. The issue concerning the location of cathodic reactions will be continued below in a later section. On freshly exposed carbon steel surfaces, Fontana (1986:374) reports typical corrosion rates in sea water (Table 5.31).

Vertical Position On Structure	i_{corr} (mpy)
Marine atmosphere	3
Splash Zone	17
High Tide	8
Low Tide	5
Quite Sea Water	5-8
Mud Line	2 ½-3

Table 5.31. Typical Corrosion Rates for Mild Steel in Sea Water

A comparison of rates in Table 5.30 with those in Table 5.31 indicates that marine concretion attached to the hull significantly reduces the corrosion rate. Jones (1996:53, 59, 381) discusses macrofouling organisms and reports that they are often acidic, accelerating the corrosion of metal substrates but at the same time shelter the underlying metal from access to oxygen and create differential aeration cells which also accelerate corrosion. The oxygen free (anaerobic) environment beneath macro organisms can further host sulfate reducing bacteria, which can have further implications for corrosion rate.

Direct Measurements

As an initial control for corrosion rate research on USS *Arizona*, in August 2002 NPS-SRC partnered with the Naval Facilities Engineering Service Center-Ocean Construction Division, the U.S. Navy's Mobile Diving and Salvage Unit One (MDSU) and Titan Maritime Industries, Inc. to collect 4-in (10-cm) diameter hull plate samples ("coupons") from *Arizona*'s hull. MDSU surface-supplied divers removed each coupon from prescribed locations using a 4-in (10-cm) diameter proprietary hydraulic-powered hole-saw developed by Titan (Figure 5.59). This hole-saw did not utilize a pilot hole, which would compromise sample integrity. The coupons were removed from external, vertical hull locations marked by SRC archeologists. For analytic purposes, each sample had to be collected with concretion intact on both sides of the coupon (Figure 5.60), so a task-specific bit was designed to retain the coupon plus interior and exterior concretion. Eight coupons were removed from external, vertical hull locations on both port and starboard sides at frame 75 (Figure 5.61). On each side of the ship, one sample was taken from the upper deck level near the water line; from the second deck level above the torpedo blister; from the third deck level in the torpedo blister; and from the first platform level in the torpedo blister below the mud line. Ship plans were consulted for each location to ensure no compartments potentially containing oil would be penetrated. As a precaution, a half-inch hole was drilled near the sample location with a drill-tap that could be easily plugged should oil be encountered. Immediately after coupon removal, each location was plugged using a plumber's pipe plug and sealed with marine epoxy to prevent formation of localized corrosion cells and minimize exchange of interior and exterior water. Drilling operations were directed, monitored, filmed and photographed in-water by SRC personnel using scuba equipment.

Figure 5.59. U.S. Navy diver using Titan's hydraulic hole-saw to remove samples from Arizona's hull (NPS Photo by Brett Seymour).

Figure 5.60. Steel hull sample with intact interior and exterior concretion (NPS Photo by Brett Seymour).

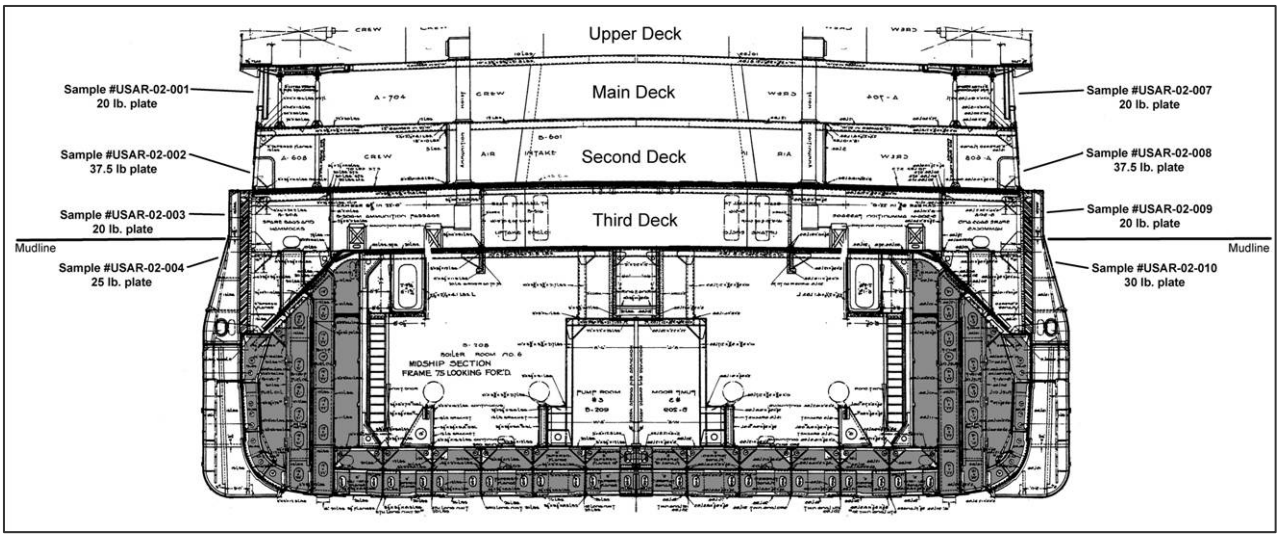

Figure 5.61. Location of samples removed from Arizona's hull at frame 75.

Hull coupon thickness was measured three different times. Preliminary field examination of each sample was performed as soon as the drill housing containing the coupon was detached from the drill and carried to the dock. This measurement is a rough field estimate using a millimeter scale. The second measurement was recorded at Rail Sciences, Inc. (RSI) in Omaha, Nebraska in September 2002 using calipers. Before the coupons were returned to SRC at Santa Fe, NM for long-term curation, UNL researchers removed a small chord from each sample for metallographic examination and optical measurement of plate thickness. The third measurement was obtained metallographically on a cross-section of each chord by Johnson at RSI laboratories (Johnson, et al. 2003:77). Because of some unevenness through the cross section of each chord, nine thickness measurements were obtained and combined to provide an average thickness for each coupon (Figures 5.62-5.69)(Table 5.32). Metallographic examination revealed that the most reliable thickness measurements were obtained from the polished cross sections, so it was decided to only use the optical data obtained at RSI for insertion into equation [19] (see below).

Averaged thickness of each coupon was compared to original steel thickness compiled from ship's plans to determine overall metal loss from December 1941 (it was assumed that minimal corrosion occurred during the ship's active use) to August 2002. The original ship cross-section at frame 75 provided as-built steel thickness in terms of theoretical weight, in pounds per square foot, at each location (Johnson, et al. 2003:82). Standard tables were used to convert theoretical weight to nominal thickness in inches—unfortunately, no thickness tolerances

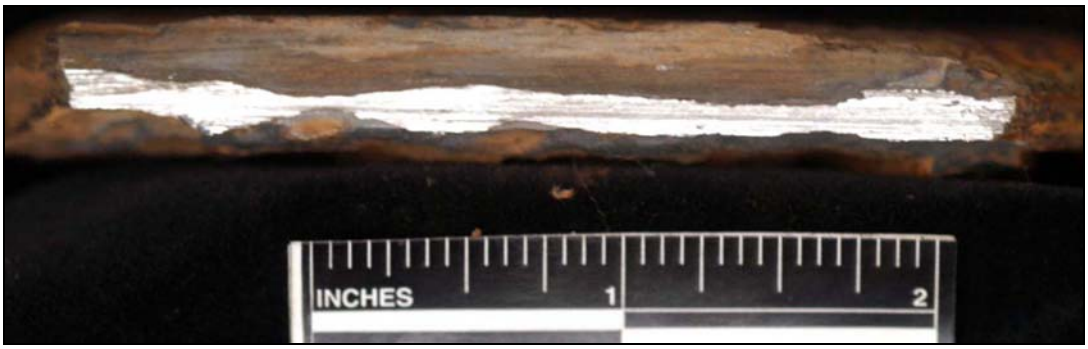

Figure 5.62. Cross section photograph of steel hull sample #USAR-02-001.

Figure 5.63. Cross section photograph of steel hull sample #USAR-02-002.

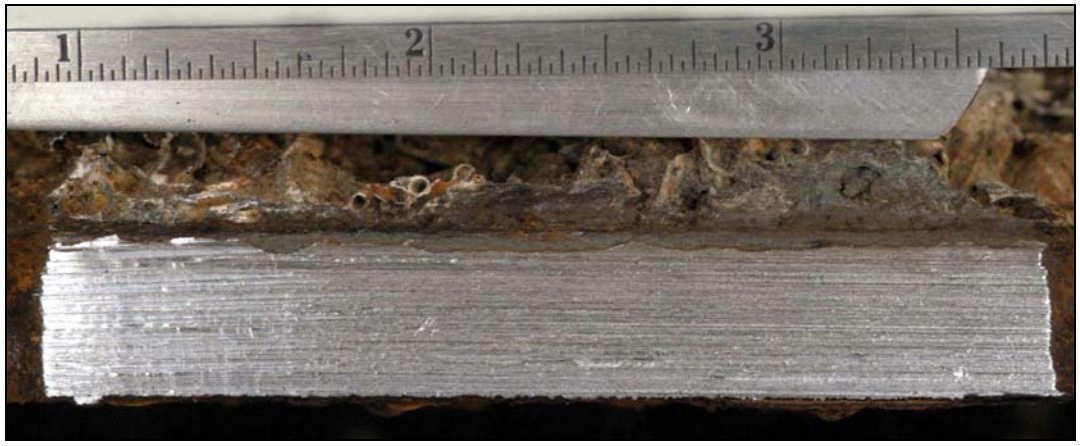

Figure 5.64. Cross section photograph of steel hull sample #USAR-02-003.

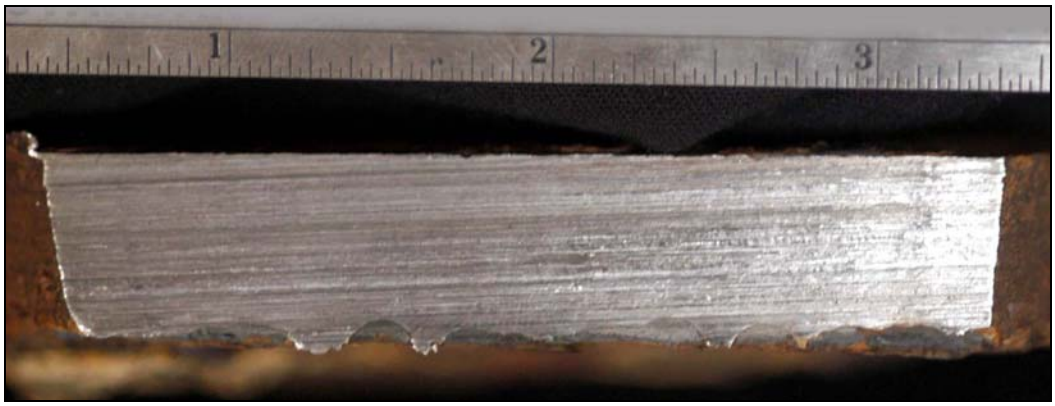

Figure 5.65. Cross section photograph of steel hull sample #USAR-02-004.

Figure 5.66. Cross section photograph of steel hull sample #USAR-02-005.

Figure 5.67. Cross section photograph of steel hull sample #USAR-02-006.

Figure 5.68. Cross section photograph of steel hull sample #USAR-02-007.

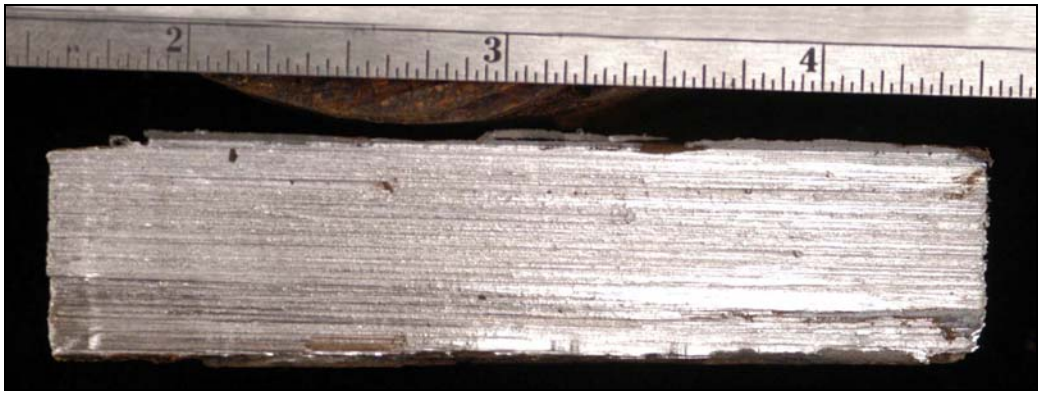

Figure 5.69. Cross section photograph of steel hull sample #USAR-02-008.

Measurement	USAR-02-001	USAR-02-002	USAR-02-003	USAR-02-004	USAR-02-007	USAR-02-008	USAR-02-009	USAR-02-0010
1	.116	.642	.4555	.5255	.223	.7755	.4545	.652
2	.1575	.6755	.4625	.597	.2015	.7845	.4845	.667
3	.087	.66	.4375	.5345	.201	.81	.4535	.6555
4	.1505	.683	.4225	.5554	.195	.807	.43	.663
5	.11	.6865	.4305	.579	.1895	.8005	.358	.654
6	.128	.642	.433	.5665	.177	.77	.3895	.658
7	.1165	.7095	.429	.553	.174	.792	.367	.6425
8	.178	.708	.4235	.5355	.1615	.7815	.36	.652
9	.174	.6325	.4125	.578	.241	.786	.33	.642
Average	.1323	.671	.4341	.5583	.1959	.7897	.403	.654

Table 5.32. Hull sample thickness measurements, in inches, from Rail Sciences Laboratory, March 2003.

are available. Assuming that the plate mill targets a nominal rather than a theoretical weight in lbs./ft.^{2}, the corresponding nominal thickness is shown in the top row of Table 5.33.

Data Analysis

With this data, corrosion rates are calculated according to the following:

$$\text{Metal loss} = T_o - T_a \quad [18]$$

where

T_o is original thickness

T_a is actual thickness

The corrosion rate, (i_{corr}), in metal loss per unit of time, is given by:

$$i_{corr} = \underline{(T_o - T_a)/t} \quad [19]$$

When using English units, corrosion rate is given in mpy. In the International System of Units (SI), corrosion rate is given in microns per year (μm/yr) where one micron is 1/1000 of a millimeter. When the original and actual plate thicknesses are defined in either inches or millimeters, the corrosion rate equation becomes:

$$i_{corr} = \frac{T(o) - T(a)}{t} \times 1000 \quad [20]$$

where

t is the exposure time in years (yr)

Nominal Thickness (Inches)	1/8	3/16	1/4	5/16	3/8	7/16	1/2	9/16	5/8	3/4	7/8
Theoretical Weight (lbs./sq. ft.)	6.15	8.7	11.25	13.8	16.35	18.9	21.45	24	26.55	31.65	36.75
Arizona Plate Weight (lb/sq.ft)							20		25	30	37.5

Table 5.33. Plate Thickness Conversion.

When metal loss is defined in inches, equation [20] expresses corrosion rate in mpy; when the metal loss is defined in millimeters, equation [20] expresses corrosion rate in μm/yr. This is a simplified expression that assumes a constant corrosion rate and essentially uniform corrosion. Although initial corrosion rates are high and decrease over time as concretion forms, it is assumed that corrosion rates stabilized fairly quickly (within a matter of a few years) and that for most of *Arizona*'s lifespan underwater, the rate has been nearly constant.

Results from equation [18] for each coupon are given in Figure 5.70 as a function of water depth, and the results from equation [20] are given in Table 5.34 and Figure 5.71. Because coupons were collected in 2002, t = 61 yr for these calculations. Note that for the two shallowest samples in Table 5.34 (USAR-02-001 and USAR-02-007, both in 5 ft. [1.52 m] water depth), i_{corr} was halved from the absolute value obtained from the direct measurement technique. Values were halved because, at those two locations, both the inside and outside of the hull are open to free-circulating seawater causing corrosion and concretion formation on both the interior and exterior sides of the hull at the same rate, effectively doubling the corrosion rate. On all other samples, there was little observable interior corrosion or concretion formation, and internal dissolved oxygen levels measured after coupon removal were at or near zero, indicating the majority of corrosion was taking place on the exterior side only.

It is significant to note that metal loss is greatest on the port side between the surface and about 20 ft. This is consistent with greater flow velocities on that side of the hull. Below about 20 ft., metal loss is nearly the same. An additional factor is the turbulence created by Navy launches and other port-side vessel traffic. The effect of water depth on corrosion rate is clearly evident in Figure 5.71 and Table 5.34. The two uppermost coupons, taken at the upper-deck level at approximately 5 ft. (1.52 m) water depth, incur the highest hull steel loss to corrosion (i.e. highest corrosion rate) of close to 3.0 mpy for the port side coupon (USAR-02-001) and 2.5 mpy for the starboard side coupon (USAR-02-007). To put this into perspective, 6 mpy (actual corrosion rate from both sides) corresponds to an average loss of 360 mils (0.009 μm) or 0.360 in. (9 mm) in 61 years, or the loss of nearly 75% of thickness on a ½ in. (12.7 mm) steel plate. Two reasons for the relatively high corrosion rate near the surface is maximum availability of oxygen and corrosion attack from both sides of the hull plate. Neither of these locations, however, is structural in nature nor supports any critical vessel elements.

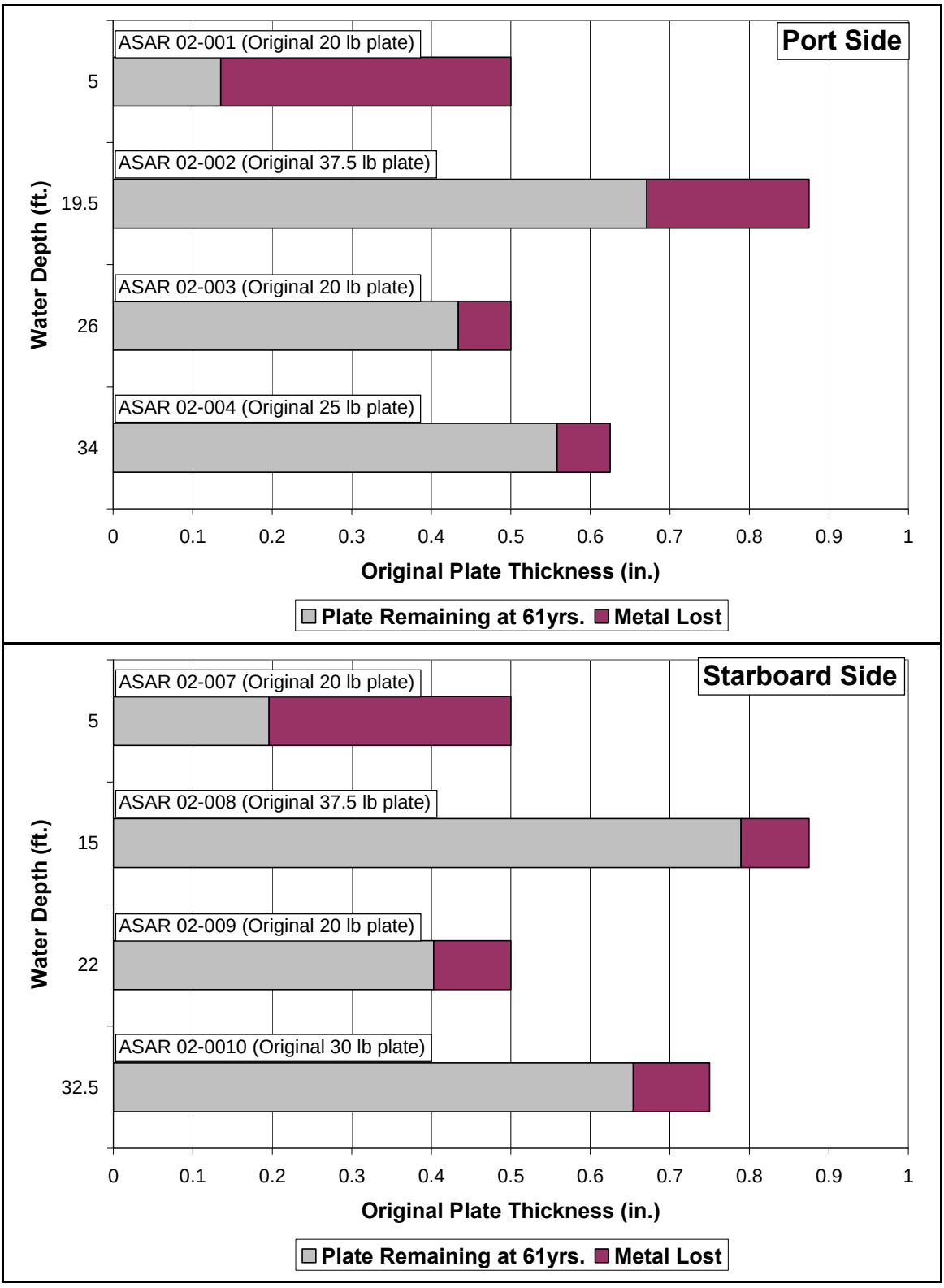

Figure 5.70. Metal loss as a function of original plate thickness and water depth

Sample	Original Thickness		Average Thickness (2002)		Water Depth		i_{corr}	
	in	mm	in	mm	ft	m	mils/yr	µm/yr
USAR-02-001	0.500	12.70	0.135	3.43	5.00	1.52	2.99*	75.98*
USAR-02-002	0.875	22.20	0.671	17.04	19.50	5.94	3.34	84.59
USAR-02-003	0.500	12.70	0.434	11.02	26.00	7.92	1.08	27.54
USAR-02-004	0.625	15.90	0.558	14.17	34.00	10.36	1.10	28.36
USAR-02-007	0.500	12.70	0.196	4.97	5.00	1.52	2.49*	63.36*
USAR-02-008	0.875	22.20	0.790	20.07	15.00	4.57	1.39	34.92
USAR-02-009	0.500	12.70	0.403	10.24	22.00	6.71	1.59	40.33
USAR-02-010	0.750	19.05	0.654	16.61	32.50	9.91	1.57	40.00
*values halved								

Table 5.34. Corrosion rate as a function of water depth from direct coupon measurement.

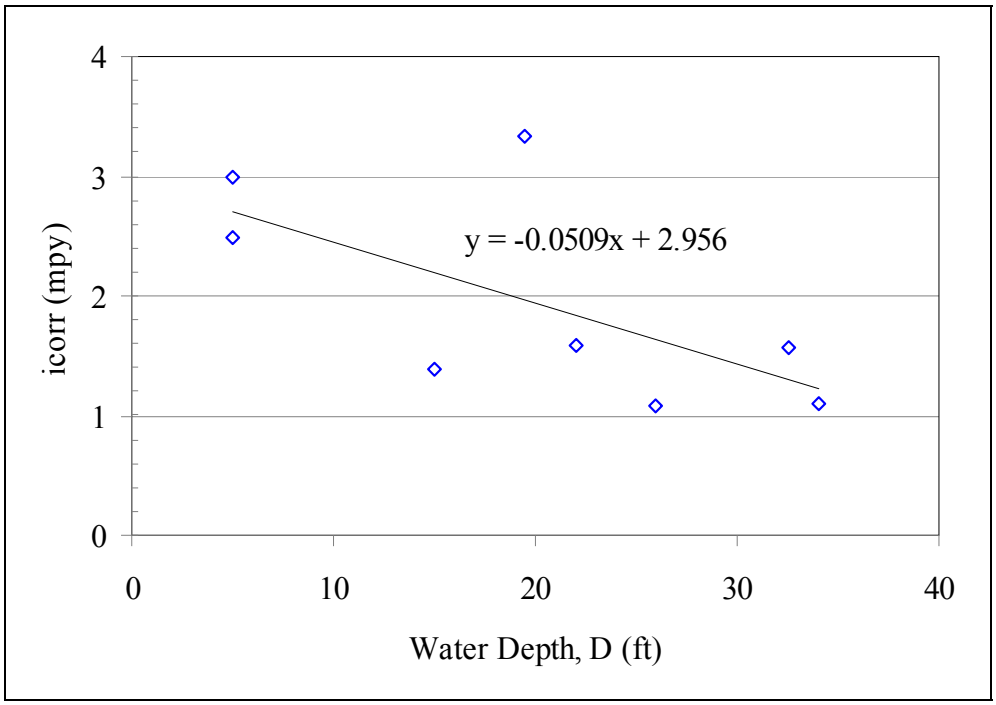

Figure 5.71. Corrosion rate (i_{corr}) of hull samples as a function of water depth.

Hull corrosion rate at the second-deck level varies from 3.3 mpy on the port side at a depth of 19.5 ft. (5.9 m) (USAR 02-002) to 1.4 mpy on the starboard side at a depth of 15 ft. (4.5 m) (USAR 02-008) (Table 5.34)(Figure 5.71). Examination of each of these coupons reveals a very thin layer of interior concretion, indicating limited marine activity on the interior side just above the torpedo blister. Average oxygen concentration of the interior spaces adjacent to the interior side of each sample was about 4.25 mg/L or 65% of the maximum at the surface. This was determined by inserting an oxygen probe into the interior space water immediately after removing the sample. Corrosion on interior surfaces of the hull likely contributes to the total metal loss in spaces where there is some exchange with fresh seawater, concretion is minimal, and oxygen is available to support corrosion in accord with equation [3]. However, such seawater exchange seems to be limited in this area.

Similarly, coupons removed from the torpedo blister above the harbor bottom vary from 1.1 mpy at a depth of 26 ft. (7.9 m) on the port side (USAR-02-003) to 1.6 mpy at a depth of 22 ft. (6.7 m) on the starboard side (USAR-02-009). Interior spaces at this level are inside the torpedo blister rather than inside the ship's hull. Dissolved oxygen on the interior side approaches zero on the portside and 2.5 mg/L (approximately half the exterior levels) on the starboard side, and the interior surface of the coupons are generally smooth with virtually no contribution to metal loss. The torpedo blisters at these locations are sealed from the exterior environment, so oxygen replenishment is negligible.

From the torpedo blister coupons removed from just below the harbor bottom (USAR-02-004 and USAR-02-010), the corrosion rate is unchanged at 1.1 and 1.6 mpy, respectively. It was only possible to measure the port side sample interior torpedo blister space for dissolved oxygen. The readings were near zero, indicating that available oxygen has been consumed, likely during initial corrosion, and not replenished through exchange with fresh seawater. Historically, it is interest to note that while the original intent of the torpedo blister addition during reconstruction in 1929-1930 was to provide added protection from torpedo attack, it now provides additional corrosion protection to the original external hull of the ship in lower regions of the hull where oil bunkers are still intact.

Just below the harbor bottom, i_{corr} appears to hold steady or increase slightly. This may be related to the fact that the maximum bacterial populations are found in the upper 1.6 ft. (0.5 m) of the seabed sediment according to MacLeod (1982). With oxygen depletion into the mud

and E_{corr} falling below the hydrogen evolution potential, hydrogen reduction becomes dominant according to equation [4] as sulphate reducing bacteria (SRB) catalyze the discharge of hydrogen and i_{corr} accelerates. When bacteria break down organic matter, they use the energy stored in their chemical bonds and subsequently shuttle electrons to dissolved oxygen. Since oxygen disappears deeper than a few inches into the mud, the bacteria use sulfate ion in sea water by chemically reducing sulfate to sulfide (Kerr 2001). Little (personal communication, 2003) notes that iron sulfide formed below the harbor bottom is cathodic to the iron oxide directly above it in sea water and could be the cause of accelerated corrosion at or near the harbor bottom. The depth of maximum bacterial activity is variable but is known to be active at interfacial sites such as that represented at the harbor bottom. For example, in the Gulf of Mexico, the depth of maximum activity is only a few millimeters. Based on these observations, i_{corr} may decrease substantially with increasing depth into the mud. Corrosion well below the harbor bottom is not fully understood, and may be investigated further in the future. It should be noted that SRB may also be present at the metal/concretion interface, and as such, may have an impact on corrosion over the entire hull of the ship.

Corrosion rate gradient (change in corrosion rate relative to water depth) is 0.05 mpy/ft. or 0.17mpy/m (Figure 5.71). MacLeod (2002:703) reports that the corrosion rate gradient of pre-steel-era iron shipwrecks, determined from annualized depth of corrosion as measured by penetration of graphitization into cast iron, is 0.36 mpy/m. The difference can be explained in terms of microstructural and chemical differences between cast iron and low carbon steel, as well as differences in environmental variables such as temperature, oxygen concentration, salinity, tidal conditions and marine organism activity.

Further Considerations – Relating Direct Measurements to E_{corr} and Limiting Current (i(L))

Experimental observation clearly indicates that E_{corr} and i_{corr} are each linear when plotted as a function of water depth (Figures 5.24, 5.29 and 5.71), hence a plot of i_{corr} as function E_{corr} is also linear. By eliminating water depth as a variable and combining the results with equation [11], Tafel equations are derived for each frame location (Table 5.35).

The Tafel constant β is the slope of the anodic polarization line (Figure 5.1). A high value of β means that the electrode is highly polarized, the line steeply increases and the

Frame	Tafel Expression*	β (mV/decade)
9	E_{corr} = 42 log(i_{corr}) 358	42
75	E_{corr} = 30 log(i_{corr}) 354	30
82	E_{corr} = 22 log (i_{corr}) 352	22
76-88	E_{corr} = 23 log (i_{corr}) 356	23
128	E_{corr} = 28 log (i_{corr}) 352	28
*E_{corr} (SHE,mV), i_{corr} (mpy)		

Table 5.35. Corrosion Rate as a Function of Corrosion Potential

corrosion current is relatively low. If β is low, polarization is limited and the corresponding corrosion rate is relatively high. The ability of iron ions to go into solution in seawater and be removed from hull metal is variable depending upon the proximity of concretion to hull metal, its thickness, oxygen permeability and flow patterns at the concretion/metal interface. Observations indicate the Tafel constants β for each frame location is highest near the bow, decrease uniformly aft towards midships, and then increase somewhat towards the stern (Table 5.35). The Tafel equations provide an alternative method to determine corrosion rate, where E_{corr} is substituted into the equation closest to the location where E_{corr} is taken and solved for i_{corr}. Although not as accurate as other methods, these equations provide a corrosion rate estimate at frame locations outside of the midships area.

Below the harbor bottom, significant shifts in E_{corr} both port and starboard occur to suggest that bacteria are active in the interface area near the harbor bottom. For example, a comparison of coupon sample locations USAR-02-003 and USAR-02-004 on the port side indicate that E_{corr} values are more positive in the latter case by more than 40 mV. However, i_{corr} is identical at 1.1 mpy. A similar comparison of coupon sample locations USAR-02-009 and USAR-02-010 on the starboard side show that E_{corr} values are more negative in the latter case by more than 130 mV. However, i_{corr} is identical at 1.6 mpy. It is apparent that corrosion data are not consistent from just above to just below the harbor bottom. This inconsistency above and below the harbor bottom may be due to accelerated bacterial activity near the water/harbor bottom interface (Brenda Little, personnal communication, 2003). According to Little et al. (2000), bacteria consume oxygen and anoxic conditions are created in this area. Sulphate is reduced to sulphide and iron sulfide formed below the harbor bottom is cathodic to the oxide above it. With significant change in conditions at the harbor bottom, acid forming bacteria and SRB are likely active all over the hull. Hydrogen evolution occurs as bacterial activity

accelerates hydrogen discharge. It is difficult, however, to separate hydrolysis effects (equation [7]) from bacterial effects. Corrosion measurements below the harbor bottom are limited and more data is needed to elucidate corrosion behavior in this complex environment. In addition, E_{corr} acquisition needs to extend to well below the harbor bottom to better elucidate the effect of low oxygen content deep in the mud to that of much higher oxygen in water above. A further understanding of bacterial activity is also needed to relate E_{corr} and i_{corr}, not only at the harbor bottom and below but at the metal/concretion interface in other parts of the hull.

Oxygen availability directly or indirectly controls corrosion of steel in seawater, and equation [14] incorporates the significant variables necessary to evaluate oxygen transport rate across the surface barrier (in this case, the concretion). If oxygen consumption according to equation [3] were the only cathodic reaction, then the corrosion rate would be directly proportional to both the diffusion coefficient and oxygen concentration gradient across the concretion, and indirectly proportional to the concretion thickness. Hence, in such a circumstance, the corrosion rate could be determined knowing the amount of oxygen consumed according to equation [14], rather than resorting to the more difficult method of determining the amount of metal lost. However, corrosion seldom involves a single cathodic reaction, such as oxygen consumption, and equation [14] is utilized instead as an important diagnostic tool in assessing the complex role of oxygen. This is particularly true for *Arizona* since hydrolysis underneath the concretion creates an entirely different environment at the metal surface where corrosion actually takes place. As will be noted later, equation [14] incorporates numerous environmental variables either directly or indirectly to evaluate oxygen concentration and diffusivity, including salinity, temperature, viscosity and concretion permeability.

The E_{corr} gradient across the concretion for each of the hull coupon sites varies depending on the coupon site, but is typically about 1 mV/mm (Figure 5.72). pH also decreases through the thickness of the concretion (Figure 5.73)(Makinson, et al. 2002), the cause related to hydrolysis given by equation [7]. Bacterial activity may also be a cause of reduced pH, but the extent that each contributes is complex and variable from one site to another (Brenda Little, personal communication, 2003). As mentioned earlier, SRB accelerates the formation of hydrogen gas and hence has been shown to accelerate corrosion at low pH. Applying equation [14] to a typical set of data corresponding to coupon #USAR-02-008:

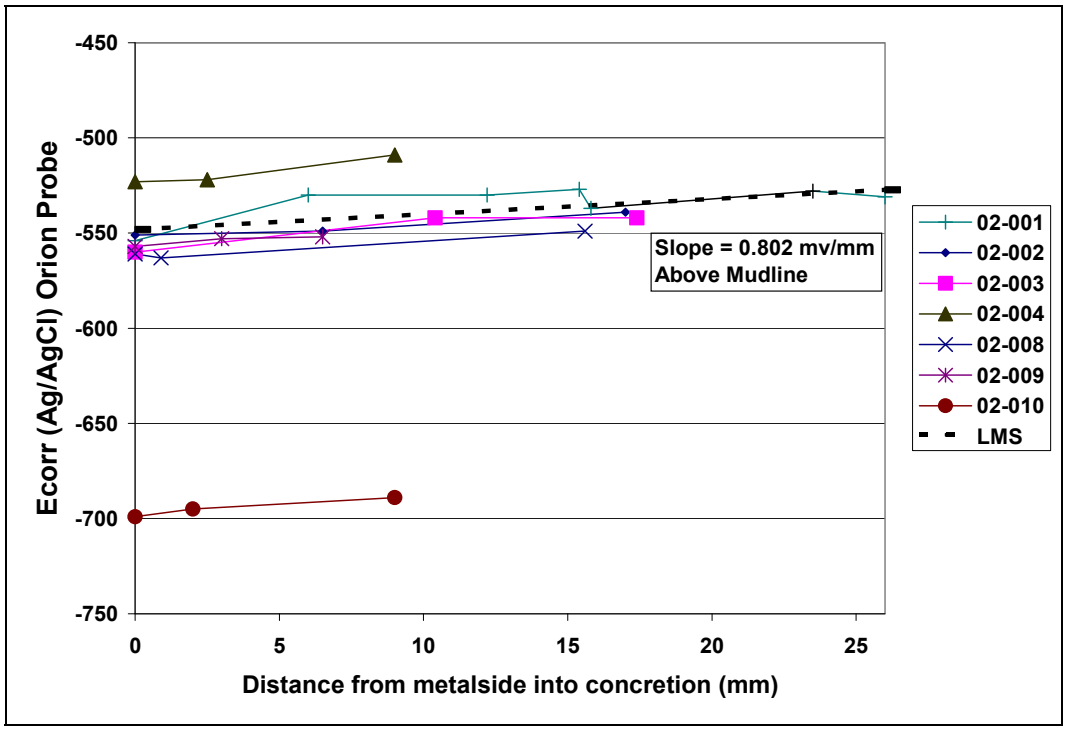

Figure 5.72. Corrosion potential as a function of distance from hull surface into concretion, August 2002.

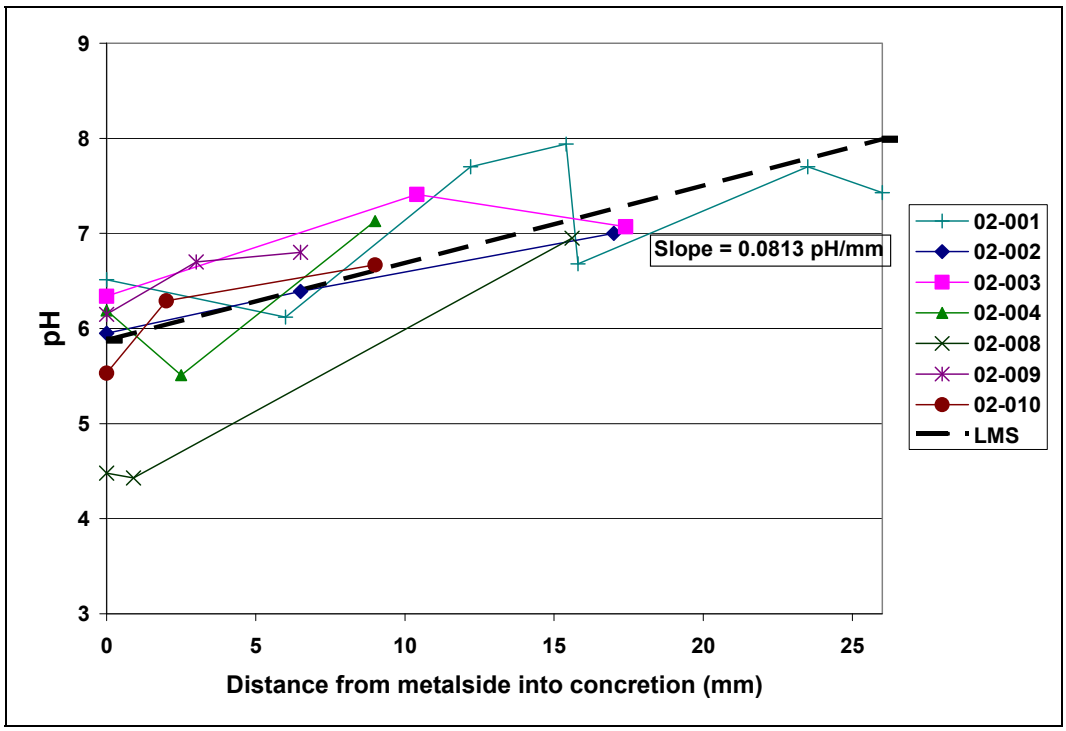

Figure 5.73. pH as a function of distance from hull surface into concretion, August 2002.

$$i(L) = i_{corr} = 0.46\ DnFC/d \qquad [21]$$

where

$D(O_2)$= 2.45 x 10(exp [-5])(cm/sec^2)*

n = 4/gr mole O_2 = 4/32gr O_2 = 0.125

F = 96,500 (coulomb/equivalent, coulomb is amp sec)

CO_2 = 6.1 mg/L

d = 1.56 cm

* Diffusivity of oxygen in water

then

i_{corr} = 0.5 mpy

The actual corrosion rate, i_{corr}, obtained from coupons removed from hull is 1.4 mpy or 3.04 microamps/cm^2 (Figure 5.71). Since this value of i_{corr} is higher by a factor of about three than that calculated from equation [21], hydrogen discharge in addition to oxygen reduction must occur to support a corrosion rate of 1.4 mpy. On the other hand, if the cathodic reaction occurs in the concretion, d could be as low as 0.6 cm near the concretion/water surface, thus the calculated corrosion rate would agree with the rate determined from coupon measurements. The latter would seem to be a simple solution if the cathodic reaction did indeed occur in the concretion.

Ultrasonic Thickness Evaluation

Because of the intrusive nature of the direct measurement technique, it is impractical to remove hull coupons at multiple locations around *Arizona*'s hull. The eight coupons removed in 2002 provided direct measure of corrosion rate in eight representative locations, and became control sites for applying less intrusive methods for measuring hull thickness to reliably predict corrosion rate. A major project goal was to test nondestructive hull thickness measurement techniques. In June 2001, an ROV-mounted Cygnus ultrasonic thickness gauge attached to a VideoRay ROV was used in an attempt to measure interior compartment bulkhead thickness.

Prior to mounting on the ROV, the gauge was calibrated to a 0.5 in steel test block in air. Since bulkhead readings varied from less than 0.2 in. to nearly 0.75 in. (on the same bulkhead, sometimes in the same location), it was concluded that the data were not accurate either because the unit could not compensate for marine corrosion deposits on the surface of the metal or there was electrical interference between the sensor and the ROV. In December 2001, NPS-SRC tested a diver-deployed Cygnus 1 Underwater Multiple Echo Ultrasonic Digital Thickness Gauge on *Arizona*'s hull at frame 85, in the location where concretion samples were removed during in situ E_{corr} and pH data collection (see above). This instrument proved to be unreliable (consistent, reproducible readings were unobtainable), even with significant grinding, polishing, and other surface preparation.

Because precise hull thickness is known in the location of each of the eight hull coupons collected in 2002, those locations were selected for further ultrasonic thickness (UT) instrument testing. For 2003 fieldwork, another instrument was tested. Dr. Art Leach from Krautkramer Ultrasonic Systems (Lewiston, PA, now GE Inspection Technologies) recommended their UT products, and arranged for Mr. Jay Schraan from Inspection Technologies, Inc. (Pomona, CA) to demonstrate their technology on *Arizona*. In October 2003, before beginning fieldwork in Hawaii, Dr. Leach visited NIST in Gaithersburg, Maryland, to calibrate the instrument on the hull coupons collected from *Arizona* in August 2002. This direct calibration with *Arizona* plate material allowed precise speed-of-sound measurements to be made from actual hull steel taken from the *in situ* locations to be tested.

For field operations in November 2003, a Krautkramer USN 58L ultrasonic portable flaw detector was deployed with 5 MHz composite penetration probe. The intent was to revisit the sites of five of the above-harbor bottom hull coupons collected in August 2002—because the exact hull thickness at each of these locations based on measurements made by UNL researchers was known, these locations made ideal test sites for the UT instrument. During UT operations, NPS researchers worked underwater to prepare the hull's surface and deploy the probe, while Johnson and Schraan worked topside with the instrument's user interface. The readings were again widely variable. In a final effort, surface preparation of hull metal included chipping off the strongly adhering inner oxide layer between the concretion and steel surface, and using a pneumatic grinding wheel to flatten the steel surface. The readings were still inconsistent with coupon data, even at locations where the surface was ground shiny and smooth. It was then

thought that concretion on the interior side had some effect on the readings. This issue has not been resolved, but the data does have promising application.

Eliminating extreme data, an error of less than 10% is the best that can be expected from this technology (Table 5.36). A 10% error translates to an error of 0.1 mpy at a 1.0 mpy corrosion rate, or 0.3 mpy at a 3 mpy corrosion rate, which is as good as coupon sampling could produce. The wide variation between sample location USAR-03-001 and USAR-03-007 reflect the roughness due to corrosion from both sides in each case. However, pitting or roughness is shallow and, as a result, corrosion on *Arizona* was uniform. Based on the above limitations, the trend line relating i_{corr} to water depth from UT is given by:

$$i_{corr} = 6.04 - 0.23D \text{ (mpy)} \quad [22]$$

For comparison, the trend line relating i_{corr} to water depth from coupon data is:

$$i_{corr} = 2.956 - 0.05D \text{ (mpy)} \quad [23]$$

Researchers from Inspection Technologies, Inc. returned to *Arizona* in November 2004 to apply new methodology to UT measurements, and to expand the survey beyond the original data points. Different probes were used, including a KBA 560 and an ISS probe. Because of the focus on frames 70–90 for the FEM, UT data were obtained in vertical transects as close to frames 70 and 90 as possible—three test points were selected in each vertical transect. Although better, more consistent results were obtained, the data were still ambiguous (Table 5.37). Although UT techniques look promising, further investigation is required. It is now evident that removal of the concretion and significant surface preparation (buffing and grinding to make the surface as smooth as possible) of the steel hull is essential before consistent, repeatable readings can be obtained. In some cases, even after extensive surface preparation, there are locations where UT measurements are unreliable because of unevenness of the surface due to corrosion (Figure 5.74). Uneven coupling of the face of the UT probe against the hull has been a continuing problem.

Sample	Location	Vessel Side	Water Depth (ft.)	Original Hull Thickness (in.)	Actual Thickness from Coupons (in.)	Ultrasonic Thickness (in.)	Error (%)
USAR-03-001	Frame 76.5	Port	5	0.5	0.135	0.159	+17
USAR-03-002	Frame 76.5	Port	19.5	0.875	0.671	0.73	+8.8
USAR-03-003	Frame 76.5	Port	26	0.5	0.434	0.457	+5.4
USAR-03-007	Frame 80.5	Starboard	5	0.5	0.196	0.178	-9.1
USAR-03-008	Frame 80.5	Starboard	15	0.875	0.79	0.84	+6.4

Table 5.36. Ultrasonic measurements corresponding to hull samples, 2003.

Sample	Location	Vessel Side	Water Depth (ft.)	Original Hull Thickness (in.)	Ultrasonic Thickness (in.)
USAR-04-001a	Frame 88	Port	6	0.5	0.428
USAR-04-001b	Frame 88	Port	6	0.5	0.474
USAR-04-002	Frame 88	Port	19.5	0.875	0.588
USAR-04-003	Frame 88	Port	25	0.5	0.423
USAR-04-004	Frame 88	Starboard	4	0.5	0.31
USAR-04-005	Frame 70	Port	7.6	0.5	0.19
USAR-04-006	Frame 70	Port	19.5	0.875	0.802
USAR-04-007	Frame 70	Port	26	0.5	0.442
USAR-04-008	Frame 68	Starboard	9.6	1	0.713
USAR-04-009	Frame 68	Starboard	16.5	0.875	0.753
USAR-04-010	Frame 68	Starboard	22.5	0.5	0.277
USAR-04-011	Frame 88	Starboard	16.5	0.875	0.466
USAR-04-012	Frame 87	Starboard	21	0.5	0.411

Table 5.37. Ultrasonic measurements corresponding to hull samples, 2004.

Figure 5.74. Steel surface of Arizon's hull after extensive preparation. Part of the strongly adhering layer below the concretion remains at top. Uneven steel surface is due to corrosion (NPS Photo by Brett Seymour).

Concretion Equivalent Corrosion Rate (CECR)

Because determining hull corrosion rate through direct measurement as described above is destructive and impractical, and because determining steel hull thickness with ultrasonic technology has proved unreliable, alternative indirect indicators of steel hull corrosion rate have been sought. The most promising indirect method for determine *Arizona*'s steel hull corrosion rate is correlation between hull iron loss and concretion iron gain, as measured through concretion analysis. External hull concretion analysis and its relationship to corrosion on USS *Arizona* began in the late 1980s. Henderson (1989) scraped samples of concretion from the hull, dried and weighed them, and separated the magnetic corrosion products with a bar magnet. In 1998, Johnson converted the data generated by Henderson (1989) to corrosion rate in mpy to illustrate that analysis of the concretion may have merit as a way to determine corrosion rate (Johnson, et al. 2003). Based on these observations, x-ray diffraction (XRD) and environmental scanning electron microscopy (ESEM) studies on USS *Arizona* concretion were initiated in 1999 at UNL to better understand in what form the iron exists in the concretion and how the metal hull and the concretion interact. Subsequently, x-ray studies were continued at Eglin Air Force Base, Florida and the University of Florida. Using XRD data, De Angelis (2002) identified the iron minerals siderite ($FeCO_3$), with lower residuals of aragonite ($CaCO_3$) and magnetite (Fe_3O_4), as the primary constituents in the concretion (Johnson, et al. 2003:91-92; Johnson, et al. 2006a, 2006b)(see above). Measuring distribution of iron in the concretion cross-section using ESEM and x-ray fluorescence (XRF), Johnson used graphical integration to determine the mean (total) iron content, the result, 40% to 50% by weight, was close to the same iron content obtained from chemical analysis of a sample representing the total thickness of the concretion (Johnson, et al. 2003:96-97). Data from *Arizona* concretion analysis revealed that the specific weight of the concretion per unit area (density x thickness) and total iron in concretion in weight percent (%Fe) decreases with water depth (Figure 5.75). The equation expressing the relationship between weight %Fe and water depth is given by:

$$\text{Wt\% iron} = -1.0621D + 50.12 \qquad [24]$$

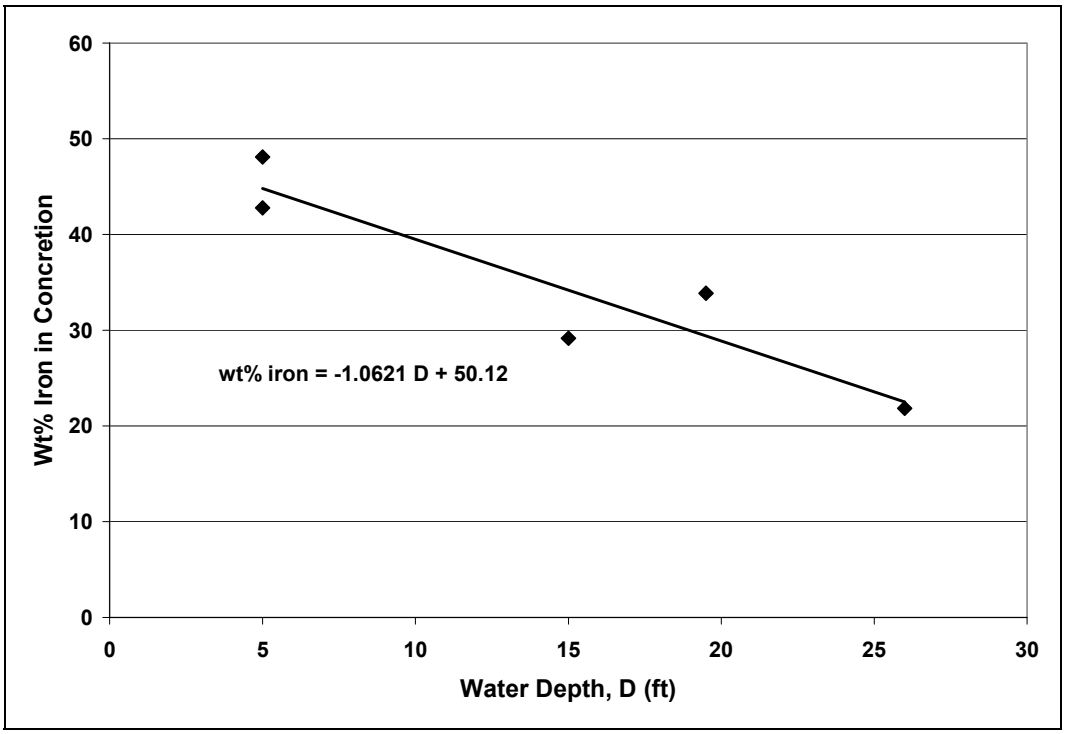

Figure 5.75. Weight % iron vs. water depth.

At the same time, concretion density, measured using standard methodology described in ASTM D572-00, also decreases with water depth, as expressed by the equation:

$$\rho = 2.3903 - 0.0027D \text{ (gr/cm2)} \qquad [25]$$

Corrosion rate, based on direct measurement analysis of hull coupons, shows a similar trend—corrosion rate decreases with water depth (Figure 5.71 and Table 5.34). Based on these results, Johnson developed a quantitative expression relating the metal lost in a specific cross-section of steel hull, and the metal gained by the concretion in the same overlying cross-sectional area (Russell, et al. 2006). The technique was refined using samples of concretion obtained from *Arizona*'s hull in 2003 and 2004. Concretion samples from 2003 and 2004 were acquired using a 3-in (7.5-cm) hole saw bit with a pneumatic drill. After the samples were removed, each location was sealed with a pH-neutral marine epoxy—others have recommended hydraulic cement (see Mardikian 2004:147).

The Concretion Equivalent Corrosion Rate (CECR) expresses corrosion rate determined from iron content, density and thickness of the concretion. This equation is based on the assumption that iron ions generated at the concretion/metal interface are captured by the concretion as $FeCO_3$ by replacement of calcium in calcium carbonate. The specifics of the exchange of calcium for iron are not well understood and are under study. To a lesser extent, iron also forms magnetite and other oxides and oxychlorides, as discussed in an earlier section. Combination of density, thickness and iron content yield the following equation in English units (mpy) as derived by Johnson:

$$i_{corr} = \frac{0.5 \times p \times wt\%\ Fe \times d}{t} \qquad [26]$$

where

i_{corr} is corrosion rate (mpy)
% Fe is weight percent iron in concretion (dry basis)
p is concretion density (gr/cm^3)
d is concretion thickness (cm)
t is exposure time in years (yr)
0.5 is a unit conversion constant

Using SI units in μm/yr, the equation becomes:

$$i_{corr} = \frac{12.7 \times p \times wt\%Fe \times d}{t} \qquad [27]$$

where the variables in equation [26] are defined, but with a unit conversion constant of 12.7.

Physical and chemical properties for 16 concretion samples and corresponding corrosion rates calculated from equations [26] and [27] are tabulated in Table 5.38. Corrosion rates from direct measurement of hull coupons and concretion analysis are compared in Figure 5.76. The actual corrosion rate obtained from metal coupons is higher than that predicted by concretion analysis using equation [26], as indicated by the separation between the two trend lines. The reasons for the difference are: (1) higher initial (pre-concretion) corrosion rates that produced

Sample	Thickness	Density*	Total Iron**	Water Depth		$i_{corr(conc)}$	
	cm	g/cm3	%Fe	ft	m	mils/yr	µm/yr
USAR-02-005	0.51	2.26	22.20	34.00	10.36	0.21	5.33
USAR-02-006a	1.15	2.25	26.00	34.00	10.36	0.55	14.01
USAR-02-006b	0.95	2.41	45.20	34.00	10.36	0.85	21.50
USAR-03-001	2.50	2.53	42.78	5.00	1.52	2.18	55.40
USAR-03-002	1.20	2.34	33.86	19.50	5.94	0.77	19.48
USAR-03-003	1.00	1.92	21.83	26.00	7.92	0.34	8.59
USAR-03-008	1.80	2.44	29.15	15.00	4.57	1.03	26.22
USAR-04-002	2.10	2.43	42.09	19.50	5.94	1.70	43.30
USAR-04-003	1.89	2.39	46.95	26.00	7.92	1.68	42.75
USAR-04-005	1.82	2.30	29.88	5.00	1.52	0.99	25.21
USAR-04-006	1.84	2.55	43.77	19.50	5.94	1.63	41.40
USAR-04-007	1.39	2.29	41.23	26.00	7.92	1.04	26.46
USAR-04-008	2.36	2.41	45.86	5.00	1.52	2.07	52.58
USAR-04-009	1.95	2.47	48.16	15.00	4.57	1.84	46.76
USAR-04-010	1.34	2.47	34.75	22.00	6.71	0.91	23.19
USAR-04-011	2.19	2.34	46.69	15.00	4.57	1.90	48.23
USAR-04-012	1.71	2.43	34.25	22.00	6.71	1.13	28.69
*Density measurements were made in accordance with ASTM D792-00							
**Dry basis							

Table 5.38. Physical and chemical properties of concretion as a function of water depth.

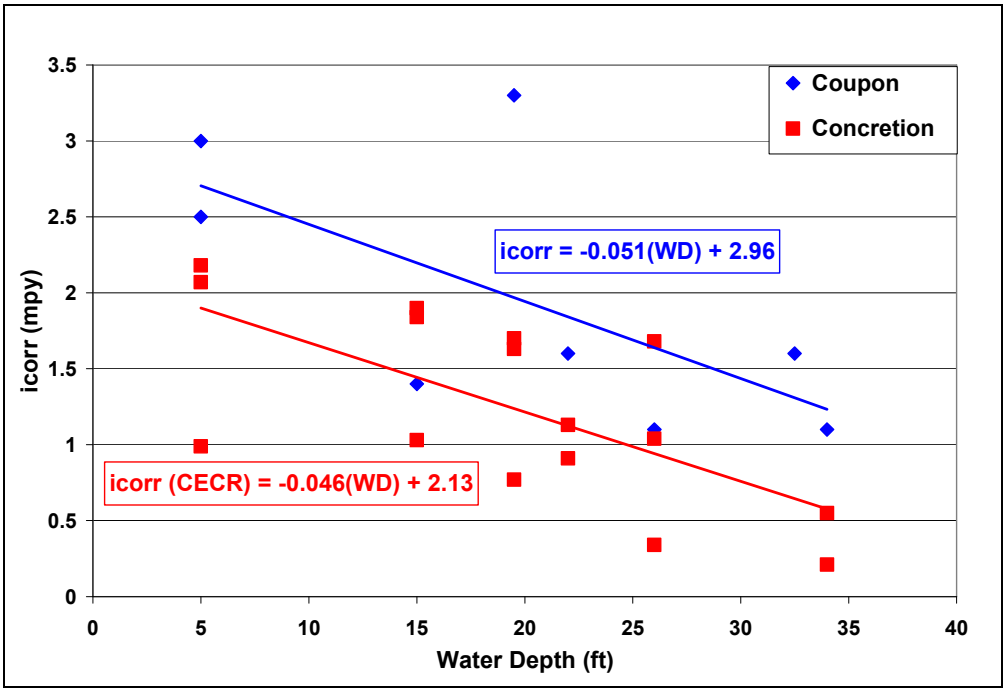

Figure 5.76. Comparison of the corrosion rate on *Arizona* compiled from both coupon data and concretion iron content measurements as a function of water depth.

soluble iron that was not incorporated into concretion; (2) formation of an oxide layer between the steel surface and the concretion, which is not captured during concretion removal and therefore the iron within it is not included in the analysis; and (3) possible corrosion on the interior side of the hull plates. Analysis of the ratios of the two trend lines in Figure 5.76 reveals that corrosion rates obtained from the coupons using the direct measurement technique is higher than corrosion rates predicted by the concretion constituent analysis by a factor of 1.6. With this ratio factored in, a general equation for estimating corrosion rate directly from physical and chemical concretion properties is given in equation [28], where the constants in equations [26] and [27] are multiplied by 1.6 for English and SI units respectively to yield an expression for the actual corrosion rate, defined as the Concretion Equivalent Corrosion Rate (CECR):

$$CECR = \frac{K \times p \times wt\%\ Fe \times d}{t} \qquad [28]$$

where

K = 0.8 for units in mpy

K = 20.32 for units in μm/yr

Note: Density is given on a wet basis whereas iron content is given on a dry basis. The correction factor 1.6 takes this into account.

Based on the results to date, concretion constituent analysis appears to be a viable proxy, minimum-impact method for estimating corrosion rates for steel vessels in seawater. Calculated CECRs between frame numbers 70 and 90 on *Arizona*'s hull are consistent with coupon analysis at frame 75. Although CECR (equation [28]) is based on analyzing concretion from the *Arizona*, further analysis continues at other sites to confirm the correction factor of 1.6 where variables such as temperature, flow velocity, organic activity, pH, salinity, and oxygen concentration may be different (Wilson, et al. 2007). A correction factor for other sites may be derivable from such variables on-site where testing is ongoing, and further refinements to the equation may be necessary.

Correlation with Environmental Parameters and Application to Interior Compartments

The preceding work focused on correlating corrosion rates obtained from direct measurement techniques from hull coupons with corrosion rates calculated from physical and chemical concretion properties on *Arizona*'s outer hull near frame 85. These correlations allow prediction of corrosion rates in other external hull areas directly accessible to researchers for concretion sample removal. A methodology for predicting corrosion rates in inaccessible hull areas, such as the outer hull below the harbor bottom and interior spaces, is also necessary to create a viable FEM of *Arizona*'s hull. While previous work correlates corrosion rate with water depth, it is believed that depth is likely a characteristic that actually represents numerous other physical and chemical properties more directly determinative of the corrosion process itself. Direct correlation with other known corrosion parameters, such as dissolved oxygen concentration, pH, temperature, the ratio of oxygen concentration to concretion thickness, and oxygen and iron mobility through the concretion, is the next step in a holistic evaluation of corrosion on *Arizona*.

Initial work in this area began with preliminary analysis of interior water chemistry data collected with the YSI sonde deployed on the VideoRay ROV. For example, average oxygen levels in Warrant Officers State Rooms 12 and 14 on the second deck, as well as the hallway between them, was about 3 mg/L. Equation [14] gives the corrosion rate as a function of oxygen concentration, diffusion layer thickness and oxygen diffusivity where oxygen reduction is assumed to be the only cathodic reaction. The latter may be a reasonable assumption since concretion is apparently limited in interior compartments and may not support hydrolysis and evolution of hydrogen to the extent that it does on exterior surfaces. Collecting the constants in equation [21]:

$$i_{corr}\,(O_2 \text{ reduction, mpy}) = 5{,}550\ D(cm^2/sec)[C[O_2]\ mg/L]/\ [d(cm)] \qquad [29]$$

where

$$J\ (O_2 \text{ flux, gr/cm2/sec}) = DC(O2)/d$$

Assuming a constant value of d = 0.2 cm for diffusion thickness, D = 2.45 x 10^{-5} and C[O_2] = 3 mg/L, the corrosion rate in interior spaces on the second deck, estimated from equation [29], is 2 mpy.

Over a 61 year period, 0.002 x 61 = 0.12 in., indicating that slightly more than 0.1 in. of bulkhead thickness has corroded away. On 10 lb/ft.^{2} bulkhead plate (¼ in.), this would mean that on average 60% of the plate remains, and within about 15 years, one-half plate thickness will remain. This is a rough estimate but the numbers illustrate the utility of this approach if better information can be obtained with regard to oxygen concentration and concretion thickness in interior compartments.

Oxygen availability is the primary variable driving corrosion and has led the authors to arrive at to two different models related to the role of oxygen in the corrosion process. The first model assumes that both anode and cathode reactions occur at the metal surface and have a direct correlation to oxygen concentration, pH and bacterial activity at the metal/concretion interface and an indirect correlation to numerous environmental parameters at the concretion/seawater interface. The second model, according to MacLeod (1982), assumes that while the anode reaction occurs at the metal surface, the cathode reaction(s) occur in the concretion at or near the concretion/water interface. The basis for these interpretations centers on the concretion and its role as a barrier to the transport of oxygen to the metal surface. Limiting current density (equation [14]) is useful in this discussion to predict the corrosion rate based on local environmental conditions. It should be noted that diffusivity values used in equations [21] and [29] are those of molecular oxygen (O_2) in water assuming that the void spaces are filled with water and allow diffusion of O_2 through a tortuous yet continuous path from sea water to the metal hull surface. The accuracy of the calculated corrosion rate is dependent on the accuracy of the diffusion coefficient (D). For the *Arizona* site, the published value of D at 25° C is used directly. At other sites, however, such as that of the Japanese Midget Submarine submerged off the coast of Oahu in deep, cold water, a correction for D must be made, as outlined above, that includes knowledge of several environmental parameters, including oxygen saturation, salinity, temperature, oxygen concentration, and viscosity. Limiting current density is used in this study as a quantitative methodology to estimate corrosion rate by incorporating a variety of environmental variables mentioned above.

Model 1: Cathode Sited at the Metal Surface

Assuming that the cathode reaction occurs at the metal surface, the value of d or length of the diffusion path for oxygen is approximately equal to the thickness of the concretion. These measurements are obtained *in situ* on the hull or measured later in the laboratory after concretion samples are removed and transported to UNL laboratories. In a typical example given by equation [21], the result for the external hull concludes that the corrosion rate predicted by oxygen consumption is lower than that actually observed by a factor of three. Since oxygen is depleted at the surface and does not satisfy the total demand for electron consumption, the difference is associated with influx of chlorine ions, the formation of HCL, and the lowering of pH. The hydrogen ions gain electrons from iron as it corrodes, and hydrogen gas is released as a result of the combination of two neutralized atoms (equation [4]). Hydrogen accumulates between the concretion and the hull and gradually migrates through the concretion to sea water either by diffusion or by migration through fissures in the concretion. Hydrogen discharge is relatively slow but accelerates in the presence of SRB as discussed above.

These theoretical considerations are summarized in Figure 5.77, a polarization diagram that characterizes Model 1, in which potential (E, SHE, mV) is plotted versus corrosion current or rate (mpy). Anodic polarization (Fe to Fe^{+2} + 2e) is derived from a composite of Tafel expressions (Table 5.35). The composite expression is given by equation [31] and plotted as line (d):

$$E_{corr} = 30 \log(i_{corr}) - 354 \qquad [31]$$

Cathodic polarization resulting from hydrogen discharge is expressed by equation [11] with data derived from Jones (1996:99) where E° = -59.2 pH (mV), β = 100 mV/decade and i° = 0.46 mpy. The result is plotted on Figure 5.77 at pH = 3, 4, 5 and 6, typical values at the metal/concretion interface from Tables 5.7–5.18 and identified by span (c). Span (a) defines the region corresponding to limiting current density or calculated corrosion rate (equation [14]) resulting from oxygen consumption shown by the vertical lines between 0.35 to 1.3 mpy. The actual corrosion rates from coupon data (Figure 5.71) are identified in span (b) between vertical

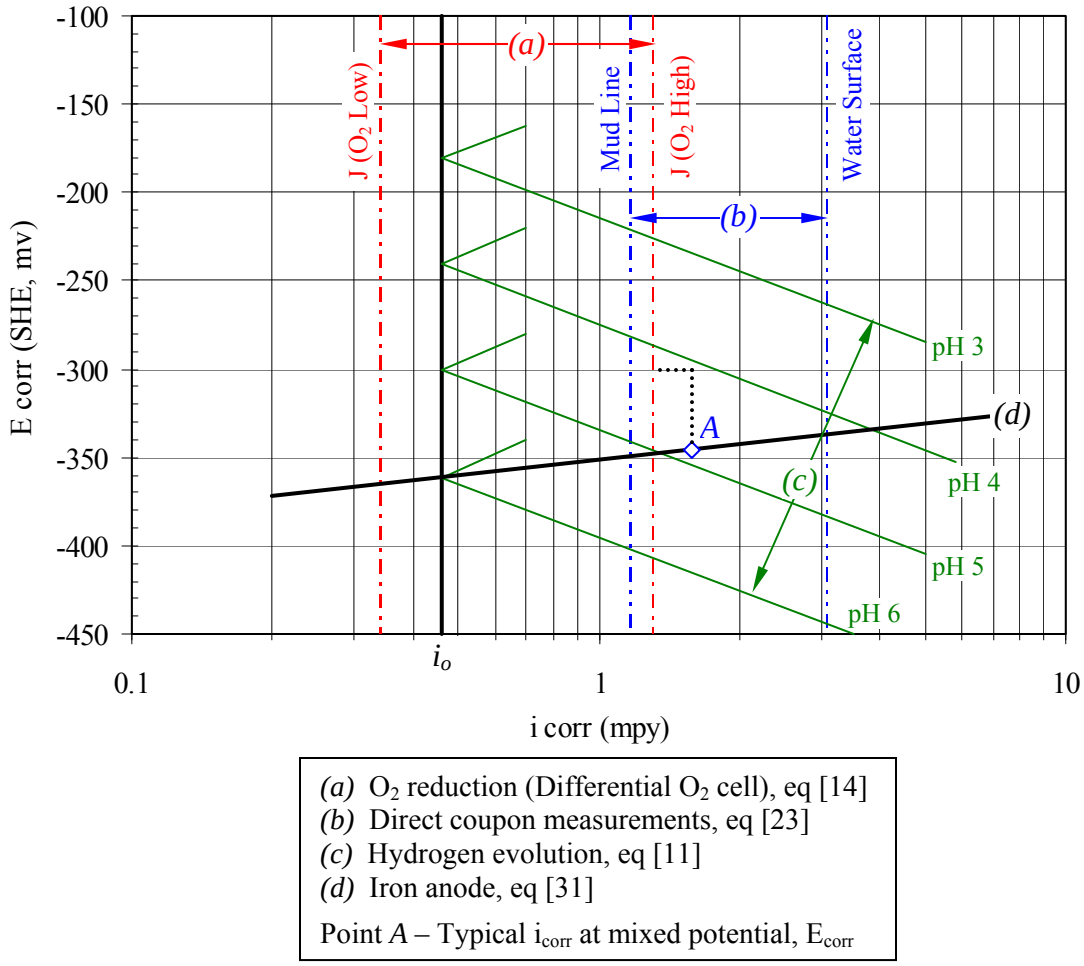

Figure 5.77. A polarization diagram plotting corrosion potential versus corrosion rate.

lines at near 1.2 and 3 mpy. Two cathodic reactions support corrosion and mixed potential theory shows a typical corrosion rate at point A. Point A lies on the dotted line representing interaction between oxygen reduction and hydrogen discharge at its point of intersection with anodic polarization, line (d). At the mixed potential, resulting typical values of E_{corr} and i_{corr} are shown in span (b). There is a wide variation in concretion thickness from the surface to the harbor bottom (Figure 5.78). According to equation [14], i(L) is inversely proportional to concretion thickness, hence oxygen concentration at the surface is highly variable from point to point promoting differential oxygen cell corrosion. As a result, oxygen flux (J) is identified corresponding to low and high availability of oxygen (Figure 5.77). The result is differential oxygen cell corrosion as discussed in an earlier section. There is a wide variability in pH at the

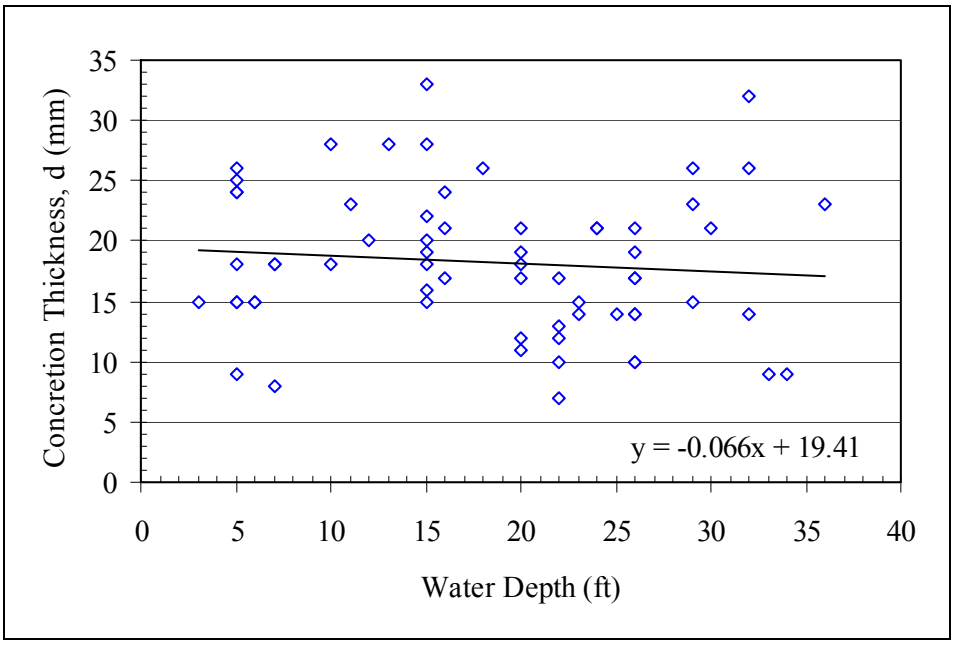

Figure 5.78. Concretion thickness as a function of water depth.

metal concretion interface with minimum pH at the sites where the concretion thickness is greatest (Figure 5.79). As oxygen consumption continues, the net oxygen level remains low on the metal surface and hydrolysis continues to maintain acidic conditions at the metal surface.

In review, oxygen consumption alone does not support the actual corrosion rates of between 1 and 3 mpy. The result concluded from this analysis is that hydrogen discharge is significant in controlling the rate of corrosion at a majority of sites on *Arizona*, although the driving force is the availability of oxygen at the concretion/metal interface as dictated by the oxygen concentration and thickness of the concretion at a particular location on the hull. The evidence for hydrogen discharge is quite evident from on-site observations of gaseous bubbles emerging from concretion and from the low pH values obtained from *in situ* data collected at numerous sites around the hull. During one field operation, a drill hole through concretion resulted in a significant flow outward of water as the bit was withdrawn. As the water poured out of the hole, it made contact with surrounding water at a pH of approximately 8. The result was immediate precipitation of iron as iron hydroxide (discussed above).

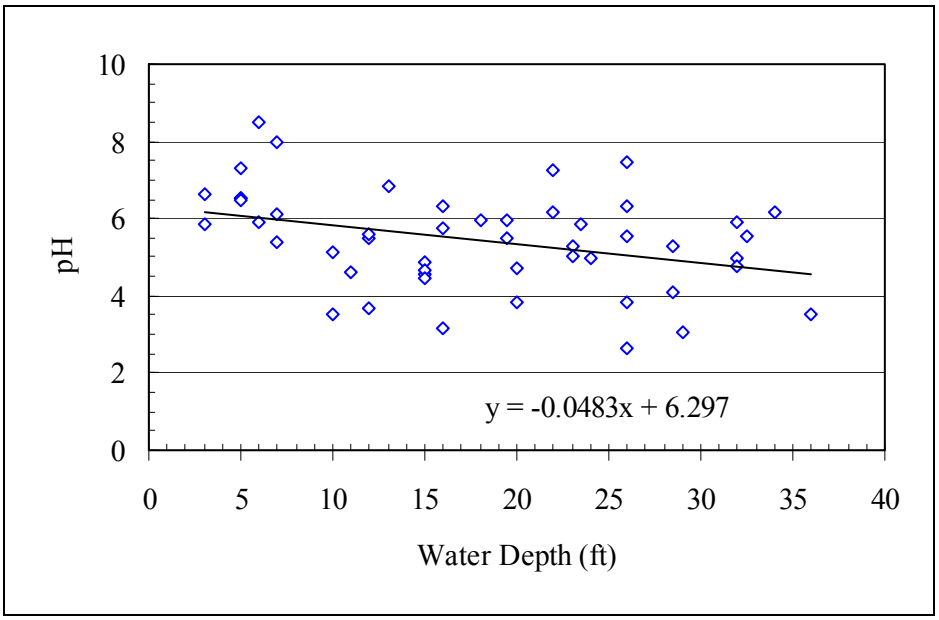

Figure 5.79. pH at metal/concretion interface as a function of water depth.

Model 2: Cathode Sited in Concretion

As mentioned above, MacLeod (1982) and North (1976) identify the concretion/seawater interface as the site for cathodic oxygen reduction. To carry this concept a step further, if the cathodic reaction takes place inside the concretion, a value of d can be determined from equation [14] that will satisfy a known value of i_{corr}. For example, solving equation [14] for d knowing C and i(L) (i_{corr}) in mpy, a diffusion thickness of d = 0.6 cm allows adequate oxygen diffusion to support a corrosion rate of 1.4 mpy without hydrogen discharge. There are several issues that make this model attractive in addition to the calculations above. Based on readings taken during *in situ* drilling and measurement sequences, the steel surface E_{corr} is consistently negative to readings taken inside the concretion and at the seawater/concretion interface. This would suggest that cathodic oxygen reduction could occur at the concretion/sea water interface or inside the concretion. Based on concretion properties, it has been determined that retained water is on the order of 20-30 wt %. Assuming there is continuity of path from open seawater to the hull surface, the concretion is an ionic conductor, and hence iron ions can migrate from the hull surface through the concretion to seawater, with chlorine ions migrating in the opposite direction. What is missing in this model is the ability of the concretion to conduct electrons.

Electrons are released during corrosion, and in order to maintain charge balance during oxidation of iron to Fe^{+2}, these electrons must be consumed at cathode sites. Since neither water nor concretion minerals conduct electrons, the cathode and anode must be located adjacent to each other on the metal surface or connected electrically somehow through a conducting path. The former seems to be the only feasible explanation.

Summary

Model 1, preferred by the authors, was not considered for some time as a reasonable explanation of factors controlling corrosion of *Arizona*, and Model 2, proposed by MacLeod, prevailed. Model 1 was reconsidered, however, upon a detailed analysis of a Japanese Midget Submarine, submerged in 1300 ft. of water just outside the entrance to Pearl Harbor (Wilson, et al. 2007). Applying the environmental parameters specific to that site to equation [14], it was concluded that oxygen does satisfy the demand for electron consumption in deep water at the Midget Submarine site, whereas just the opposite is the case on *Arizona* in shallow water. The major difference between the two is concretion thickness. On *Arizona*, concretion thickness averages about 2 cm, but with wide variability, whereas the Midget Submarine concretion thickness averages 0.4 cm, with much less variability. Based on equation [14] and XRD data, it has been proposed that the corrosion rate on the Midget Submarine is limited by the formation kinetics of minerals in the concretion (Wilson, et al. 2007). As a result of data comparisons on these submerged vessels, i(L) (equation [14]) has become an important marker to determine controlling factors at differing geographical and sea depth locations. Oxygen availability is the primary variable that determines how fast corrosion will proceed. For relatively short term exposure to sea water, oxygen concentration at the steel surface is the same as oxygen concentration in the open water and dictates the corrosion rate. However, for long term exposure at moderate water depth where marine organisms exist, concretion accumulation creates a barrier to oxygen permeation and the chemistry at the metal surface beneath the accumulating concretion becomes much different that it would be in the absence of concretion. pH and E_{corr} have been determined at the interface by drilling through the concretion to the metal surface. Although there are limitations to this approach because of unavoidable dilution in the drill hole, the results provide insight into the corrosion process and have lead to the conclusion that three

processes occur to establish a steady state corrosion rate. Cathodic reactions include hydrogen discharge and oxygen reduction or consumption. The two combine to create a mixed corrosion potential and corresponding corrosion rate. As oxygen consumption continues, low oxygen is maintained at the metal surface. Differential oxygen cell corrosion is a contributing factor because of locally large variations in concretion thickness (Figure 5.78). An attempt has been made to characterize these processes on the polarization diagram (Figure 5.77). To further understand these interactions, a spectroscopic study of metal/concretion interface chemistry is recommended for future study.

CONCLUSIONS

CONCRETION ANALYSIS

Concretion acts as a sink for iron corroded from the adjacent steel hull, accounting at one location for about 60% of the iron lost from the hull. Based XRD data, iron appears primarily as iron carbonate with lesser amounts of magnetite. These observations are confirmed from *in situ* E_{corr} and pH measurements by superimposing the data on a calculated potential/pH Pourbaix diagram. The data corresponds to fields stable with respect to iron carbonate and magnetite.

Based on a variety of data and methods of analysis, a comprehensive understanding of corrosion processes occurring on the hull above the harbor bottom has been accomplished. With this information as background, analysis of corrosion at and below the harbor bottom and in interior compartments can be inferred, however, research should continue to further refine calculated corrosion rates on inaccessible hull components.

XRD of concretion reveals the compounds $FeCO_3$, $CaCO_3$ and Fe_3O_4. A mean iron content of 53% is calculated from ESEM data while XRF reveals 43% on a different sample. Direct chemical analysis of the same sample used for XRD reveals comparable iron content. Superposition of E_{corr}/pH data on the water-iron-CO_2 system confirms the presence of siderite and magnetite from the steel hull through the concretion cross-section to sea water. Results indicate that concretion characteristics vary as a function of water depth. Studies continue to correlate these properties with iron content and corrosion rate. The relationship between CECR

and the limiting current corrosion rate (equation [14]) have lead to a more comprehensive understanding of the corrosion process on *Arizona*.

CORROSION RATE

Sufficient data at exterior hull locations are now available to determine corrosion rates from the water surface to the harbor bottom, port and starboard. While hull coupon sampling was only undertaken at frame 75, previous E_{corr} transect surveys indicate that this data is typical of corrosion rates anywhere along the hull in contact with sea water above the harbor bottom. Corrosion rate data in Table 5.34 suggest that the corrosion rate is slightly higher on the port side above about 20 ft.—below that, the rates converge to equivalent values. On the exterior hull, the corrosion rate follows the empirical equation derived from the best fit for combined data, port and starboard, which is valid to just above the harbor bottom:

$$i_{corr} = 2.956 - 0.050\ WD) \quad [31]$$

where

i_{corr} is the corrosion rate in mpy
WD is water depth in ft.

As a heuristic device, based on this data, time interval from August 2002 until the plate thickness is reduced to one–half its original thickness can be determined. One–half original thickness was arbitrarily taken as a thickness below which structural integrity is severely compromised, although the FEM provides a more precise value (see Chapter 6). At 5 ft., port, 27% of 20 lb. plate remains whereas at 5 ft. starboard, 40% of 20 lb. plate remains. Both sides have exceeded the one-half thickness criteria. At 19½ ft., port, 77% of 37½ lb. plate remains whereas at 15 ft., starboard, 90% of 37½ lb. plate remains. These data translate to time to one–half thickness of 130 years, port, and nearly twice that time, starboard. At 26 ft., port, 87% of 20 lb. plate remains whereas at 22 ft., starboard, 81% of 20 lb. plate remains. These data translate to time to one–half thickness of 160 years, port, and about 90 years, starboard. Below the harbor bottom at 34 ft., port, 90% of 25 lb. plate remains whereas at 32½ ft. starboard, 87%

of 30 lb. plate remains. These data translate to time to one–half thickness of 220 years port, and 170 years starboard.

Based on metal coupon analysis at frame 75, the corrosion rate on the USS *Arizona*'s exterior hull is approximately 3.0 mpy near the surface and decreases by nearly one third to about 1.0 mpy just below the harbor bottom. By comparison, corrosion rates for unconcreted steel in open seawater at the surface are reported to be in the 4–8 mpy range (Schumacher 1979:xx). Lower than predicted corrosion rates are directly related to metal concretion interaction, and subsequent decreased oxygen availability.

Oxygen availability, as related to direct cathodic oxygen reduction and differential oxygen cell corrosion, is the most significant variable in the corrosion process on the hull. Electrical conductivity and cation/anion transport through the concretion are also important variables. Depletion of oxygen at the steel/concretion interface leads to hydrolysis and a decrease in pH. At numerous sites, E_{corr} relative to SHE is below the potential required for hydrogen reduction, so it is not surprising to observe hydrogen evolution around the hull. Corrosion rate and E_{corr} decrease with water depth, as is consistent with a decreasing oxygen concentration to the harbor bottom. The observation that E_{corr} increases as i_{corr} increases confirms the original observation made by MacLeod (2002). Oxygen concentration inside the torpedo blister decreases into the harbor bottom, suggesting the same behavior occurs beneath the harbor bottom. Calculated limiting current density is used as a diagnostic tool to identify the role of oxygen consumption and hydrogen discharge in the corrosion process. For assessing corrosion rate of *Arizona*'s hull, direct measurement of hull thickness and comparing to original thickness is the most accurate methodology, but obviously it is impractical for quick and cost effective assessment. An alternative methodology developed on USS *Arizona* by University of Nebraska –Lincoln researchers, CECR, is beginning to prove itself in this and other applications as a minimum-impact approach for assessing corrosion rate.

The deterioration rate of *Arizona*'s hull will increase with time because corrosion from both sides of hull plate will accelerate due to the entry of fresh sea water from the top down. Steel-hull coupon samples USAR-02-001 and USAR-02-007 have reached the one-half thickness criteria and there is evidence that this is already beginning to occur on USAR-02-002. The predictions of corrosion to one-half thickness in 200 years or more on the originally thickest plate are probably optimistic in view of the accelerated corrosion that will occur with time from

the top down. It should be emphasized that corrosion rates are reported as uniform average values although localized shallow pitting is evident.

At the harbor bottom and below, where most of the fuel oil is bunkered, steel-hull coupon samples USAR-02-004 and USAR-02-010 show that the corrosion rate remains constant or increases somewhat, consistent with potential increased bacterial activity in this region. How far this region extends into the harbor bottom is unknown, although current evidence suggests that corrosion rates below the harbor bottom and in interior compartments of *Arizona* remain low.

REFERENCES

Anonymous
1975 *Metals Handbook, Failure Analysis and Prevention*. 8th ed 10. American Society for Metals.

Cook, E.
1937 *Open Hearth Steel Making*. ASM International, Cleveland.

DeAngelis, R.
2002 *X-Ray Diffraction and Environ mental Scanning Electron Microscope Investigation of Concretion from the USS Arizona*. Manuscript on File at National Park Service, Santa Fe.

Felkins, K., J. Leighly, H.P and A. Jankovic
1998 The Royal Mail Ship Titanic: Did a Metallurgical Failure Cause a Night to Remember? *Journa of Metals* 50(1):12-18.

Fontana, M. G.
1986 *Corrosion Engineering*. 3rd ed. McGraw-Hill, New York.

Gregory, D.
1999 Monitoring the Effect of Sacrificial Anodes on the Large Iron Artefacts on the Duart Point Wreck, 1997. *International Journal of Nautical Archaeology* 28(2):164-173.

Henderson, S.
1989 Biofouling and Corrosion Study. In *Submerged Cultural Resources Study: USS Arizona Memorial and Pearl Harbor National Historic Landmark*, edited by D. J. Lenihan, pp. 117-156. Submerged Resources Center Professional Papers No. 9. National Park Service, Santa Fe.

Husler, J. and C. Dodson
2003 *X-Ray Fluorescence Analysis of Concretion*. Manuscript on File at National Park Service, Santa Fe.

Johnson, D. L., J. D. Makinson, R. DeAngelis, B. M. Wilson and W. N. Weins
2003 *Metallurgical and Corrosion Study of Battleship USS Arizona, USS Arizona Memorial, Pearl Harbor*. Manuscript on File at National Park Service, Santa Fe.

Johnson, D. L., W. N. Weins and J. D. Makinson
2000 Metallographic Studies of the U.S.S. Arizona. In *Microstructural Science Vol. 27: Understanding Processing, Structure, Property, and Behavior Correlations*, edited by W. N. Weins, pp. 85-91. ASM International, New York.

Johnson, D. L., B. M. Wilson, J. D. Carr, M. A. Russell, L. E. Murphy and D. L. Conlin
2006a Corrosion of Steel Shipwrecks in the Marine Environment: USS Arizona - Part 1. *Materials Performance* 45(10):40-44.

2006b Corrosion of Steel Shipwrecks in the Marine Environment: USS Arizona - Part 2. *Materials Performance* 45(11):54-57.

Jones, D. A.
1996 *Principles and Prevention of Corrosion*. 2nd ed. Prentice Hall, New York.

Kerr, R. A.
2001 Life-Potential, Slow, or Long Dead. *Science* 294(5548):1820-1821.

Korb, L. J.
1987 *Metals Handbook: Volume 13, Corrosion*. 9th ed. American Society for Metals.

Lenihan, D. J. (editor)
1989 *Submerged Cultural Resources Study: USS Arizona Memorial and Pearl Harbor National Historic Landmark*. Submerged Resources Center Professional Papers No. 9. National Park Service, Santa Fe.

Little, B. J., R. I. Ray and R. K. Pope
2000 Relationship Between Corrosion and the Biological Sulfur Cycle: A Review. *Corrosion* 56(4):433-443.

MacLeod, I. D.
1982 The Electrochemistry and Conservation of Iron in Sea Water. *International Journal of Nautical Archaeology and Underwater Exploration* 2(4):267-275.

1987 Conservation of Corroded Iron Artifacts – New Methods for On-Site Preservation and Cryogenic Deconcreting. *International Journal of Nautical Archaeology and Underwater Exploration* 16(1):49-56.

1989 Electrochemistry and Conservation of Iron in Sea Water. *Chemistry in Australia* 56(7):227-229.

1995 *In Situ* Corrosion Studies on the Duart Point Wreck, 1994. *International Journal of Nautical Archaeology* 24(1):53-59.

2002 In Situ Corrosion Measurements and Management of Shipwreck Sites. In *International Handbook of Underwater Archeology*, edited by C. V. Ruppe and J. F. Barstad, pp. 697-714. Kluwer Academic/Plenum Publishers., New York.

Makinson, J. D., D. L. Johnson, M. A. Russell, D. L. Conlin and L. E. Murphy
2002 In situ corrosion studies on the battleship USS Arizona. *Materials Performance* 41(10):56-60.

Mardikian, P.
2004 Conservation and Management Strategies Applied to Post-Recovery Analysis of the American Civil War Submarine H. L. Hunley (1864). *International Journal of Nautical Archaeology* 33(1):137-148.

McCarthy, M.
1988 S.S. Xantho: The Pre-Disturbance, Assessment, Excavation and Management of an Iron Steam Shipwreck off the Coast of Western Australia. *International Journal of Nautical Archaeology and Underwater Exploration* 17(4):339-347.

New-York-Navy-Yard
1913 Correspondence. National Archives and Records Administration, North East Region, New York.

North, N. A.
1976 Formation of Coral Concretions on Marine Iron. *International Journal of Nautical Archaeology and Underwater Exploration* 5(3):253-258.

North, N. A. and I. D. MacLeod
1987 Corrosion of Metals. In *Conservation of Marine Archaeological Objects*, edited by C. Pearson, pp. 68-98. Butterworth & Co., London.

Pourbaix, M.
1974 *Atlas of Electrical Chemical Equilibria in Aqueous Solutions*. National Association of Corrosion Engineers, Houston.

Russell, M. A., D. L. Conlin, L. E. Murphy, D. L. Johnson, B. M. Wilson and J. D. Carr
2006 A Minimum-Impact Method for Measuring Corrosion Rate of Steel-Hulled Shipwrecks in Seawater. *International Journal of Nautical Archaeology* 35(2):310-318.

Saveur, A.
1935 *The Metallography and Heat Treatment of Iron and Steel*. McGraw-Hill, New York.

Schumacher, M. (editor)
1979 *Sea Water Corrosion Handbook*. Noyes Data Corporation, Park Ridge, NJ.

Uhlig, H. H. and R. W. Revie
1985 *Corrosion and Corrosion Control*. 3rd ed. John Wiley & Sons, New York.

Wilson, B. M., D. L. Johnson, H. Van Tilburg, M. A. Russell, L. E. Murphy, J. D. Carr, R. J. DeAngelis and D. L. Conlin
2007 Corrosion Studies on the USS Arizona with Application to a Japanese Midget Submarine. *Journal of Metals* 59(10):14-18.

Yiming, X., W. N. Weins and A. Dhir
1992 A Metallographic Investigation of Banding Diffusion of Phosphorous in Steels. In *Microstructural Science* 20. ASM International, New York.

CHAPTER 6

Finite Element Modeling of USS *Arizona*

Timothy J. Foecke and Li Ma

INTRODUCTION

A computer-based engineering model has been constructed of an 80-ft. midships section of the wreck of USS *Arizona* in an attempt to determine the current condition of the wreck and predict its future strength as it continues to corrode. This model incorporates the findings from other components of the study, corrosion rates, structural surveys, soil testing and analysis of the concretion, into a single tool that can be used to predict how the wreck will continue to degrade.

FINITE ELEMENT MODELING

The methodology chosen for this work is finite element analysis (FEA), also known as finite element modeling (FEM). In this technique, the body under study is mathematically divided into many thousands of smaller pieces called elements. Each element is given a location, a proximity to other elements, its own mechanical properties and details about how it is connected to its neighbors and how it is allowed to deform and move. Once the structure is built of these elements in the computer, loads are applied to the model and boundary conditions are set to restrain movement. The results of the model are predictions of the deformations and

deflections that will result from that loading, as well as predictions of the stresses that each element, and thus each piece of the body, will experience.

BUILDING THE MODEL

Rather than model the entire ship at a much coarser level, it was decided to choose a representative section of the ship to model with higher precision. The section of the wreck adjacent to the monument, between frames 70 and 90, was selected for several reasons. First, as will be seen, detailed original ship's plans are readily available for this portion of the ship. Accurate original plans are a necessary starting point for constructing a viable, accurate model. Second, the blast from the bomb detonated in the forward magazines and sank the ship, at least in film evidence examined, seems to have primarily vented up the main stack as it moved aft, and thus the region from frames 70 to 90 were likely less damaged below decks than regions further forward, although historical evidence suggests there was damage evident as far back as frame 78 (see Chapter 3). Nonetheless, this region of the ship likely experienced effects from the blast and subsequent fire, which may elevate corrosion rates compared to unaffected areas (see Chapter 5). Modeling this section of the ship therefore builds an element of conservatism into the model. Finally, this region of the ship is primarily composed of engine spaces below and working spaces above, and it is free from massive structures such as main gun barbettes that would make the results more difficult to generalize to other regions of the ship.

The National Park Service (NPS) Submerged Resources Center (SRC) provided the National Institute of Standards and Technology (NIST) with as many blueprints of *Arizona*'s design as available that showed the main construction details and layout of the load-bearing elements and interior spaces (Figure 6.1). Many more drawings of the smaller details of junctions and fittings were not used, as at the scale of the model the connections between major parts of the ship would need to be idealized and not modeled at the rivet level. Unfortunately, several pieces of information regarding the internal configuration of the ship, particularly the detailed placement of floor beams and wall columns and their dimensions, were not found in the drawings. Transverse sections of the ship at frames 75 and 93 gave some finer structural details (Figure 6.2), and these combined with the individual deck plans and the midships longitudinal

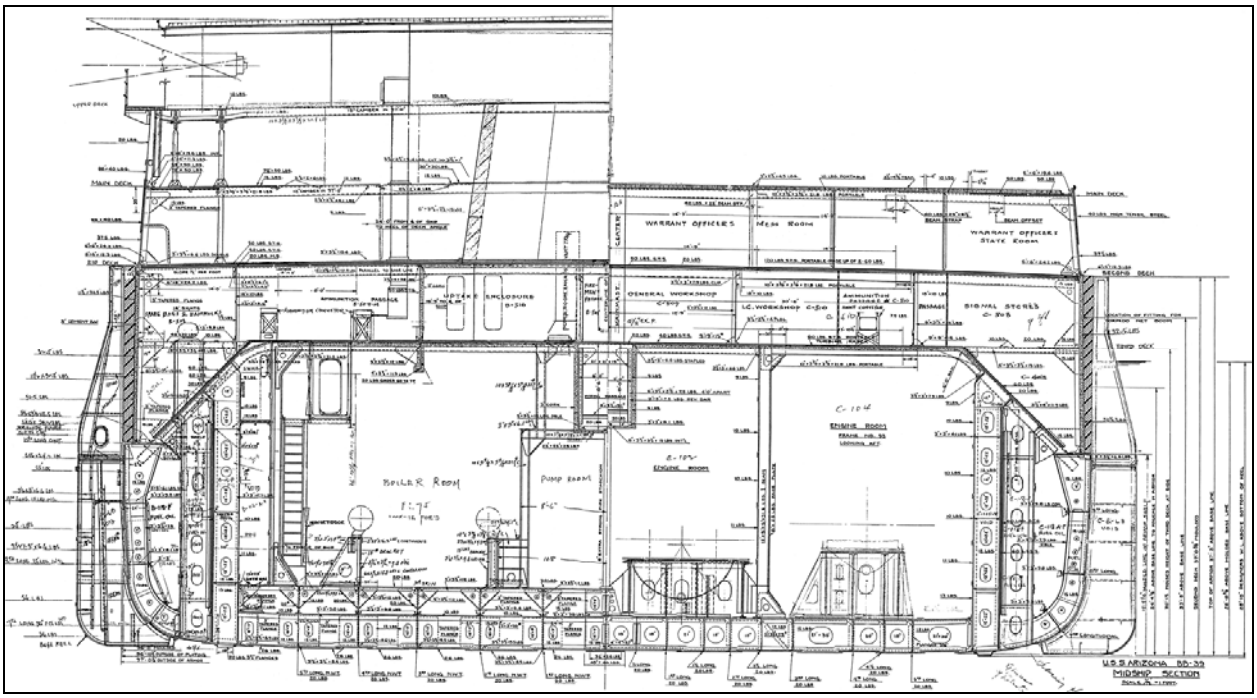

Figure 6.1. Example of as-received blueprint showing a composite frame section of frame 75 looking forward (left) and frame 93 looking aft (right) (USS *Arizona* Memorial Archive).

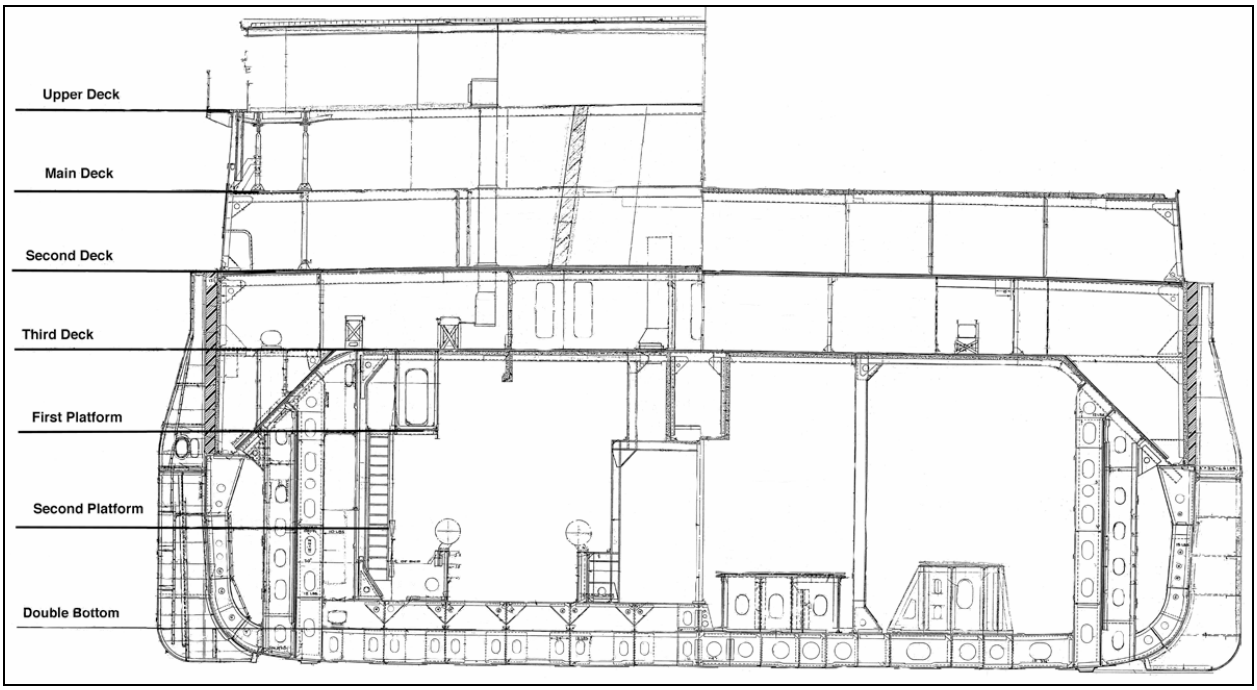

Figure 6.2 Example of cleaned blueprint showing a composite frame section of frame 75 looking forward (left) and frame 93 looking aft (right) with decks indicated (NIST Graphic).

section (Figure 6.3) allowed for reasonable assumptions about the location and dimensions of all load-bearing components to be made. As mentioned, the connections between these components were idealized to speed running of the model. In effect, the component connections were entered as if two components being joined were simply made of one piece of metal. Because riveted connections are designed to be stronger than either constituent that makes up the joint, this is a reasonable assumption. Details from archeological surveys of the wreck as to broken connections, missing deck plate and any other damage to the load bearing structures were added as modifications to the as-built design in the model. This process brought the model from its as-built state to approximate its present condition.

The model was meshed at a level of detail that can be seen in Figure 6.4. After initial runs of the FEM, if certain areas of the model were found to not converge to a satisfactory result, the area was remeshed more finely until the solutions converged. If there were areas that did not show large changes in stress as the ship corroded, these could be remeshed with coarser elements, again saving computational time. The sequence of layers of the model build is shown in Figures 6.5–6.21.

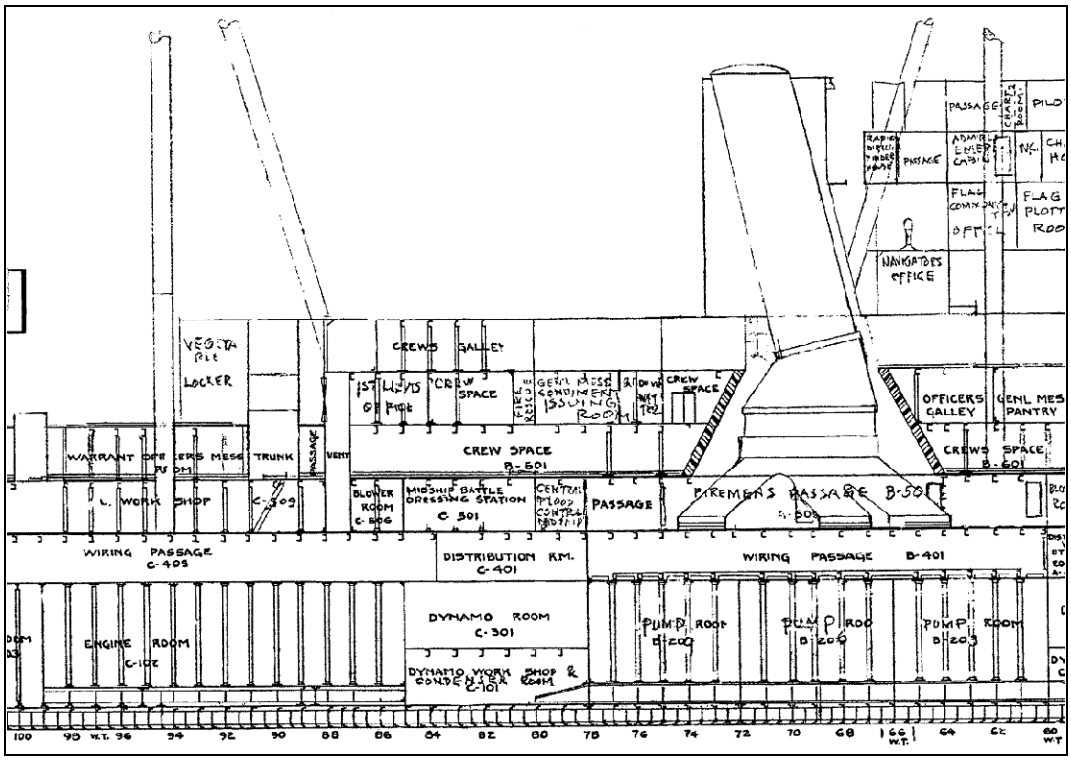

Figure 6.3. Midsection cutaway of the region from frame 60 to 100, showing beams and girders (USS *Arizona* Memorial Archive).

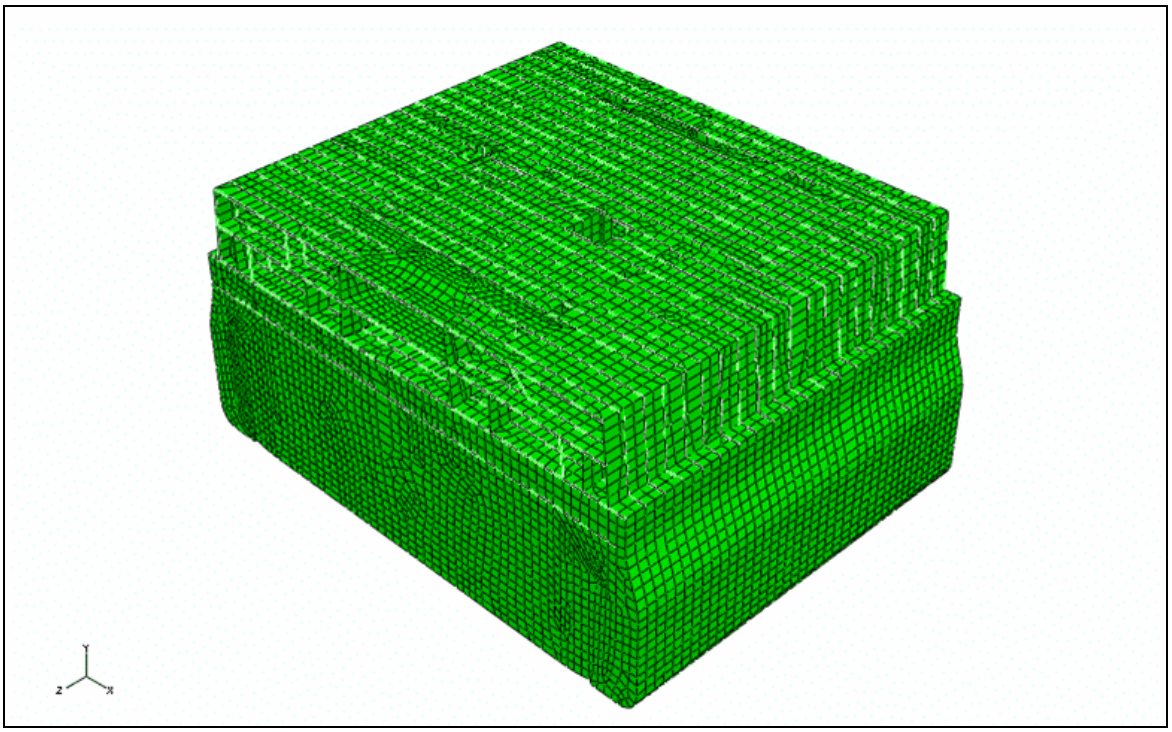

Figure 6.4. Image showing the level of meshing on the FEM. The model contains roughly 57,000 elements and 255,000 degrees of freedom, roughly equivalent to the NIST models of the collapse of World Trade Center towers 1 and 2 (NIST Graphic).

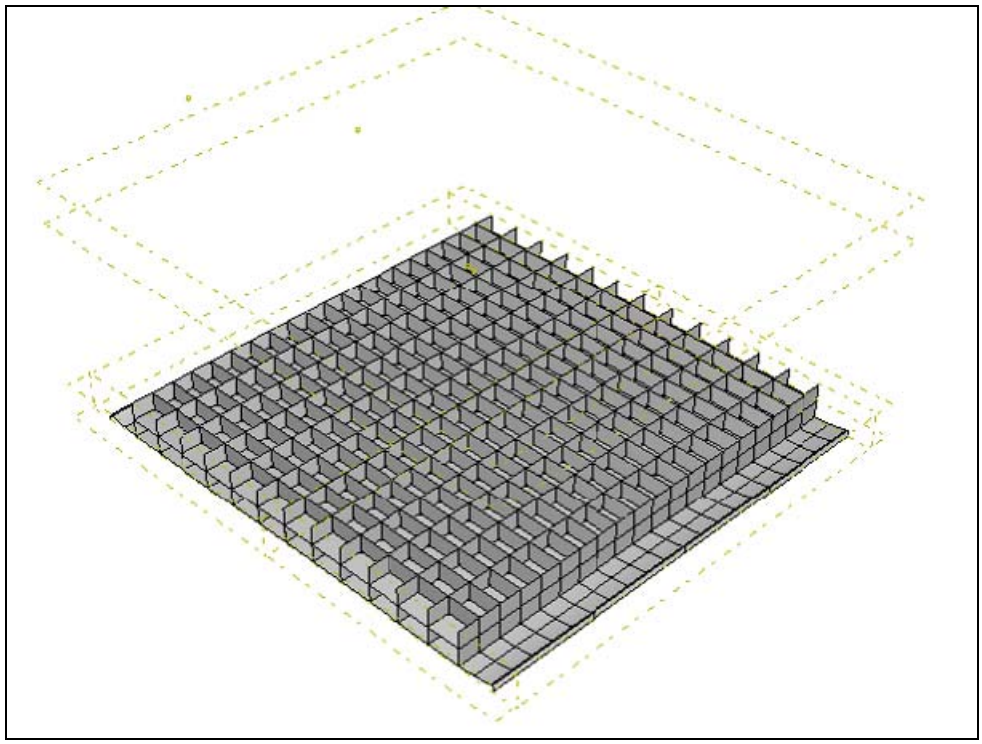

Figure 6.5. Model cutaway showing addition of double bottom framing to hull bottom (NIST Graphic).

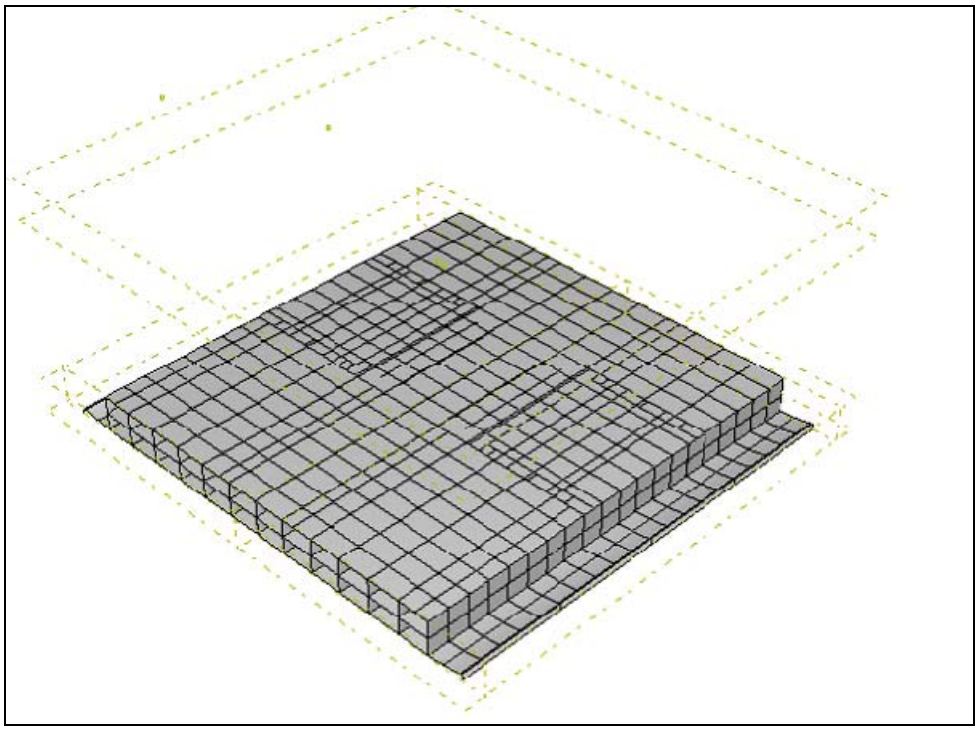

Figure 6.6. Model cutaway showing addition of hold platform decking to double bottom framing (NIST Graphic).

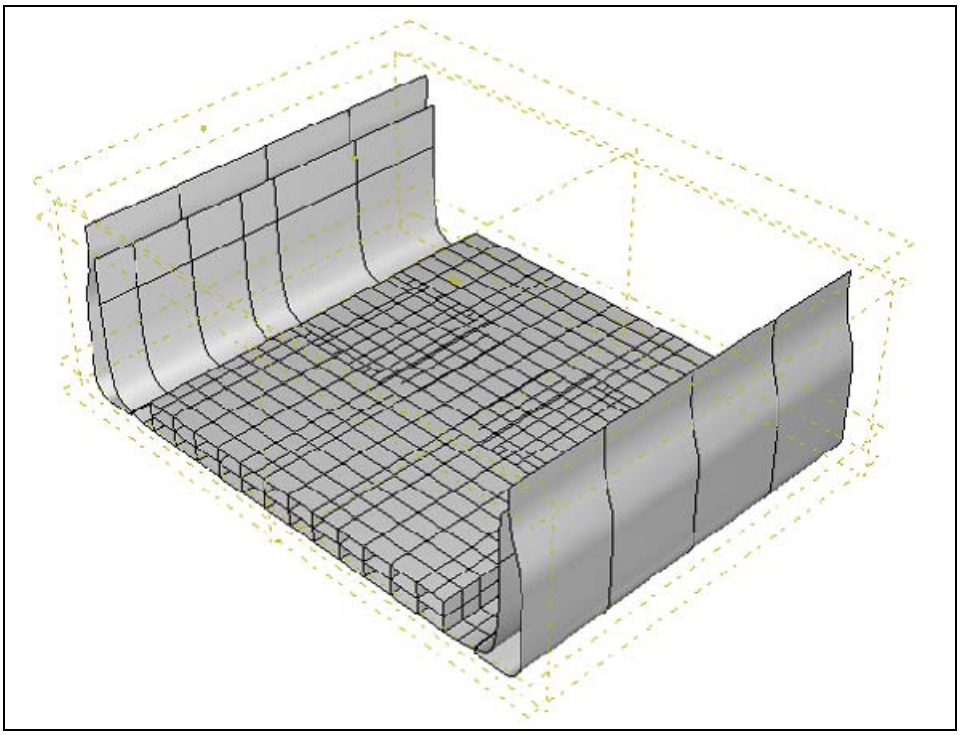

Figure 6.7. Model cutaway showing addition of side shell and torpedo blisters (NIST Graphic).

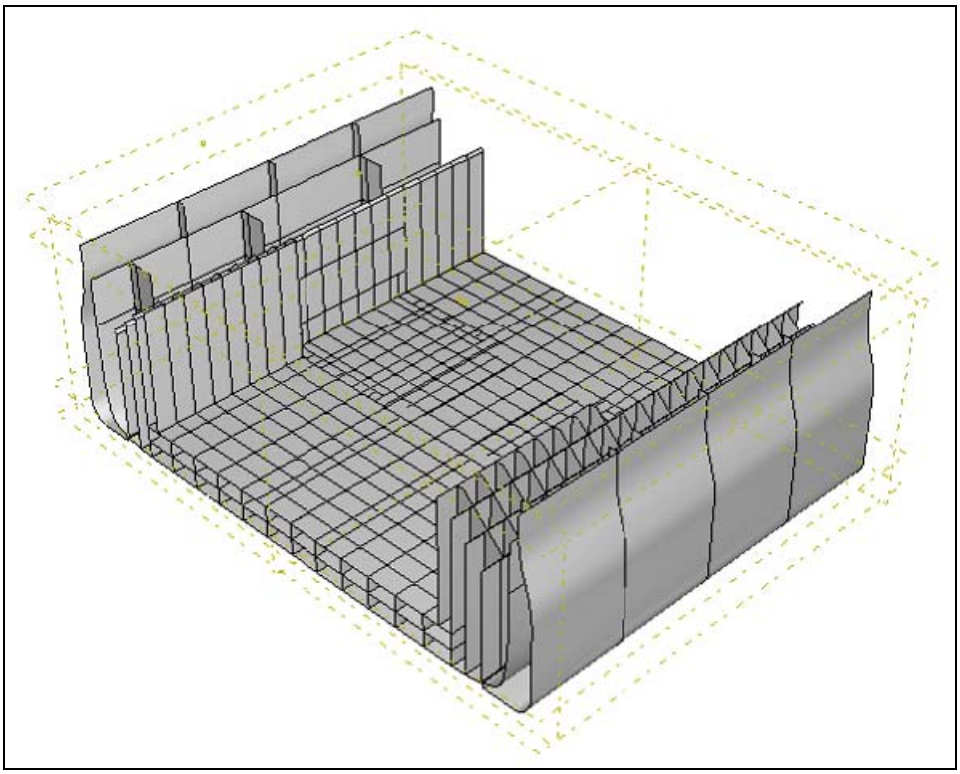

Figure 6.8. Model cutaway showing addition of side oil tanks (NIST Graphic).

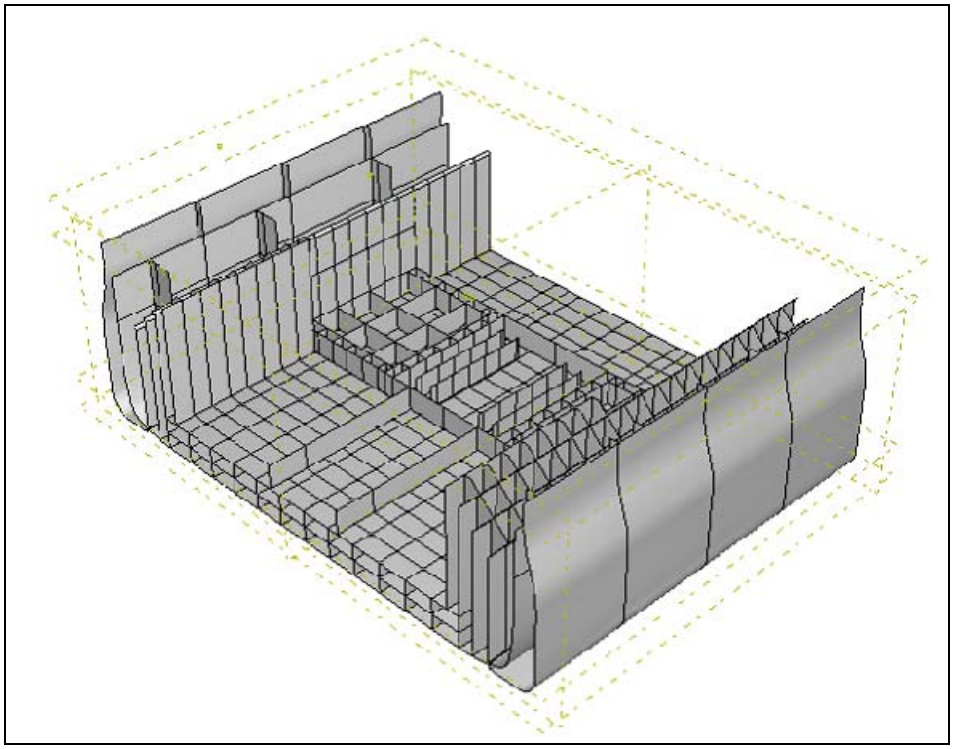

Figure 6.9. Model cutaway showing addition of bulkheads between hold platform and second platform (NIST Graphic).

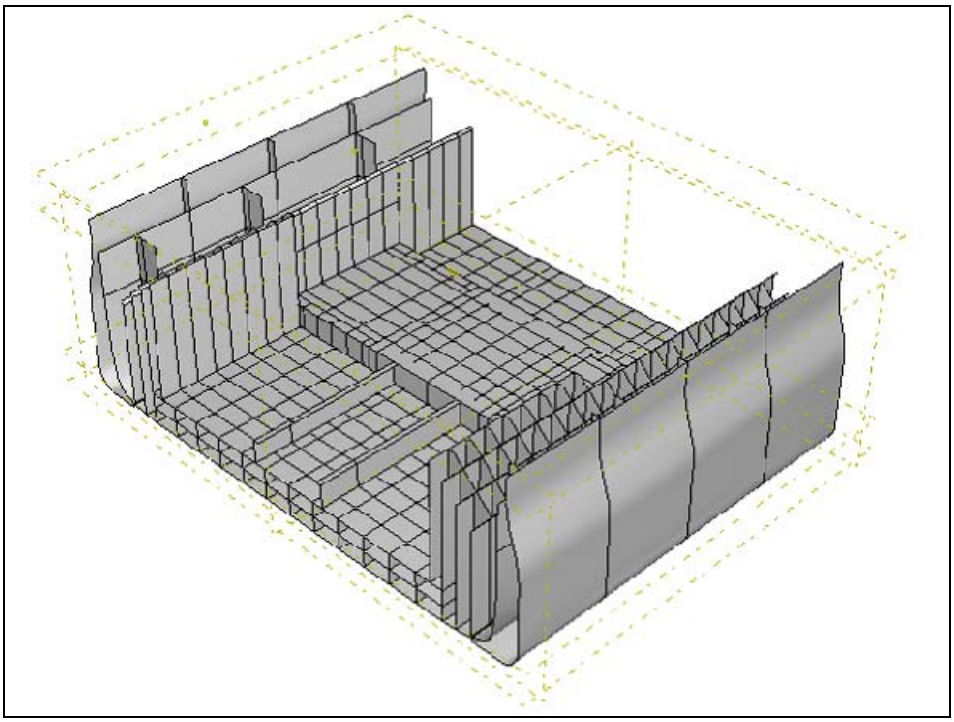

Figure 6.10. Model cutaway showing addition of second platform decking (NIST Graphic).

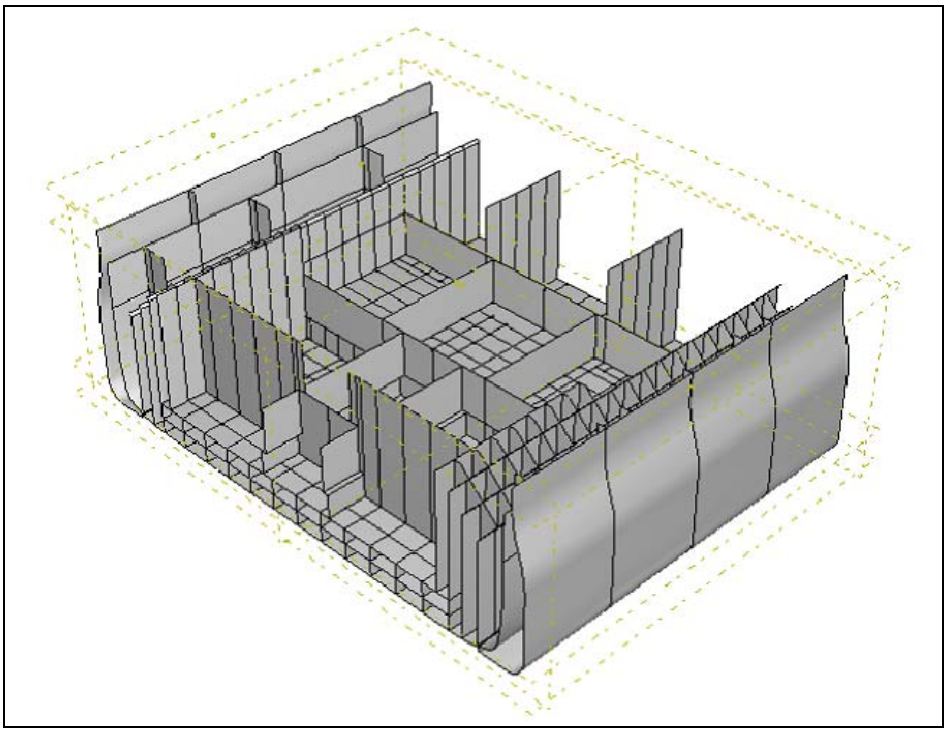

Figure 6.11. Model cutaway showing addition of bulkheads on the first platform and the third deck (NIST Graphic).

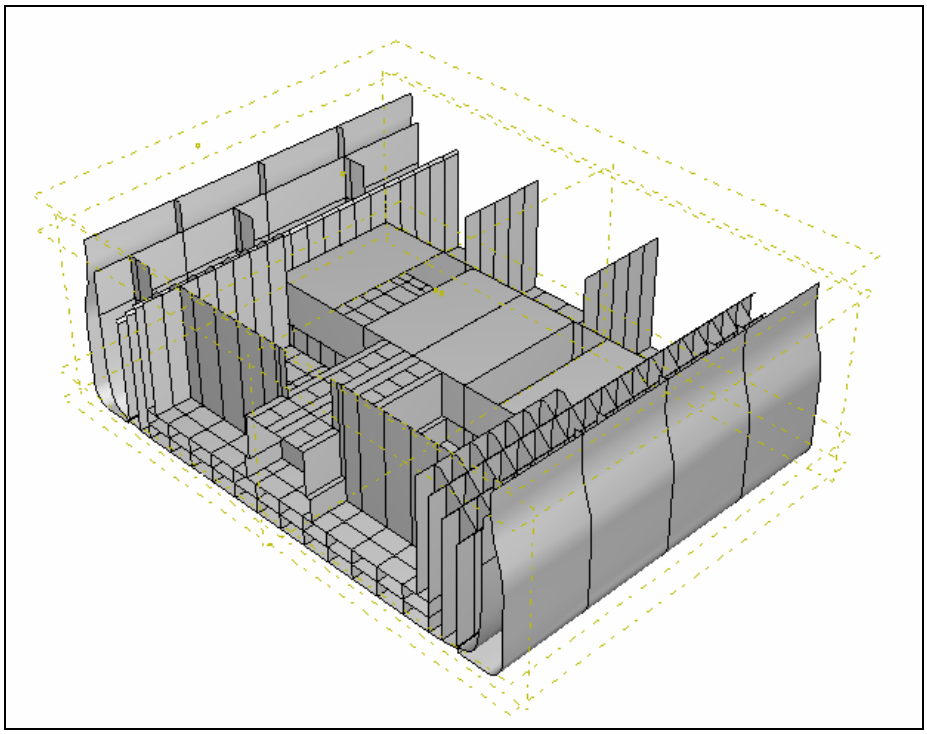

Figure 6.12. Model cutaway showing addition of first platform deck plating (NIST Graphic).

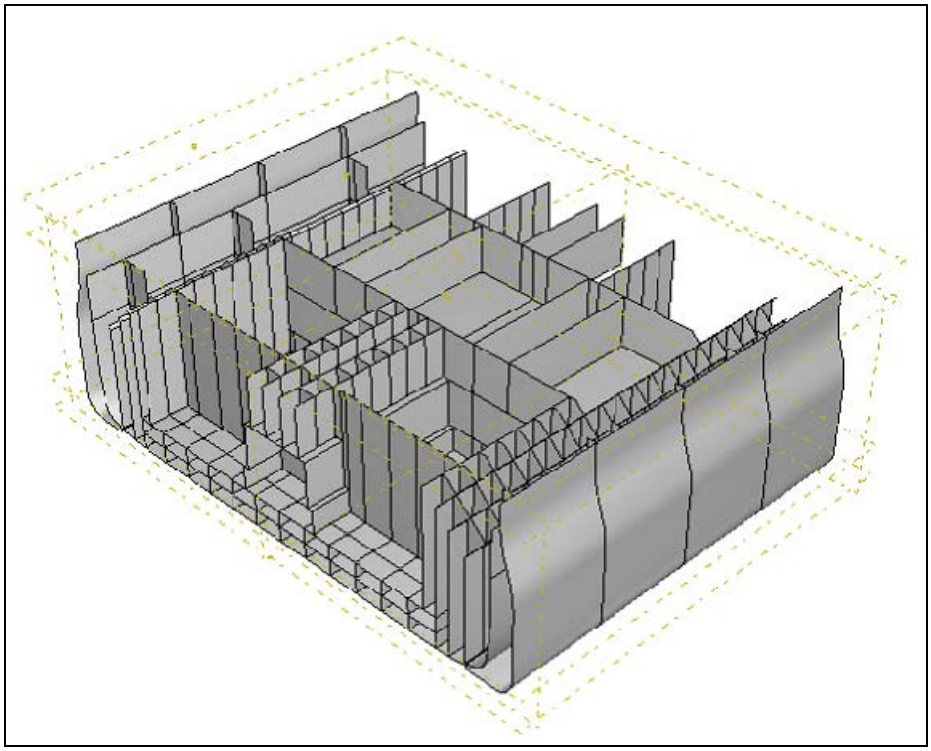

Figure 6.13. Model cutaway showing addition of bulkheads between first platform and the third deck (NIST Graphic).

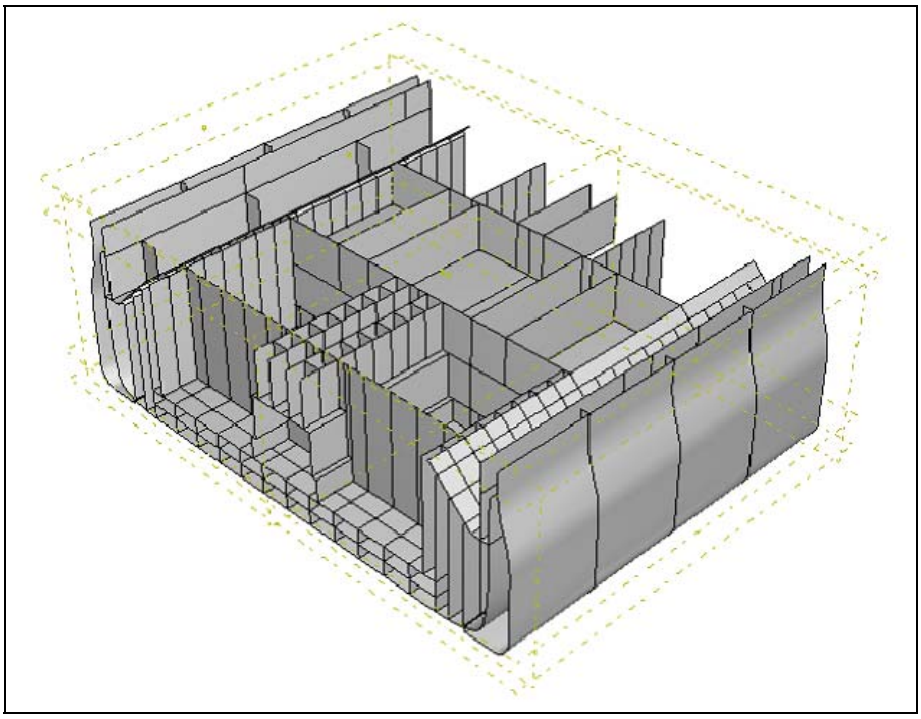

Figure 6.14. Model cutaway showing addition of the side shell armor belt and the tops of the side oil tanks (NIST Graphic).

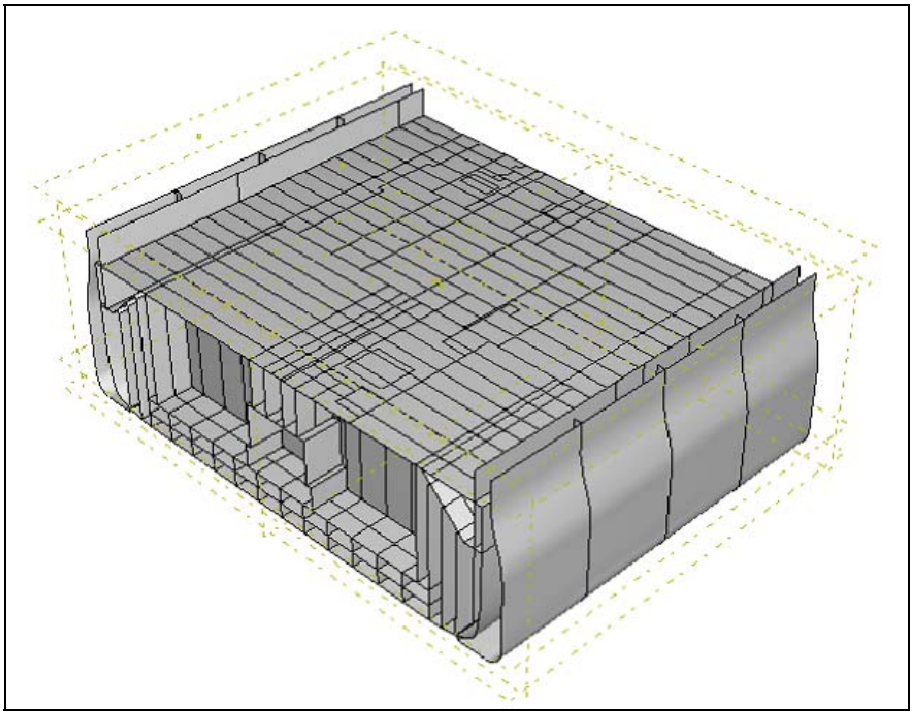

Figure 6.15. Model cutaway showing addition of third deck plating (NIST Graphic).

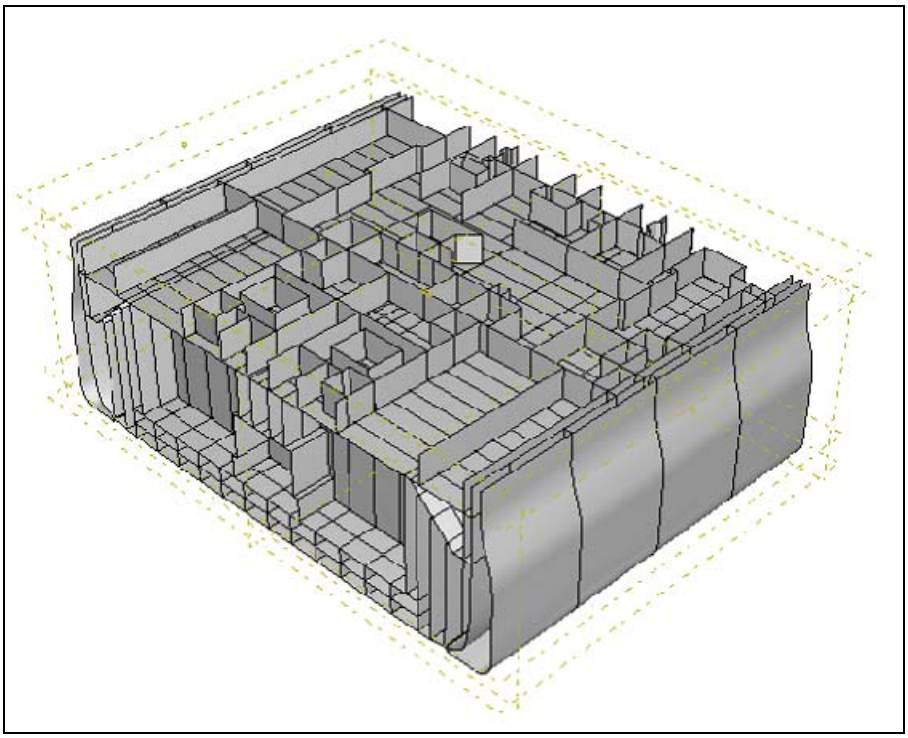

Figure 6.16. Model cutaway showing addition of bulkheads between third and second decks (NIST Graphic).

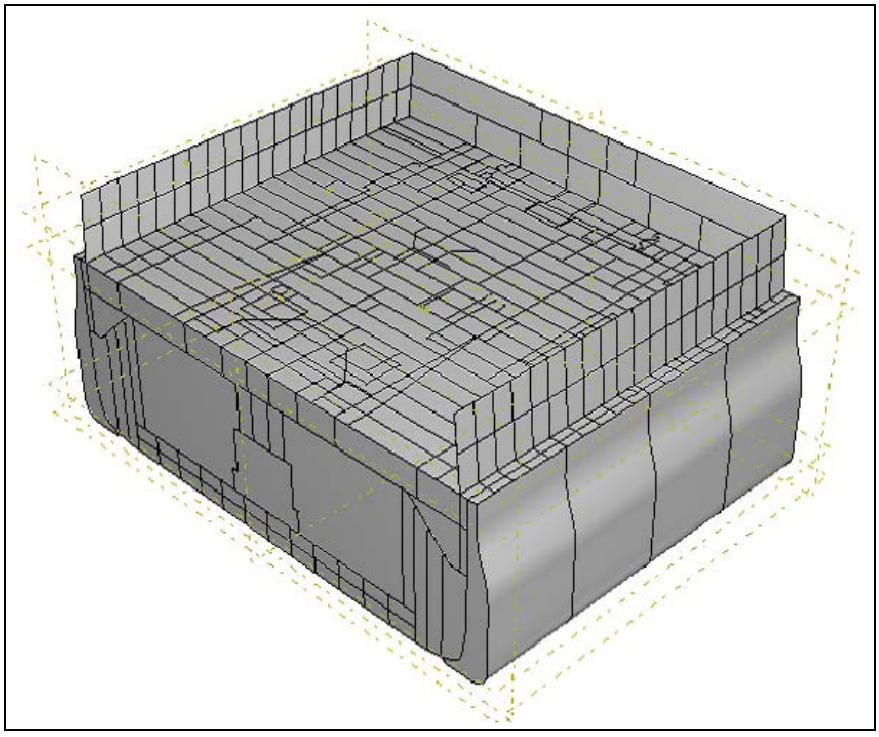

Figure 6.17. Model cutaway showing addition of second deck plating, exterior bulkheads between second and main decks, and virtual bulkheads at frames 70 and 90 to establish proper boundary conditions (NIST Graphic).

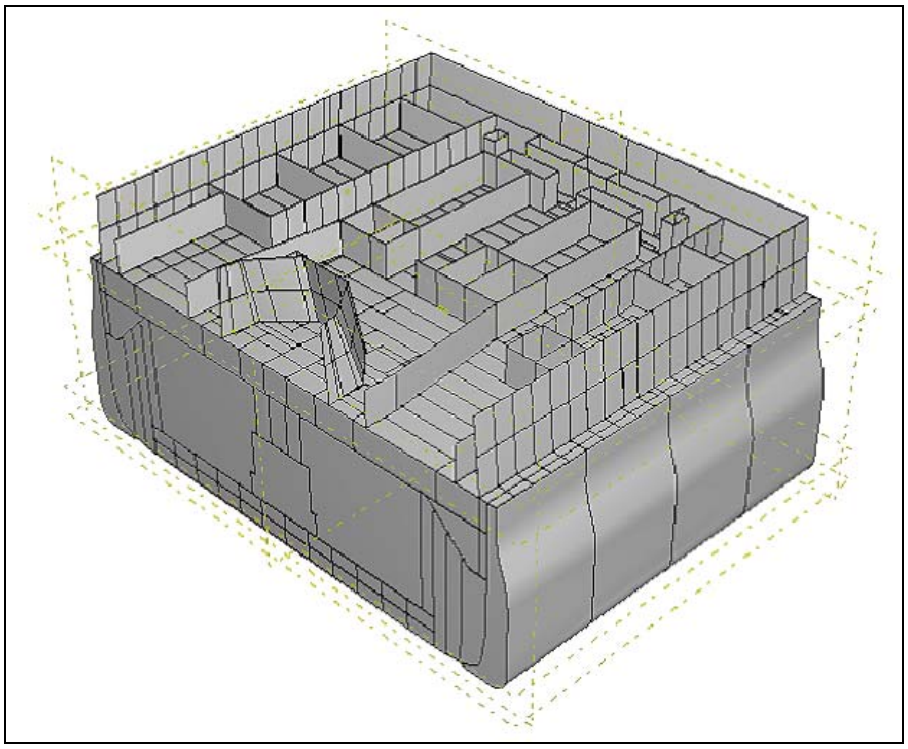

Figure 6.18. Model cutaway showing addition of internal bulkheads between second and main decks and first layer of stack armor plate (NIST Graphic).

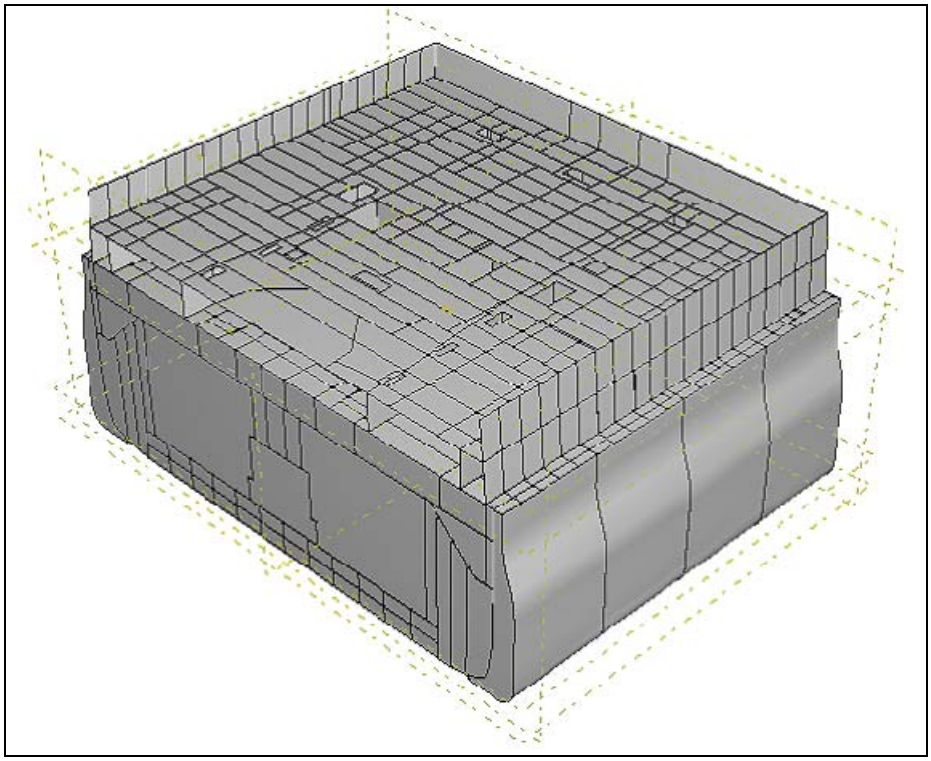

Figure 6.19. Model cutaway showing addition of main deck plating (NIST Graphic).

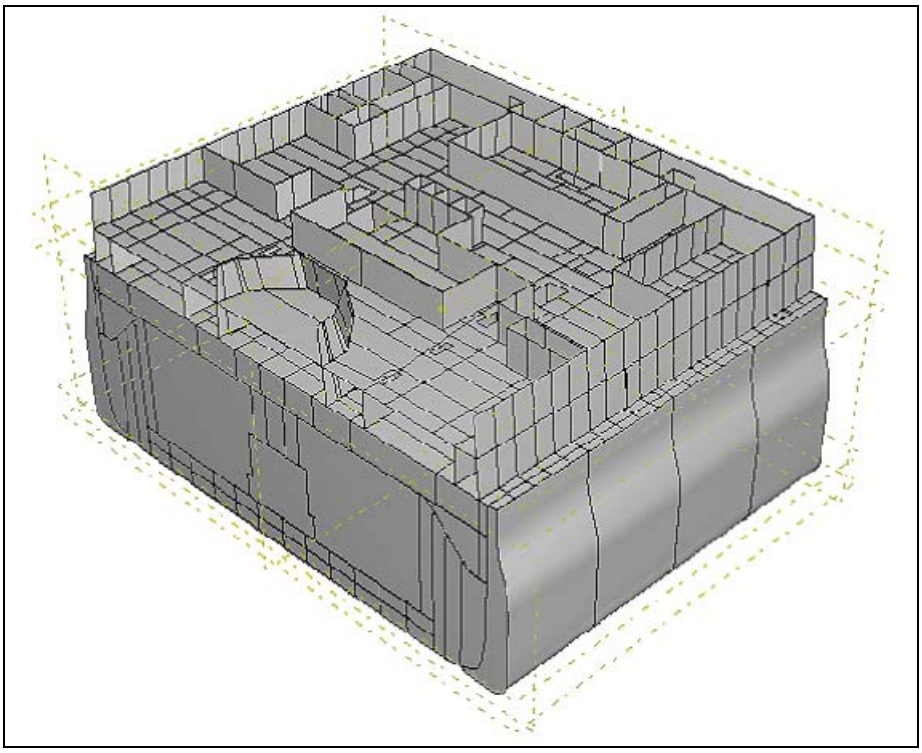

Figure 6.20. Model cutaway showing addition of interior and exterior main deck bulkheads and additional stack armor plate (NIST Graphic).

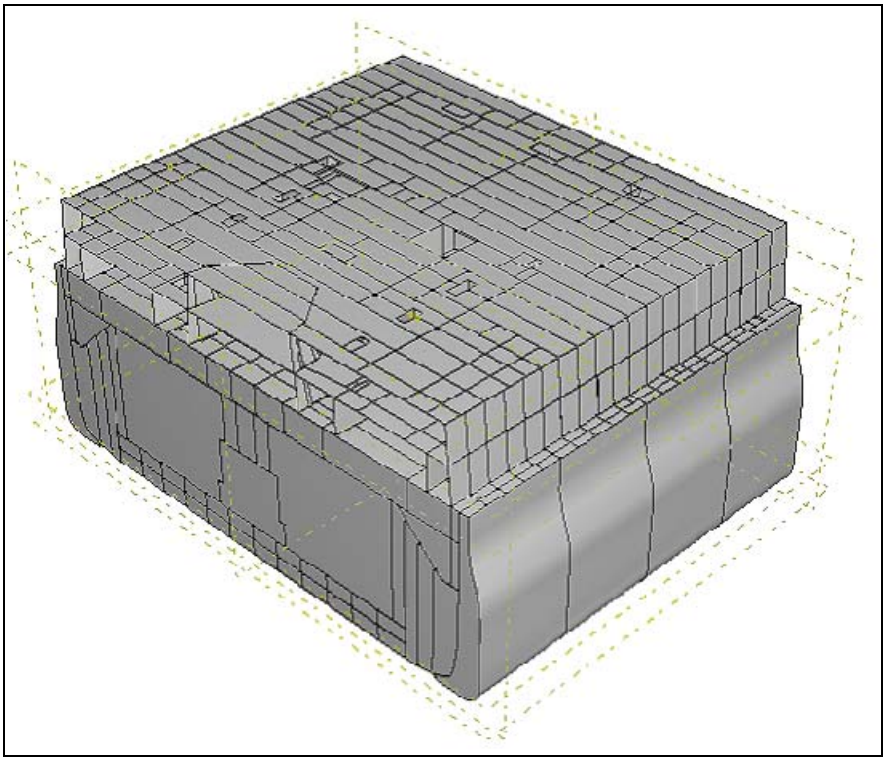

Figure 6.21. Model cutaway showing addition of upper deck plating (NIST Graphic).

The steel of the hull and structure was modeled as an isotropic elastic plastic continuum, with a linear work hardening rate from the yield strength to the ultimate tensile strength. The values of specific properties used (density: 7800 kg/m^3, Young's modulus: 200 GPa, Possion's ration: 0.3, yield stress: 309 MPa, ultimate stress: 563 MPa) are all standard literature values or measured using tensile tests on coupons of steel taken from *Arizona*.

The viscoplastic properties of the sediment upon which the wreck sits have been measured by the U.S. Geological Survey (USGS), as reported in Chapter 10. These properties were used in the model as part of the lower boundary condition, where the steel of the outer hull was proscribed to be in contact with the mud, allowing both load transfer and for the mud/steel interface to slip as the ship settles and deforms.

The concretion on *Arizona* has been found to have a fairly dramatic impact on the decay and eventual collapse of the wreck. The layer of biomass, shells, mud, sand and corrosion product that is encasing the wreck has been described and discussed in Chapter 5. The encrustation layer, while stiff and fairly hard, is also quite brittle, with the constituents being poorly bonded to both each other and the surface of the steel. The mechanical effect of the encrustation on the collapse of the wreck is in its weight. As the wreck's steel components corrode, they lose thickness and weight. But overall the encrustation grows faster than the steel corrodes, and thus over time the wreck gains mass. This deadweight must be added to the self-weight of the steel, and it is both together that is driving the collapse of the wreck.

The oil that fueled *Arizona*, Bunker C fuel oil, has a density of 0.97 that of sea water at 25 degrees C. It has been reported that *Arizona* contained as much as one million gallons of oil just prior to the attack, and it is estimated that much as one-half million gallons may still remain within the wreck. It is unknown whether the oil is primarily contained within the original fuel cells or whether a significant portion has leaked out and lies underneath the decks. Because the oil is more buoyant than sea water, it will exert a lifting force on the wreck structure wherever it is located. As a worst case estimate, we calculated the lifting force of a half-million gallons of Bunker C as if it was located at one spot, and the result was approximately 62 tons of lift. This equates to 2 pounds per square inch if the oil were idealized as a cube of liquid under a single deck. This is an insignificant loading on the structure, and it would not contribute in any way to the eventual failure in comparison to the self-weight and the weight of the encrustation, as will be seen. Thus, the mechanical effect of the lifting force of the oil is not considered further.

To facilitate changes in properties and/or boundary conditions within the model, it was divided into zones, or collections of elements, that could have their properties changed in unison. These generally consisted of pairs of decks within the structure, as the main parameter to be varied is the density, reflecting changes in corrosion in the steel plates and members at different water depths and under the mudline, and thus differences in steel thicknesses.

Once the model is developed in geometry and element placement, a definition of the boundary conditions needs to be imposed (Figure 6.22). The open ends at frames 70 and 90 were constrained from motion along a line parallel to the long axis of the ship. The steel elements in contact with the first layer of mud elements were prescribed to remain in contact as both are allowed to deform. The extent of the mud was set at a dimension that would ensure that all of the mud deformation that results from the motion of the wreck was entirely contained within the volume of the mud in the model. The boundary of the mud was constrained from motion in all three axes. Each element was given a self-weight with a density that can be independently set or changed as part of a zone, and the surfaces of the elements were allowed to bear additional loads from the concretion.

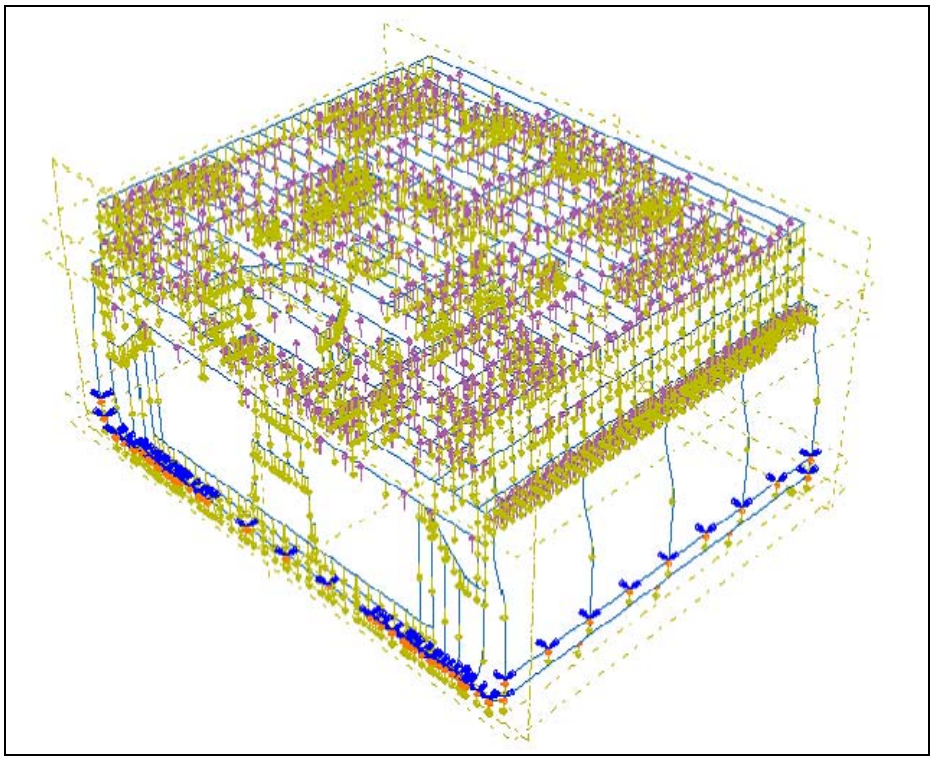

Figure 6.22. Diagram of boundary conditions and loadings in the model. Gold - weight, purple - encrustation, blue - no longitunal motion, orange - support from mud (NIST Graphic).

A major limitation of the finite element method involves the fact that the geometry of the body being studied is fixed, while the loads, boundary conditions and material properties are changed, to study how a design performs under different conditions. This works very well for design issues, which is where FEA is commonly used. In the present study, the inverse problem is being studied: the loads and material properties are fixed, while the geometry is changing with time due to corrosion of the steel. Under ordinary circumstances, the entire model would need to be re-meshed with the new measurements for every state of the wreck to be studied. In order to be able to run a parameter study, where the variables that can be changed are varied in a systematic way to evaluate the stability of the system, a model was developed where the density of the elements was changed.

The critical parameter in this study is the stress that any given component experiences under the weight of itself, what it is attached to, and the concretion. Stress is load divided by cross-sectional area. The stress increases if the area decreases (due to corrosion) or the load increases (due to, in this case, increasing density). Using this technique, the physical dimensions of the element are kept constant, but the density is increased such that the stress in the component increases as it "thins" in the model. There is a small error introduced using this method, as the bending moment of inertia is being kept constant in the model with the constant dimensions of the load bearing sections, while thinning by corrosion would decrease the bending moment of inertia, allowing for collapse sooner than the model predicts. This effect is believed to be small, and is being checked by performing an actual remesh of the model using the new, corroded thicknesses and directly comparing the stresses from this model to the original results.

RESULTS

It is perhaps most illustrative to present the results from the model in chronological order as the wreck decays, describing issues that develop and warrant examination. In the figures to follow, stresses are shown in a color scale ranging from dark blue through green, yellow, orange and red. These roughly correspond to stress levels of less than 10%, 10-25%, 25-50%, 50-75%, and more than 75%of the breaking stress of the steel, respectively. Once an element has reached the breaking stress, it is defined as having no strength in the model, and is removed. The results presented are those where the steel not covered by mud is allowed to degrade 3 times faster than

the buried steel, which appears from corrosion analysis (Chapter 5) to be a reasonable scenario. The approximate equivalent dates were determined by assuming a linear corrosion rate from 1941 through the dates of the actual thickness measurements on the wreck, and extrapolating into the future. Since the corrosion rate is most likely non-linear, being affected by many factors such as the presence and thickness of the encrustation, this is only an approximation that will need to be refined in future work. For the purposes of this chapter, the approximation is useful for fixing the "age" of the wreck for planning purposes at the present day at 20% degredation.

Stresses in the Structure—As Built

Figure 6.23 shows the computed stresses in the model when dimensions of the ship are taken directly from the design blueprints, and thus as the ship was built. The stresses everywhere are very low, which is to be expected as this is a warship and it was considerably overbuilt to be able to withstand battle damage. The stresses are higher in the vertical walls in the lower levels, as expected, since these walls are supporting much of the weight of the ship above.

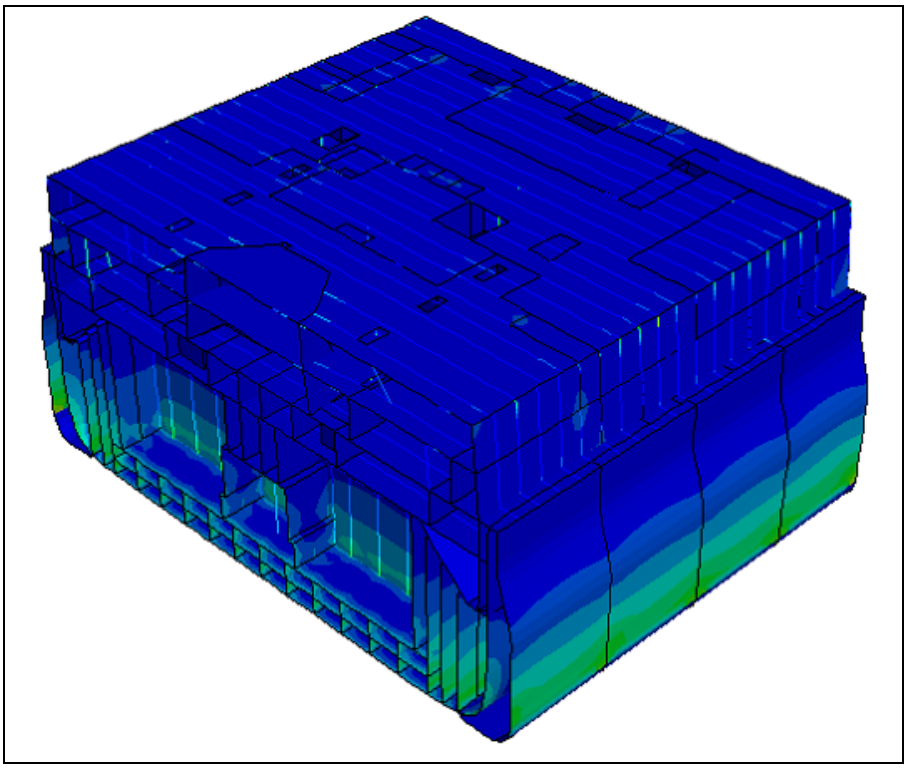

Figure 6.23. Self-weight stresses in as-built condition (NIST Graphic).

Stresses in the Structure—10% Corrosion Thickness Loss (rough equivalent to 1980)

Overall the stress distribution is very similar to the as-built condition, with the overall stress levels somewhat higher. It is noteworthy that the deck beams in the upper deck have jumped significantly in stress, and the second, first and main decks remain almost unstressed (Figure 6.24).

Stresses in the Structure—20% Corrosion Thickness Loss (rough equivalent to 2020)

The upper deck is now showing sagging of the beams and deck plates as they continue to thin. Stresses at the turn of the bilge of the torpedo blisters are approaching the tensile strength of the steel. Stresses in the vertical members continue to increase (Figure 6.25).

Stresses in the Structure—30% Corrosion Thickness Loss (rough equivalent to 2050)

The turn of the bilge area of the torpedo blister, as well as the connections of the lower bulkheads to the hold platform are very close to critical. There is additional sagging in the upper deck, as well as increased stresses in the bulkheads of the lower deck (Figure 6.26).

Stresses in the Structure—50% Corrosion Thickness Loss (rough equivalent to 2120)

Localized collapse events have begun to appear, including the torpedo blisters, double bottom vertical wall segments, upper deck beams and the region around the stack armor, undoubtedly collapsing under the weight of this very thick steel (Figure 6.27).

Stresses in the Structure—60% Corrosion Thickness Loss (rough equivalent to 2150)

There is general collapse of the deck plating on the upper and main decks, collapse of the outer hull plating and torpedo blisters, very high stresses in the bulkheads at the hold platform in the engine spaces. Buckling of the hull shell plating has begun (Figure 6.28).

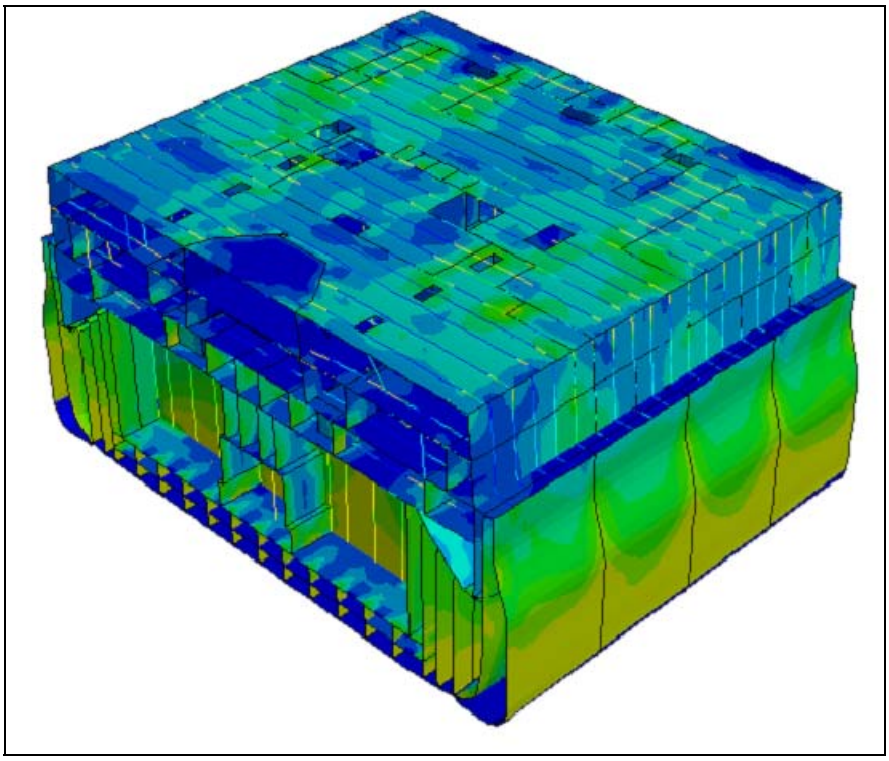

Figure 6.24. Self-weight stresses after 10% thickness loss due to corrosion, approximate date = 1980 (NIST Graphic).

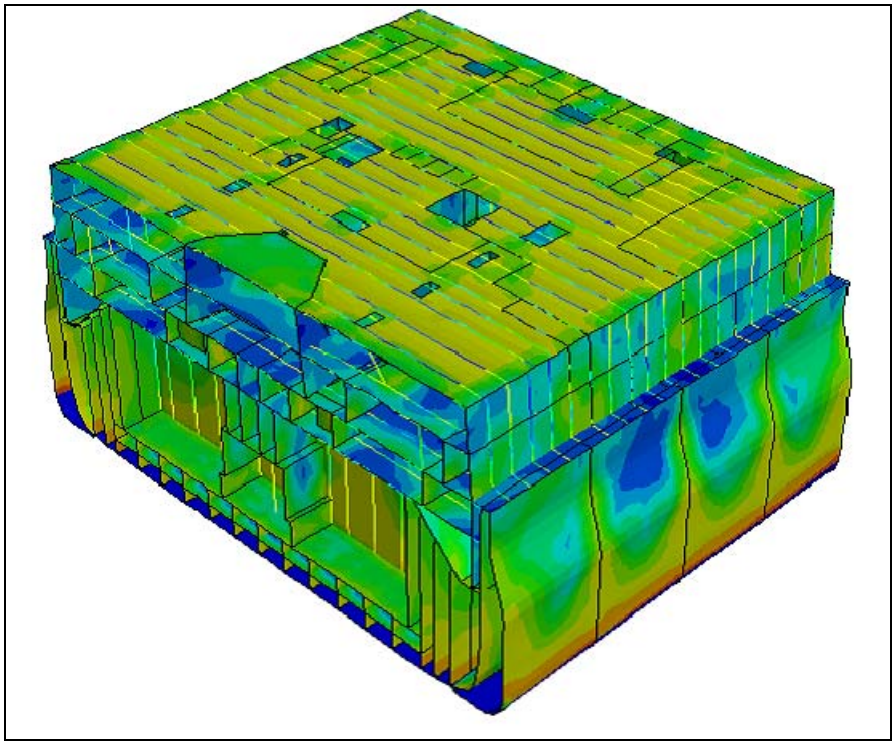

Figure 6.25. Self-weight stresses after 20% thickness loss due to corrosion, approximate date = 2020 (NIST Graphic).

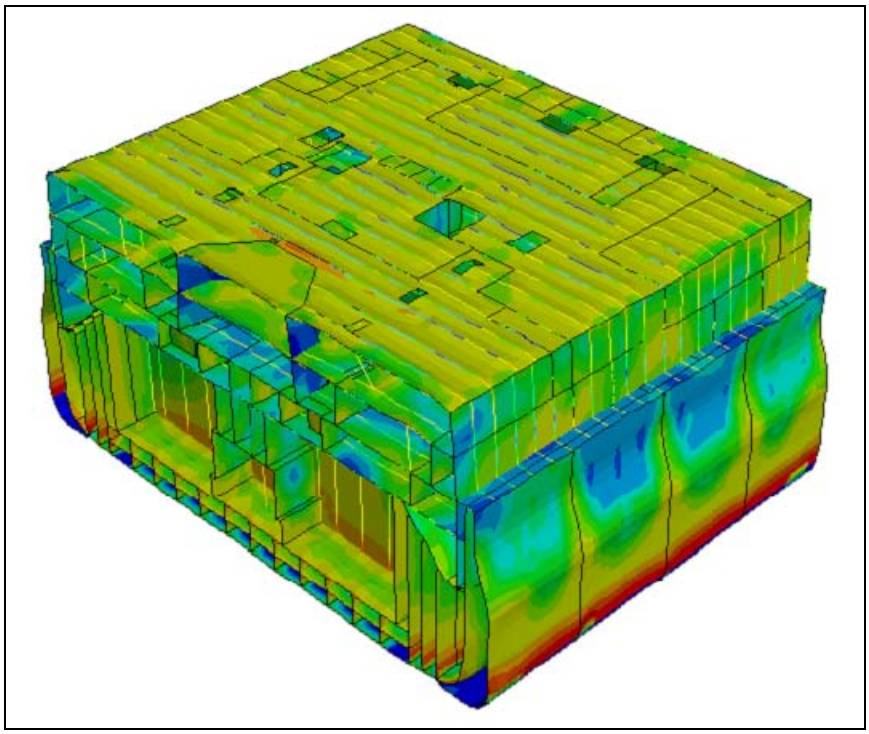

Figure 6.26. Self-weight stresses after 30% thickness loss due to corrosion, approximate date = 2050 (NIST Graphic).

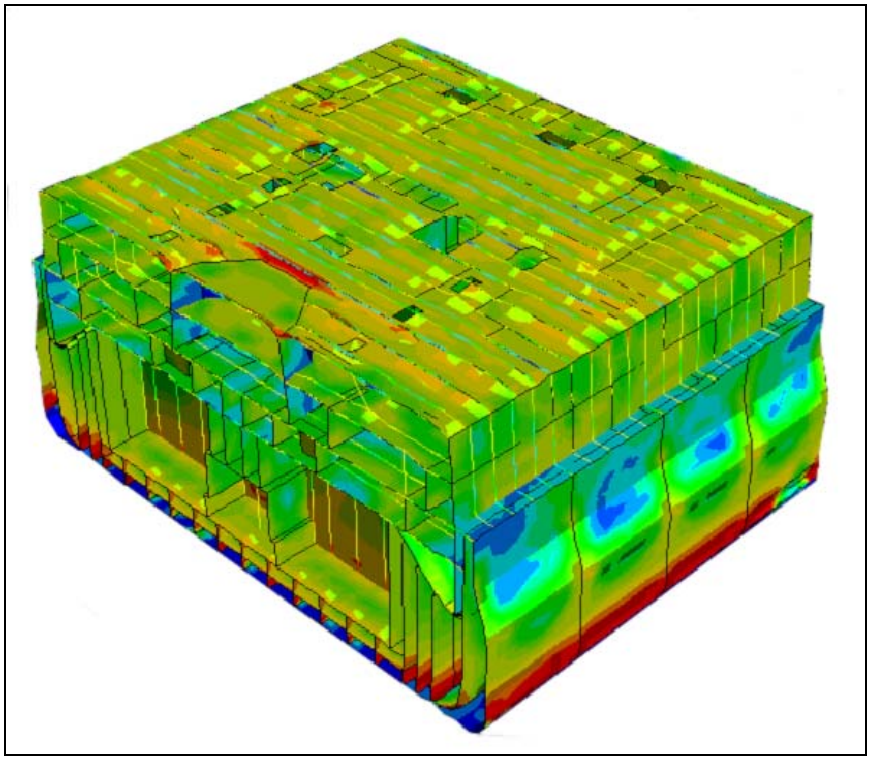

Figure 6.27. Self-weight stresses after 50% thickness loss due to corrosion, approximate date = 2120 (NIST Graphic).

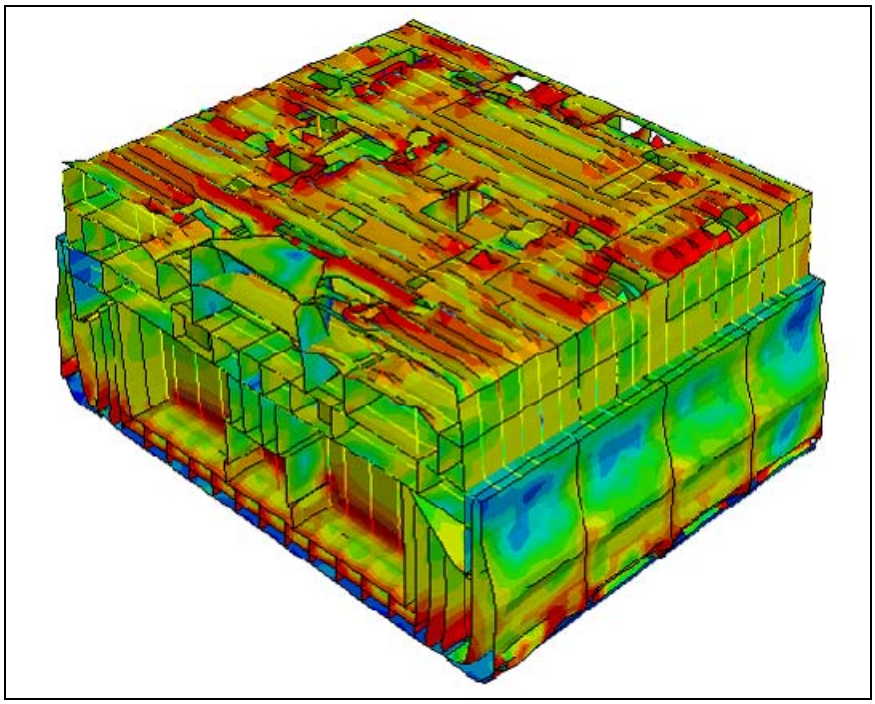

Figure 6.28. Self-weight stresses after 60% thickness loss due to corrosion, approximate date = 2150 (NIST Graphic).

Stresses in the Structure—70% Corrosion Thickness Loss (rough equivalent to 2180)

The upper deck is now unrecognizable, and much of the deck plating and deck beams will have fallen onto and accelerated the collapse of the main deck and those further below. The hull shell and torpedo blister continue to collapse, as does now the double bottom (Figure 6.29).

Stresses in the Structure—80+% Corrosion Thickness Loss (rough equivalent to 2210 and beyond)

The decks of the superstructure (upper, main, and second) can be expected to further collapse and pancake onto the third deck. The double bottom has now completely collapsed. Note however that the core cylinder of the wreck, consisting of the volume bounded by the third deck, the inner bottom and the side oil tanks is still relatively intact (Figure 6.30–6.32).

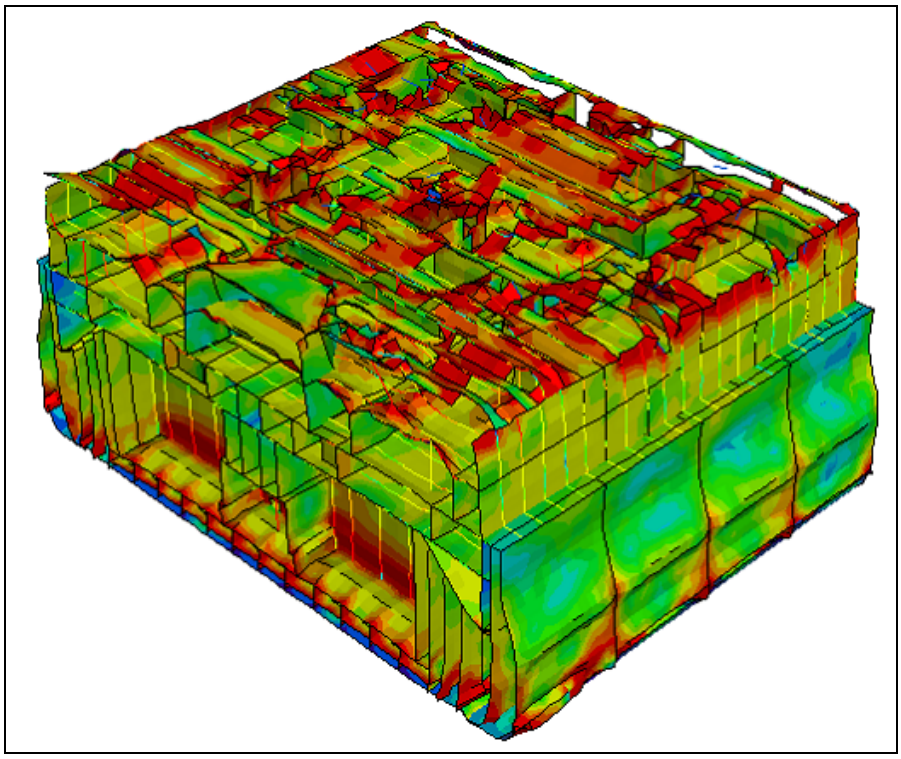

Figure 6.29. Self-weight stresses after 70% thickness loss due to corrosion, approximate date = 2180 (NIST Graphic).

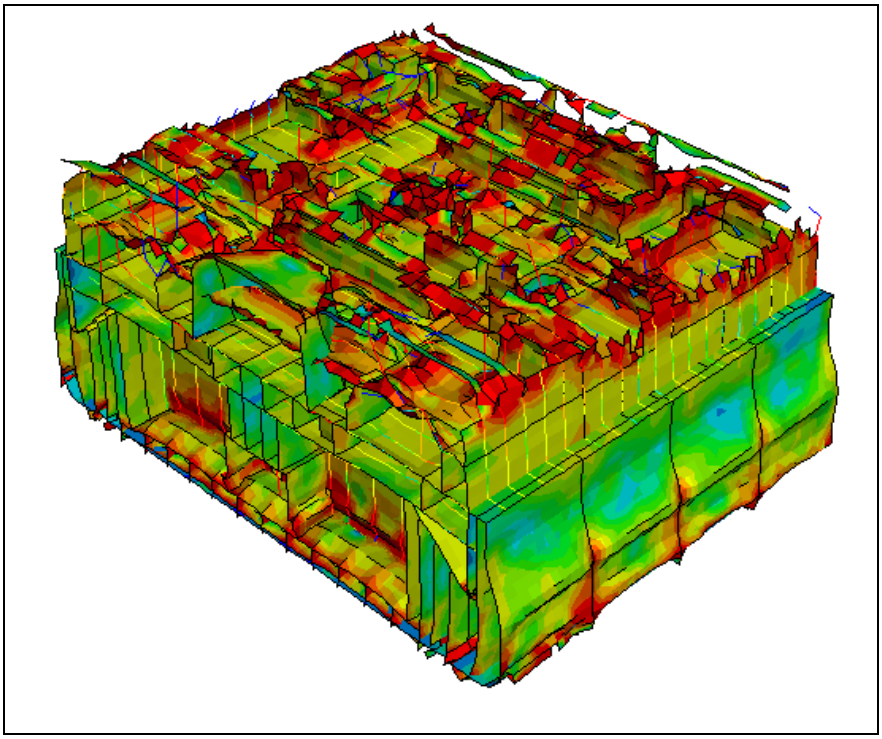

Figure 6.30. Self-weight stresses after 80% thickness loss due to corrosion, approximate date = 2210 (NIST Graphic).

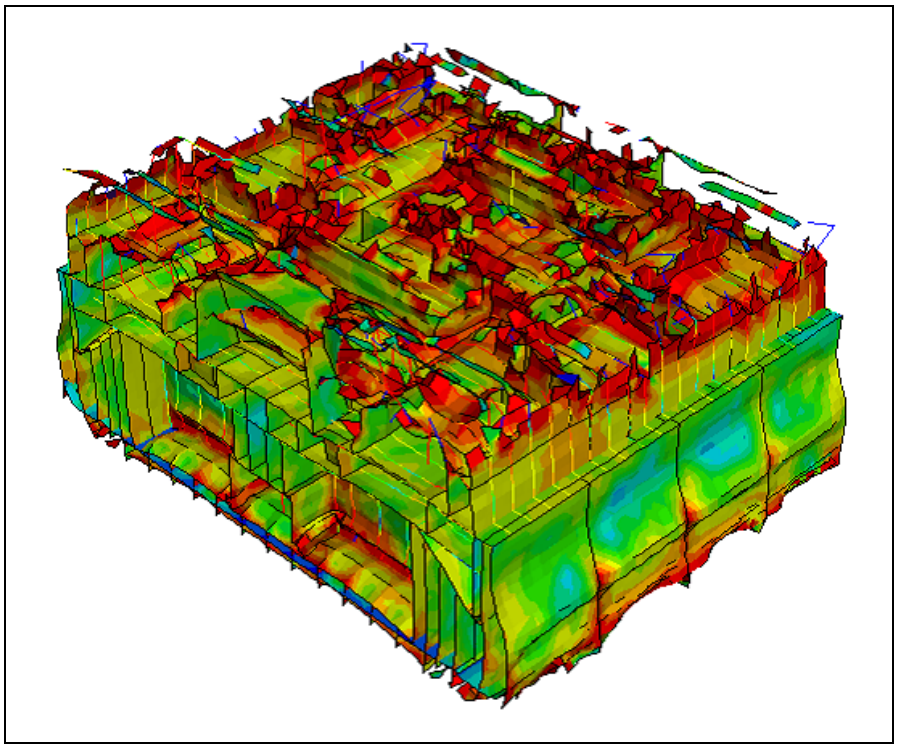

Figure 6.31. Self-weight stresses after 90% thickness loss due to corrosion, approximate date = 2240 (NIST Graphic).

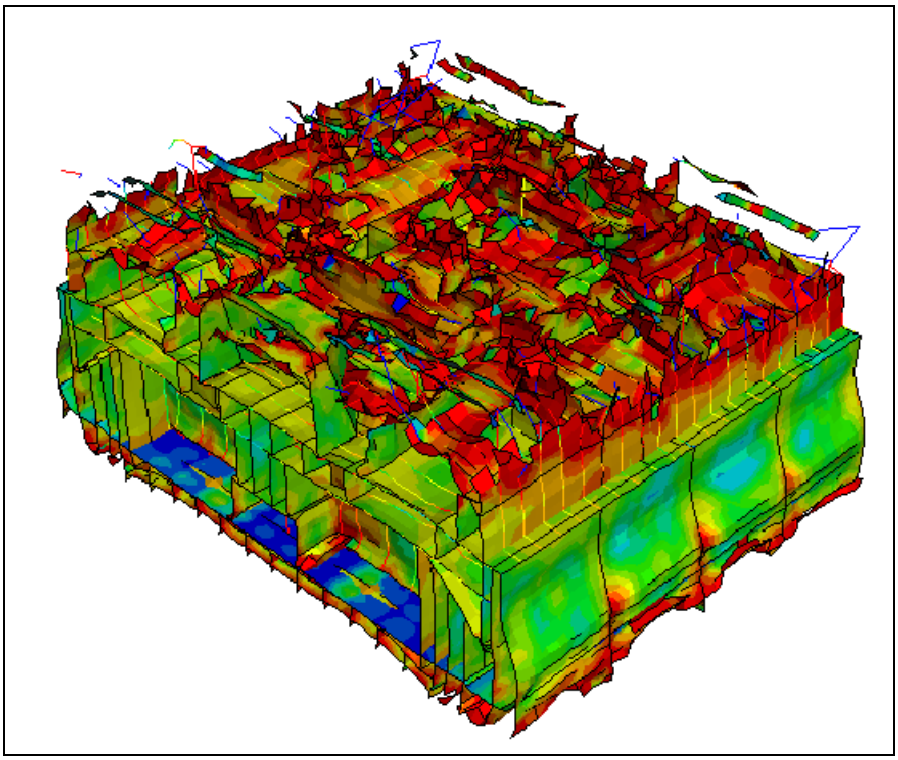

Figure 6.32. Self-weight stresses after 95% thickness loss due to corrosion, approximate date = 2250 (NIST Graphic).

OBSERVATIONS AND CONCLUSIONS

The results of this FEA of the wreck of USS *Arizona* seem to indicate that the wreck is approximately one fifth to one fourth of the way to an eventual collapse due to corrosion. A surprising aspect of the results is that collapse is predicted to initiate in the side and bottom of the hull before any significant collapse events in the exposed regions of the upper decks. This is likely due to the fact that the boundary condition of the wreck is that it rests on a viscoplastic solid representing the mud, rather than a pure fluid of sea water. The mud will rather quickly compress and become quite hard, concentrating the load on the bottom of the hull rather than distributing it more generally.

FURTHER WORK

Many refinements and extensions to this analysis of the wreck of *Arizona* are possible, and will be performed on a time-available basis by staff at NIST. Now that the methodologies for simulating the degredation and eventual collapse of a submerged steel-hulled ship using FEA have been developed, this work can be easily extended to answer several key questions concerning the future of USS *Arizona*.

First, this model can, in a very straightforward way, be extended to the entire length of the ship. Of course, this would increase the calculation time needed dramatically, but key insights into the behavior of structural elements in the present study can be used to cut down the computation time. For example, once it is determined how a section of deck plating and supporting deck beam deform as the members thin, and it is found to be consistent across the model, this region can be replaced with a single element that has hybrid parameters calculated from the model. Thus, instead of performing calculations on thousands of connected elements, one could be used.

One large unknown in this study is the damage to the internal load-bearing structures in the lower decks due to the events on December 7, 1941. It is almost certain that the region forward of the main stacks suffered significant damage, but since submersibles and divers cannot reach these regions for direct observations, we must speculate and make best and worst case scenario assumptions for our analyses. These assumptions could be fine-tuned with input from

experts in blast damage in the naval community, perhaps at the Naval Surface Warfare Center in Carderock, Maryland. Initial contacts with researchers at that facility indicated interest but inability to assist due to lack of funding.

The wreck is listing slightly to port, and this causes the self-load to be directed slightly off of vertical onto the load bearing structures. Elastic-plastic collapse of columns and stanchions will be significantly affected by deviations from vertical, and the effect of the list will be for some structures to collapse sooner than predicted in this model. The effect of the list and how it is changing over time is a factor that could be added to refine the model, based on analysis by USGS.

Corrosion data has been collected on the wreck by the NPS-SRC since the early 1980s. These data, coupled with the direct measurements of corrosion via coupon removal from the wreck, has allowed modeling of the corrosion rate at many locations on the wreck. In the present study, the differences in corrosion rates were only modeled as differences between whole decks above and below the mud line. A further refinement to the model that would allow for more accurate spatial location of potential developing weak points would be to map the measured differences in corrosion rate onto the structure.

The eventual goal of this model is to construct a tool that can not only give some predictions as to eventual collapse of the wreck, but also be able to virtually test out potential remediation techniques before going through the time, expense and intrusion of working on the ship. One of the easier things that can be controlled is the accumulation of concretion. If it is found that the corrosion rate is significantly reduced by the presence of this layer, as it appears to be the case, then encouragement of its formation would be useful. Conversely, if the FEA model is expanded to test the effect of having more or less mass on the wreck surfaces from concretion, a removal or preventative routine would be of value. This would be a straightforward extension of the current study.

Finally, Pearl Harbor is an active naval base, with ship traffic constantly entering and exiting. Each of these ships produces a wake that can, depending on the distance from the wreck, deliver a significant impact to the hull. In the case of *Nimitz*-class carriers, nearly the entire water column under the ship is being displaced as they pass in salute, delivering a mini-tsunami. The present model deals with slow, steady-state decay of the structure, attempting to predict the timeframe of collapse. It is more likely that a significant failure will be precipitated

by a more sudden event such as a wave or a large storm. Using new modules developed to study the effect of landslide-induced waves within reservoirs upon dams, a study could be conducted looking at the magnitude of stress spikes in the wreck with the passing of ships or during large storms.

CHAPTER 7

Microbiological Research on USS *Arizona*

Christopher J. McNamara, Kristen Bearce Lee, and Ralph Mitchell

INTRODUCTION

The purpose of this research is to investigate the possible role of microorganisms in USS *Arizona* corrosion and concretion formation. Specific goals include isolating and identifying microorganisms from Pearl Harbor, especially within the concretion covering *Arizona*'s steel hull; determining the organisms within the community responsible for corrosion of steel similar to that found in USS *Arizona*; and investigating environmental parameters that may influence the rate of corrosion by microrganisms (e.g., temperature, nutrients, and redox).

POTENTIAL FOR MICROBIOLOGICALLY INFLUENCED CORROSION OF USS *ARIZONA* STEEL

BACKGROUND AND PREVIOUS WORK

Biofilms are communities of microorganisms attached to an interface and embedded in a polysaccharide matrix produced by the microorganisms. Biofilms are ubiquitous in nature (Costerton et al. 1995) and are a common cause of medical infections (Costerton et al. 1999) and

industrial biofouling (Costerton et al. 1995). In the latter two situations, biofilms present persistent problems because of their inherent resistance to antibiotics and disinfectants (Anwar et al. 1992).

Biofilm formation is a multistage, complex process that begins with the initial adhesion of microorganisms to a surface. Surface adhesion is facilitated by a variety of factors. Biotic factors include motility as well as cell surface features such as capsules, fimbrae, and hyrdophobicity (McEldowney and Fletcher 1987). Abiotic factors that affect attachment include surface hydrophobicity, and the presence of polycations and organic coatings (van Loosdrecht et al. 1990).

Once microorganisms have attached to a surface, cell division occurs producing masses of cells referred to as microcolonies (Costerton et al. 1999). In addition, biofilm organisms produce large amounts of exopolymer, which consist mainly of polysaccharides (Christensen and Characklis 1990). The exopolymer serves a variety of functions, including protection from desiccation, erosion, antibiotics, and disinfectants as well as nutrient and energy storage (Costerton et al. 1995).

The polymer matrix may also limit the movement of materials through the biofilm. The result is the formation of microhabitats within the biofilm caused by gradients in factors such as pH, O_2, nutrients, and organic carbon (Whitfield 1988, Rittmann et al. 1999). Areas within the polymer matrix may differ dramatically from the adjoining sections of the biofilm and from the overlying bulk fluid (de Beer et al. 1994). The polymer matrix may be able to limit the transport of gases to the extent that anoxic areas can form within biofilms in aerobic habitats. The depletion of oxygen from microhabitats within biofilms has important consequences for the corrosion of metals. The metal surface under the exopolymer becomes anodic relative to nearby areas with higher O_2 concentrations. Electrons flow from the anodic site to the cathode where they combine with O_2 and H^+, resulting in dissolution of the metal at the anode (Ford and Mitchell 1991, Gu et al. 2000).

Consumption of O_2 by microbial respiration and limitation of O_2 diffusion into the biofilm by the polymer matrix can lead to the formation of completely anaerobic microhabitats within and beneath the biofilm. Anaerobic conditions can result in the growth of sulfate-reducing bacteria (SRB), a frequent cause of microbiologically influenced corrosion (MIC).

Metal corrosion is driven by the hydrogenase activity of the SRB. Electrons flow from

the anodic site to the cathodic site, where they combine with H^+ produced from the dissociation of H_2O to form H_2. SRB remove H_2 and reduce SO_4^{2} to S^{2-}, which reacts with dissociated Fe^{2+} to produce an FeS precipitate (Ford and Mitchell 1991, Gu et al. 2000). Prevention of microbial growth on the metal surface can effectively reduce rates of corrosion (Ford and Mitchell 1991, Gu et al. 2000).

Recent work in the Harvard University Mitchell laboratory has focused on microbial corrosion of aircraft fuel tanks. Microorganisms frequently contaminate jet fuel and cause corrosion of fuel tank metals. Little is known about the microbial community currently found in aircraft fuel tanks. We examined the composition of the microbial community found in fuel tanks containing jet fuel to determine the potential of this community to cause corrosion of aluminum alloy 2024 (AA2024). The microbial community of these fuel tanks is composed almost entirely of Bacillus and a small number of fungi (Figure 7.1). These microorganisms grew abundantly using hydrocarbons in the fuel as the sole carbon source. Electrochemical impedance spectroscopy and open circuit potential measurements indicated that the Bacillus-dominated community accelerated corrosion of AA2024 (Figure 7.2). This was confirmed by metallographic analysis. Despite the limited taxonomic diversity of microorganisms recovered from jet fuel, the bacterial community has the potential to corrode fuel tanks.

CURRENT WORK

We examined the potential role of microorganisms from Pearl Harbor in corrosion of the steel. Water samples from Pearl Harbor were collected by Ralph Mitchell and plated onto Difco nutrient agar. Isolates were collected and are being screened for the ability to use Bunker C fuel oil as a carbon source by inoculating cultures into minimal salt medium (0.22 g l^{-1} $(NH_4)_2SO_4$, 1.20 g l^{-1} KH_2PO_4, 0.23 g l^{-1} $MgSO_4 \cdot 7H_2O$, 0.25 g l^{-1} $CaCl_2$, 0.024 g l^{-1} yeast extract) with 1% Bunker C fuel oil.

As a surrogate for steel from USS *Arizona*, we used A36 steel which is similar to some steel on the *Arizona* (Johnson et al. 1999, see Chapter 5). Coupons were polished to 320 grit and inserted into corrosion cells containing minimal salt medium with 1% Bunker C fuel oil. One-half of the cells were inoculated with bacteria isolated from water in Pearl Harbor and the remaining cells were uninoculated controls. One hour after construction and weekly thereafter,

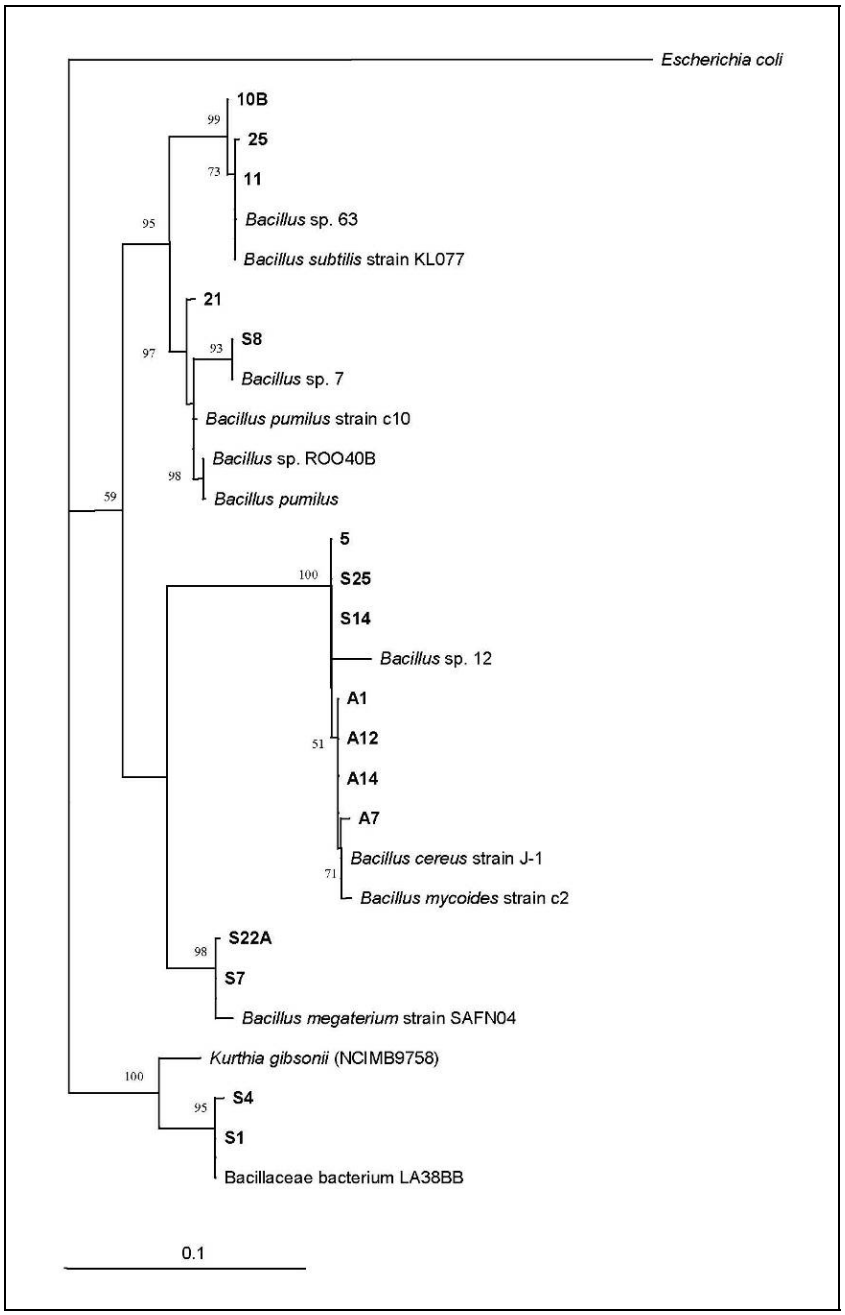

Figure 7.1. Phylogenetic relationships based on partial 16S rDNA sequences of bacterial isolates from aircraft fuel tanks and closely related sequences from the GenBank database. Neighbor joining tree; bootstrap values based on 1000 replicates are indicated for branches supported by >50% of trees. Scale bar represents 0.1 nucleotide changes per position.

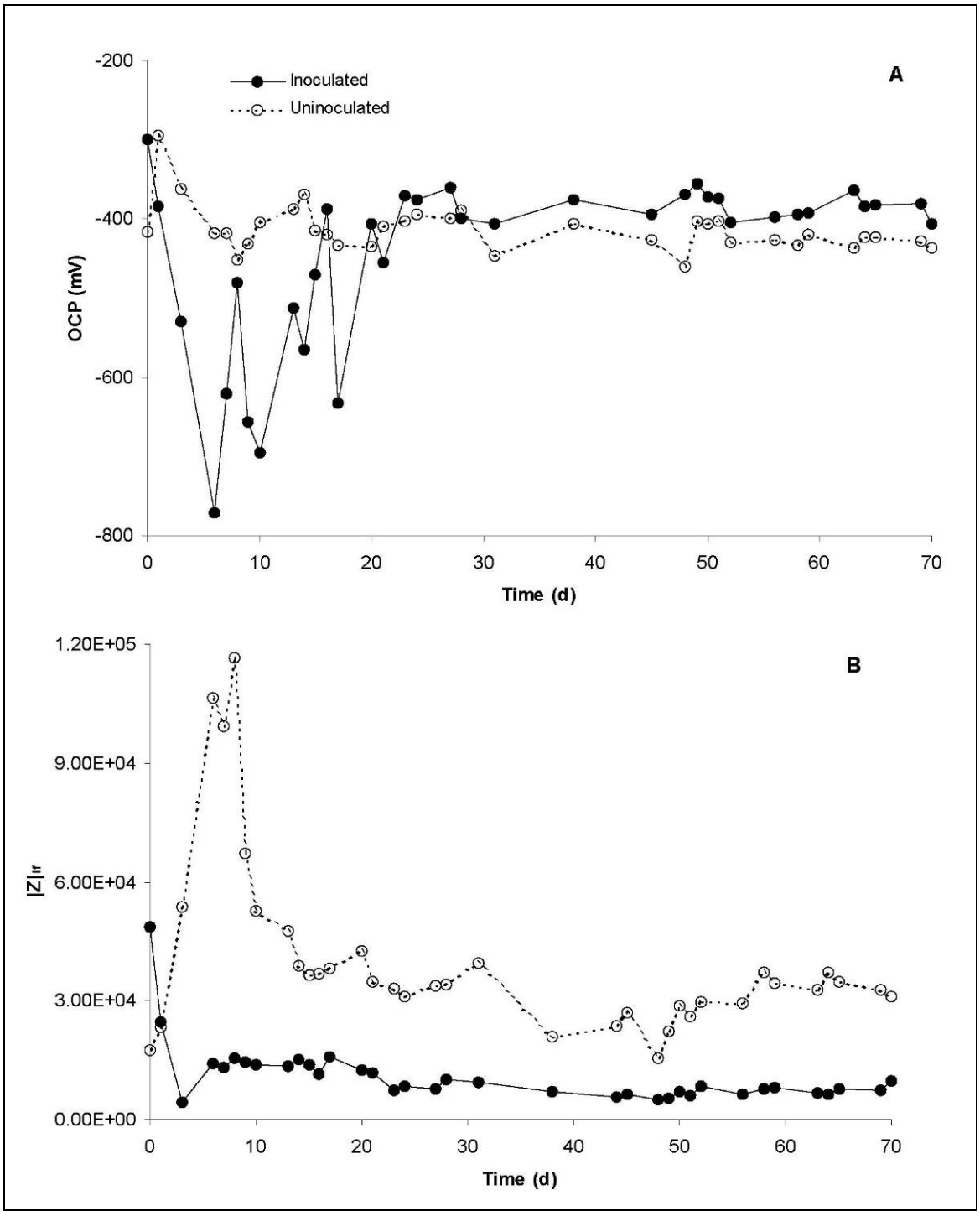

Figure 7.2. Open circuit potential (OCP) of aluminum alloy 2024 (AA2024) coupons (A). Low frequency impedance (|Z|lf, 50 mHz) response of AA2024 coupons (B).

the open circuit potential was measured, followed by a cyclic polarization (CP) scan (Figure 7.3). Coupons were polarized from –0.25 V vs. open circuit potential (OCP) to a vertex potential of 1.0 V vs. OCP, and then a final potential of 0.0 V vs. OCP. The scan rate was 5.0 mV s^{-1}. All measurements were made using a saturated calomel reference electrode.

Initial CP scans of the A36 stainless steel coupons were similar (Figures 7.4A and 7.5A). After 1 week incubation inoculated and uninoculated cells are still similar (Figures 7.4B and 7.5B). Hysteresis of the curves is negative, there is no distinct primary passivation potential (E_{pp}), and there appears to be a transpassive region and a breakdown potential (E_b). In addition, the OCP is located within the passive region and is lower than the repassivation potential (E_{rp}). After 3 weeks, differences between cyclic polarization (CP) scans for the inoculated and uninoculated cells are apparent. The uninoculated cell did not change substantially from week 1 (Figure 7.4C). However, in the inoculated cell the E_{rp} decreased ~200 mV and while the hysteresis was still negative, it was shifted in the positive direction. A passive film is damaged when the potential is raised into the transpassive region. Negative hysteresis indicates that the film repairs itself and pits do not initiate, while positive hysteresis indicates that the film is not repaired and may indicate pit formation. Additionally, when the OCP is less than E_{rp} it is believed that pits will not grow, while in the opposite case it is believed that pits will continue to grow. Movement of the hysteresis in the positive direction and the decrease in the E_{rp} in the inoculated cell may indicate a trend toward pitting corrosion caused by the biofilm.

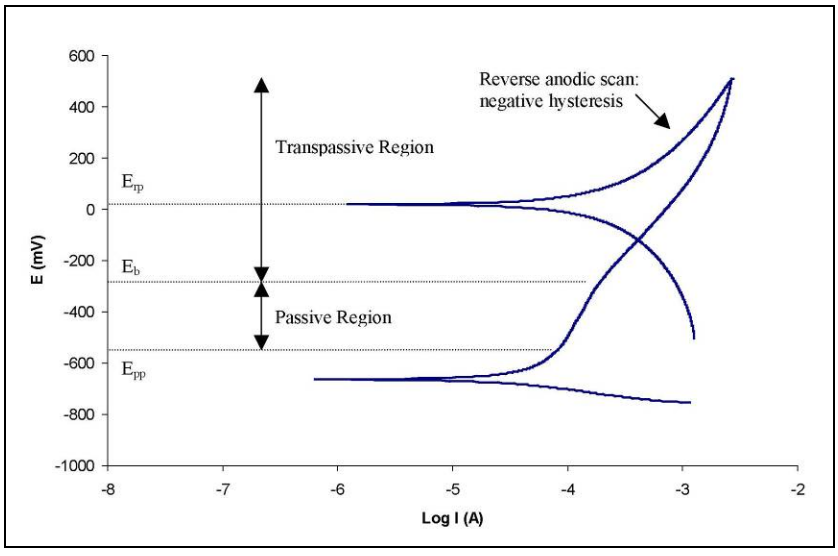

Figure 7.3. Generalized cyclic polarization scan illustrating characteristics of the curve.

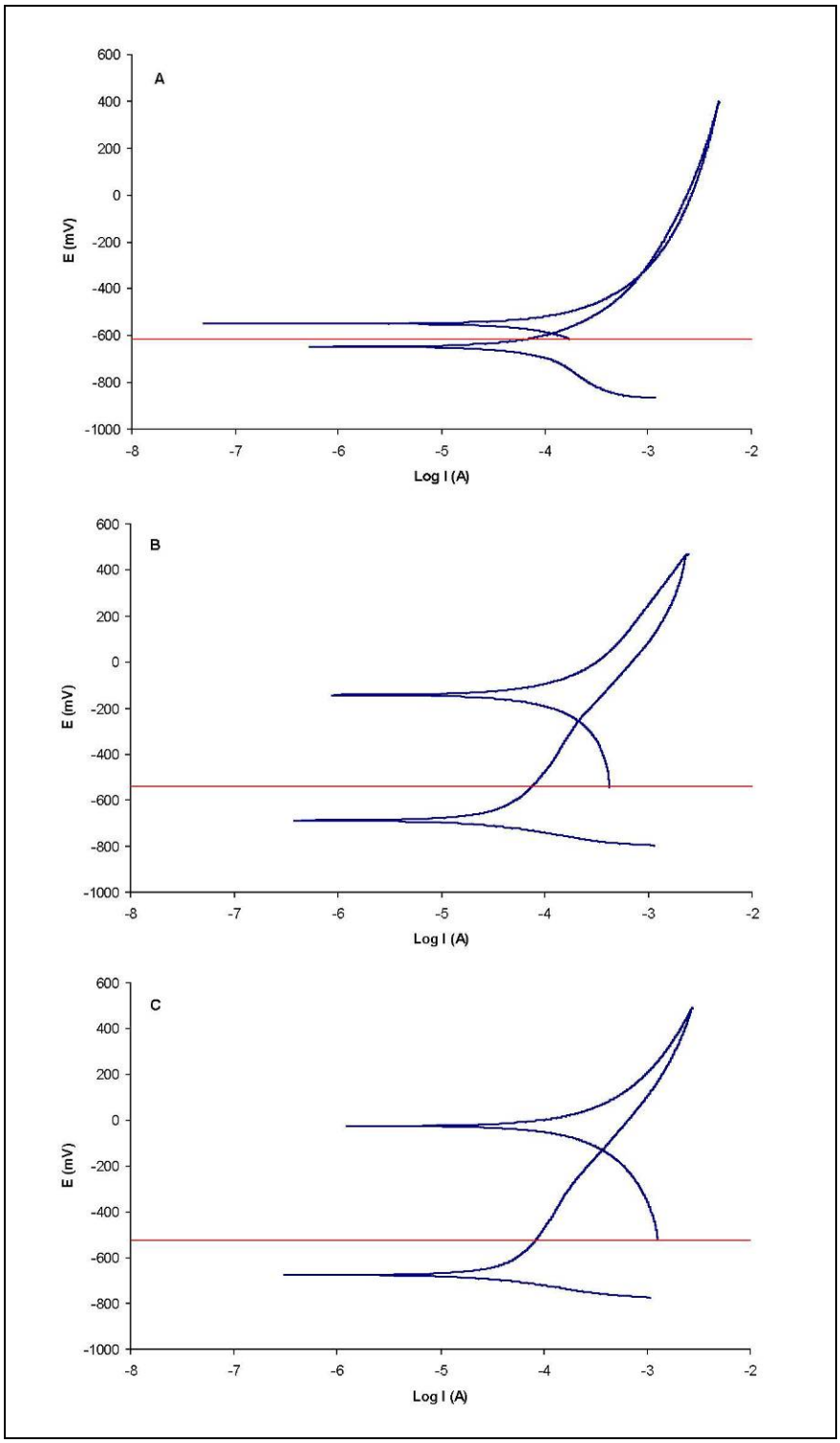

Figure 7.4. Cyclic polarization scans of uninoculated cells after 0 (A), 1 (B), and 3 (C) weeks. The open circuit potential is indicated by the horizontal line.

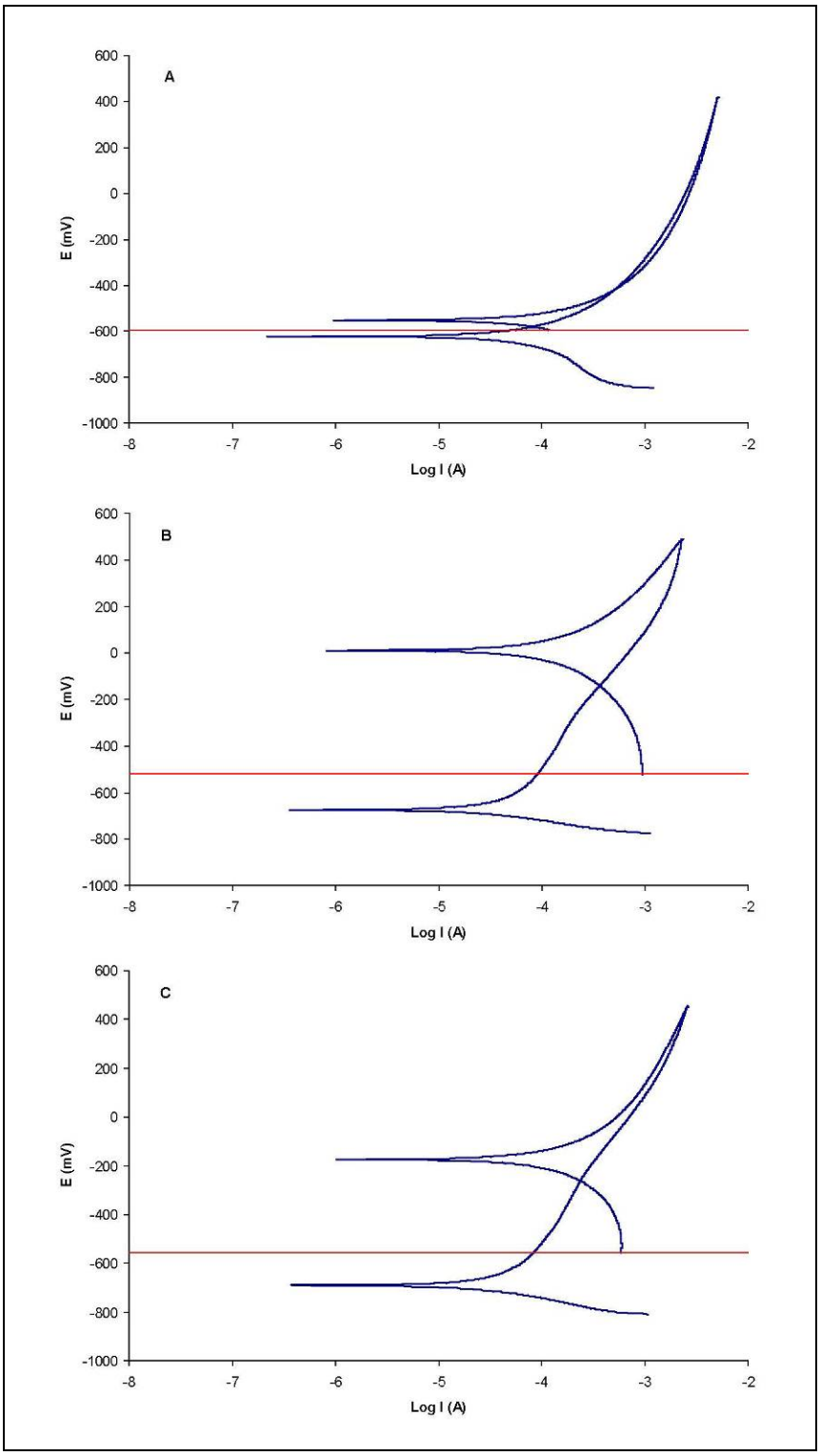

Figure 7.5. Cyclic polarization scans of inoculated cells after 0 (A), 1 (B), and 3 (C) weeks. The open circuit potential is indicated by the horizontal line.

ANALYSIS OF BACTERIAL COMMUNITY COMPOSITION IN USS *ARIZONA* CONCRETIONS

Invertebrate fouling communities called concretions form on archaeological metals submerged in marine environments. The concretions are inhabited by bacteria that play a role in formation and persistence of the concretion layer. We analyzed the bacterial community in concretion samples collected from the external hull of USS *Arizona* in Pearl Harbor, HI. Variability in the size of the bacterial community was high, and the concretions appear to harbor approximately 10^6 bacteria/g. Analysis of 16S rDNA clones indicated that the community consisted of bacteria related to three phyla: Firmicutes, Bacteroidetes, and Proteobacteria. The low bacterial diversity may indicate a late-succession stage community within the stable concretion. Alternatively, the low diversity could be the result of residual antifouling chemicals applied to the ship hull. It is likely that the bacterial community detected in these concretions plays an important role in the continuing corrosion of USS *Arizona*.

Thick biofouling layers referred to as concretions or encrustations form on archaeological materials in marine environments (Makinson et al. 2002). North (1976) characterized concretions formed on iron from the *Batavia* wreck, which sank in 1629 off the coast of Western Australia. The concretions consisted of a multilayered mixture of iron oxides (e.g., goethite and magnetite) and fragmented shell or skeletal material with an outer layer of living organisms that was indistinguishable from surrounding reef material.

Formation of concretion layers begins with the adhesion of bacteria to surfaces, which occurs rapidly in marine environments (Marshall et al. 1971). Attached bacteria subsequently impact the settlement and attachment of marine invertebrates (Maki et al. 1989). The invertebrate assemblages undergo a succession of organisms that begins with tunicates, bryozoans, amphipods, sponges, and barnacles, and is dominated in later stages by barnacles, sponges, and mussels (Bram et al. 2005).

Other locations where these communities have been studied include offshore oil and gas platforms, where fouling layers 10 - 20 cm thick have been found (Page et al. 1999). On these platforms, biofouling causes increased structural loads and wave resistance, and increased corrosion rates (e.g., within cracks and crevices or due to reduction in cathodic protection)

(Zvyaginstev 1990; Zvyaginstav and Ivin 1995). Concretions may have similar impact on archaeological materials.

The purpose of this study was to investigate the bacterial composition of concretions on USS *Arizona*. USS *Arizona*, a national shrine, war grave and naval memorial located in Pearl Harbor, Hawaii, is visited annually by more then 1.5 million people. In addition to the remains of more than 900 sailors and marines, the ship contains an estimated minimum 2,300 tons of fuel oil. Corrosion and deterioration of the ship both threaten an important national monument and represent a severe environmental hazard. This study is part of a larger effort by the National Park Service Submerged Resources Center to analyze the current condition of USS *Arizona*, to predict the future course of deterioration of the ship, and to preserve the site for future generations (Russell et al. 2004).

EXPERIMENTAL METHOD

Concretion samples were collected from two locations on the exterior hull of USS *Arizona* in November 2004. Samples were collected with a pneumatic drill fitted with a 7.6 cm diameter hole saw. Sample 14 was collected on the ship's port side near the stern at a depth of 5.9 m below the water surface. Sample 15 was collected on the ship's starboard side near the stern at a depth of 4.7 m below the water surface. Samples were shipped on ice overnight to Harvard University (Figure 7.6).

In the Mitchell Laboratory, samples were wrapped in sterile aluminum foil and pulverized with a hammer, sonicated (Branson model 2510 Ultrasonic Bath, Danbury, CT) for 5 min. to detach bacteria, and preserved with 1% formaldehyde. Bacteria were concentrated by filtration (15 kPa vacuum) onto 0.22 μm pore size black polycarbonate membranes (Poretics, Livermore, California), stained for 5 min. with 1.0 ml of 1.0 μg/ml 4',6-diamidino-2-phenylindole (DAPI), and rinsed with 1.0 ml deionized water (Porter and Feig 1980). Bacteria were then enumerated in three subsamples from each concretion using epifluorescence microscopy. Cells were counted in randomly selected fields at 1000X magnification until between 300 and 400 cells were enumerated.

DNA was extracted from concretions using the UltraClean Soil DNA Kit (MoBio Labs, Carlsbad, CA). The 16S rDNA was amplified using the polymerase chain reaction (PCR) as

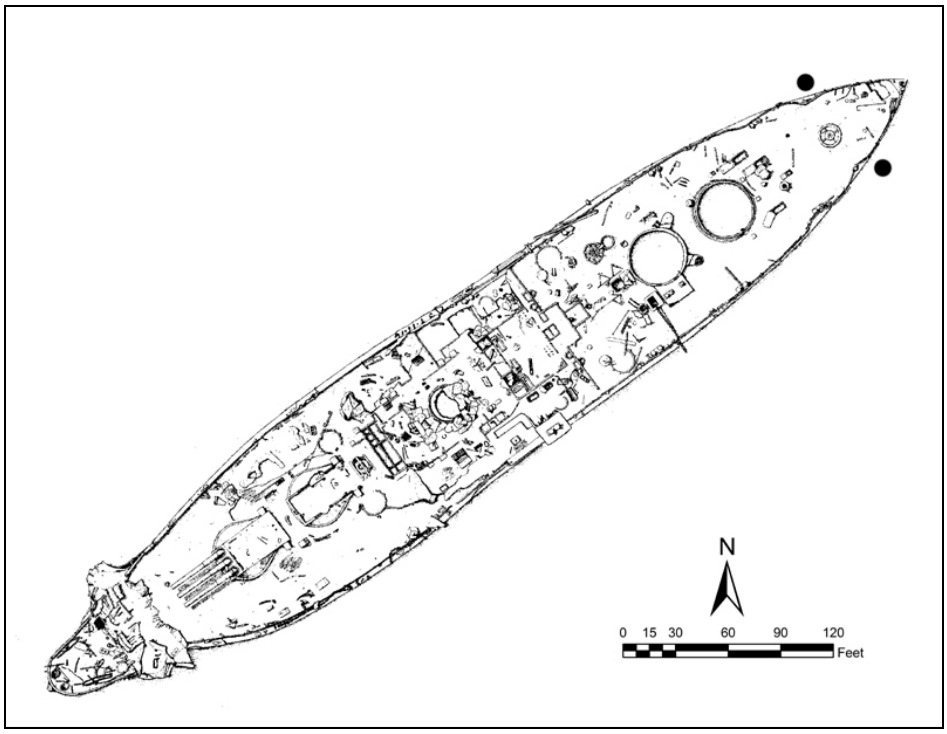

Figure 7.6. Points at the stern indicate sample locations on the exterior hull of USS *Arizona.* Sample 14 was collected on the port side of the ship and sample 15 on the starboard side (Drawing by NPS-SRC).

previously described (Perry et al. 2005) with primers 27f and 1492r (Lane 1991). The size of PCR products was verified by agarose gel electrophoresis. PCR products were purified using the QIAQuick PCR Purification Kit (Qiagen, Valencia, CA), cloned into the pCR 2.2-TOPO vector, and transformed into competent *Escherichia coli* as described in the manufacturer's instructions (TOPO TA Cloning Kit K4500-01, Invitrogen, Carlsbad, CA).

Clone inserts were PCR amplified from lysed colonies with vector specific primers. PCR products were simultaneously digested with *Msp*I and *Hha*I (Mills et al. 2003). Restriction digests contained 1.0 µg DNA and 5 units of each enzyme and were incubated at 37°C for three hours. Clones were grouped according to restriction fragment length polymorphism (RFLP) banding patterns and rarefaction curves were calculated for the RFLP patterns (Simberloff 1978). The diversity of sample 15 was estimated using Chao1 (Hughes et al. 2001).

Representative clones from each RFLP group were sequenced at the Dana Farber/Harvard Cancer Center High-Throughput DNA Sequencing Facility (Cambridge, MA) using a 3700 DNA Analyzer (Applied Biosystems, Foster City, CA) as described in the

manufacturer's instructions. Unaligned sequences were compared to the National Center for Biotechnology Information database using the Basic Local Alignment and Search Tool (BLAST) to find closely related sequences (Altschul et al. 1997). Alignments were constructed using Clustal X (Thompson et al. 1997) and phylogenetic analysis was performed using Paup 4.0 beta 10 (Swofford 2003). Sequences were deposited in the National Center for Biotechnology Information (NCBI) GenBank database.

RESULTS

We examined the bacterial community from two concretion samples removed from the exterior hull of USS *Arizona*. Bacterial numbers were not significantly different between samples (sample 14: $1.6 \times 10^6 \pm 7.6 \times 10^4$ bacteria/g; sample 15: $6.9 \times 10^6 \pm 1.4 \times 10^6$ bacteria/g; mean±se). Rarefaction analysis of RFLP patterns indicated that bacterial diversity of the concretion samples was low (Figure 7.7). Only six different RFLP patterns were found in sample 14, and 12 different RFLP patterns were observed in clones from sample 15. Using Chao1, the estimated diversity of sample 15 was 14.7.

Representative clones from each RFLP pattern were sequenced and compared to the NCBI database using BLAST (Table 7.1). The closest BLAST matches to all sequences were from organisms isolated from marine environments. All clones, with the exception of clone 15-1, contained sequences that were ≥ 96% similar to the closest BLAST match. Clone 15-1 was 92% similar to the 16S rDNA of an uncultured bacterium from a hypersaline endoevaporitic microbial mat.

All clones were closely related to sequences obtained from bacteria belonging to three Phyla: Firmicutes, Flavobacteria, and Proteobacteria (Figure 7.8). Two of the clones (11% of all clones) were affiliated with the Firmicutes. Both clones were phylogenetically associated with organisms that are endospore forming anaerobes (i.e., *Alkaliphilus*, *Clostridum*, and *Tepidibacter*). Six of the clones (33% of all clones) were affiliated with the Proteobacteria. Three of these clones were closely associated with α-Proteobacteria and three were closely associated with γ-Proteobacteria. The majority of clones that were sequenced (10 clones or 55%) were phylogenetically affiliated with the Bacteroidetes.

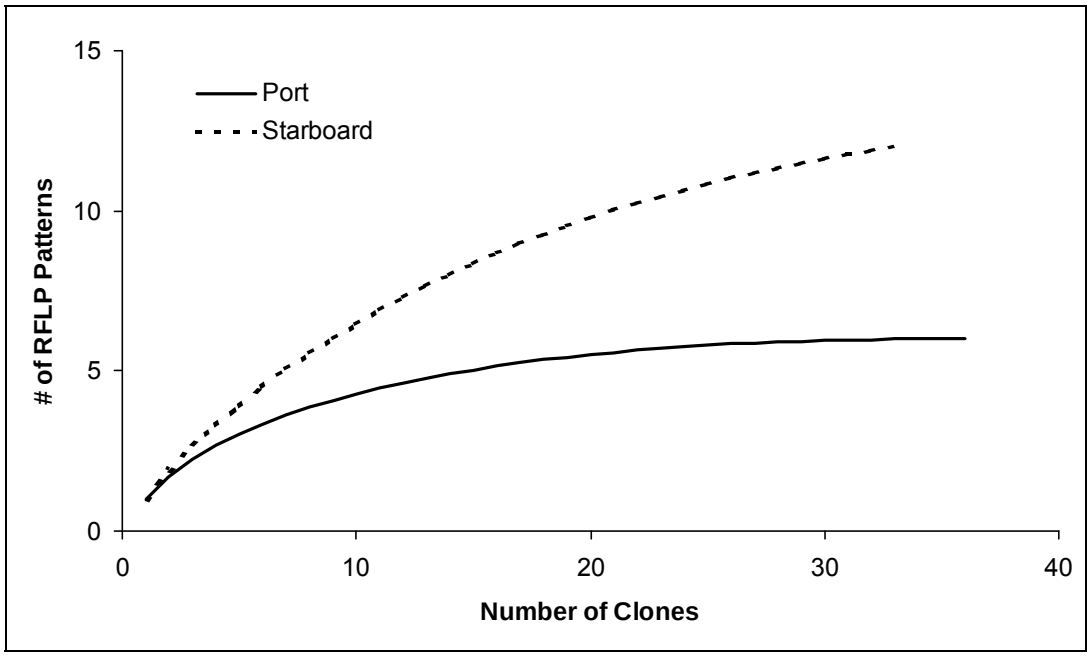

Figure 7.7. Rarefaction analysis of RFLP patterns from concretion samples.

DISCUSSION

Bacterial abundance in the concretions was similar to abundances typically reported for aquatic communities and for bacteria associated with stone and mineral formations (Linley 1983; McNamara et al. 2006). Despite the rather typical densities of microorganisms, the diversity of bacteria in the concretion was quite low, consisting of 18 different RFLP patterns representing bacteria from just three Phyla. The low bacterial diversity of the concretion communities was unexpected given the high diversity commonly found in marine systems (Giovannoni et al. 1990; Bernard et al. 2000).

All of the sequenced clones were similar to bacteria from seawater or marine invertebrates (based on the BLAST results). Phylogenetic affiliation of two clones with class Clostridia in the Firmicutes (anaerobic endospore formers) may indicate that there are anoxic microhabitats within the concretion. On the other hand, their presence could be due to the persistence of endospores in the concretion. The three clones that were phylogenetically associated with the α-Proteobacteria clustered with sequences from the genera *Roseobacter* and *Hyphomonas*, which are common in sea water and have been found associated with shellfish

(Jannasch and Wirsen 1981; Prabagaran et al. 2007). Among the γ-Proteobacteria-affiliated clones, *P. eurosenbergii* is associated with corals and coral bleaching (Thompson et al. 2004) while *H. venusta* is a moderate halophile that may be associated with fish (von Graevenitz et al. 2000). Within the Bacteroidetes, almost all clones were affiliated with the class Flavobacteria, which is extremely common in many environments, including seawater (Weeks 1981).

Sample Location	Clone	Putative Group	Closest BLAST Match (GenBank Accession No.)	% Similarity	No. of Clones (% Representation)[a]	Accession No.
Port	14-2	Bacteroidetes	*Formosa* sp. 5IX/A01/134 (AY576730)	100	3 (13)	EF173601
Port	14-3	γ-Proteobacteria	*Photobacterium eurosenbergii* strain LMG 22223T (AJ842344)	99	2 (8)	EF173602
Port	14-9	Bacteroidetes	*Flavobacterium* sp. V4.MO.31 (FSP244697)	97	4 (17)	EF173603
Port	14-14	α-Proteobacteria	*Roseobacter* sp. H454 (AY368572)	99	2 (8)	EF173604
Port	14-27	Bacteroidetes	*Flavobacterium* sp. V4.BO.21 (FSP244691)	97	12 (50)	EF173605
Port	14-29	Bacteroidetes	*Winogradskyella poriferorum* strain UST030701-295 (AY848823)	99	1 (4)	EF173606
Starboard	15-1	Bacteroidetes	Uncultured bacterium clone E2aA01 (DQ103638)	92	1 (3)	EF173607
Starboard	15-2	Bacteroidetes	*Formosa* sp. 5IX/A01/134 (AY576730)	100	1 (3)	EF173608
Starboard	15-4	Bacteroidetes	*Muricauda aquimarina* strain SW-72 (AY445076)	99	1 (3)	EF173609
Starboard	15-8	Firmicutes	Uncultured Gram-positive bacterium isolate MZ-31.NAT (AJ810555)	99	3 (9)	EF173610
Starboard	15-14	Bacteroidetes	*Salegentibacter* sp. 6-16 (AJ783959)	99	11 (33)	EF173611
Starboard	15-18	Bacteroidetes	*Gillisia mitskevichiae* (AY576655)	96	3 (9)	EF173612
Starboard	15-23	α-Proteobacteria	*Roseobacter* sp. JL-126 (AY745859)	100	3 (9)	EF173613
Starboard	15-25	α-Proteobacteria	*Hyphomonas jannaschiana* strain ATCC 33883 (T) (HJJ227814)	97	1 (3)	EF173614
Starboard	15-30	γ-Proteobacteria	*Halomonas* sp. BYS-1 (AY062217)	99	2 (6)	EF173615
Starboard	15-31	Firmicutes	Uncultured Gram-positive bacterium clone LR-39 (DQ302459)	98	2 (6)	EF173616
Starboard	15-39	Bacteroidetes	Marine bacterium KMM 3909 (AF536383)	96	3 (9)	EF173617
Starboard	15-40	γ-Proteobacteria	*Vibrio* sp. V261 (DQ146982)	98	2 (6)	EF173618

[a]Percent representation within each sample.

Table 7.1. Summary of 16S rRNA gene sequences identified in the clone library.

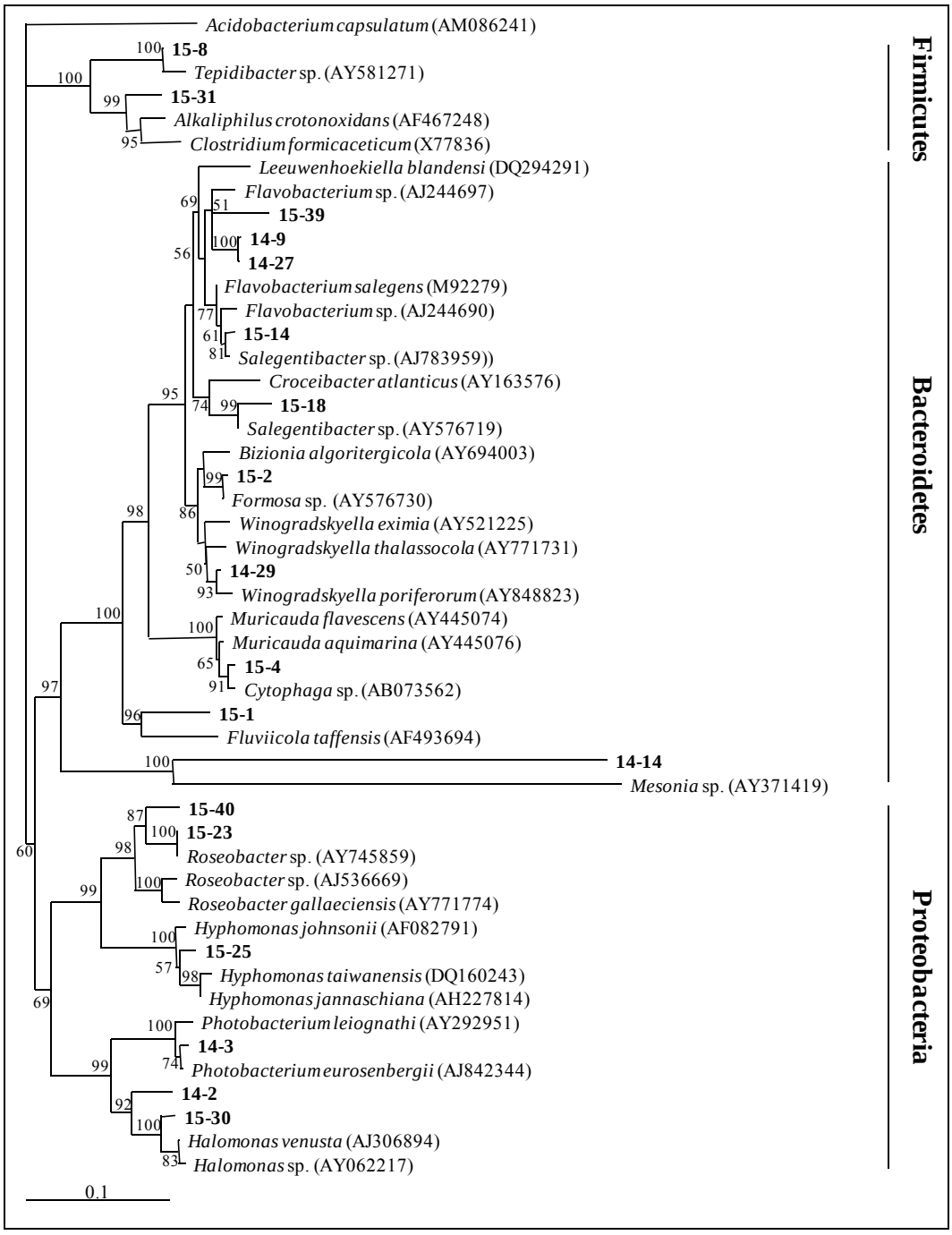

Figure 7.8. Neighbor joining tree based on 16S rDNA sequences of clones isolated from USS *Arizona*. Bootstrap values based on 1000 replicates are indicated for branches supported by >50% of trees. Scale bar represents 0.1 nucleotide changes per position.

There are similarities between the concretion communities from USS *Arizona* and other biofouling communities. For example, Moss et al. (2006) found that large percentages of estuarine biofilms were composed of Proteobacteria. Shikuma & Hadfield (2005) examined changes in biofilms in Pearl Harbor and found a stable community, composed mainly of Proteobacteria, which persisted over time at increasing densities. Similarities between these early-stage fouling communities and the bacterial community observed in concretions on USS *Arizona* suggest that the concretion community may be a stable, late successional-stage community that has developed from earlier attached communities.

Alternatively, the low diversity in concretions could result from residual antifouling paint on the hull. USS *Arizona* was completely retrofitted in March 1939. At that time, the U.S. Navy used copper or mercuric oxides contained in a variety of binders as antifoulants (Candries 2000). Many groups within the Bacteroidetes, a significant component of USS *Arizona* clones, are metal resistant (Jackson et al. 2005). The toxic antifouling paint may have limited early colonization and survival by bacteria, thereby resulting in low diversity in the mature fouling layer.

CONCLUSIONS

The bacterial community in concretions on the hull of USS *Arizona* is dominated by organisms from three groups: Firmicutes, Flavobacteria, and Proteobacteria. To our knowledge, this is the first study to examine the bacterial community of a late stage marine fouling concretion on archaeological materials. Further investigations of concretion microorganisms are needed to determine if the results obtained here are applicable to concretions on other submerged heritage sites and to determine the effect of the microorganisms on corrosion of the underlying metal.

Ultimately, this research is a work in progress. Because key elements remained unfunded during the USS *Arizona* Preservation Project, few conclusions can be made regarding the role of microorganisms in *Arizona*'s corrosion rate. Future work to be done on this project includes further study of the potential of microorganisms to cause corrosion of A36 steel, determining the effects of environmental factors such as temperature, nutrient levels and redox on MIC, and examining microbial corrosion rates on other types of steel that may be found both in hull structural steel and oil bunkers on both the sea water side and on the interior oil/steel interface.

REFERENCES

Altschul S.F., T.L. Madden, A.A. Schäffer, J. Zhang, Z. Zhang, W. Miller, and D.J. Lipman
1997 Gapped BLAST and PSI-BLAST: a New Generation of Protein Database Search Programs, *Nucleic Acids Research* 25:3389-3402.

Anwar, H., J.L. Strap, and J.W. Costerton
1992 Establishment of Aging Biofilms: Possible Mechanism of Bacterial Resistance to Antimicrobial Therapy. *Antimicrobial Agents and Chemotherapy* 36:1347-1351.

Bernard L., H. Schäfer, F. Joux, C. Courties, G. Muyzer, and P. Lebaron
2000 Genetic Diversity of Total, Active and Culturable Marine Bacteria in Coastal Sea Water, *Aquatic Microbial Ecology* 23:1-11.

Bram J.B., H.M. Page, and J.E. Dugan
2005 Spatial and Temporal Variability in Early Successional Patterns of an Invertebrate Assemblage at an offshore oil Platform, *Journal of Experimental Marine Biology and Ecology* 317:223-237.

Candries M.
12 December 2000 Paint Systems for the Marine Industry, *Notes to Complement the External Seminar on Antifoulings*, Department of Marine Technology, University of Newcastle-upon-Tyne, http://www.geocities.com/maxim_candries

Christensen, B.E. and W.G Characklis
1990 Physical and Chemical Properties of Biofilms, In *Biofilms*, edited by W.G. Characklis and K.C. Marshall, John Wiley and Sons Inc., New York.

Costerton, J.W., Z. Lewandowski, D.E. Caldwell, D.R. Korber, and H.M. Lappin-Scott.
1995. Microbial Biofilms. *Annual Review of Microbiology* 49:711-745.

Costerton, J.W., P.S. Stewart, and E.P. Greenberg
1999. Bacterial biofilms: A Common Cause of Persistent Infections. *Science* 284:1318-1322

de Beer, D., P. Stoodley, F. Roe, and Z. Lewandowski
1994. Effects of Biofilm Structures on Oxygen Distribution and Mass Transport. *Biotechnology and Bioengineering* 43:1131-1138.

Ford, T.E. and R. Mitchell
1991. The Ecology of Microbial Corrosion. In *Advances in Microbial Ecology,* Vol. 11, edited by K.C. Marshall, Plenum Press, New York

Giovannoni S.J., T.B. Britschgi, C.L. Moyer, and K.G. Field
1990 Genetic Diversity in Sargasso Sea Bacterioplankton, *Nature* 345:60-63

Gu, J.-D., T.E. Ford, and R. Mitchell
2000 Microbial Corrosion of Metals. In *Uhlig's Corrosion Handbook, Second Edition,* edited by R. Winston Revie, John Wiley and Sons Inc., NY.

Hughes J.B., J.J. Hellman, T.H. Ricketts, and J.M. Bohannan
2001 Counting the Uncountable: Statistical Approaches to Estimating Microbial Diversity, Applied Environmental Microbiology 67:4399-4406.

Jackson CR, KG Harrison, and S.L. Dugas
2005 Enumeration and Characterization of Culturable Arsenate Resistant Bacteria in a Large Estuary, *Systematic Applied Microbiology* 28:727-734.

Jannasch H.W., and C.O. Wirsen
1981 Morphological Survey of Microbial Mats Near Deep Sea Thermal Vents, Applied Environmental Microbiology 41:528-538.

Johnson, D.L., W.N. Weins, J.D. Makison, and D.A. Martinez
1999 Metallographic Studies of the USS *Arizona*. Proceedings of the International Metallographic Society.

Lane D.J.
1991 16S/23S rRNA Sequencing, In *Nucleic Acid Techniques in Bacterial Systematics*, edited by E. Stackebrandt, and M. Goodfellow, pp. 115-175, John Wiley and Sons, New York

Linley E.A.S., R.C. Newell, and M.I. Lucas
1983 Quantitative Relationships Between Phytoplankton, Bacteria, and Heterotrophic Microflagellates in Shelf Waters, *Marine Ecology Progress Series* 12:77-89.

Maki J.S., D. Rittschof, A.R. Schmidt, A.G. Snyder, and R. Mitchell
1989 Factors Controlling Attachment of Bryozoan Larvae: A Comparison of Bacterial Films and Unfilmed Surfaces, *Biology Bulletin* 177:295-302.

Makinson J.D., D.L. Johnson, M.A. Russell, D.L. Conlin, and L.E. Murphy
2002 *In situ* Corrosion Studies on the Battleship USS *Arizona*, *Materials Performance* 41:56-60.

Marshall K.C., R. Stout, and R. Mitchell
1971 Mechanism of the Initial Events in the Sorption of Marine Bacteria to Surfaces. *Journal of General Microbiology* 68:337-348.

McEldowney, S. and M. Fletcher
1987 Adhesion of Bacteria from Mixed Cell Suspensions to Solid Surfaces. *Archives of Microbiology* 148:57-62.

McNamara C.J., T.D. Perry, K. Bearce, G. Hernandez-Duque, and R. Mitchell
2006 Epilithic and Endolithic Bacterial Communities in Limestone from a Mayan Archaeological Site, *Microbial Ecology* 51:51-64.

Mills H.J., C. Hodges, K. Wilson, I.R. MacDonald, and P.A. Sobecky
2003 Microbial Diversity in Sediments Associated with Surface-Breaching Gas Hydrate Mounds in the Gulf of Mexico, *FEMS Microbiology and Ecology* 46:39-52.

Moss J.A., A. Nocker, J.E. Lepo, and R.A. Snyder
2006 Stability and Change in Estuarine Biofilm Bacterial Community Diversity, *Applied Environmental Microbiology* 72:5679-5688.

North N.A.
1976 Formation of Coral Concretions on Marine Iron, *International Journal of Nautical Archaeology and Underwater Exploration* 5:253-258.

Page H.M., J.E. Dugan, D.S. Dugan, J.B. Richards, and D.M. Hubbard
1999 Effects of an Offshore Oil Platform on the Distribution and Abundance of Commercially Important Crab Species, *Marine Ecology Progress Series* 185: 45-57.

Perry IV T.D., V. Klepac-Ceraj, X.V. Zhang, C.J. McNamara, M.F. Polz, S.T Martin., N. Berke, and R. Mitchell
2005 Binding of Harvested Bacterial Exopolymers to the Surface of Calcite, *Environmental Science and Technology* 39:8770-8775.

Porter K.G., and Y.S. Feig
1980 The Use of DAPI for Identifying and Counting Aquatic Microflora, *Limnology and Oceanography* 25:943-948.

Prabagaran S.R., R. Manorama, D. Delille, and S. Shivaji
2007 Predominance of Roseobacter, Sulfitobacter, Glaciecola, and Psychrobacter in Seawater Collected off Ushuaia, Argentina, Sub-Antarctica, *FEMS Microbiology and Ecology* 59:342-355.

Rittman, B.E., M. Pettis, H.W. Reeves, and D.A. Stahl
1999 How Biofilm Clusters Affect Substrate Flux and Ecological Selection. *Water Science and Technology* 39:99-105.

Russell M.A., L.E. Murphy, D.L. Johnson, T.J. Foecke, P.J. Morris, and R. Mitchell
2004 Science for Stewardship: Multidisciplinary research on *USS Arizona*, *Marine Technology Society Journal* 38:54-63.

Shikuma N.J., and M.G. Hadfield
2005 Temporal Variation of an Initial Marine Biofilm Community and its Effects on Larval Settlement and Metamorphosis of the Tubeworm *Hydroides elegans*, *Biofilms* 2:231-238.

Simberloff D.
1978 Use of Rarefaction and Related Methods in Ecology, In *Biological Data in Water Pollution Assessment: Quantitative and Statistical Analysis*, edited by K.L. Dickson, J. Cairns Jr., and R.J. Livingston, ASTM STP 652, American Society for Testing and Materials.

Swofford D.L.
2003 *PAUP*. Phylogenetic Analysis Using Parsimony (*and Other Methods),* Ver. 4, Sinauer Associates, Sunderland, Massachusetts.

Thompson F.L., T. Iida, and J. Swings
2004 Biodiversity of Vibrios, *Microbiology And Molecular Biology Reviews* 68:403-431.

Thompson J.D., T.J. Gibson, F. Plewniak, F. Jeanmougin, and D.G. Higgins
1997 The ClustalX Windows Interface: Flexible Strategies for Multiple Sequence Alignment Aided by Quality Analysis Tools, *Nucleic Acids Research* 24:4876-4882.

von Graevenitz A., J Bowman., C. Del Notaro, and M. Ritzler
2000 Human infection with *Halomonas venusta* Following Fish Bite, *Journal of Clinical Microbiology* 38:3123-3124.

van Loosdrecht, M.C.M., J. Lyklema, W. Norde, and A.J.B. Zehnder
1990 Influence of Interfaces on Microbial Activity. *Microbiological Reviews* 54:75-87.

Weeks O.B.
1981 The Genus Flavobacterium, *In The Prokaryotes: a Handbook on Habitats, Isolation, and Identification of Bacteria*, edited by M.P. Starr, H. Stolp, H.G. Trüper, A. Balows, pp. 1365-1370, H.G. Schlegel, Springer-Verlag, New York.

Whitfield, C.
1988 Bacterial Extracellular Polysaccharides. *Canadian Journal of Microbiology* 34:415-420.

Zvyaginstev A.Y.
1990 Fouling and Corrosion Damage to Supporting Pillars of Oil Platforms in the South China Sea, *Soviet Journal of Marine Biology* 15:392-397.

Zvyaginstav A.Y., and V.V. Ivin
1995 Study of Biofouling of the Submerged Structural Surfaces of Offshore Oil and Gas Production Platforms, *Marine Technology Society Journal* 29:59-62.